# CLASSICAL WAVE SIMULATION OF QUANTUM MEASUREMENT

by

Kim Fook Lee

Department of Physics
Duke University

Date:____________________________
Approved:

____________________________
Dr. John E. Thomas, Supervisor

____________________________
Dr. Daniel J. Gauthier

____________________________
Dr. Konstantin Matveev

____________________________
Dr. Robert P. Behringer

____________________________
Dr. Henry Everitt

Dissertation submitted in partial fulfillment of the
requirements for the degree of Doctor of Philosophy
in the Department of Physics
in the Graduate School of
Duke University

2002

ABSTRACT

(Physics)

# Classical Wave Simulation of Quantum Measurement

by

Kim Fook Lee

Department of Physics
Duke University

Date:____________________________
Approved:

________________________________
Dr. John E. Thomas, Supervisor

________________________________
Dr. Daniel J. Gauthier

________________________________
Dr. Konstantin Matveev

________________________________
Dr. Robert P. Behringer

________________________________
Dr. Henry Everitt

An abstract of a dissertation submitted in partial fulfillment of
the requirements for the degree of Doctor of Philosophy
in the Department of Physics
in the Graduate School of
Duke University

2002

# Abstract

This dissertation explores classical analogs of one particle wave mechanics and multi-particle quantum entanglement by using classical wave optics. We develop classical measurement techniques to simulate one particle wave mechanics and quantum entanglement for up to four particles. Classical simulation of multi-particle entanglement is useful for quantum information processing (QIP) because much of the QIP does not require collapse and decoherence is readily avoided for classical fields. The simulation also allows us to explore the similarities and differences between quantum optics and classical wave optics.

We demonstrate the simulation of one particle wave mechanics by measuring the transverse position-momentum (Wigner) phase-space distribution function for a classical field. We measure the Wigner function of a classical analog of a Schrödinger cat state. This Wigner phase-space distribution function exhibits oscillatory behavior in phase space and negativity arising from interference of two spatially separated wave-packets in the cat state. The measurement of Wigner functions for classical fields has practical applications in developing new coherence tomography methods for biomedical imaging.

We develop a classical method to simulate projection measurement in coincidence detection of two entangled photons. This is accomplished by using an analog multiplier and a band pass filter. We measure the classical analog of the joint probability of detection of two photons for the entangled states $\frac{1}{\sqrt{2}}[|H_1V_2\rangle \pm |V_1H_2\rangle]$ and $\frac{1}{\sqrt{2}}[|H_1H_2\rangle \pm |V_1V_2\rangle]$, where $H$ is horizontal polarization and $V$ is vertical polarization. Our measurement method reproduces nonlocal Einstein-Podolsky-Rosen (EPR) correlations for four polarization-entangled Bell states of two particles and violates Bell's inequality. A most interesting result of our measurements is the experimental simulation of three and four particle Greenberger-Horne-Zeilinger (GHZ) entanglement for the entangled states $\frac{1}{\sqrt{2}}[|H_1H_2H_3\rangle + |V_1V_2V_3\rangle]$ and $\frac{1}{\sqrt{2}}[|H_1H_2H_3H_4\rangle + |V_1V_2V_3V_4\rangle]$ respectively. We are able to reproduce the 32 elements of the GHZ polarization correlations between three spatially separated superposition beams which leads to a conflict with local realism for nonstatistical predictions of quantum mechanics. That is in contrast to the two entangled particles test of Bell's inequalities, where the conflict arises for statistical predictions of quantum mechanics. In addition, our classical wave system can be extended to demonstrate a type of entanglement swapping in a four-particle basis. We are able to show that the fundamental technical limitations on distinguishing between all four Bell states in the quantum entanglement swapping experiments is similarly encountered in our classical wave optics experiments.

In our first classical experiments, the joint detection signals are stable oscillatory sinusoidal waves so that probability language is not applicable. To simulate a test of Bell's inequality in a probabilistic way, such as the mean of the product of two observables, we use a classical random noise field which interferes with a classical stable wave field. We develop a classical noise system to reproduce an EPR nonlocal correlation function of two observers A and B. Our setup is able to reproduce measurements of the correlation function and also is able to simulate in part the wave-particle duality property of a two-particle quantum system. We also demonstrate the ability of our optical noise system to reproduce the violation of Bell's inequality.

We believe that the techniques we have developed will provide a foundation for future experiments which simulate simple quantum networks. Implementation of Shor's algorithm, for example, may enable rapid factorization of large numbers using classical wave methods.

# Acknowledgments

Over the past five years, I am grateful for having John Thomas as my advisor. I have learned a great deal under John's supervision from embarking on a new experiment to publishing it. John has shown me how to design classical optics experiment such as two-window heterodyne imaging technique from which the idea was obtained from quantum teleportation experiments. The most exciting part was when John decided to work on classical wave simulation of quantum entanglement which at that time basically both of us didn't know what it meant. After endless spirited discussions and magical twists on the relationships between quantum and classical concepts of quantum entanglement, we are able to come out with an idea to simulate two photon coincidence detection by using analog multipliers and band pass filters. Surprisingly, we ended up measuring two-field correlations instead of two-photon correlations. From my experiences in a few optics laboratories, there is no man to give me guidance like John. John has been a very fair and judicious advisor. I am sure that I will look back on this time in my life with fond memories of how much I have enjoyed working with such a great advisor.

I am particularly indebted to Samir Bali, who introduced Duke University to me when we were in the same laboratory in Arkansas. Samir has introduced me the beautiful physics subject - quantum optics when I was in Arkansas, where at that time I only had knowledge about classical optics. He taught me how to calibrate the single photon photomultiplier tube before it is used to study photon statistics of the nonclassical light. I wish him well in his career at Miami University.

I am also indebted to Adam Wax who provided invaluable guidance for using the equipment in the laboratory for measuring optical phase-space distribution. I am glad he is back from MIT as a faculty member in BioMedical Engineering in Duke.

I am thankful to Frank Reil who built the phase-locked loop used in the two-window heterodyne imaging technique. Without the loop, the whole idea of two-window heterodyne detection would have been useless.

I would like to thank Zehuang Lu for accompanying me so that I am not the only Asian in the group. I enjoyed fishing trips with him and also eating lunch in Chinese restaurants around Durham. He also discussed quantum optics with me.

I would like to thank Ken O'hara for being my officemate. I appreciated his patience to listen to all my physics. I did enjoy to hear the Christmas season song "little drummer boy" from the radio on his desk. I need him to be my future referee.

I enjoyed working with Mike Gehm and Stephen Granade who provided invaluable assistance in part of this project. I appreciated their suggestions for helping me to make my presentation looks more clearly. I did enjoy to "pool" with them in the spare night of the QELS Conference in Baltimore.

I also had fun with Ming Shien when he was in Duke. I wish him good luck at George Tech.

I have also enjoyed working with the newer students in our group: Joe Kinast and Staci Hemmer. The reason is they leave me alone!

I have had the opportunity to work with a number of bright and talented graduate students while at Duke. Umit Ozgur is always willing to help whatever new piece of equipment was required for my experiment such as lenses, analog multipliers, lock-in amplifier and DC power supply. I am also thankful to Jonathan Blakely, Michael Stenner and Seth Boyd in Daniel Gauthier's group who lent me the NeHe laser source and analog multiplier. I hope that I can return the favor in the near future.

I would also like to acknowledge the contributions of my dissertation committee which included Dr. Daniel Gauthier, Dr. Konstantin Matveev, Dr. Bob Behringer and Dr. Henry Everitt. I appreciate the many helpful comments that they have made regarding this thesis.

Finally, I am thankful to have had my wife Wan Yee by my side throughout my graduate career. I could not have made it through graduate school without her. She is my best friend and has been incredibly supportive of me in our life together.

*For Wan Yee Koh, with love*

# Contents

# List of Figures

# Chapter 1

# Introduction

Quantum mechanics has been applied to develop quantum information technology by exploiting the fundamental features of quantum mechanics such as superposition and entanglement. In this dissertation, I present optical methods for classical wave simulation of these two fundamental quantum features. Simulation has become an important topic because of similarities between quantum and classical wave interference. The potential of classical wave optics to simulate multi-particle state superposition and entanglement is the primary motivation and objective for the current work. As an introduction, I discuss the basic concepts of the linear superposition principle and entanglement. Then, I outline some recent developments in quantum information technology and the classical wave simulation of this technology. Finally, I schematically outline the organization of this thesis chapter by chapter. I will begin by describing the motivation of this work.

## 1.1 Motivation

Classical wave simulation of the linear superposition principle and entanglement is an initial step to develop an alternative tool to implement quantum information processing. The study is motivated by the knowledge that much of quantum information processing does not require collapse, and particle properties of a quantum system are not required. Since classical fields are able to simulate superposition and entanglement, it is important to explore these simulations for quantum information processing. Classical simulation of multi-particle entanglement is useful to study the similarities and differences between quantum optics and classical wave optics especially in quantum applications such as quantum cryptography and teleportation, quantum computation, and also development of quantum sensor devices.

Quantum interference features of a single particle such as an electron in the two-slit Young experiment can be reproduced by using a classical beam. In addition, the wave equation of an optical field in a lens-like medium is identical in structure to the Schrödinger wave equation of a quantum harmonic oscillator. The phase-space representation of a quantum harmonic oscillator, where its trajectory is represented by position $x$ and momentum $p$ coordinates, can be simulated by classical spatial transverse modes. However, classical fields normally lack of the wave-particle duality properties. Hence, it is important to explore the possibility of simulation of wave-particle duality properties of a quantum system by using classical fields.

Most of the nonclassical features of quantum mechanics such as nonlocality and entanglement are best exhibited by systems containing more than one particle. Quantum entanglement has been applied to information processing and communication [1–5]. It is a consequence of correlations in second order coherence theory of quantum interferences exhibited by two spatially separated particles. A pair of entangled particles which exhibits quantum entanglement always shows nonlocality features: A measurement of one particle will reveal a property of its entangled pair even though they are initially separated in space. Before a quantum system is used for quantum information processing, the nonlocal character of the system is tested, such as a test of Bell's inequalities for two entangled particles or a Greenberger-Horne-Zeilinger (GHZ) test of local realism for three entangled particles. Classical wave simulation of nonlocal entanglement analogs of second or higher order coherence, i.e., multi-particle states, have been relatively unexplored.

In quantum information processing, an quantum system is subjected to imperfections of preparation and measurement of the state, and also the imperfection of evolution in the Hamiltonian of the system. Decoherence is a primary problem in quantum information processing, because a quantum state might interact with its environment and randomize its relative phase with all possible states in the quantum system. However, this will not be the case if classical wave optics is used to implement quantum information processing.

In addition, applications such as quantum computing requires engineering of very large entangled states in a reasonable amount of time and using a reasonable amount of resources. The preparation of entanglement involving many particles remains an experimental challenge. Thus, the studies of classical wave simulation of linear superposition and entanglement will provide us with alternative resources in quantum information processing.

In the following, I will describe two fundamental features of quantum mechanics in quantum information technology.

## 1.2 Fundamental Features of Quantum Mechanics

Two features of the quantum world are superposition and entanglement. I would like to illustrate each idea by giving a brief introduction to the linear superposition principle and entanglement from both particle and wave viewpoints.

### 1.2.1 Superposition Principle

The principle of superposition is the first principle of quantum mechanics. The properties of this principle in both particle and wave viewpoints have been discussed in detail in the popular Feynman lectures on physics vol.III [6]. They can be summarized by three statements. First, the probability of an event $P$ in an ideal experiment is given by the absolute square of a complex number or wave function $\phi$ which is also called a probability amplitude. Second, when the same event can occur in several alternative ways, the probability amplitude for the event is the sum of the probability amplitudes for each way, that is $\phi$=$\phi_1$+$\phi_2$+.. . Then the probability exhibits interference since $P$=$|\phi_1 + \phi_2 + ...|^2$. Third, if an experiment is performed which is capable of determining whether one or another alternative is actually taken, such as to determine which path an electron follows in a two-slit experiment, the probability of the event is the sum of the probabilities for each alternative, that is $P$=$|\phi_1|^2 + |\phi_2|^2 + ...$, so the interference terms are lost. Quantum information processing, such as quantum computation and quantum communication, requires operations on quantum bits, or qubits. A qubit is a superposition of two orthogonal quantum states $|0\rangle$ and $|1\rangle$.

### 1.2.2 Quantum Entanglement

Entanglement is a consequence of quantum interference of two particles. A two-particle entangled state is a product state that cannot be factorized such as $|\psi^-\rangle = \frac{1}{\sqrt{2}}(|H_1V_2\rangle - |V_1H_2\rangle)$, where $H$ and $V$ are horizontal and vertical polarizations for particles 1 and 2. Entanglement of these two particles can then be described as follows: Before particle 1 is measured, it has 50% to be $|H_1\rangle$ and 50% to be $|V_1\rangle$, and similarly for particle 2. Suppose now that particle 1 is measured to have horizontal polarization, $H_1$. Then the state $|\psi^-\rangle$ collapses into the product state $|H_1 V_2\rangle$. This implies that particle 2 will have vertical polarization even though it hasn't been measured. A similar situation holds for the collapse of the state $|\psi^-\rangle$ into the state $|V_1 H_2\rangle$. In addition, contributions from these two amplitudes $|H_1 V_2\rangle$ and $|V_1 H_2\rangle$ for a joint probability measurement in coincidence detection with arbitrary polarizations leads to two particle in interference and the violation of Bell's inequalities. From an experimental point of view, the significance of the entangled state $|\psi^-\rangle$ is exhibited by coincidence detection of two particles. The duality properties of the two-photon entangled system $|\psi^-\rangle$ can be described as follows: First, the particle character of the two photons is exhibited in coincidence detection, that is a '*click*' in one detector and a '*click*' in another detector. Second, the wave character of the two photons is exhibited in quantum interference that arises from interfering contributions from $|H_1 V_2\rangle$ and $|V_1 H_2\rangle$.

## 1.3 Quantum Information Technology

Since the seminal paper describing the Einstein-Podolsky-Rosen (EPR) paradox [7], countless discussions on interpretation of quantum mechanics have given rise to the invention of Bell's theorem, concepts of nonlocality, and interpretation of measurements in quantum physics. In recent years, however, the foundations of quantum mechanics have been applied to information technology. Bell's theorem [8, 9] has shown that two spatially separated particles in a system described by a entangled state exhibit a strong quantum correlation for a measurement made on one of the particles. According to Bell's theorem, these bipartite correlation measurements cannot be simulated by any classical system or predicted by any hidden variable theory. It is this nonlocality behavior of these two particles that make quantum mechanics so unique for certain applications [10] such as quantum teleportation, quantum cryptography and quantum computation.

Quantum information processing can be implemented by using single particle entanglement and multi-particle entanglement. The Deutsch-Jozsa algorithm [11, 12] and Shor's quantum algorithm for factoring large numbers [13] show that quantum physics enriches our computation possibilities far beyond classical computers. Classical computers perform operations on information stored as classical bits (1 or 0). Quantum computers perform operations on quantum bits, or qubits, each of which is in a superposition of two orthogonal quantum states. Quantum search algorithms in a database of N objects allows a speed up of $\sqrt{N}$ over classical devices [14].

Linear optics devices and single photon sources can be used in quantum information processing. In single photon interferometry experiments, "which path" variables can be substituted for a quantum bit. Linear optics simulation of quantum logic using single photon experiments that exhibit local entanglement, such as polarization and position, have been proposed [15]. A linear optics circuit involving n qubits requires in general n successive splitting stages of the incoming beam, that is $2^n$ optical paths are obtained via $2^n - 1$ beam splitters. Hence, for a single-photon optical setup, it is difficult to avoid an exponential increase in the size of the apparatus as n increases. Linear optics techniques employing single photon representation are thus limited to the simulation of quantum networks involving a relatively small number of qubits. This is in contrast with traditional optical models of quantum logic, where in general n photons interacting through nonlinear devices (acting as two-bit quantum gates) are required to represent n qubits. Such models typically make use of the Kerr nonlinearity [16, 17] to produce intensity-dependent phase shifts, so that the presence of a photon in one path induces a phase shift to a second photon. However, a scheme has been proposed to exhibit efficient quantum computation in a single photon model by using linear optics with conditional feedback [18], where the exponential expansion of physical system can be avoided. Similarly, it has been shown theoretically that linear optics and projective measurements are able to create large photon number path entanglement [19].

Recently, a hybrid approach has been suggested employing single photon implementations using quantum nondemolition measurement (QND) to entangle separated one-photon interferometers [20]. A controlled Not gate has been proposed by employing QND and linear integrated optics. Two single photon input bits are required, one is control bit and another one is target bit. When the control bit is $|0\rangle$, the target bit is left alone. When the control bit is $|1\rangle$, the target bit is changed from initial $|0\rangle$ to final $|1\rangle$ and vice versa.

Quantum cryptography employing single photon sources for key distributions has been proposed. The scheme is called BB84 [21] named after Bennet and Brassard for their paper on quantum key distributions. In this scheme, single photons are prepared at random in four partly orthogonal polarization states: $0°$, $45°$, $90°$ and $135°$, where they are transmitted from observer A to observer B. If the eavesdropper, Eve, interrupts the channel, she will inevitably introduce errors, which observers A and B can detect by comparing a random subset of the generated keys. Instead of using the four polarization states, a novel method based on single photon interference in the sidebands of phase modulated light has been demonstrated for key distributions [22].

Quantum information processing involving multi-particle entanglement is more efficient than a single particle system. In general, the more particles that can be entangled, the more clearly nonclassical effects are exhibited and the more useful the states are for quantum applications.

Quantum key distributions employing two entangled photons have been proposed by Ekert [23]. The Ekert scheme uses Bell's inequality to establish security of a quantum communication channel between observers A and B. Alternatively, a novel key distribution scheme using Bell's inequality has been experimentally demonstrated to test the security of the quantum channel [24]. Any attempt by the eavesdropper, Eve, to steal the information by replacing the entangled photon by another photon from another source will be detected by two observers A and B, because the interruption reduces the degree of violation of Bell's inequality. This fact is substantiated by the quantum no-cloning theorem [25].

Nuclear magnetic resonance (NMR) quantum computation has been demonstrated to be a promising idea to realize quantum algorithms such as to implement the Deutsch-Jozsa (D-J) algorithm [12] in a bulk nuclear magnetic technique [26]. However, the technique is complicated to implement because it involves nuclear spins of complex systems such as chloroform molecules. Further, it does not prepare pure states, only mixtures.

Teleportation of a photon with an arbitrary quantum state was proposed by Bennet [27]. Quantum teleportation of a photon with an arbitrary quantum state has been experimentally demonstrated in Zeilinger's group [28] by using two entangled photons. In this experiment, observers A and B each possesses one entangled photon. Observer A performs a joint measurement on the entangled photon and the photon from an arbitrary quantum state which is going to be teleported. After this measurement is performed, the second photon of the two entangled photons is projected onto a state which is identical to the teleported state. According to Bennet's scheme, the teleportation efficiency is 25%. In addition, experimental demonstration of entanglement swapping or teleportation in a four photon basis has been observed by using two independently created photon pairs [29].

Quantum information processing with continuous quantum variables by using correlated nonclassical fields has become important [30]. Theories for quantum teleportation of continuous variables have been developed for broad bandwidth teleportation [31] and for teleportation of atomic wave packets [32]. Teleportation of a quantum state by using two-particle Einstein-Podolsky-Rosen (EPR) correlations is also proposed [33]. Experimental verification of the teleportation scheme with continuous variables has been implemented by Kimble's group [34, 35], where the arbitrary teleported state is represented by a Wigner phase-space distribution. In this teleportation experiment, nonclassical correlations between the quadrature-phase amplitudes of two spatially separated optical fields are exploited.

### 1.3.1 Problems in Quantum Information Processing

In an ideal quantum computer, a qubit is assumed to be perfectly isolated from its environment. In other words, the logical qubit is supposed to evolve unitarily in accordance with Schrödinger's equation. Frequently, this is unattainable because of unavoidable decoherence of a quantum system with its environment. The logical qubit no longer evolves in accordance with Schrödinger's equation. However, this can be readily avoided if the qubits representing the computation basis are simulated by classical fields.

The weak point of nuclear magnetic resonance (NMR) computing is that the computation results are always given by an average over a large number of quantum systems, so projection measurement cannot be implemented. In addition, the input qubits in NMR processing are prepared in incoherent entangled states. Even though the NMR technique is able to demonstrate multi-particle entanglement, the incoherent mixture and inability to perform projection measurement have increased the complexity of the technique. Projection measurements in a nonlinear optical system are ideal for creating multi-particle entanglement. However, until recently, the preparation of entanglement between three or more particles has been an experimental challenge. Quantum computation by using linear optics devices which allow projection measurement has become an alternate testing ground for quantum algorithms.

Another problem in quantum information processing is that current two-particle quantum teleportation experiments have encountered fundamental technical limitations on distinguishing between all four Bell states. This restriction reduces teleportation efficiency to 25%. It is worth illustrating this problem in detail because it is one of the goals of this dissertation to show that similar problems are encountered in classical wave systems.

The problem can be described as follows: In a two-photon system, the four Bell states are given by

$$\begin{aligned}|\Psi^{\pm}\rangle_{12} &= \frac{1}{\sqrt{2}}\left(|H_1V_2\rangle \pm |V_1H_2\rangle\right)\\ |\Phi^{\pm}\rangle_{12} &= \frac{1}{\sqrt{2}}\left(|H_1H_2\rangle \pm |V_1V_2\rangle\right)\end{aligned} \tag{1.1}$$

where $|H\rangle$ and $|V\rangle$ are vertical and horizontal polarizations. As shown in Figure 1.1, beam 1 consists of a superposition state $\frac{1}{\sqrt{2}}(|H_1\rangle + |V_1\rangle$, and similarly, beam 2 is in the state $\frac{1}{\sqrt{2}}(|H_2\rangle + |V_2\rangle$. These two beams are mixed on a beamsplitter and then measured by coincidence detection with two detectors 1 and 2. When the polarizers 1 and 2 are orthogonal to each other [36], the coincidence detection of

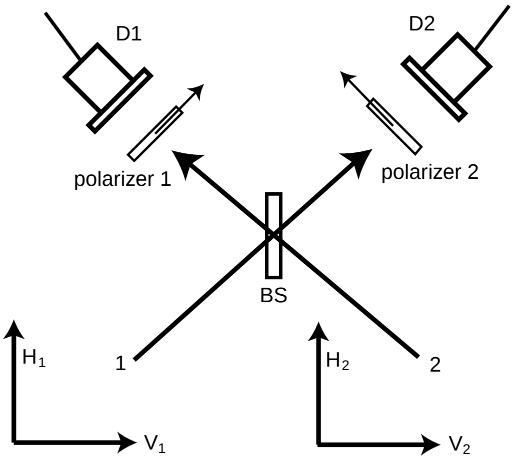

**Figure 1.1**: The detection scheme of coincidence detection of two photons in a 50-50 beamsplitter.

two photons identifies only the state $|\Psi^-\rangle_{12}$. This is because of the $\pi$-phase shift introduced by the beamsplitter. Thus, with the orthogonal setting of polarizers 1 and 2, the state $|\Psi^+\rangle_{12}$ cannot be identified by looking at the coincidence detection of two photons. Similarly, the remaining two states $|\Phi^\pm\rangle_{12}$ are identified together by detecting two photons at either one detector when the polarizers 1 and 2 are parallel to each other. Then, coincidence detection is only able to identify the state $|\Psi^-\rangle_{12}$. This restriction has reduced quantum teleportation efficiency to 25% [37]. This technical problem encountered by quantum measurements in quantum entanglement swapping or teleportation scheme is also encountered in our classical scheme, as described in a later chapter.

## 1.4 Previous Study of Classical Wave Simulation of Quantum Entanglement

The previous study of classical wave simulation of quantum entanglement has been limited for a single particle entanglement. As mentioned in Section 1.2, a fundamental principle of quantum mechanics is the linear superposition principle, that is a summation of quantum mechanical amplitudes, which leads to a wide range of quantum interference phenomena. Similarly, wave theory based on Maxwell's equations leads to a linear superposition principle for the electric field amplitudes that produces all classical interference phenomena. The linear superposition principle in classical and quantum mechanics arises from the linearity of their corresponding wave equations. The fundamental conceptual difference between quantum and classical interference is that the wave-particle duality exhibited by quantum systems leads to interference between probability amplitudes rather than between measurable classical fields such as the electromagnetic waves.

In the paraxial approximation, the transverse mode of an electromagnetic field obeys a propagation equation which is formally identical to the Schrödinger equation with the time replaced by the axial coordinate. Hence, the transverse modes of the field in a lens-like medium are identical in structure to harmonic oscillator wave functions in two dimensions. This has given rise to the study of a number of classical-wave analogs of quantum wave mechanics, including analogs of Fock states [38] and measurement of Wigner functions for an optical gaussian beam [39]. The exploration of classical mode concepts has been limited principally to measurement of first order coherence, i.e., single particle states. It has also been shown that single photon quantum interference can be fully reproduced by classical wave interference [40,41].

Currently, there is great interest in classical wave simulation of quantum logic and quantum measurement. Classical wave simulation of quantum entanglement has been receiving considerable attraction [42–44] because some of the essential properties of quantum information processing are wave mechanical, such as in a single photon implementation of quantum logic [20, 40]. The simulation is equivalent to an analog electronic computer which reproduces the interferences that arise in a quantum system. Analogous to quantum systems, classical wave fields obey a superposition principle, enabling operations with superposition states on which much of quantum information processing is based. Since decoherence is readily avoided, classical fields are well suited for simulating the unitary evolution of a quantum system.

The reversibility of the optical matrix transformation method for classical wave propagating through linear optical devices such as beam splitters, polarizers and phase shifters (half and quarter-wave plates) can be used to simulate the unitary operations in quantum information processing. In search algorithms without entanglement, it is possible to construct quantum and classical wave devices that provide a $\sqrt{N}$ speed up over classical search devices that use particles [45]. Recently, a Grover's quantum search algorithm has been implemented as by using classical Fourier optics [46]. This work also demonstrated that classical wave simulation of Grover's algorithm can search a N-item database as efficiently as a quantum system. The exploration of these analogs is necessary to develop a classical wave analog of quantum algorithms in quantum computation, quantum teleportation and cryptography.

Classical simulation of properties of a single particle entanglement has been discussed in detail by Spreeuw [44], including quantum information processing and violation of generalized Bell's inequalities where the proposal scheme depends only on sums of single particle detection signals. It has also shown theoretically that classical wave systems which simulate single particle interference fail to simulate quantum nonlocality because a single particle cannot be sent to two spatially separated observers. In addition to potential practical applications, study of classical wave systems will help to elucidate the fundamental similarities and differences between classical wave and quantum systems.

## 1.5 Organization of the Thesis

This thesis contains seven chapters. This section provides a brief introduction to the subjects that will be discussed in each chapter.

Chapter 2 presents the linear superposition principle and quantum entanglement from classical and quantum viewpoints. Similarities between first order classical and quantum interferences are illustrated theoretically by plotting a Wigner function for an classical wave analog of a Schrödinger cat state. Entanglement, which is the main topic of the classical simulation work in this thesis, is discussed in detail together with non-quantum and quantum formulations of Bell's Inequalities. The "*bracket*" notation for a quantum state is represented in classical simulation notation as "*parenthesis*" notation [44].

In Chapter 3, measurement of Wigner phase space distributions for an optical classical field is used to study the similarities between quantum and classical interference. This measurement shows an interesting analog between quantum and classical fields, such as Wigner distributions with a negative region. A novel two-window heterodyne imaging technique is developed for these measurements [39]. In this technique, a local oscillator beam is comprised of a phase-locked superposi-

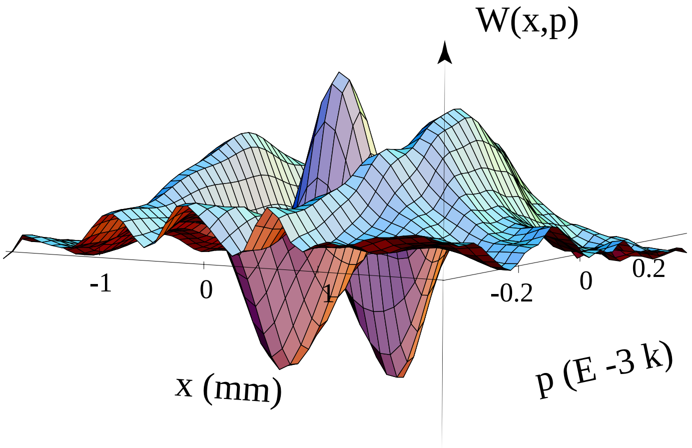

**Figure 1.2**: The experimentally measured Wigner phase space distribution for an optical classical field analog to the Schrödinger's cat state.

tion of a large collimated gaussian beam and a small focused gaussian beam. This scheme permits independent control of the position $x$ and momentum $p$ resolution. The technique measures the $x-p$ cross correlation, $\langle E^*(x)E(p)\rangle$, of an optical field $E$ in transverse position $x$ and transverse momentum $p$. A simple linear transform of the $x-p$ correlation function yields the Wigner phase space distribution. For example, a gaussian beam blocked by a wire produces a classical analog of a Schrödinger cat state, which has a negative Wigner distribution as shown in Figure 1.2. The oscillatory behavior in the phase-space distributions and negative values of the measured Wigner phase space distributions are also observed. In addition, measurement of a product state $E_{H1}(x_1)E_{V2}(x_2)$ for two spatially separated and orthogonally polarized fields is also implemented by using dual heterodyne detection and an analog multiplier. Measurement in a product basis is our initial step for simulating quantum entanglement using classical fields.

In Chapter 4, the experimental simulation of two-particle quantum entanglement using classical fields is demonstrated. We simulate entanglement of two quantum particles using classical fields of two frequencies and two polarizations. The two fields are combined on a beam splitter and the two spatially separated outputs beams are measured by heterodyne detection with two local oscillators of variable polarizations. Multiplication of optical heterodyne beat signals from two spatially separated regions simulates coincidence detection of two particles. The product signal so obtained contains several frequency components, one of which can be selected by band pass frequency filtering. The band passed signal contains two indistinguishable, interfering contributions, permitting simulation of four polarization-entangled Bell-like states. The absolute square of the band passed signal amplitude is analogous to the joint probability $P(\theta_1, \theta_2)$ of detecting two particles with polarization angles $\theta_1$ and $\theta_2$ respectively. The success of reproducing joint probability measurements analogous to quantum predictions encouraged our measurement of violation of Bell's inequalities. Bell's inequality is given as $F(a, b, c){=}P(a, b) + P(b, c) - P(a, c) \geq 0$, where a, b and c are polarization angles of two observers. Local realism theory predicts that $F(a, b, c) \geq 0$. Quantum theory predicts that $F(a, b, c) \leq 0$, and so violates the inequality. The classical analog of violation of the Bell's inequality for one of the four Bell states is shown in Figure 1.3. The classical analog of the inequality is given as $F_{cl}(\theta, 0, \theta) \geq 0$, where the $F_{cl}(a, b, c){=}P_{cl}(a, b) + P_{cl}(b, c) - P_{cl}(a, c)$ and the subscript *cl* denotes classical. The maximum violation, $F_{cl}(\theta, 0, \theta) = -0.25$, occurs when $\theta = 30°$. These classical field methods may be useful in small scale simulations of quantum logic operations that require multi-particle entanglement without collapse.

Chapter 5 demonstrates simulation of three-particle Greenberger-Horne-Zeilinger (GHZ) entanglement [29] by using classical fields. Our experimental scheme produces four spatially separated superposition beams, each consisting of two orthogo-

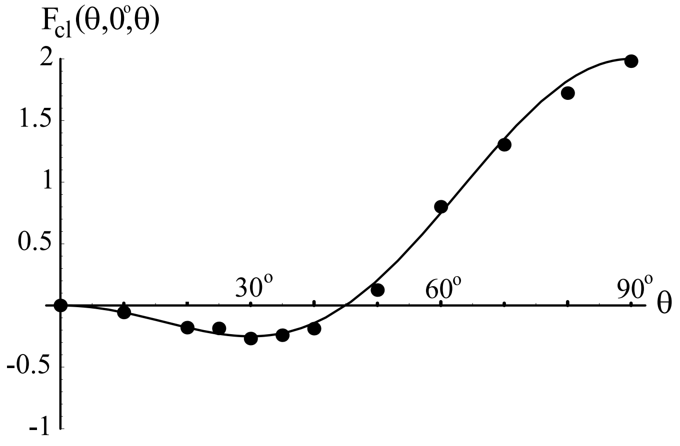

**Figure 1.3**: Classical violation of Bell's inequality for the classical analog Bell state $1/\sqrt{2}[|H_1V_2)+|V_1H_2)]$. A classical analog of the inequality is $F_{cl}(\theta,0,\theta)\geq 0$, where the $F_{cl}(a,b,c)$=$P_{cl}(a,b)+P_{cl}(b,c)-P_{cl}(a,c)$. The maximum violation, $F_{cl}(\theta,0,\theta)=-0.25$, occurs when $\theta=30°$.

nally polarized fields with different frequencies. Multiplication of optical heterodyne beat signals from the four spatially separated regions simulates the fourfold coincidence detection of four particles. Three analog multipliers are used to multiply the signals from the four detectors, where after each multiplication the desired product signal is selected by using band pass frequency filtering. The band passed signal so obtained contains two indistinguishable and interfering contributions, proportional to the projections of $|\mathbf{H_1})|\mathbf{H_2})|\mathbf{H_3})|\mathbf{H_4})+|\mathbf{V_1})|\mathbf{V_2})|\mathbf{V_3})|\mathbf{V_4})$ onto the four LO polarizations, where the subscripts 1, 2, 3 and 4 denote beams 1, 2, 3 and 4. By using three of the four spatially separated beams, our classical system simulates the three-particle GHZ entanglement.

Three particle GHZ entanglement predicts that the three particle element of reality $X_1X_2X_3$ of three photons is equal to $+1$, where the element of reality X has value $\pm1$ when the detected photon has polarization state at $\pm45°$ respectively. The $+45°$ and $-45°$ polarization states are denoted as $H'$ and $V'$ respectively. Lo-

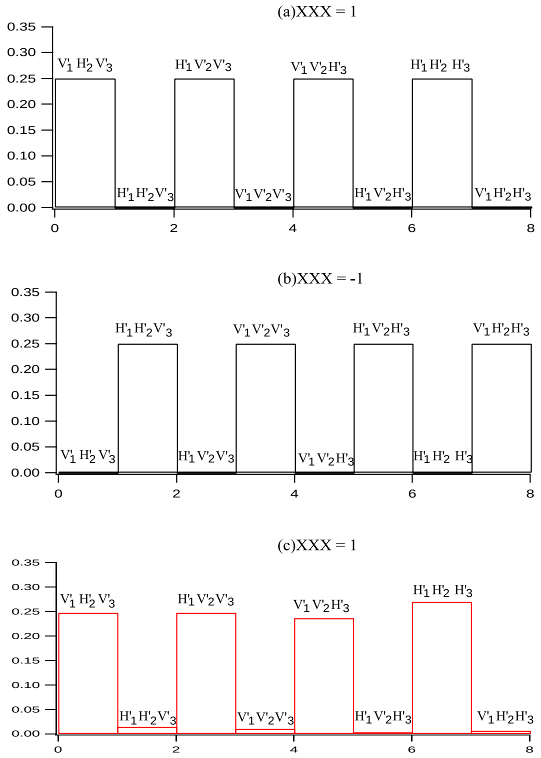

**Figure 1.4**: (a) $X_1X_2X_3 = 1$. Quantum GHZ entanglement predicts the elements of reality $V_1'H_2'V_3'$, $H_1'V_2'V_3'$,$V_1'V_2'H_3'$ and $H_1'H_2'H_3'$ yield nonzero joint probability. (b)XXX = -1, local realism theory predicts elements of reality $H_1'H_2'V_3'$, $V_1'V_2'V_3'$,$H_1'V_2'H_3'$ and $V_1'H_2'H_3'$. (c) Classical wave optics experiment reproduces $X_1X_2X_3 = 1$ analogous to the prediction of quantum theory.

cal realism theory predicts that $X_1X_2X_3$ = -1, in contradiction to the quantum mechanical prediction $X_1X_2X_3 = +1$. Our classical wave optics experiment reproduces the measurement $X_1X_2X_3 = +1$ as shown in Figure 1.4. The classical wave system is able to reproduce measurements analogous to the quantum mechanical predictions and in contradiction with the measurements as predicted by local realism theory. The measurement demonstrates that we can reproduce quantum mechanical three-particle correlations.

Chapter 6 employs the measurement methods developed in Chapter 5 to simulate a type of entanglement swapping in a projection measurement of four photon entanglement. The measurement method shows that similar problems occur in the classical wave system and quantum systems, that is, inability to distinguish between all four Bell states in the process of teleportation or entanglement swapping. In the demonstration of entanglement swapping by using classical fields, the measurement method simulates the projection measurement for a four photon entangled state $|\Psi)_{1234} = |\mathbf{H_1})|\mathbf{H_2})|\mathbf{H_3})|\mathbf{H_4}) + |\mathbf{V_1})|\mathbf{V_2})|\mathbf{V_3})|\mathbf{V_4})$. Observer A possesses beams 1 and 2 and observer B possesses beams 3 and 4. Beams 1 and 2 never interact with one another before measurement and similarly for beams 3 and 4. The four photon entangled state $|\Psi)_{1234}$ obtained from separate projection measurements of A and B can be viewed as follows: A's measurement on beams 1 and 2 yields the classical entangled state $|\phi^+_{cl})_{12} = \frac{1}{\sqrt{2}}[|H_1H_2) + |V_1V_2)]$. Then, the projection ${}_{12}(\phi^+_{cl}|\Psi)_{1234} \propto \frac{1}{\sqrt{2}}[|H_3H_4) + |V_3V_4)]$, showing that observer B will measure the classical entangled state $|\phi^+_{cl})_{34}$. One may notice that measurements of A and B have entangled the beams 1 and 2 and beams 3 and 4 in the same Bell states $|\phi^+_{cl})_{12}$ and $|\phi^+_{cl})_{34}$ respectively. This is the interesting property of entanglement swapping. In this experiment, the projection measurement of the four photon entangled state $|\Psi)_{1234}$ exhibits the entanglement swapping for product pair $|\phi^+_{cl})_{12}|\phi^+_{cl})_{34}$. The advantages of the above version of entanglement swapping are also outlined. Figure 1.5(a) and (b) shows the classical wave simulation of entanglement swapping for the product pair $|\phi^+_{cl})_{12}|\phi^+_{cl})_{34}$ and not the $|\phi^+_{cl})_{12}|\phi^-_{cl})_{34}$ respectively.

The classical wave optics experiments of Chapter 4 and 5 are able to reproduce the wave character of a quantum system, but not the particle character of a quantum system. In addition, the classical wave interference signal is a stable oscillatory signal, so the probabilistic nature of quantum mechanics is not applicable in the classical system. The measurement methods discussed in Chapters 4 and 5, and 6

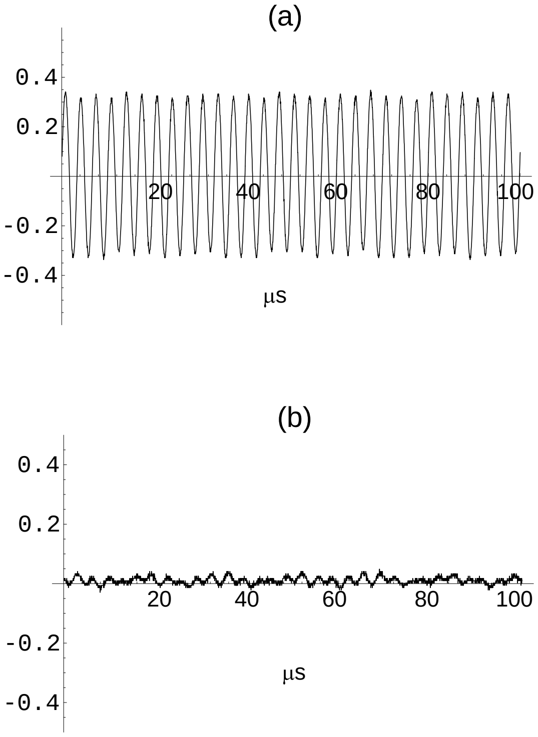

**Figure 1.5**: Entanglement swapping with classical fields. Observer A selects the Bell state $|\phi_{cl}^{+})_{12}$. Observer B's signal are then proportional to the projections of the corresponding the classical analog Bell state (a) $|\phi_{cl}^{+})_{34}$ gives a large signal (b) $|\phi_{cl}^{-})_{34}$ gives zero signal.

do not exhibit wave-particle duality properties.

In Chapter 7, a noise classical field and a stable classical field with orthogonal polarization are used to simulate in part the particle character and probabilistic nature of a quantum system. The detection schemes of two quantum observers A and B in a two-photon entangled system are simulated in this classical noise experiment. First, polarization correlation of two spatially separated particles is reproduced by mixing these two fields. These two fields are combined in a beamsplitter and the outputs of the beamsplitter are sent to observers $\mathcal{A}$ and $\mathcal{B}$. The interference of these two fields in each detector is a random noise signal. The random noise amplitudes in detectors $\mathcal{A}$ and $\mathcal{B}$ are anti-correlated. These noise amplitudes are used to simulate the particle-like behavior of two entangled photons. These signals are then multiplied by using an analog multiplier. The mean value of the multiplied anti-correlated noise amplitude is found to be equivalent to the quantum nonlocal polarization correlation function, $C(a,b)$=$\langle\mathbf{AB}\rangle = -\cos 2(\theta_a - \theta_b)$, that is the expectation value of the signals for two observers with their analyzers oriented along directions $\theta_a$ and $\theta_b$ respectively. Since the measurement method in this noise experiment is able to reproduce the correlation function of two entangled particles, then a similar method can be used to reproduce the measurement of violation of a Bell's inequality. The Bell's inequality is given by $F(a,b,c)$=$|C(a,b) - C(a,c)| - 1 - C(b,c) \leq 0$. Local realism theory predicts $F(a,b,c) \leq 0$. Quantum theory predicts $F(a,b,c) \geq 0$ and hence the violation of Bell's inequality. Figure 1.6 shows that the measurement method in this classical noise experiment is able to reproduce the violation of Bell's inequality for the classical analog Bell state $|\psi_{cl}^{-}\rangle = 1/\sqrt{2}\,(|H_1\rangle|V_2\rangle - |V_1\rangle|H_2\rangle)$. The figure shows that the maximum violation, $F(a=0, b=30°, c=\theta_2) \nleq 0$, occurs at $\theta_2 = 60°$. In this experiment, the classical noise field and detection scheme are able

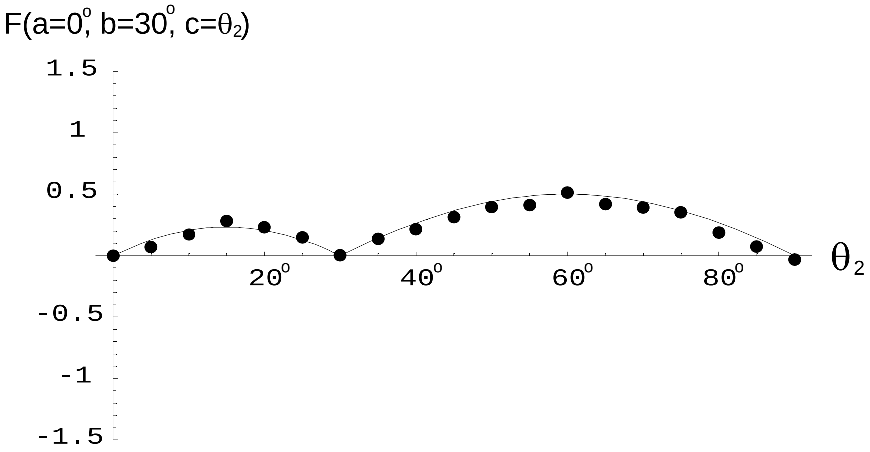

**Figure 1.6**: Classical violation of Bell's inequality, $F(a = 0, b = 30°, c = \theta_2)$ as a function of $\theta_2$ for the classical analog Bell state $\frac{1}{\sqrt{2}}(|H_1\rangle|V_2\rangle - |V_1\rangle|H_2\rangle)$. The maximum violation occurs at $\theta_2$= 60°.

to simulate in part the wave-particle duality properties and probabilistic nature of a quantum observer. The difference between our classical system and a quantum system is that we measure the random beat signal amplitude of the correlated fields, not the coincidences of the correlated particles.

In the conclusions, Chapter 8, our work is summarized and suggestions for future work are given.

# Chapter 2

# Theory of Wave and Particle Interference

## 2.1 Overview

In the Introduction, we mentioned that the objective of this thesis is to simulate the linear superposition principle and quantum entanglement using classical wave optics. Here, in this chapter, we will discuss both concepts in relation to our classical wave optics experiments which are demonstrated in the next chapters.

We first present the linear superposition principle in quantum and classical wave systems where the Wigner phase space distribution is used to illustrate the similarities between single-particle quantum interference and single field classical wave interferences. Then, we discuss the properties of the Schrödinger cat state proposed by Erwin Schrödinger. The cat state is analogous to an even coherent state in position space. Since the even coherent state is identical in structure with two spatially separated $TEM_{00}$ gaussian mode wave packets, then their Wigner functions have the same properties. The most interesting feature exhibited by these Wigner functions are negative values in some regions of the phase space distributions. Some workers believe that the negative value is a unique property of quantum mechanics because it implies that a particle cannot have definite position and momentum values at the same time. However, this is not true. The negative values in the phase-space distribution can be attributed to interference of a single particle or a single classical wave field.

We then describe the concept of entanglement in a two-particle system. We also layout two fundamental types of entanglement, nonlocal and local entanglement. The nonlocal quantum entanglement between two-particles exhibits behavior which contradicts Einstein's local realism theory. The proof that nonlocality is a true quantum effect was given by J. S. Bell in 1964. We present a standard proof of Bell's theorem in two different models, non-quantum and quantum models. Understanding of these conceptual tests of entanglement is important since our experiments reproduce quantum observations by using classical wave fields.

## 2.2 Wigner Function

The Wigner function is named after E. P. Wigner as a result of his famous paper "On the Quantum Correction for Thermodynamic Equilibrium" [47]. Since then, the Wigner function has been used in quantum optics to represent the phase-space distribution of a quantum particle [48]. It was later applied to classical optical beams [49] and biomedical imaging [50, 51]. Wigner distribution functions can be used to provide a complete description of the coherence properties of the wave function $\psi(x)$ and classical wave fields $\mathcal{E}(x)$ [41]. For a classical field varying in one spatial dimension, $\mathcal{E}(x)$, the Wigner phase space distribution is Fourier transform related to the mutual coherence function [52]

$$W(x,p) = \int \frac{d\epsilon}{2\pi}\, exp(i\epsilon p)\, \langle \mathcal{E}^*(x+\epsilon/2)\mathcal{E}(x-\epsilon/2)\rangle \ . \tag{2.1}$$

The above definition of the Wigner function is identical to that of a wave function $\psi(x)$. Here $x$ is a transverse position, $p$ is a transverse wave vector (momentum) in the $x$ direction, and $< .. >$ denotes a statistical average. Hence, similarities of wave functions and classical wave fields are reflected in the similarities of the quantum and classical Wigner functions.

It is well-known that in the paraxial approximation [53], the transverse mode of an optical field of frequency $\omega$ obeys an equation which is formally identical in structure to the Schrödinger wave equation of quantum mechanics,

$$i\frac{\partial \mathcal{E}(x,y,z)}{\partial z} = -\frac{\nabla_{tr}^2 \mathcal{E}(x,y,z)}{2k} - 2\pi k \bigtriangleup\chi(x,y)\,\mathcal{E}(x,y,z) \tag{2.2}$$

Here, $k = n_o w/c$ is the wave vector in the medium, $n_o$ is the background index of refraction, and $\bigtriangleup\chi(x,y)$ is the spatially varying part of the susceptibility, which determines the effective potential. The role of the time is played by the axial position $z$. For a lens-like medium, where $\bigtriangleup\chi \propto x^2$, the paraxial wave equation is identical in form to the Schrödinger equation for a harmonic oscillator. From Eq. (2.2), it is evident that in a lens-like medium, the lowest gaussian $TEM_{00}$ mode is analogous to the ground state of a quantum oscillator, while higher order Hermite-Gaussian modes correspond to excited states. Then, it is interesting to notice that $W(x,p)$ for a quantum particle bound in a harmonic well has the same properties as $W(x,p)$ for a gaussian beam in a lens-like medium.

The Heisenberg uncertainty principle applies to two variables whose associated operators do not commute, such as the position and momentum of a quantum particle. In the second quantized field theory, the in- and out-of phase quadratures of a quantum field are analogous to the canonical position and momentum of an harmonic oscillator. Hence, the in-phase and out-of-phase components of a quantized electric field are subject to the uncertainty principle. Normally, the in- and out-of phase quadratures noise exhibits Poisson statistics called shot noise. According to the relation $\triangle^2\hat{P} \propto \frac{1}{\triangle^2\hat{X}}$, one could squeeze the variance of in-phase quadrature $\triangle^2\hat{X}$ to zero, and extend the variance of out-of-phase quadrature $\triangle^2\hat{P}$ to infinity and vice versa. Light which exhibits this property is called squeezed light. Such nonclassical light can be produced by parametric down conversion processes.

The terminology of squeezing in quantum optics can be represented by the transverse mode of an optical beam. A coherent state is obtained by the displacement of the position and momentum in a vacuum state. A gaussian beam of the same size as the lowest mode in a lens-like medium, but displaced in transverse position and momentum corresponds to a coherent state, whereas gaussian beams of smaller (larger) size than the lowest mode correspond to position (momentum) squeezed states. The Wigner function for an optical gaussian beam is $W(x,p){=}\frac{1}{\pi}exp(-\frac{x^2}{a^2} - a^2p^2)$, where $a$ is the beam waist. Figure 2.1 shows the Wigner function for a focused beam where $a = 0.5$ is analogous to an in-phase quadrature squeezed field in a medium where $a = 1$ is the lowest $TEM_{00}$ mode. Figure 2.2 shows the Wigner function for a collimated beam where $a = 1.5$ is analogous to an out-of-phase quadrature squeezed field. These figures are plotted by using dimensionless units for $x$ and $p$ in terms of $a$ and $\frac{1}{a}$, respectively.

The Wigner distribution function plays a role that is closely analogous to a classical phase-space distribution in position and momentum, permitting an intuitive particle-like description of the underlying wave propagation. The wave-particle duality property is inherent in the Wigner function as shown by its definition in Eq. (2.1). The particle character is the particle property of the variables position $x$ and momentum $p$ used in the Wigner function. This is analogous to Hamiltonian optics representing light in $x - p$ representation as a ray in free space. The wave character is the wave property of the wave function used in Wigner function. This is described by the first order mutual coherence function $\langle \mathcal{E}^*(x)\mathcal{E}(x')\rangle$ in the definition of Wigner function of Eq. (2.1).

For a linear superposition of two quantum states of a particle system such as $\psi_a+\psi_b$, the corresponding Wigner function is $W_a+W_b+W_{int}$, where the last term describes the phase-space interference between the two wave functions. This phase space interference is analogous to the interference of two possible paths for which particle can be detected, that is $|\psi_a+\psi_b|^2$. These interferences exhibit oscillatory behavior in the phase space representation and also nonpositive values. It has been shown that the Wigner function of an atomic matter wave passing through a double slit exhibits strong oscillations and negative regions [54]. It has been suggested by several authors [55] that negative values of the Wigner function for a quantum state is a nonclassical effect which has no classical counterpart. That is, it implies the impossibility of a particle simultaneously having a precise position and momentum. However, it is not true that negative values in the phase space distribution are a unique property of quantum theory. We will illustrate this idea by measuring a classical field analog of a Schrödinger cat state in the following section.

### 2.2.1 Schrödinger Cat State

The cat state is described in an imaginary experiment by Erwin Schrödinger [56]. A box, which is closed from the outside observer, contains a cat and a glass of poisonous gas. A mechanism can release a hammer which destroys the glass. This kills the cat. The mechanism for the release of the hammer is triggered by a radioactive decay and is hence determined by chance. As time elapses, the whole system, as it

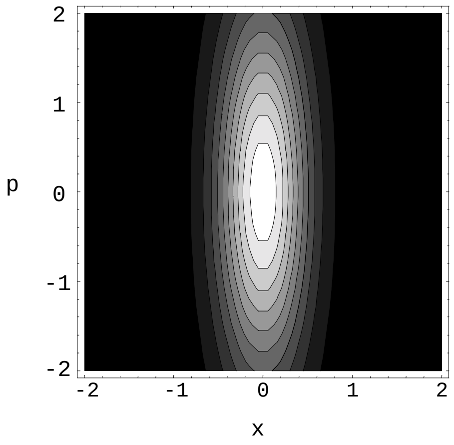

**Figure 2.1**: The Wigner function for a focussed gaussian beam, $W(x, p)$ with $a$=0.5.

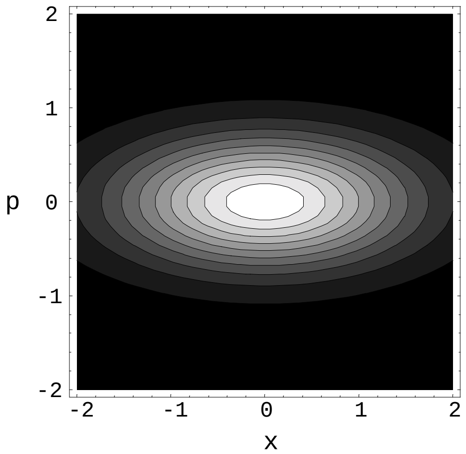

**Figure 2.2**: The Wigner function for a collimated gaussian beam, $W(x, p)$ with $a$=1.5.

represented in quantum theory, will evolve into a system that is a superposition of two parts: (i) when the hammer has not fallen down and the glass is still intact, the cat is still alive. This is denoted by a two system state vector $|a, i\rangle$ where $a$ denotes the alive state of the cat and $i$ the intact glass. In the other alternative the hammer has broken the glass and the cat is dead. This state is described by the vector $|d, b\rangle$ where $d$ represents the dead cat and $b$ the broken glass. Then, the whole system can be represented as the state,

$$|\phi\rangle = \frac{1}{\sqrt{2}}(|a, i\rangle + |d, b\rangle) \ . \tag{2.3}$$

However, the state $|\phi\rangle$ in Eq. (2.3) given by Schrödinger is not a one-particle state, but a two-particle state, where the alive cat is correlated with the intact glass and the dead cat with the broken glass. The state is a two-particle entangled state.

Most important, the cat is a superposition of two macroscopically distinguishable states, namely dead and alive, which we can write as,

$$|\phi\rangle_{cat} = \frac{1}{\sqrt{2}}(|a\rangle + |d\rangle) \ . \tag{2.4}$$

Now, the paradox is not that the cat can be dead or alive. Eq. (2.4) shows that the state consists of a superposition of two states, dead $|d\rangle$ and alive $|a\rangle$, which indicates the interference between these two states.

In quantum optics, the simplest case of such as a superposition is given by a linear combination of two "mirror-like" coherent states [41]

$$|\phi\rangle_{cat} = \frac{1}{\sqrt{2N}}(|\alpha\rangle + |-\alpha\rangle) \tag{2.5}$$

where the normalization constant $N = 1 + exp(-2\alpha^2)$ due to the over-completeness of the coherent state $|\alpha\rangle$. Eq. (2.5) is called the even coherent state (ECS).

The natural classical analog of the state $|\phi\rangle_{cat}$ is a linear superposition of two spatially separated mutually coherent gaussian beams,

$$E(x) = E_\circ(x - D/2) + E_\circ(x + D/2) \tag{2.6}$$

where D is the spatial distance between these two gaussian beams and $E_\circ(x) = exp(-\frac{x^2}{2a^2})$ is one dimension complex electric field amplitude. This linear superposition of two or more electric fields exhibits classical interference very similar to the interference of coherent states. The classical Wigner function for such a linear superposition of two gaussian beams is given as,

$$W_{cl}(x, p) \propto W_\circ(x + D/2, p) + W_\circ(x - D/2, p) + 2W_\circ(x, p)\cos(Dp) \tag{2.7}$$

where $W_\circ(x, p)$ is the Wigner function for $E_\circ(x)$. The Wigner function for two gaussian beams is shown in Figure 2.3. This figure is plotted using dimensionless units of $\frac{x}{a}$ and $ap$ and the distance $D = 4.5a$.

The quantum version of the Wigner function for the even coherent state is similar to $W_{cl}(x, p)$ because the $\langle x|\alpha\rangle$ is identical in structure with the field of a displaced gaussian beam. Note that the minimum-uncertainty wave packet is a gaussian, $\langle x|\alpha\rangle \propto e^{-A\frac{(x-<x>)^2}{2\hbar}} e^{i\frac{<p>x}{\hbar}}$, where $A$ is a real constant [57]. The quantum and classical Wigner functions are non-positive, with the negative contributions arising from the interference terms. The oscillation in momentum $p$ has a frequency inversely proportional to the spatial separation $D$. In the next chapter, we place a wire in the center of a gaussian beam to obtain a field similar to Eq. (2.6), where

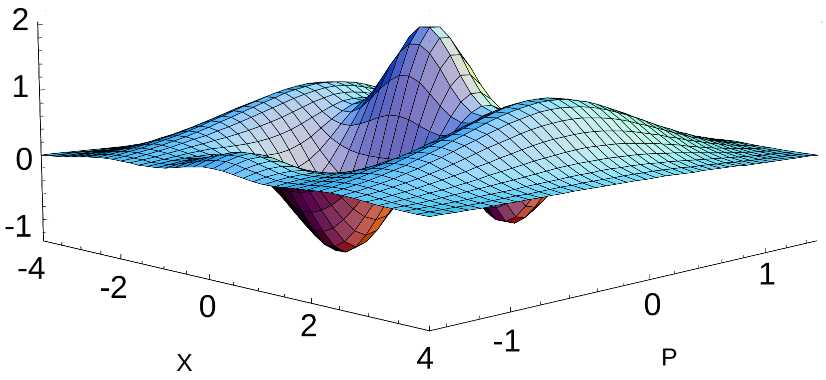

**Figure 2.3**: The Wigner function for the Schrödinger cat state

D is the thickness of the wire. We measure a Wigner function which is exactly the same form as in Figure 2.3.

## 2.3 Entanglement

Quantum entanglement was appreciated by Schrödinger in his famous discussion of the Schrödinger cat as shown in Eq. (2.3). The concept of nonlocality in a two particle system is related to the EPR paradox: The initials refer to Albert Einstein, Boris Podolsky and Nathan Rosen, the authors of a famous 1935 scientific paper entitled " Can a Quantum Mechanical Description of Physical Reality Be Considered Complete? " [7]. Within the mathematical structure of quantum theory the position and the velocity of an electron cannot both be well defined simultaneously: If one of these quantities has a definite value the other cannot. The EPR paper noted that within quantum theory one can set up an experimental situation that in principle allows one to predict with certainty either the position or the velocity of one electron by measuring either the position or the velocity of a second correlated electron. EPR argued that measurements performed on the second electron cannot disturb the properties of the first electron, and hence that the first electron must have, simultaneously, a well defined value position and a well defined value of velocity. This is not allowed by the quantum Heisenberg uncertainty principle. In a two-photon entangled system, the detection of the first photon in one detector will disturb the outcome of the measurements of the second photon in a spatially separated region even though it hasn't been measured. This is called nonlocality which is attributed to the entanglement of the two photons.

Entanglement is one of the central concepts in quantum information processing such as quantum teleportation and cryptography, and quantum computation. There are two types of entanglement: (i) entanglement between different properties of a single particle and (ii) entanglement between separate particles. Here, we illustrate the properties of these two types of entanglement in detail.

An example of type (i) entanglement is provided by the polarization and position of a single polarized photon. A 45° polarized photon is incident on a cube polarized beamsplitter and the outputs of the cube polarizer have the horizontal component of the photon in one port and vertical component of the photon in another port. Since it is a single photon experiment, then the photon is in an entangled state $|H, x_1\rangle + |V, x_2\rangle$, where $x_1$ and $x_2$ denoted the positions at ports 1 and 2. This entangled state exhibits local entanglement as follows: if the photon is detected at port 1, the entangled state collapses to $|H, x_1\rangle$. This means that the photon must be horizontally polarized at position $x_1$. It is obvious that the correlation exhibited by the photon in $|H, x_1\rangle$ is local. And similarly, if the photon is detected at port 2, then the entangled state collapses to $|V, x_2\rangle$ indicating that the photon is vertically polarized at position $x_2$. The component $|V, x_2\rangle$ also shows the local correlation of the photon. Even though the components $|H, x_1\rangle$ and $|V, x_2\rangle$ are spatially separated product states, they exhibit local correlation between the position and polarization.

Type (ii) entanglement is a central concept for the realization of the EPR paradox and hence the discussions on interpretation of quantum mechanics. The type (ii) entangled state is used to study the nonlocality of quantum theory such as Bell's theorem and three-particle GHZ correlations. This type of entanglement is always exhibited by a quantum system that is associated with at least two quantum particles. These two particles have to be entangled or correlated in an entangled state. An entangled state is a product state that cannot be factorized such as $|\psi^+\rangle = \frac{1}{\sqrt{2}}[|H_1V_2\rangle + |V_1H_2\rangle]$ for a pair of photons produced from the parametric down-conversion process. These two photons are called signal and idler. The signal photon is horizontally polarized and the idler photon is vertically polarized. They are then combined through a beamsplitter. The outputs of the beamsplitter are two spatially separated beams, beams 1 and 2. If photon in beam 1 is measured to have the polarization state $|H_1\rangle$, the entangled state is collapsed to $|H_1V_2\rangle$. Thus, the photon in beam 2 is known to be in the polarization state $V_2$ even though it hasn't been measured. This behavior is called nonlocality. Another possibility is the collapse of the entangled state to $|V_1H_2\rangle$. Then, the contributions from these two possibilities exhibit quantum wave interferences in this two-photon system. One may notice that the horizontal components $|H_1\rangle$ and $|H_2\rangle$ in two spatially separated beams 1 and 2 are due to the wave character of the signal photon in the beamsplitter. And similarly, for the vertical components $|V_1\rangle$ and $|V_2\rangle$ are from the idler photon. Hence, the duality property of this system is observed as a photon takes two possible paths at the same time. This is the interesting feature of nonlocal entanglement.

The type (i) entanglement is not as useful as the type (ii) because it is locally entangled and doesn't exhibit nonlocality as required by most of quantum applications such as teleportation. Since a single photon quantum interference can be fully described by a classical wave field, then classical analog of type (i) entanglement by using a classical beam can be implemented. It has been proposed by Spreeuw [44] that classical analog of type (ii) entanglement can be achieved by adding product states of type (i) for two spatially separated classical beams, that is, $|upper\, beam\, 1, H) + |lower\, beam\, 2, V)$. However, this classical state fails to exhibit non-locality as exhibited by the example given in the discussion of type (i) entanglement because a single beam cannot be sent to two spatially separated detectors.

In the next chapters, we are able to experimentally demonstrate the simulation of two-, three- and four-particle nonlocal entanglement by using classical wave fields. Our measurement method is able to reproduce measurements of the violation of Bell's inequality as predicted by quantum mechanics [58]. So, it is interesting to discuss Bell's theorem in the following section.

### 2.3.1 Bell's Theorem

According to quantum theory, a two-photon entangled state is given by the state $|\psi^-\rangle = \frac{1}{\sqrt{2}}(|H_1V_2\rangle - |V_1H_2\rangle)$ where the two photons are spatially separated. When a measurement on one of the photon pair yields a horizontally polarized photon in detector 1, then the state $|\psi^-\rangle$ is immediately collapsed to $|H_1V_2\rangle$ providing the information that the second photon will be in the vertical polarization state even though it hasn't been measured. Einstein called this "spooky action-at-a-distance" unacceptable because no influence can propagate faster than the speed of light. EPR claimed that quantum mechanics is therefore an incomplete description of physical reality. The wave function is not enough and some other quantity, $\lambda$, a hidden variable which is local, is needed in addition to $|\psi^-\rangle$ to describe the state of the system fully. Until 1964 it was believed that one could always construct a hidden-variable theory that would give all the same results as quantum mechanics. But in that year J. S. Bell proved that any local hidden variable theory is incompatible with quantum mechanics. Below, we discuss two methods of formulating Bell's inequality.

### A Non-quantum Model of the Bell's Inequalities

For two spin-$\frac{1}{2}$ particles system in the singlet state, $|\psi^-\rangle = \frac{1}{\sqrt{2}}(|\uparrow_1\downarrow_2\rangle - |\downarrow_1\uparrow_2\rangle)$, particles 1 and 2 are sent to observers A and B respectively, where each of them has an analyzer (Stern-Gerlach apparatus). Observable **A** is said to have eigenvalue +1 (-1) which corresponds to particle 1 parallel (anti-parallel) to the analyzer oriented at **a**. Similarly for particle 2 with observable **B** with the analyzer oriented at **b**, the eigenvalues are ±1. Suppose now that A and B agree to make measurements along one of three polarization angles, in general, nonorthogonal, coplanar directions specified by the vectors **a**, **b** and **c**. In order to understand the formulation of Bell's Inequalities by a non-quantum model [59], we first need to explain the meaning of a particle belonging to a type $\{+\mathbf{a}, -\mathbf{b}, +\mathbf{c}\}$. A measurement by A or B on a particle of this type would yield +1 if the analyzer is oriented along the direction specified by **a** or **c** respectively, but would yield -1 if the analyzer in B is oriented along the direction specified by **b**. Since the state $|\psi^-\rangle$ exhibits perfect anti-correlation for spin polarization measurements along parallel axes, then if particle 1 is of the type $\{+\mathbf{a}, -\mathbf{b}, +\mathbf{c}\}$, then particle 2 must be of the type $\{-\mathbf{a}, +\mathbf{b}, -\mathbf{c}\}$. Now, there are eight different groups that the two particles might belong in:

| Population | Observer A | Observer B |
|---|---|---|
| $N_1$ | {+a,+b,+c} | {-a,-b,-c} |
| $N_2$ | {+a,+b,-c} | {-a,-b,+c} |
| $N_3$ | {+a,-b,+c} | {-a,+b,-c} |
| $N_4$ | {+a,-b,-c} | {-a,+b,+c} |
| $N_5$ | {-a,+b,+c} | {+a,-b,-c} |
| $N_6$ | {-a,+b,-c} | {+a,-b,+c} |
| $N_7$ | {-a,-b,+c} | {+a,+b,-c} |
| $N_8$ | {-a,-b,-c} | {+a,+b,+c} |

Before we use the table to obtain Bell's inequality, let's discuss an experiment in which A and B orient their analyzers along different axes. In particular, let's see what fraction of their measurements yield values for the two particles that have opposite signs, for example, if A finds particle 1 along **a** to have eigenvalue +1 and B finds particle 2 along **c** to have eigenvalue -1. Clearly, all measurements made on particles in populations $N_1$ and $N_8$ will yield opposite signs for the polarizations of the two particles. On the other hand, for population $N_2$, when A measures along **a** and obtains +1, B's measurement along **b** yields the result -1 (with opposite sign), but if instead B's analyzer is oriented along **c** axis, B obtains +1 (with the same sign). Similarly, if A's analyzer is oriented along **b** axis, A obtains +1 while B obtains -1 along **b** or +1 along **c**. Finally, for population $N_2$, if A's analyzer is oriented along the **c** axis, A obtains -1, while B obtains -1 along **a** or -1 along **b**. Thus, overall for population $N_2$, $2/6 = 1/3$ of the measurements yield results with opposite signs when their analyzers are oriented along different axes. This ratio holds for all of the populations $N_2$ through $N_7$, yielding (3/4) of the eight different populations. And similarly, for populations $N_1$ and $N_8$ (that is (2/8)=(1/4) of the eight different populations), (6/6) of their measurements yield results with opposite signs when their analyzers are oriented along different axes. Hence, overall that is $1/3(3/4) + (1/4)(6/6) = 1/2$ of the measurements will find the particles with their polarizations anti-correlated when the two experimentalists orient their analyzers along different axes.

Interestingly, we can extract a variety of inequalities from the table. We may quickly see, for example, that

$$N_3 + N_4 \leq (N_2 + N_4) + (N_3 + N_7) \tag{2.8}$$

must hold since $N_2$, $N_7 \geq 0$. But

$$\frac{N_3 + N_4}{\sum_i N_i} = P(+a; +b) \tag{2.9}$$

is the probability that a measurement by A yields +1 along axis **a** for particle 1 and a measurement by B yields +1 along axis **b** for particle 2. Only populations $N_3$ and $N_4$ contain particle types satisfying both these conditions. Similarly,

$$\frac{N_2 + N_4}{\sum_i N_i} = P(+a; +c) \tag{2.10}$$

is the probability that a measurement by A yields +1 along axis **a** for particle 1 and a measurement by B yields +1 along axis **c** for particle 2. Also,

$$\frac{N_3 + N_7}{\sum_i N_i} = P(+c; +b) \tag{2.11}$$

Thus the inequality Eq. (2.8) may be expressed as

$$P(+a, +b) \leq P(+a, +c) + P(+c, +b)$$

or,

$$P(+a, +c) + P(+c, +b) - P(+a, +b) \geq 0 \tag{2.12}$$

which is known as a Bell's inequality. The joint probability $P(+a, +c)$ is obtained from the coincidence counting of two particles when the A and B have their analyzers oriented at directions **a** and **c** respectively, and similarly for $P(+a, +b)$ and $P(+c, +b)$. The mathematical form of the joint probability is dependent on the experimental setup of the quantum system. For the entangled state, $|\psi_-\rangle$, the joint probability $P(+a, +c)$ is given as $(1/2)\sin^2(\theta_a - \theta_c)$ [24]. The analyzer settings $\mathbf{a} = -30°$, $\mathbf{c} = 0°$, and $\mathbf{b} = 30°$ lead to a maximum violation of Bell's inequality Eq. (2.12) as,

$$\begin{aligned} P(+a = -30°, +c = 0°) &+ P(+c = 0°, +b = 30°) - P(+a = -30°, +b = 30°) \\ &= 1/8 + 1/8 - 3/8 = -1/8 \not\geq 0 \ . \end{aligned} \tag{2.13}$$

### Deterministic Local Hidden-Variables Theories in Bell's Theorem

Bell's inequalities can have different forms. Besides the approach discussed above, a different formulation of Bell's inequalities can be obtained by considering the deterministic local hidden variables theory of the correlation function for polarization measurements by two observers A and B [9]. The Bell's inequalities derived in 1965 by Bell were for two spin-$\frac{1}{2}$ particles where the two spins are entangled in a singlet state. In this section, we discuss a two particle system where the two photons are entangled in a polarization-entangled state $|\psi^-\rangle = \frac{1}{\sqrt{2}}(|H_1V_2\rangle - |V_1H_2\rangle)$. Observer A has his analyzer oriented along the **a** axis and projects out polarization state $|a\rangle$, where $|a\rangle$ is expressed in terms of vertical $\hat{V}$ and horizontal $\hat{H}$ unit vectors as;

$$|a\rangle = \cos\theta_a \hat{V} + \sin\theta_a \hat{H} \ . \tag{2.14}$$

Similarly the orthogonal photon polarization state is

$$|a^{\perp}\rangle = -\sin\theta_a \hat{V} + \sin\theta_a \hat{H} \tag{2.15}$$

Then the analyzer (measuring apparatus) for observer **A** is represented by the projector

$$\mathbf{P}_a = |a\rangle\langle a| \ . \tag{2.16}$$

where $P_a$ has eigenvalues 1 and 0. For a parallel discussion of Bell's theorem with the previous section, it is convenient to introduce an operator for A which has eigenvalue ±1. We introduce an operator $\mathbf{A}_a$ to represent the measuring apparatus for observer A as,

$$\begin{aligned}\mathbf{A}_a &= 2\mathbf{P}_a - \mathbf{1} = \mathbf{P}_a - \mathbf{P}_{a\perp} \\ &= 2\begin{pmatrix} \cos^2\theta_a & \sin\theta_a\cos\theta_a \\ \sin\theta_a\cos\theta_a & \sin^2\theta_a \end{pmatrix} - \begin{pmatrix} 1 & 0 \\ 0 & 1 \end{pmatrix} \\ &= \cos 2\theta_a(|V\rangle\langle V| - |H\rangle\langle H|) + \sin 2\theta_a(|V\rangle\langle H| + |H\rangle\langle V|)\ . \qquad (2.17)\end{aligned}$$

where $\mathbf{P}_{a\perp}$ is the projection operator for the polarization orthogonal to $a$. The operator $\mathbf{A}_a$ will be called a spin projection operator, since its eigenvalues $\pm 1$ correspond to the eigenvalues 1 and 0 of $\mathbf{P}_a$ and 0 and 1 of $\mathbf{P}_{a\perp}$ respectively. Similarly for the observer B, the operator $\mathbf{B}_b$ is given as a function of $\theta_b$. We can immediately verify that for the photon pair in the state $|\psi^-\rangle$ the product $(\mathbf{A}_a\mathbf{B}_b)$ has eigenvalues $\pm 1$, which correspond respectively to identical and opposite results for the two measuring systems.

The average value of the observable $(\mathbf{A}_a\mathbf{B}_b)$ is the so-called correlation function $E(a,b)$ of the outcomes of the two measuring devices. One obtains,

$$E(a,b) = \langle\psi_-|\mathbf{A}_a\mathbf{B}_b|\psi_-\rangle = -\cos 2(\theta_a - \theta_b) \qquad (2.18)$$

For $\theta_a = \theta_b$, the correlation function $E(a,b)$ in Eq. (2.18) implies that the two photons are anti-correlated, that is if A obtains a $H(V)$ polarized photon and B obtains a $V(H)$ polarized photon. If $\theta_a - \theta_b = \pm\pi/2$, then the correlation function has value 1 which means that the two photons are perfectly correlated and A obtains an $H(V)$ polarized photon and B obtains an $H(V)$ polarized photon. Thus, when $\theta_a = \theta_b$ or $\theta_a - \theta_b = \pm\pi/2$ in the correlation function, one can predict with certainty the result obtained for B, by previously obtaining the result for A.

In the EPR argument, the result for observer B is predetermined, since there exists a more complete specification of the state in which this determinism is manifest. Then this state is denoted by a symbol $\lambda$, although it may well have many dimensions and different parts of it interacting with either apparatus, etc. The distribution function $\rho(\lambda)$ for the states $\lambda$ in the $\Lambda$ space has the norm

$$\int_{\Lambda} \rho(\lambda) d\lambda = 1\,. \tag{2.19}$$

In a deterministic hidden variables theory the observable $(\mathbf{A}_a\mathbf{B}_b)$ has a define value $(\mathbf{A}_a\mathbf{B}_b)(\lambda)$ for the state $\lambda$. For the theory, Bell defines locality as follows: A deterministic hidden variables theory is local if for all $\mathbf{a}$ and $\mathbf{b}$ and all $\lambda \in \Lambda$ we have

$$(\mathbf{A}_a\mathbf{B}_b)(\lambda) = \mathbf{A}_a(\lambda)\mathbf{B}_b(\lambda)\ . \tag{2.20}$$

This means that as the state $\lambda$ is specified and the particles are spatially separated, then measurements of A depend only on $\lambda$ and $\mathbf{a}$ but not $\mathbf{b}$. Similarly, measurements of B depend only on $\lambda$ and $\mathbf{b}$. Then, any reasonable physical theory that purports realism, determinism, and denies the existence of action-at-a-distance is local in this sense. Thus, the expectation value of $(\mathbf{A}_a\mathbf{B}_b)$ is given by

$$E(a,b) = \int_{\Lambda} \mathbf{A}_a(\lambda)\mathbf{B}_b(\lambda)\rho(\lambda) d\lambda \tag{2.21}$$

By using this expectation value, a Bell's inequality can be obtained. Eq. (2.18) for polarization $\mathbf{b} = \mathbf{a}$ can hold if and only if

$$\mathbf{A}_a(\lambda) = -\mathbf{B}_a(\lambda)\ . \tag{2.22}$$

holds for all $\lambda \in \Lambda$. Then using Eq. (2.21) and Eq. (2.22) to evaluate the function $F(a,b,c)$ =$E(a,b) - E(a,c)$ which involves three different possible orientations of the analyzers,

$$\begin{aligned} F(a,b,c) &= -\int_{\Lambda}[\mathbf{A}_a(\lambda)\mathbf{A}_b(\lambda) - \mathbf{A}_a(\lambda)\mathbf{A}_c(\lambda)]\rho(\lambda)d\lambda \\ &= -\int_{\Lambda}\mathbf{A}_a(\lambda)\mathbf{A}_b(\lambda)[1 - \mathbf{A}_b(\lambda)\mathbf{A}_c(\lambda)]\rho(\lambda)d\lambda \end{aligned} \tag{2.23}$$

where $\mathbf{A}_b(\lambda)^2 = 1$ is used. Since the maximum obtainable values for $\mathbf{A}_a(\lambda)\mathbf{A}_b(\lambda)$ are ±1, the last expression in Eq. (2.23) can be written

$$|F(a,b,c)| \leq \int_{\Lambda}[1 - \mathbf{A}_b(\lambda)\mathbf{A}_c(\lambda)]\rho(\lambda)d\lambda \tag{2.24}$$

Finally, using Eq. (2.19), Eq. (2.21) and Eq. (2.22) with $\mathbf{A}_c(\lambda) = -\mathbf{B}_c(\lambda)$, one obtains the Bell's inequality as,

$$|E(a,b) - E(a,c)| \leq 1 + E(b,c) \tag{2.25}$$

The inequality in Eq. (2.25)is violated by taking **a**, **b** and **c** to be coplanar, with **c** making an angle of $\pi/3$ with **a**, and **b** making an angle of $\pi/6$ with both **a** and **c**. Using the correlation function in Eq. (2.18) for the state $|\psi^-\rangle$, we obtain

$$\begin{aligned} |E(a,b) - E(a,c)| - (1 + E(b,c)) &= |-\cos 2(0 - 30^\circ) + \cos 2(0 - 60^\circ)| \\ &- \quad 1 + \cos 2(30^\circ - 60^\circ) \\ &= |-1/2 - 1/2| - 1 + 1/2 = 1/2 \not\leq 0 \end{aligned} \tag{2.26}$$

showing the violation of Bell's inequality.

# Chapter 3

# Wigner function and Product States

## 3.1 Overview

In this chapter, two experiments are described: First, we demonstrate measurement of the Wigner function for a classical field analog of a Schrödinger cat state to study the similarity between quantum and classical first order coherence theory. The Wigner function for a classical field $\mathcal{E}(x)$ is given by $W(x,p) = \int \frac{d\epsilon}{2\pi}\, exp(i\epsilon p)\, \langle \mathcal{E}^*(x+\epsilon/2)\mathcal{E}(x-\epsilon/2)\rangle$. Second, we describe heterodyne measurements of classical analog of product states for two spatially separated gaussian beams.

In the first experiment, we show that Wigner distributions for classical optical fields can be determined by use of a novel two-window heterodyne detection scheme [39]. Measurement of Wigner phase space distributions is a joint intensity measurement for transverse position $x$ and momentum $p$ coordinates of a classical field. The two-window heterodyne technique was originally designed for biomedical imaging, that is for optical phase space coherence tomography of the light transmitted through or reflected from biological tissue. Now, we use this measurement to reproduce the properties of one particle wave mechanics. In this heterodyne detection, we use a local oscillator (LO) field comprising a coherent superposition of a tightly focused beam and a highly collimated beam. This scheme permits independent control of the $x$ and $p$ resolution, permitting concurrent localization of $x$ and $p$ with a variance product that surpasses the minimum uncertainty limit associated with Fourier-transform pairs. The method allows us to measure the $x - p$ cross correlation, $\langle \mathcal{E}^*(x)\mathcal{E}(p)\rangle$, of an optical field $\mathcal{E}$ for transverse position $x$ and transverse momentum $p$. A simple linear transform of the $x-p$ correlation function yields the required Wigner function. We observe the non-positive properties of the Wigner function for a superposition of two spatially separated gaussian fields analogous to a Schrödinger cat state. We also show that an interesting analogy exists between our choice of LO field and that employed in a recent quantum-teleportation experiment [34]. We also point out that similar problems are encountered in our experiments and in the quantum teleportation experiments which teleport an arbitrary state as a Wigner function via EPR beams [34].

In the second experiment, we demonstrate classical wave methods for simulating two-mode quantum states by using heterodyne detection to directly measure products of the transverse modes of bichromatic fields, i.e, $E_{H1}(x_1)E_{V2}(x_2)$. This is accomplished by taking advantage of the fact that beamsplitters preserve the transverse mode and polarization of a classical field. Field product states are measured by two-port heterodyne detection with pinholes. Analog multiplication followed by detection of the in-phase and out-of-phase voltage components at specific frequencies enables determination of the product state. The success of this technique motivated our experimental study of classical simulation of multi-particle quantum entanglement as described in later chapters.

### 3.1.1 Brief Description of Two-Window Heterodyne Measurement

We include a brief description of two-window heterodyne measurement of Wigner functions as shown in Figure 3.1. In a balanced heterodyne detection scheme, a local oscillator (LO) beam is mixed with a signal beam. The LO beam comprises a focused gaussian beam and a collimated gaussian beam. The focussed gaussian beam is frequency shifted at 110 MHz and the collimated gaussian beam is frequency shifted at 110 MHz plus 5 kHz. These two LO beams are overlapped with each other and phase locked at 5 kHz. The signal beam is frequency shifted at 120 MHz. Two imaging lenses L1 and L2 are used to overlap the dual LO beam with the signal beam at two detectors. The position distribution of the signal beam is measured by moving the position of the dual LO beam relative to the lens L1. The momentum distribution of the signal beam is measured by moving the position of the lens L2. The interference beat signal between the signal beam and the dual LO beam is obtained at detectors 1 and 2 and consists of 10 MHz and 10 MHz plus 5 kHz components. These signals are sent to a spectrum analyzer. The output of the analyzer is then squared by using an analog multiplier. The mean square signal has components at 5 kHz. A lock-in amplifier is used to measure the in- and out-of phase components of the multiplier output at 5 kHz. The measurements of the quadrature amplitudes at 5 kHz yield the real and imaginary parts of the $x-p$ cross correlation function, $\langle\mathcal{E}^*(x)\mathcal{E}(p)\rangle$ of the signal beam. Then, the Wigner function of the signal is obtained by a simple linear transform of the $x-p$ correlation function.

In the following section, we will discuss the detection apparatus used in measuring the Wigner function.

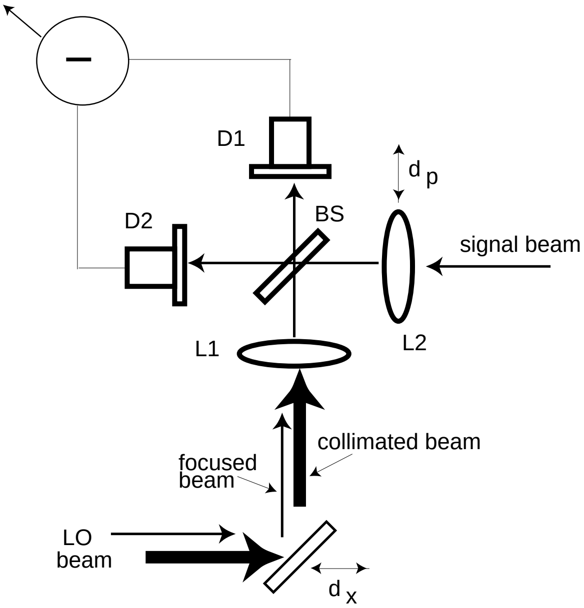

**Figure 3.1**: Wigner function of a signal beam is measured with the dual LO beam in a balanced heterodyne detection scheme.

## 3.2 Detection Apparatus

In this experiment, two LO beams are frequency shifted at 110 MHz and 110 MHz + 5 kHz and phase-locked at 5 kHz using acousto-optic modulators. The signal beam is frequency shifted at 120 MHz. Then, we obtain two heterodyne beat signals at 10 MHz and 10 MHz +5 kHz from the balanced heterodyne detection scheme. Figure 3.2 is the detection diagram for the two-window heterodyne method. It shows a schematic which traces the heterodyne beat signals from the point where they are detected by the photodiodes, D1 and D2, through the transimpedence amplifier to the spectrum analyzer. The signal is then squared using a low noise multiplier and finally fed to a lock-in amplifier.

For convenience in aligning two LO beams with a single signal beam, the heterodyne beat signal $V_B$ from the interference of the signal beam with each independent

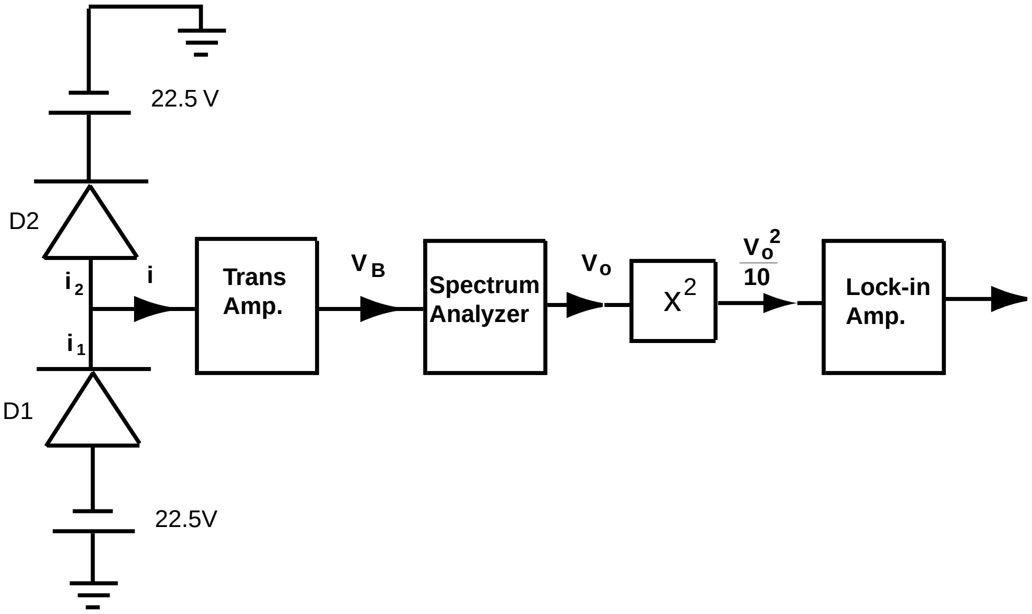

**Figure 3.2**: Detection Diagram for the two window technique.

LO beam is measured and compared with the calculated value $V_B$. The calculation to obtain the $V_B$ from the heterodyne beat signal at the detectors through our detection apparatus in Figure 3.2 is given in Appendix A.

### 3.2.1 Photodetectors and Transimpedence Amplifier

Two EGG FFD-040B photodiodes are used and each reverse-biased by 22.5 V batteries to decrease their response time. They are connected as shown in Figure 3.2 so that their outputs subtract ($i = i_1 - i_2$). The photocurrent is converted to a voltage by a wide bandwidth operational amplifier (model:CLC425) as a transimpedence amplifier.

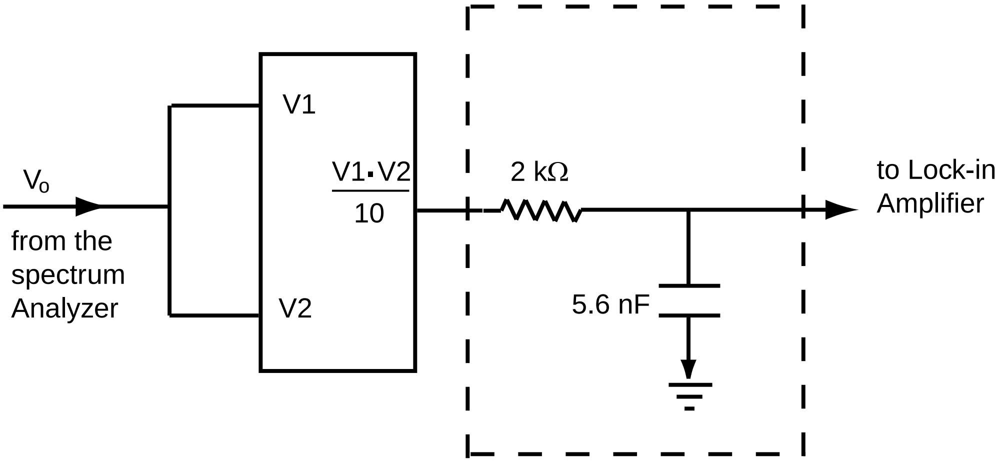

**Figure 3.3**: The squarer.

### 3.2.2 Spectrum Analyzer and Lock-in Amplifier

The transimpedence amplifier output $V_B$ is then fed to a spectrum analyzer (Hewlett Packard model $ESA - L1500A$). An analog video output $V_0$ of the analyzer is squared by using a low noise multiplier (Analog Devices AD534) to yield a signal that measures the $x - p$ cross correlation function. Squaring the signal yields the power spectrum, allowing us to subtract electronic noise in real time by using a lock-in amplifier. The multiplication circuit in Figure 3.3 shows that the signal from the spectrum analyzer is feed into the both inputs of the multiplier. The multiplier thus produces a signal proportional to the square of its input. The output of the squarer is low pass filtered at 40 kHz before being sent to a lock-in amplifier, *EGG* Princeton Applied Research Model 124A, where the in-phase and out-of-phase components of the $|V_0|^2$ are measured.

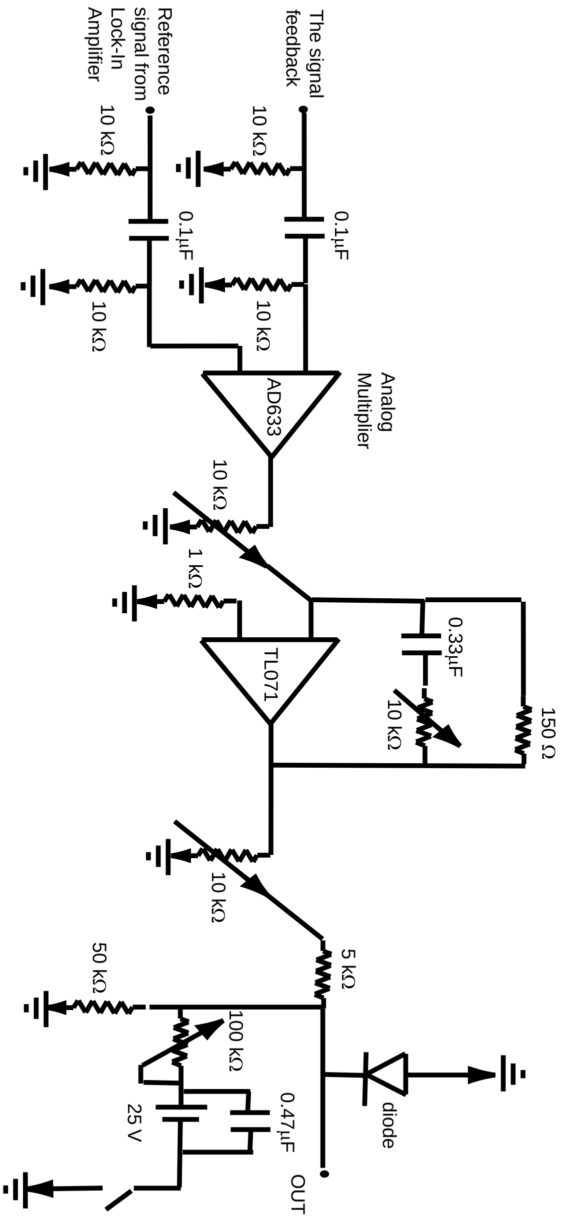

**Figure 3.4**: The circuit diagram for Phase Locking Loop used in measuring the Wigner function.

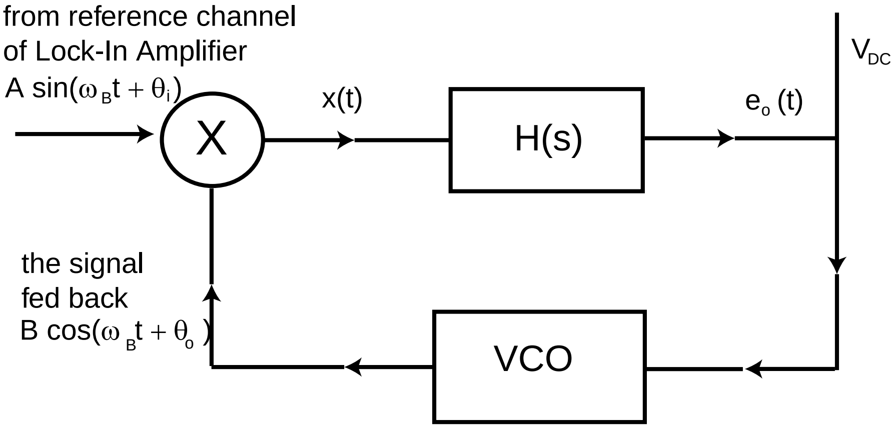

**Figure 3.5**: The schematic for the PLL.

### 3.2.3 Phase Locked Loop

The phase locked loop (PLL) is used to lock the phase of two LO beams which differ in frequency by 5 kHz. The first LO beam is frequency shifted at 110 MHz plus 5 kHz by using a tunable AO modulator and the second LO beam is shifted by a fixed acousto-optic (AO) modulator at 110 MHz. The circuit diagram is shown in Figure 3.4. The schematic operation of the PLL can be illustrated in a feedback system as shown in Figure 3.5. It contains three basic components: (A), a voltage-controlled oscillator (VCO), (B), a multiplier functioning as phase detector or a phase comparator, (C), a loop filter $H(s)$.

In a typical feedback system, the beat signal from the two LO beams follows the reference signal obtained from a reference channel of a lock-in amplifier. If the beat signal is not equal in frequency to the reference signal, the difference (known as the error) will change the signal fed back until it is close to the reference signal. The VCO in the AO driver adjusts its own frequency or phase until the beat signal is equal to that of the reference sinusoid. At this point, the frequency and phase of the two signals are in synchronism with constant phase offset of 90°.

A VCO in the tunable acousto-optic modulator has a frequency that can be controlled by an external voltage comprised of a DC voltage and error signal. Its oscillation frequency varies linearly with the input voltage that is 4 MHz/V. If the input external voltage is $V_{dc} + e_o(t)$, it produces a sinusoid of frequency $\omega$,

$$\omega(t) = \omega_\circ + 4\frac{MHz}{V}e_\circ(t) \tag{3.1}$$

where $\omega_o$ is 110 MHz + 5 kHz due to DC voltage supply $V_{dc}$. The first LO beam modulated by this tunable AO is beat with the second LO beam at 110 MHz, then the beat signal $\omega_B$ at 5 kHz is fed into the input of the analog multiplier. Let's denote the sinusoid beat signal as $B\cos(\omega_B t + \theta_o)$ and the reference sinusoid as $A\sin(\omega_B + \theta_i)$. The output of the multiplier $x(t)$ is given by,

$$\begin{aligned} x(t) &= A\,B\sin(\omega_B t + \theta_i)\,\cos(\omega_B t + \theta_o) \\ &= \frac{AB}{2}[\sin(\theta_i - \theta_o) + \sin(2\omega_B t + \theta_i + \theta_o) \end{aligned} \tag{3.2}$$

The last term on the right-hand side is a high frequency signal and is suppressed by the loop filter, which is low-pass narrow-band filter. Hence, the error signal $e_o(t)$,

$$e_\circ = \frac{AB}{2}\sin\theta_e\,, \quad \theta_e = \theta_i - \theta_o \tag{3.3}$$

where $\theta_e$ is the phase error $(\theta_i - \theta_o)$. Figure 3.6 shows the plot of $e_o$ vs $\theta_e$. Using this plot, we can explain the locking mechanism. If the loop is locked, then the frequencies of both the reference and the beat sinusoids are identical. Then, the loop is in a steady state, and $\theta_e$, $\theta_i$ and $\theta_o$ are constant. The Figure 3.6 shows a

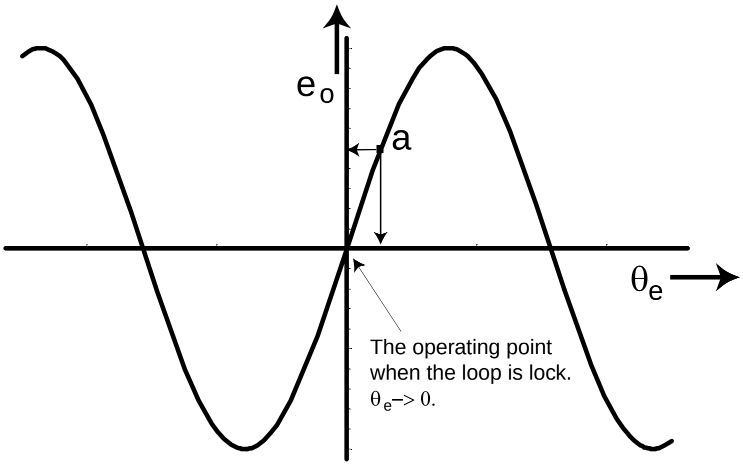

**Figure 3.6**: The error signal diagram

typical operating point $a$ and the corresponding values of $e_o$ and $\theta_e$.

Now, if the reference sinusoid frequency suddenly increases from $\omega_B$ to $\omega_B + k$. This means the incoming beat signal is $Acos[(\omega_B + k)t + \theta_i] = Acos(\omega_B t + \theta_i')$, where $\theta_i' = kt + \theta_i$. Thus, the increase in the incoming beat frequency causes $\theta_i$ to increase to $\theta_i + kt$, thereby increasing $\theta_e$. The operating point $a$ now shifts upward. This increases $e_\circ$, which, in turn, increases the frequency of the tunable AO output to match the increase in the reference frequency. This also means that if the reference sinusoid frequency decreases, the loop output frequency will also decrease correspondingly. Thus, the loop locks the reference sinusoid. The two signals are said to be mutually phase coherent or in phase lock. The VCO (tunable AO) thus locks the frequency and the phase of the incoming beat signal. A PLL can lock the incoming beat frequency only over a finite range of frequency shift. This range is called the hold-in or lock range. Also if the reference or beat signal frequency changes too rapidly, the loop may not lock. In order to have the loop stays locked, the difference $\theta_e = \theta_i - \theta_\circ$ is a small number $\rightarrow 0$.

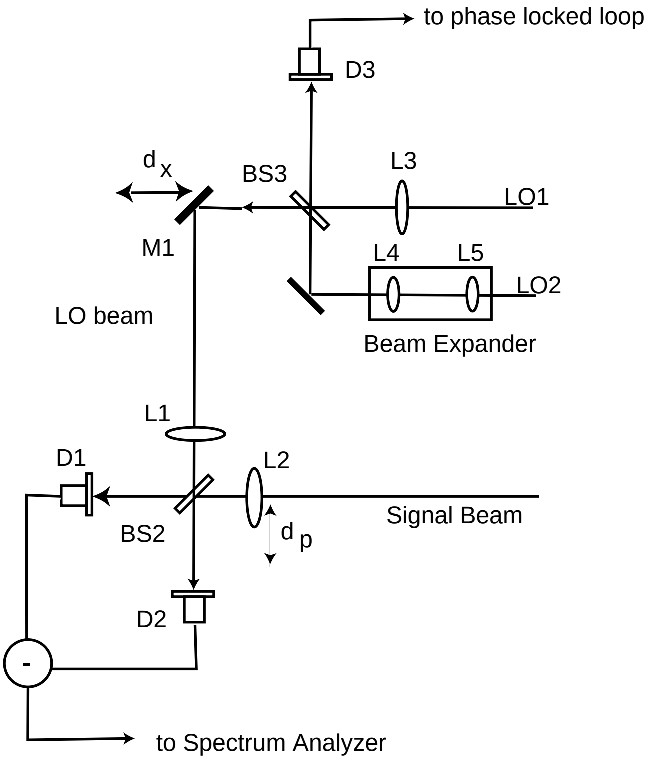

**Figure 3.7**: Experimental setup for the two window technique.

## 3.3 Two-Window Heterodyne Method

### 3.3.1 Experimental Analysis

In 1932, E.P.Wigner introduced a wave mechanical phase space distribution function that plays a role closely analogous to that of a classical phase space distribution in position and momentum. For a wave field varying in one spatial dimension, $\mathcal{E}(x)$, the Wigner phase space distribution is given by

$$W(x,p) = \int \frac{d\epsilon}{2\pi} exp(i\epsilon p)\langle\mathcal{E}^*(x+\epsilon/2)\mathcal{E}(x-\epsilon/2)\rangle \tag{3.4}$$

where $x$ is the position, $p$ is a wave vector (momentum), and the angle brackets denote a statistical average.

In our previous work [60], we described the measurement of smoothed Wigner phase space distributions for classical fields by use of balanced heterodyne measurement of the mean-square beat amplitude $\langle |V_B|^2 \rangle$. The mean-square beat amplitude is proportional to the square of the magnitude of the spatial overlap integral of the LO and signal fields in the detector planes, $D_1$ and $D_2$, which can be written in terms of the overlap of the Wigner functions for the LO and signal beams

$$\langle |V_B(d_x, d_p)|^2 \rangle \propto \int dx\, dp\, W_{LO}(x - d_x, p + kd_p/f) W_S(x, p) \ . \tag{3.5}$$

The detailed derivation of Eq. (3.5) is given in Appendix B. Here $W_S(x,p)[W_{LO}(x,p)]$ is the Wigner distribution of the signal (LO) field in the input planes of lenses L2 (L1). The variables $d_x$ and $d_p$ respectively indicate the positions of a mirror M1 and a lens L2 as in Figure 3.7. The $y$ integration is suppressed for simplicity. Eq. (3.5) shows that the mean-square beat signal yields a phase-space contour plot of $W_S(x,p)$ with phase space resolution determined by $W_{LO}(x,p)$. For a gaussian LO beam the position resolution is determined by the diameter of the LO beam, whereas the momentum resolution is determined by the corresponding diffraction angle. Hence the phase space resolution is minimum uncertainty limited, and the measured Wigner distribution is smoothed. The measurement of phase space distributions is accomplished by translation of optical elements. These elements are all mounted on translation stages driven by computer controlled linear actuators. The motion control system is based on the MotionMaster 2000 (MM2000) system from Newport Research Corporation (NRC). The MM2000 system can be controlled using Labview software from National Instruments with drivers downloaded from

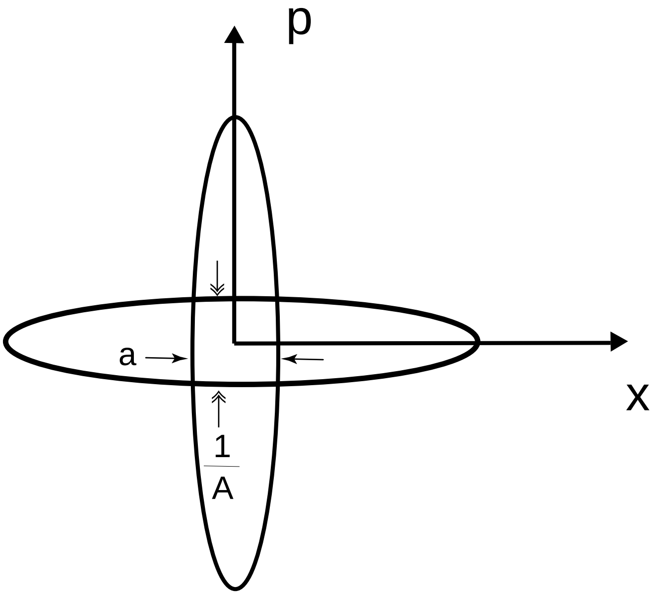

**Figure 3.8**: The overlapping area is the position and momentum resolutions of the combined LO beams. The uncertainty is proportional to $\frac{a}{A}$ less than 1.

the world wide web (http://www.natinst.com). The system scans the LO position over a distance $d_x = \pm 1$ cm by translating mirror M1 in the LO path. The LO momentum is scanned over $\pm 0.3\,k$, where $k = 2\pi/\lambda$ is an optical wave vector, by translation of the signal-beam input lens L2 (focal length $f = 6$ cm) by a distance $d_p$.

To obtain independent control of the $x$ and $p$ resolution in heterodyne measurement, we employ a slowly varying LO field containing a focused and a collimated field with a well defined relative phase $\theta$

$$\mathcal{E}_{LO}(x) = \mathcal{E}_\circ[\,\exp(-\frac{x^2}{2a^2}) + \beta\,\exp(-\frac{x^2}{2A^2})\,\exp(i\theta)] \qquad (3.6)$$

Here $a$ is chosen to be small compared with the distance scales of interest and $1/A$ is chosen to be small compared with the momentum scales of interest in the signal field.

The schematic picture of the overlapping of the LO beam with the spatial width $a$ and another LO beam with the spatial width $A$ is shown in Figure 3.8. One can see that the overlapping area is determined by the position and momentum resolutions for the LO fields in Eq. (3.6). The Wigner function for the LO field is obtained by substituting Eq. (3.6) into Eq. (3.4). We take $A^2 \gg a^2$. In this case the phase-($\theta$-) dependent part of the Wigner function for the LO takes the form

$$\begin{aligned} W_{LO}(x,p) &\propto exp(-\frac{2x^2}{A^2} - 2a^2p^2)\cos(2xp+\theta) \\ &\simeq \cos(2xp+\theta), \end{aligned} \tag{3.7}$$

where the last form assumes that the range of the momentum and position integration in relation (3.5) is limited by the signal field.

In the experiments, as illustrated in Figure 3.7, the LO beam is obtained by combination of two fields that differ in frequency by 5 kHz, so that $\theta = (2\pi \times 5kHz)t$. Lens L3 focuses beam LO1 to a waist of width $a$, and lenses L4 and L5 expand beam LO2 to width $A$. We combine these two components at beam splitter BS3 to obtain an LO field of the form given in Eq. (3.6). We monitor one output of the beam splitter with detector $D_3$ to phase lock the 5 kHz beat signal to the reference channel of the lock-in amplifier. Each component of the LO beam is shaped so that it is at a beam waist at the input plane of the heterodyne imaging system (lens L1). The dual LO and signal fields are mixed at BS2, and the rms beat amplitude at 10 MHz is measured with an analog spectrum analyzer. The spectrum analyzer bandwidth, 100 kHz, is chosen to be large compared with 5 kHz difference frequency. The output of the spectrum analyzer is squared in real time with a low-noise multiplier, the output of which is sent to the lock-in amplifier as described above. The lock-in outputs for in- and out-of-phase quadratures then directly determine the real and the imaginary parts of the quantity

$$\begin{aligned} S(x_\circ, p_\circ) &= \int \frac{dx'dp'}{\pi} \exp[2i(x'-x_\circ)\times(p'-p_\circ)]W_S(x',p') \\ &= \langle \mathcal{E}^*(x_\circ)\mathcal{E}(p_\circ)\rangle \exp(ix_\circ p_\circ) \end{aligned} \tag{3.8}$$

where the $W_{LO}(x,p)$ in Eq. (3.7) is replaced by $e^{i(2xp+\theta)}$ in Eq. (3.5) yielding the in-phase and out-of-phase contributions from $\theta$. Here $x_\circ = d_x$ is the center position of the LO fields and $p_\circ = -kd_p/f$ is the center momentum. Appendix C shows the calculation for the amplitude of real and imaginary parts of $S(x_\circ, p_\circ)$ from the heterodyne beat signal at detectors $D_1$ and $D_2$.

As the position of mirror M1 is scanned a distance $d_x$, the optical path lengths of the LO fields change. For the current experiments, the HeNe laser is a source, the change in path lengths is small compared with the Raleigh length and the coherence length of the beams, so translating M1 simply changes the center position of the LO fields.

We can readily invert the detected signal given in Eq. (3.8) to obtain the Wigner function by a linear transformation. Using the reality of $W_S(x,p)$, we obtain

$$\begin{aligned} W_S(x,p) &= \int \frac{dx_\circ dp_\circ}{\pi} \cos[2(x-x_\circ)(p-p_\circ)] \times S_R(x_\circ - p_\circ) \\ &+ \int \frac{dx_\circ dp_\circ}{\pi} \sin[2(x-x_\circ)(p-p_\circ)] \times S_I(x_\circ - P_\circ) \end{aligned} \tag{3.9}$$

where $S_R$ and $S_I$ are the real and the imaginary parts of Eq. (3.8), i.e. the in- and out-of-phase lock-in signals.

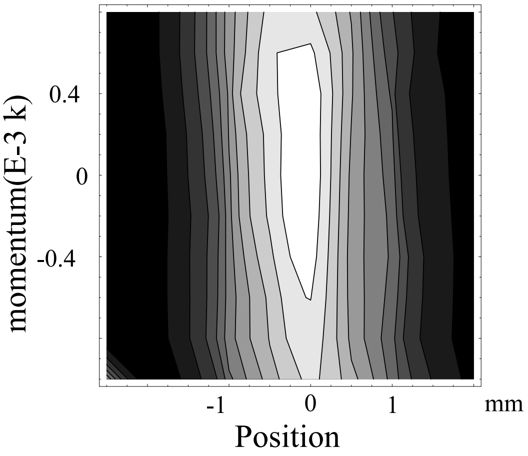

**Figure 3.9**: The optical phase space distribution of the signal beam using the tightly focused LO1 beam.

## 3.4 Experimental Results

### 3.4.1 The Alignment of Two LO Beams

It is important to ensure that two LO beams are overlapping with the signal beam exactly at the same origin, that is at $x$=0 and $p$=0, so that the reference phase of lock-in amplifier at 5 kHz can be set at the right phase angle, which will be a reference phase for the measurement of in-phase $S_R$ and out-of-phase $S_I$ components. The alignment procedure can be accomplished as follows: First, we align the tightly focused LO1 parallel with the signal beam and obtain the smoothed Wigner function as shown in Figure 3.9. One can see that the smoothed Wigner function has the origin at $x$=0 and $p$=0. Then, we fix the locations of the position lens L1 and momentum lens L2. Secondly, we use two mirrors for beam steering to align the collimated LO2 parallel with the signal beam and obtain the smoothed Wigner function as shown in Figure 3.10. One can see that the smoothed Wigner functions in Figure 3.10 and Figure 3.9 are located at the same origin that is at $x$=0 and $p$=0.

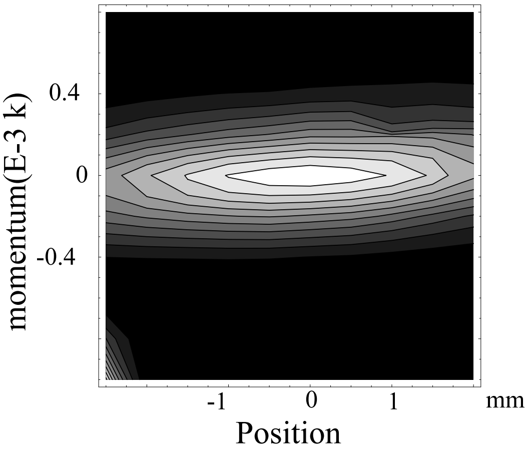

**Figure 3.10**: The optical phase space distribution of the signal beam using the collimated beam.

Finally, two LO beams are overlapped and phase locked at 5 kHz. Note that the smoothed Wigner function is obtained by using a single LO beam with a mechanical chopper in the signal beam to give a reference frequency of 500 Hz for the lock-in amplifier.

It is interesting to notice that Figure 3.9 contains the position distribution of the signal beam because of the position resolution of the tightly focussed LO beam. Similarly, the Figure 3.10 contains the momentum distribution of the signal beam because of the momentum resolution of the collimated LO beam.

## 3.4.2 Measurement of Wigner Functions

### Gaussian Beam

As an initial demonstration of the capability of this system, we measure the Wigner function for an ordinary gaussian beam. The signal beam is shaped by a telescope so that its waist coincides with input plane L2 of the heterodyne imaging system.

For a gaussian beam at its waist, Eq. (3.4) gives the Wigner distribution as,

$$W_S(x,p) = \frac{1}{\pi}\exp(-\frac{x^2}{w^2} - w^2p^2) \tag{3.10}$$

where $w$=0.85 mm is the $1/e$-intensity width. The $x-p$ correlation function for the signal field is measured by use of the LO beam of the form given by Eq. (3.6) with $a$ =81 $\mu$m, $A$ = 2.6 mm, and $\beta$ =1. The measurement result for a gaussian beam is shown in Figure 3.11. The top row is our experimental results and the bottom row is a theoretical prediction obtained by using Eq. (3.10) in Eq. (3.8). The real and the imaginary parts of the detected signal, Eq. (3.8), are shown in Figure 3.11(a) and (b). These two measurements are used in Eq. (3.9) to recover the Wigner distribution of the signal field in Figure 3.11(c). We $\chi^2$ fit the width of the measured in-phase signal in position for $p = 0$ to obtain a spatial width $w$ =0.87 mm, whereas the corresponding momentum distribution for $x = 0$ yields $w$ =0.83 mm. Both results are in excellent agreement with the measured width $w$=0.85 mm obtained by use of a diode array, demonstrating that high position and momentum resolution can be jointly obtained.

### A Classical Analog of A Schrödinger Cat State

A more interesting example is the Wigner function for the same gaussian beam with a wire placed at its center in the input plane L2. Then, the electric field $\mathcal{E}_s(x)$ as a function of position is shown in Figure 3.12. It is analogous to a Schrödinger cat state. In this case the slowly varying field is gaussian as before but multiplied by a split function that sets the field equal to zero for $|x| \leq 0.5$ mm. Figure 3.13 shows contour plots of the real and the imaginary parts of the detected signal and the Wigner function (top row) and the corresponding predicted distributions for the

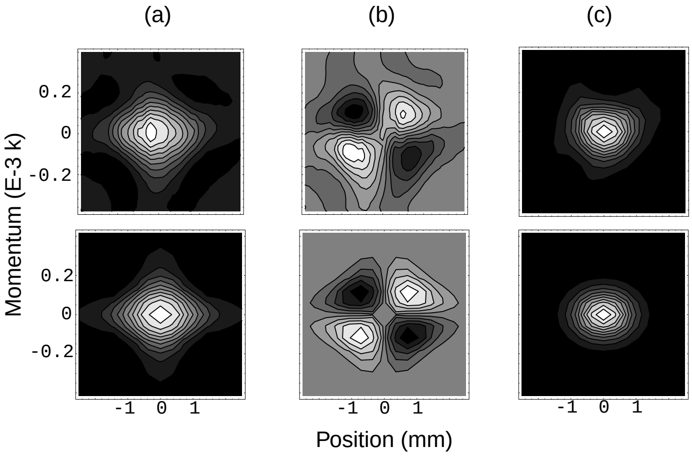

**Figure 3.11**: The Wigner function for a gaussian beam. Top row is experimental results and bottom row is theoretical prediction for a gaussian beam. (a) is in-phase component of $S(x_\circ, p_\circ)$ and (b) is out-of-phase component of $S(x_\circ, p_\circ)$. (c) is the recovered Wigner function for a gaussian beam with spatial width = 0.87 mm.

field (bottom row). The coherence between these two wave packets in the signal field leads to an interference pattern in the momentum distribution. The signature of this coherence in the Wigner distribution is the oscillating positive and negative values between the main lobes. An interesting feature of this Wigner distribution is the oscillation in momentum at $x$ =0, the position of the wire. We observe the negative values which is analogous to quantum interference in phase space. This feature can be seen in Figure 3.13(d), in which the inverted data are shown as a three dimensional plot (top) and compared with the predicted distribution (bottom). The negative values highlight the impossibility of a particle simultaneously having a precise position and momentum, and also to make sure the sum over momentum along x = 0 in Wigner phase space distribution has zero intensity at the center. The negative and positive parts of the Wigner phase space distribution are important features to obtain full information about the field. The position distribution, $|\mathcal{E}_S(x)|^2$, and momentum distribution, $|\mathcal{E}_S(p)|^2$, of the signal field, can be

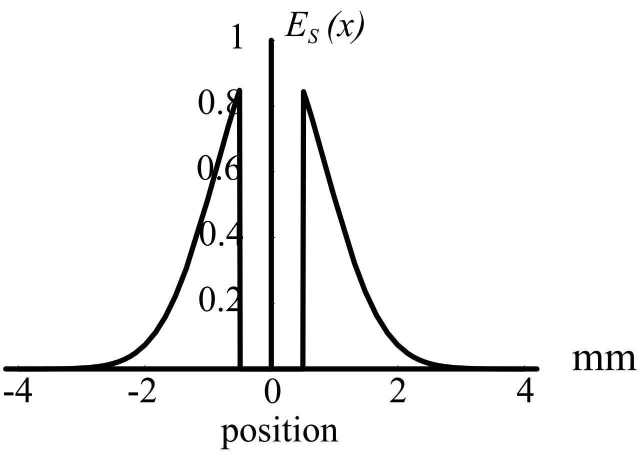

**Figure 3.12**: The classical analog of Schrödinger cat state.

obtained by integration.

From the obtained Wigner function, one can obtain the position and momentum distribution of the $\mathcal{E}_s(x)$ by using the formulas $|\mathcal{E}_S(p)|^2{=}\int_{-\infty}^{\infty} W_S(x,p)\,dx$ and $|\mathcal{E}_S(x)|^2{=}\int_{-\infty}^{\infty} W_S(x,p)\,dp$ as shown in Figure 3.14(b) and (d) respectively. The measurements are in agreement with the theoretical predictions as shown in Figure 3.14(a) and (c) respectively. The dashed-line in Figure 3.14(c) is obtained by using the theoretical Wigner function in Figure 3.13(c)(bottom). The momentum distribution contains the interference features of two spatially separated wave packets of $\mathcal{E}_S(x)$ as shown in Figure 3.14(b).

### 3.4.3 Discussion

In this first experiment, we have demonstrated the similarities between quantum and classical interference via the measurement of the Wigner function for a classical analog of Schrödinger cat state. We also note that an interesting analog exists between the small and the large beams of our two-window LO and the superposition

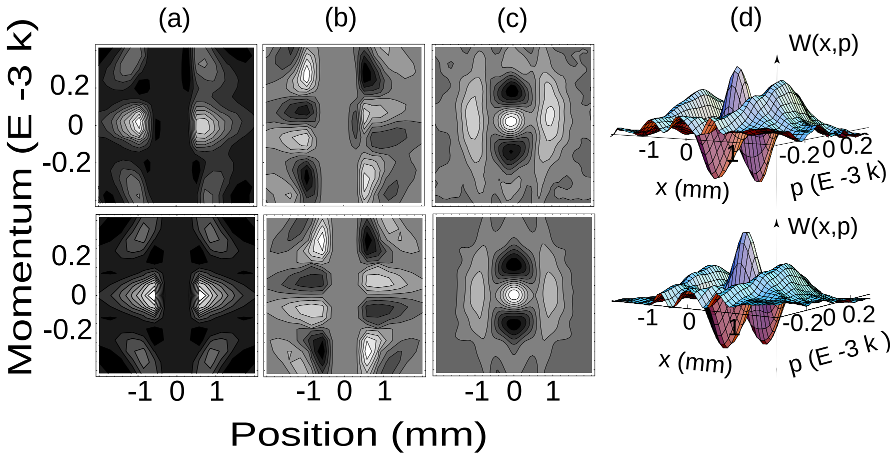

**Figure 3.13**: The Wigner function for the Schrödinger cat state. Top row shows experimental results and bottom row shows theoretical predictions for a gaussian beam blocked by a wire. (a) in-phase component of the $S(x_\circ, p_\circ)$ and (b) out-of-phase component of the $S(x_\circ, p_\circ)$. (c) Wigner distribution (d) 3D plot of the recovered Wigner function for classical analog of the cat state. The negative values are also observed.

of the position (in-phase) and the momentum (out-of-phase) squeezed fields. This analogy is expected from the discussion in Chapter 2, since the transverse modes in a lens-like medium provide a natural harmonic oscillator basis. A $TEM_{00}$ gaussian beam is the lowest mode and analogous to a coherent state. Gaussian beams of smaller (larger) size than the lowest mode correspond to position (momentum) squeezed states. The two window technique here can only be used if we know the nominal size of the signal beam. The focussed and collimated LO beams must be chosen to achieve sufficient $x-$ and $p-$ resolution for the given signal beam.

## 3.5 Measurement of Product States

In the second experiment, we made a measurement of a product state $E_{H1}(x_1)E_{V2}(x_2)$ by using an analog multiplier (AD 633). Here, $H$ is the horizontal polarization of

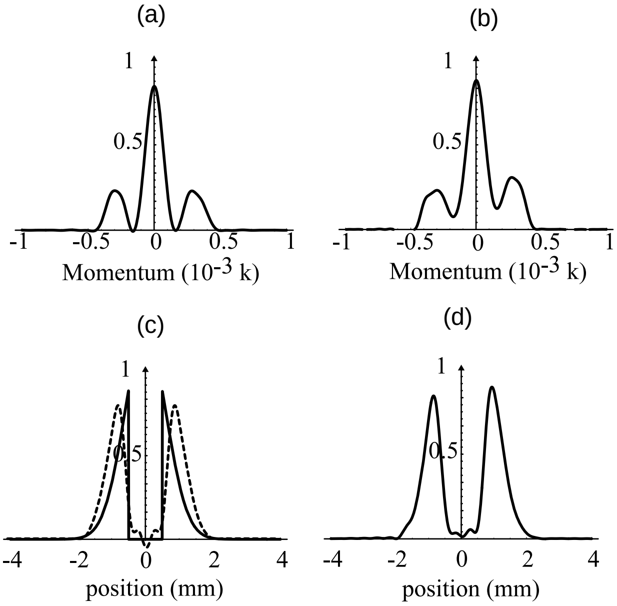

**Figure 3.14**: The momentum and position distribution for the Schrödinger cat state. (a) and (c) are theoretical prediction of momentum and position distributions of the cat state. (b) and (d) are the corresponding experimental results of momentum and position distribution of the cat state obtained by integrating the measured Wigner distribution over $p$ and $x$ respectively.

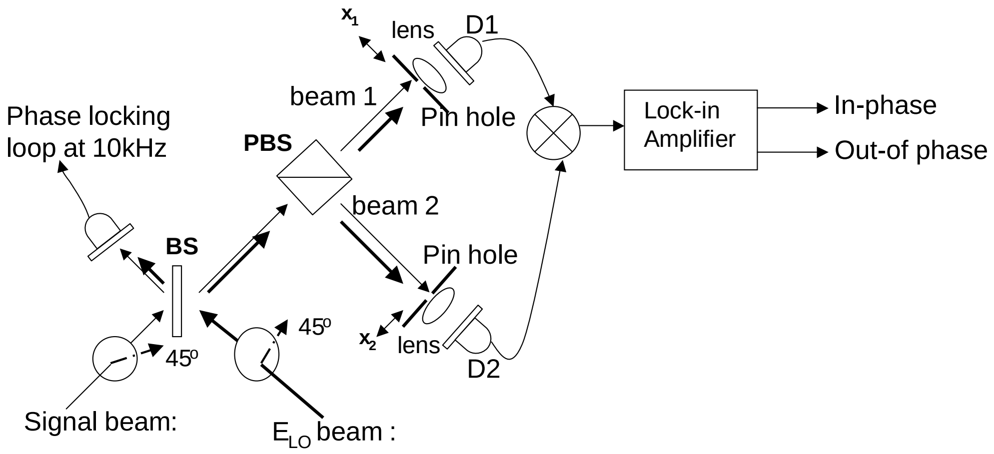

**Figure 3.15**: The experimental setup for product state measurement.

optical beam 1 and $V$ is the vertical polarization of optical beam 2. The spatial profiles of two spatially separated and orthogonally polarized classical beams 1 and 2 are measured by placing a pinhole of 200 $\mu$m at each beam. The heterodyne beat signals from these two detectors 1 and 2 are then multiplied. The in-phase and out-of-phase components of the product signal are measured in a lock-in amplifier, yielding to the real and imaginary parts of the product state $E_{H1}(x_1)E_{V2}(x_2)$.

### 3.5.1 Experimental Setup

The experimental setup for the measurement of product states is shown in Figure 3.15. The signal beam with the polarization at 45° is modulated by a tunable acoustic-optic modulator at frequency 110 MHz + 10 kHz. The beam is phase locked at 10 kHz with a local oscillator beam which is shifted by a fixed frequency acoustic-optic modulator at frequency 110 MHz. The local oscillator beam has a beam waist 20 times larger than the signal beam and also polarized at 45°. It is obtained by using a beam expander with the magnification of $\frac{f_1}{f_2} = \frac{50cm}{2.5cm} = 20$. The local oscillator beam and the signal beam are combined with a beamsplitter. One of the output fields from of the beamsplitter is used as a feedback signal to the phase locking loop where the input reference frequency is provided by a function generator. Another output field of the beam splitter is incident on a cube polarizing beamsplitter (CPBS) and produces two beams; beams 1 and 2. Beam 1 contains horizontal polarization components of the local oscillator beam $E_{LO1}$ and the signal beam $E_{H1}(x_1)$. The $E_{LO1}$ beam is spatially constant compared to the transverse position dependence of $E_{H1}(x_1)$ because of the size of the LO beam. Similarly, beam 2 contains vertical polarization components of the local oscillator beam $E_{LO2}$ and the signal beam $E_{V2}(x_2)$. The $E_{LO2}$ beam is spatially constant compared to the transverse position of $E_{V2}(x_2)$. Then, the fields in beam 1, $E_1(t)$, and in beam 2, $E_2(t)$, are given by,

$$\begin{aligned} E_1(t) &= E_{LO1}e^{-i(\omega+\Omega_{LO})t} + E_{H1}(x_1)e^{-i(\omega+\Omega_S)t} \\ E_2(t) &= E_{LO2}e^{-i(\omega+\Omega_{LO})t} + E_{V2}(x_2)e^{-i(\omega+\Omega_S)t} \end{aligned} \tag{3.11}$$

where $\omega$ and $\Omega$ are optical and modulated frequencies respectively. Then, interference beat signals at beams 1 and 2 are written as;

$$\begin{gathered} V_1(t) \propto E^*_{LO1}E_{H1}(x_1)e^{-i(\Omega_S-\Omega_{LO})t} + E_{LO1}E^*_{H1}(x_1)e^{i(\Omega_S-\Omega_{LO})t} \\ V_2(t) \propto E^*_{LO2}E_{V2}(x_2)e^{-i(\Omega_S-\Omega_{LO})t} + E_{LO2}E_{V2}(x_2)^*e^{i(\Omega_S-\Omega_{LO})t} \ , \end{gathered} \tag{3.12}$$

where,

$$E(x) = \exp(-\frac{x^2}{2a})\exp(ik\frac{x^2}{2R}) \tag{3.13}$$

and $\Omega_S - \Omega_{LO} = 10$ kHz. We neglect the constant terms that are the intensities of the local oscillator and signal beams. The beat signals $V_1(t)$ and $V_2(t)$ at detectors D1 and D2 are multiplied by using an analog multiplier. The multiplication beat signal at 20 kHz is proportional to

$$V_1(t)V_2(t) \propto E^*_{LO1}E^*_{LO2}E_{H1}(x_1)E_{V2}(x_2)e^{-i2(\Omega_S-\Omega_{LO})t} + cc \tag{3.14}$$

The beat signal at 20 kHz is then fed to the lock-in amplifier. The in-phase and out-of-phase components of the beat signal $V_1(t)V_2(t)$ determine the product state, that is the real and imaginary parts of $E_{H1}(x_1)E_{V2}(x_2)$ as,

$$\begin{aligned} Re[E_{H1}(x_1)E_{V2}(x_2)] &\propto e^{-\frac{x_1^2}{2a_1}}e^{-\frac{x_2^2}{2a_2}}\cos[k\frac{x_1^2}{2R_1}+\frac{x_2^2}{2R_2}] \\ Im[E_{H1}(x_1)E_{V2}(x_2)] &\propto e^{-\frac{x_1^2}{2a_1}}e^{-\frac{x_2^2}{2a_2}}\sin[k\frac{x_1^2}{2R_1}+\frac{x_2^2}{2R_2}] \end{aligned} \tag{3.15}$$

where $a$ and $R$ are beam waist and radii of curvature for the corresponding gaussian beam.

Position information for the horizontally polarized signal field $E_{H1}(x_1)$ and vertically polarized signal field $E_{V2}(x_2)$ is measured by translating pinhole 1 and 2 respectively as shown in Figure 3.15. The diameter of the pin hole is 200 $\mu$m. A lens is placed behind the pinhole to collect the optical power on the detector which is located at its focal point.

### 3.5.2 Measurement of $E_{H1}(x_1)E_{V2}(x_2)$

In view of symmetry property of the spatial profile of a gaussian beam, the measurement of product state $E_{H1}(x_1)E_{V2}(x_2)$ can be simplified in the ideal case by

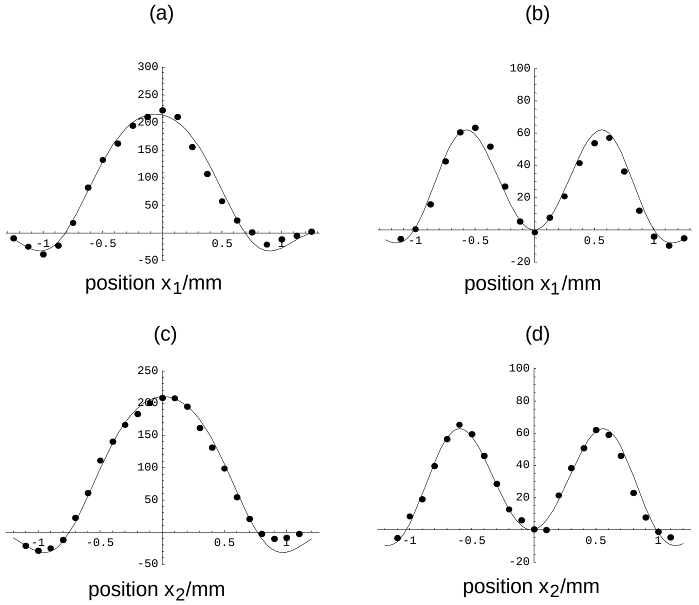

**Figure 3.16**: The measurement of the product state.(a) and (b) are in-and out-of phase components of $E_{H1}(x_1)E_{V2}(x_2 = 0)$. (c) and (d) are in- and out-of phases components of $E_{H1}(x_1 = 0)E_{V2}(x_2)$. Data = dotted line. Theory = solid line.

measuring the product components $E_{H1}(x_1)E_{V2}(x_2 = 0)$ and $E_{H1}(x_1 = 0)E_{V2}(x_2)$ respectively. Figure 3.16(a) and (b) are the in-phase and out-of-phase components of the product optical fields $E_{H1}(x_1)E_{V2}(x_2 = 0)$. The solid lines in the figures are plotted by using Eq. (3.15) with $x_2$=0, $a_1$=0.5 mm and $R_1$=1700 mm. Figure 3.16(c) and (d) are the in-phase and out-of-phase components of the product optical fields $E_{H1}(x_1 = 0)E_{V2}(x_2)$. Similarly, the solid lines in the figures are plotted by using Eq. (3.15) with $x_1$=0, $a_2$=0.52 mm and $R_2$=1800 mm. The parameters $a_1$, $a_2$, $R_1$ and $R_2$ obtained from the measurements of in-phase and out-of-phase components of $E_{H1}(x_1)E_{V2}(x_2 = 0)$ and $E_{H1}(x_1 = 0)E_{V2}(x_2)$ are then used to plot the 3-D of the product state $E_{H1}(x_1)E_{V2}(x_2)$.

Figure 3.17(a) and (b) are the 3-D plot of the in-phase and out-of-phase components of the product state $E_{H1}(x_1)E_{V2}(x_2)$ that determined from Eq. (3.15) with

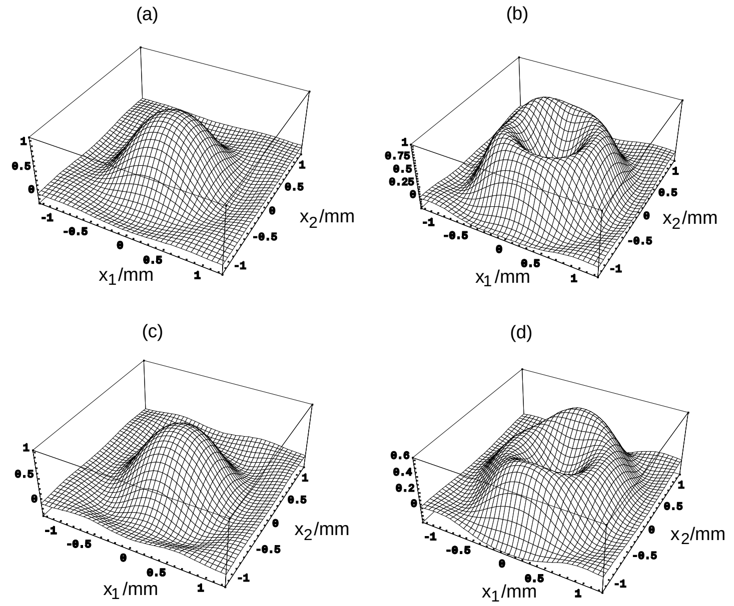

**Figure 3.17**: The measurement and theoretical prediction of the 3D plot of the product state. (a) and (b) are the measured in- and out-of phase components of $E_{H1}(x_1)E_{V2}(x_2)$. (c) and (d) are the theoretical predictions for in- and out-of phase components of $E_{H1}(x_1)E_{V2}(x_2)$

$a_1 = 0.5$ mm, $a_2 = 0.52$ mm, $R_1 = 1700$ mm and $R_2 = 1800$ mm. Figure 3.17(c) and (d) are the theoretical prediction for the product state of two optical Gaussian fields with beam waist, $a_1 = a_2 = 0.5$ mm and $R_1 = R_2 = 1800$ mm. The beam waists $a_1$ and $a_2$ are obtained by use of a diode array and the radii of curvature $R_1 = R_2$=1800 mm is chosen from the previous measurements Figure 3.16(c) and (d).

## 3.6 Discussion

The success in using the multiplication technique to obtain the product state motivated the possibility of simulation of quantum entanglement for more than one particle by using classical fields. The multiplication beat signal from two spatially separated fields followed by band pass filtering is analogous to coincidence detection of two particles. It is discussed in detail in the following chapters.

# Chapter 4

# Two-Field Correlations

## 4.1 Overview

In this chapter, we demonstrate classical wave simulation of nonlocal entanglement of two-photons. We reproduce the measurement of classical analogs of four Bell polarization-entangled states which are $\frac{1}{\sqrt{2}}[|H_1V_2)\pm|V_1H_2)]$ and $\frac{1}{\sqrt{2}}[|H_1H_2)\pm|V_1V_2)]$, where a parenthesis $|\,)$ is used to denote a classical state. The simulations employ optical heterodyne detection of two fields of different frequencies with orthogonal polarizations. Essential to the method is the use of analog multiplication of the heterodyne signals from two spatially separated detectors to simulate coincidence measurement of two photons. The product signal so obtained contains several frequency components, one of which can be selected by band pass frequency filtering. The band passed signal generally contains two indistinguishable, interfering contributions, permitting simulation of the classical analog of four Bell polarization-entangled states. Our classical method reproduces measurements of violation of Bell's inequality as predicted by quantum mechanics.

We first give a brief description of the experimental setup to reproduce the measurement of the classical entangled state $\frac{1}{\sqrt{2}}[|H_1V_2) - |V_1H_2)]$. Then, we show our experimental apparatus, including phase locking loops, analog multiplier and biquad band pass filter in our signal detection scheme. We also give a detailed

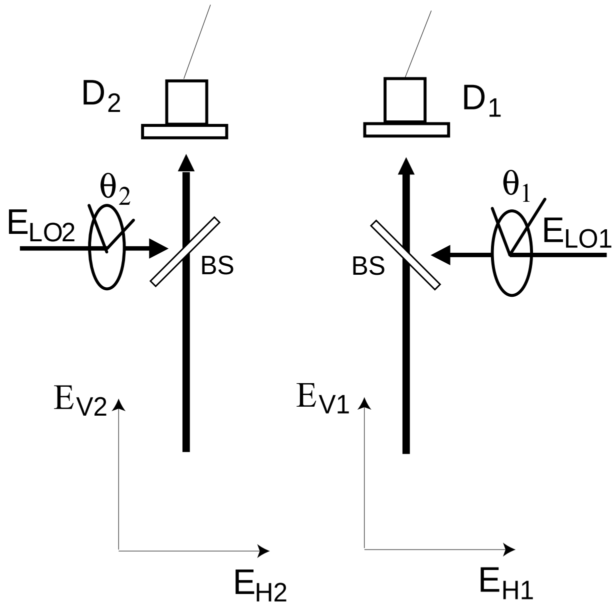

**Figure 4.1**: Two spatially separated classical beams are mixed with local oscillator beams in heterodyne detection systems.

analysis of the setup which can be extended to measure other Bell states. We discuss the experimental results as predicted by quantum theory. Finally, we discuss the achievement of this classical wave system.

### 4.1.1 Description of Two-Field Correlations

We give a brief description of our experimental setup as shown in Figure 4.1. Two spatially separated classical beams are obtained as follows: A beam of frequency $\omega_V = \omega + 2\pi \times 100$ kHz with vertical polarization is combined on a 50-50 beamsplitter with a beam of frequency $\omega_H = \omega + 2\pi \times 25$ kHz with horizontal polarization. By using "*parenthesis*" notation [44] for classical state, $|\mathcal{E})$, the two output fields of the beamsplitter can be represented as states $|\mathcal{E}_1) = [|H_1)\exp(-i\omega_H t) + |V_1)\exp(-i\omega_V t)]/\sqrt{2}$ and $|\mathcal{E}_2) = [|H_2)\exp(-i\omega_H t) - |V_2)\exp(-i\omega_V t)]/\sqrt{2}$. These output beams are sent to two spatially separated measurement systems, $D_1$ and $D_2$, each of which employs heterodyne detection with an independent local oscillator (LO) of frequency $\omega$ and a variable polarization $\hat{e}_{\theta_1}$ and $\hat{e}_{\theta_2}$, respectively. For arbitrary polarizations, each heterodyne signal contains two frequency components, at 25 and 100 kHz. These signals are multiplied together in an analog multiplier, and the product signal is band passed at 125 kHz to obtain a signal containing two indistinguishable contributions, one from $|V_1)|H_2)$ which is $\propto \cos\theta_1 \sin\theta_2$ and one from $-|H_1)|V_2)$ which is $\propto -\sin\theta_1 \cos\theta_2$. The 125 kHz component of the product signal is $\propto (\hat{e}_{\theta_1}, \hat{e}_{\theta_2}|\Psi_{cl}^-)$ where the state $|\Psi_{cl}^-) = \frac{1}{\sqrt{2}}[|H_1V_2) - |V_1H_2)]$. The squared magnitude of the product signal at 125 kHz is then $\propto \sin^2(\theta_1 - \theta_2)$, independent of the phases of the independent LO fields. The $\sin^2(\theta_1 - \theta_2)$ is the polarization correlation function of the two spatially separated classical fields. This function is used to study the classical analog of four polarization entangled Bell states and to reproduce the measurements of violation of Bell's inequality in order to demonstrate that the classical field system reproduces the correlations of the quantum mechanics system.

We will discuss in detail the detection apparatus for this experiment including the phase locking loop, analog multiplier and band pass filter.

## 4.2 Detection Apparatus

As mentioned previously, we use two spatially separated fields to simulate two-particle entanglement. Each of these beams consists of two orthogonally polarized fields with different frequencies which are sent to optical heterodyne detection regions. The heterodyne beat signals from the two spatially separated detectors are multiplied and then band pass filtered to select the desired frequency component.

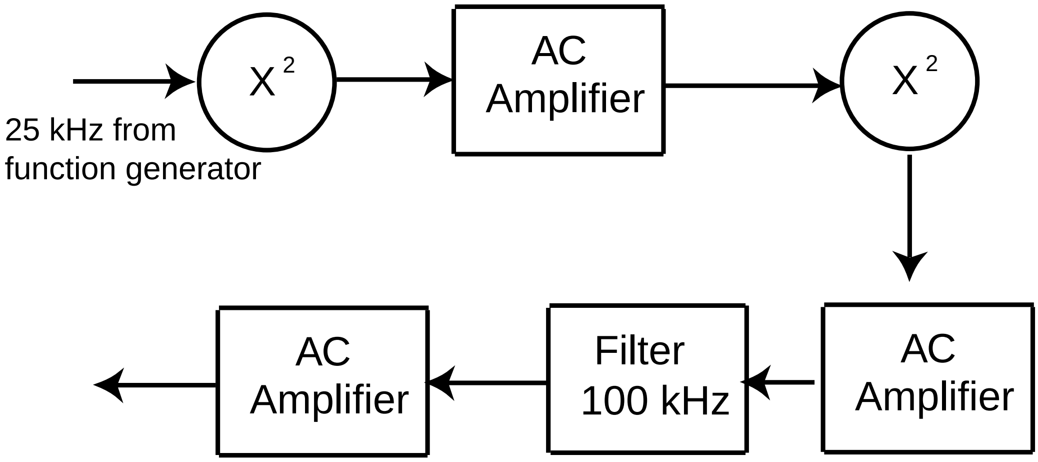

**Figure 4.2**: The diagram to generate $4f$ from a function generator $f$.

The use of an analog multiplier to obtain the multiplication beat signals from two detectors is analogous to coincidence detection of two particles. A few biquad active filters are cascaded to obtain a narrower full half width maximum (FHWM) frequency bandwidth. The combination of an analog multiplier and a band pass filter in this experiment provides post projection measurement of a specified entangled state. Two orthogonally polarized optical beams are used to simulate two-particle entanglement. These beams are frequency shifted by using tunable acousto-optic (AO) modulator and phase-locked at frequencies 25 kHz and 100 kHz.

### 4.2.1 Phase Locked Loops

The working principle of the phase locked loop has been discussed in Chapter 3. For classical wave simulation experiments on two-particle entanglement, two phase-locked loops are built to lock the two orthogonally polarized fields. The horizontally polarized beam is phase-locked at frequency 110 MHz + 25 kHz and similarly the vertically polarized beam is phase-locked at frequency 110 MHz + 100 kHz. The frequency of the local oscillator beam is shifted at 110 MHz by using a fixed AO. The circuit diagram for the phase-locked loop is similar to that of in Chapter 3. The reference frequency at 25 kHz for the first phase-locked loop is obtained from the function generator. The reference frequency at 100 kHz for the second phase-locked loop is obtained by using two analog multipliers as shown in Figure 4.2. The circuit diagram is shown in Figure 4.3. As shown in the figure, two cascaded biquad active filters centered at 100 kHz after the second analog multiplier are used to filter out the fundamental harmonic 25 kHz and second harmonic 50 kHz from the first analog multiplier. The two phase locked loops are completed as follows; As shown in Figure 4.4, 50% of the local oscillator beam is polarized at $45^o$ and then mixed with 50% of the superposition beams made of the horizontally and vertically polarized fields. These three fields are incident on a cube polarized beamsplitter (CPBS) and produce two independently and orthogonally polarized output beams. The beat signal at 100 kHz from the vertical component is fed to the first phase locked loop and similarly the beat signal at 25 kHz from the horizontal component is fed to the second phase locked loop.

### 4.2.2 Signal Detection Diagram

The detection diagram is shown in Figure 4.5. There are two spatially separated beams, each of them containing a superposition of horizontal and vertical polarizations. The heterodyne beat signals are obtained at detectors $D_1$ and $D_2$ respectively. At each detector, the beat signals contain two frequencies i.e. 25 kHz and 100 kHz. The 25 kHz is obtained from the interference between the local oscillator beam and the horizontally polarized beam. And similarly, the 100 kHz is obtained from the interference between the local oscillator beam and the vertically polarized beam.

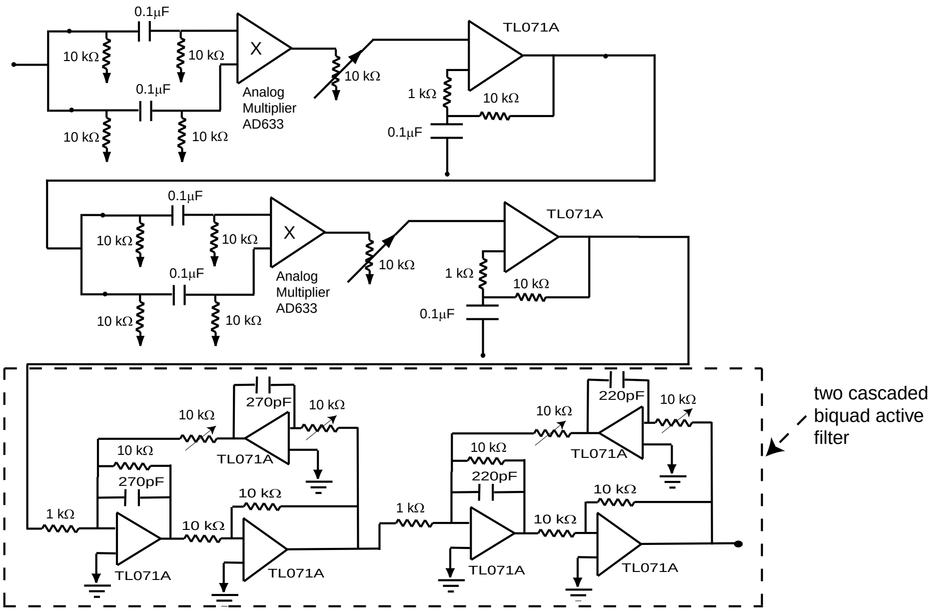

**Figure 4.3**: The circuit diagram for generating $4f$ from a function generator $f$.

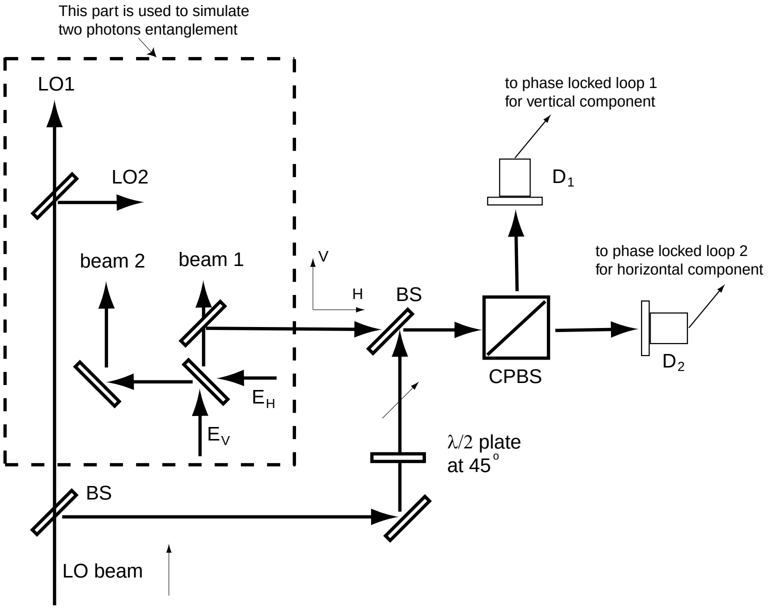

**Figure 4.4**: The optical phase locked configuration for the horizontal and vertical components in the simulation of two photon entanglement. BS, beamsplitter. CPBS, cube polarizing beamsplitter.

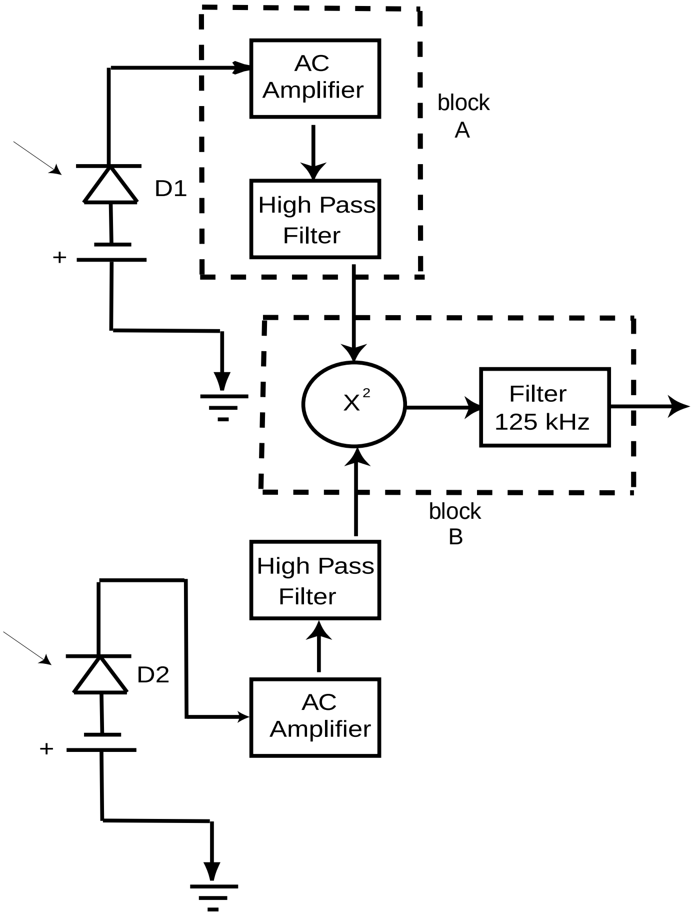

**Figure 4.5**: The detection diagram for the classical analog of Bell states measurements

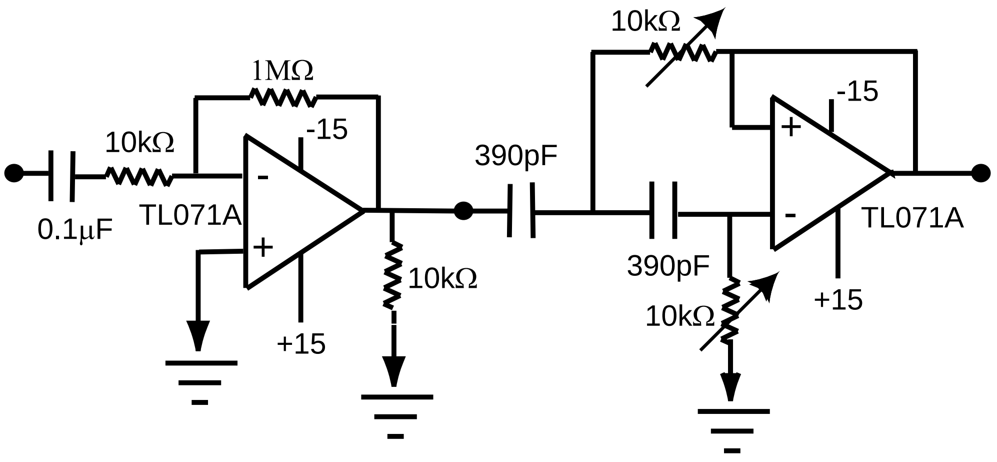

**Figure 4.6**: The circuit diagram for AC amplifier and high pass filter.

The beat signals are then amplified by using a AC amplifier. The amplitude of 25 kHz is usually higher than the 100 kHz because of the frequency response of the amplifier. Hence a high pass filter is used to equalize slight differences in amplitude between these two beat frequencies. Large attenuation in one of these frequencies will introduce phase shift between them and this should be avoided in this experiment. The equalized amplitudes of 25 kHz and 100 kHz from the detector $D_1$ are then multiplied with the equalized amplitudes of 25 and 100 kHz from the detector $D_2$. The product signal is band passed at 125 kHz by using two cascaded biquad active filters. The amplitude at 125 kHz corresponds to the contributions from two components that are $H_1V_2$ (25+100) kHz and $V_1H_2$ (100+25) kHz. The circuit diagrams for blocks A and B are shown in Figure 4.6 and Figure 4.7 respectively.

### 4.2.3 Analog Multiplier

An analog devices AD633 analog multiplier is used in this experiment. The circuit for connecting the analog multiplier to the beat signals from detectors $D_1$ and $D_2$ is

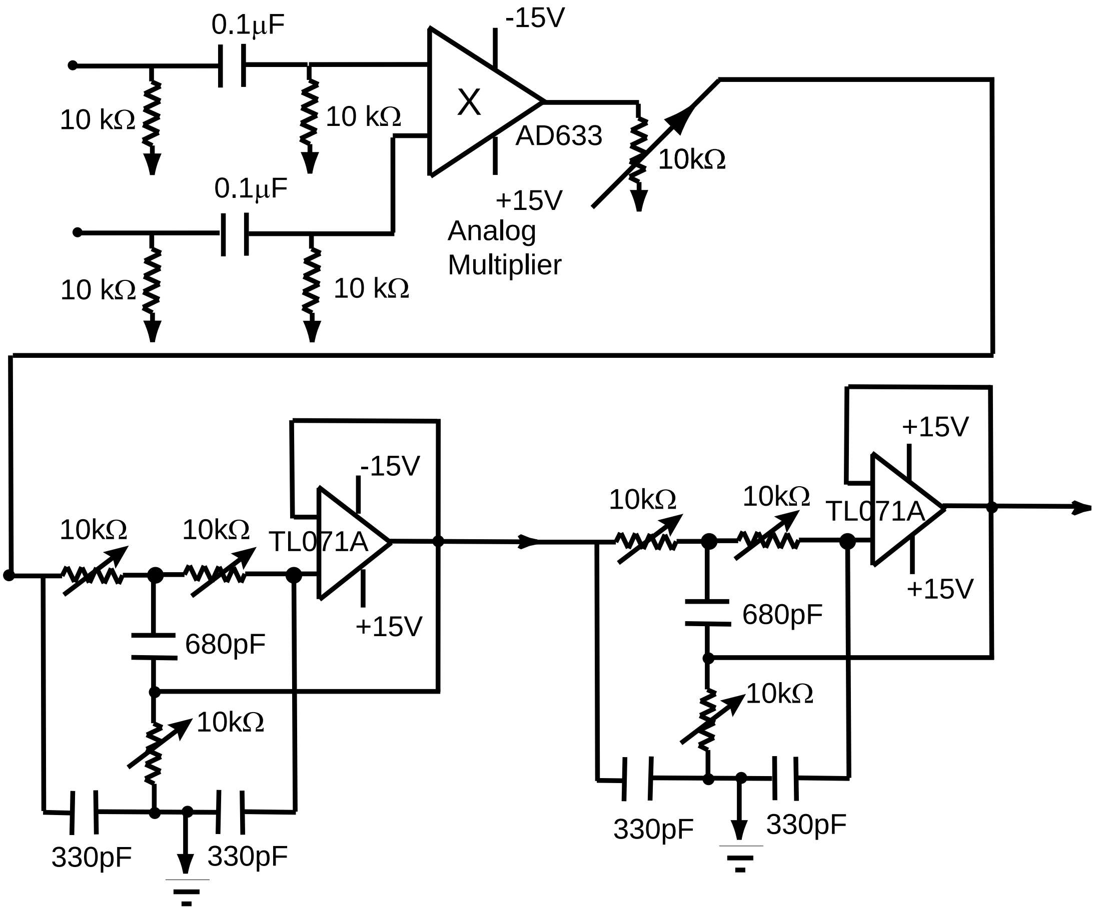

**Figure 4.7**: The circuit diagram for analog multiplier and two cascaded biquad active filters.

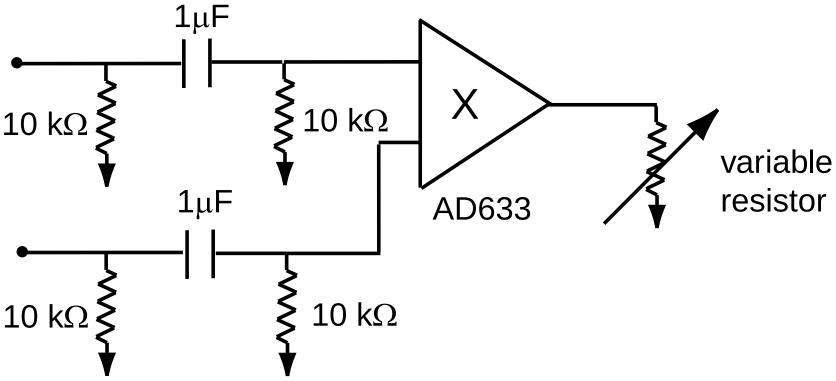

**Figure 4.8**: The circuit diagram for an analog multiplier

shown in Figure 4.8. The power supply for the multiplier is ±15 volts. This analog multiplier is needed to multiply the beat signals from the two spatially separated detectors. The multiplication provides coincidence detection of two particles. The input signal is AC coupled before it is connected to the multiplier. The reason is to avoid the multiplication of the beat signals with the DC voltage offsets produced by the amplifier and the intensities of the incident beams. The input signals cannot exceed ±5 volts and there is no nonlinearity in operating the input frequencies at 25 and 100 kHz. The circuit for the multiplier has to be grounded properly so that the phase of the product signal can be stabilized.

### 4.2.4 Biquad Band Pass Filter

After the multiplication of the beat signals in an analog multiplier, a band pass filter is used to select the desired frequency. The band pass filter used in this experiment is a biquad active filter as shown in Figure 4.9 (from the Art of Electronics by Horowitz and Hill [61]). This circuit uses three op-amps. The interesting property about this

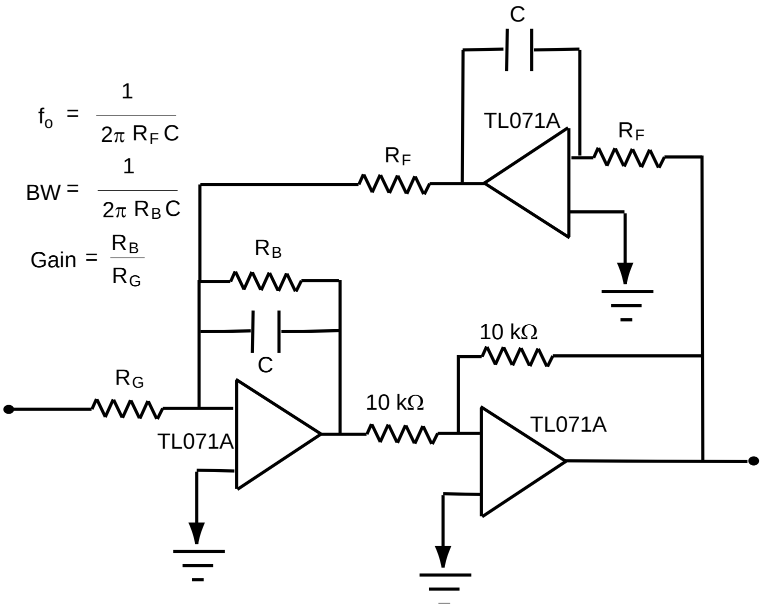

**Figure 4.9**: The biquad active filter

filter is its center frequency can be tuned while maintaining constant bandwidth. Two filters can be cascaded to obtain a narrower bandwidth at the center frequency. The desired frequency in this experiment is at 125 kHz and the nearest frequency component is at 75 kHz. This cascaded filter provides the ratio 1/20 for these two frequencies, that is the amplitude at frequency 75 kHz is attenuated and is a factor 20 smaller than the amplitude at 125 kHz.

## 4.3 Experimental Setup and Analysis

In our experiments, Figure 4.10, a HeNe laser beam is split and sent through two fixed-frequency acousto-optic modulators to produce a beam of frequency $\omega_H = \omega + \delta_H$ with horizontal polarization and a beam of frequency $\omega_V = \omega + \delta_V$ with vertical polarization, where $\delta_H = 2\pi \times 25$ kHz and $\delta_V = 2\pi \times 100$ kHz. These two beams are combined on beamsplitter BS1. The output of this beamsplitter is mixed with a local oscillator of frequency $\omega$ to obtain beat signals at frequencies $\delta_H$ and $\delta_V$. The beat signal at frequency $\delta_H$ is phase locked to a signal generator of frequency $f = 25$ kHz, while the signal at frequency $\delta_V$ is phase locked to the fourth harmonic, $4f = 100$ kHz, generated using analog multipliers from $f$ as described above.

Note that the relative phase between the 25 kHz and 100 kHz fields is the same for each port of BS1, except for a $\pi$ phase shift which arises from the beamsplitter. The total output field from each port 1 and 2, denoted $\mathbf{E}_1$ and $\mathbf{E}_2$, is sent to heterodyne detection systems at beamsplitters BS2 and BS3 respectively. The fields $\mathbf{E}_1$ and $\mathbf{E}_2$ at detectors $D_1$ and $D_2$ respectively are given by

$$\begin{aligned}\mathbf{E}_1 &= \mathcal{E}_1 e^{-i(\omega+\delta_H)t}\,\hat{H} + \mathcal{E}_1 e^{-i(\omega+\delta_V)t}\,\hat{V}\\ \mathbf{E}_2 &= \mathcal{E}_2 e^{-i(\omega+\delta_H)t}\,\hat{H} + \mathcal{E}_2 e^{-i(\omega+\delta_V)t}\,\hat{V}\ ,\end{aligned} \tag{4.1}$$

where $\mathcal{E}$ is amplitude of the field and H(V) denote the horizontal(vertical) direction. They are mixed with independent local oscillator beams LO1 and LO2 of variable polarizations and equal frequencies. The LO polarizations are given by

$$\begin{aligned}\hat{e}_{LO1} &= \cos\theta_1\,\hat{V} + \sin\theta_1\,\hat{H}\\ \hat{e}_{LO2} &= \cos\theta_2\,\hat{V} + \sin\theta_2\,\hat{H}.\end{aligned} \tag{4.2}$$

The polarization configurations of the local oscillator beams LO1 and LO2 with respect to beams 1 and 2 are shown in Figure 4.11.

The beat signal amplitudes $A_1$ and $A_2$, at the outputs of BS2 and BS3 respec-

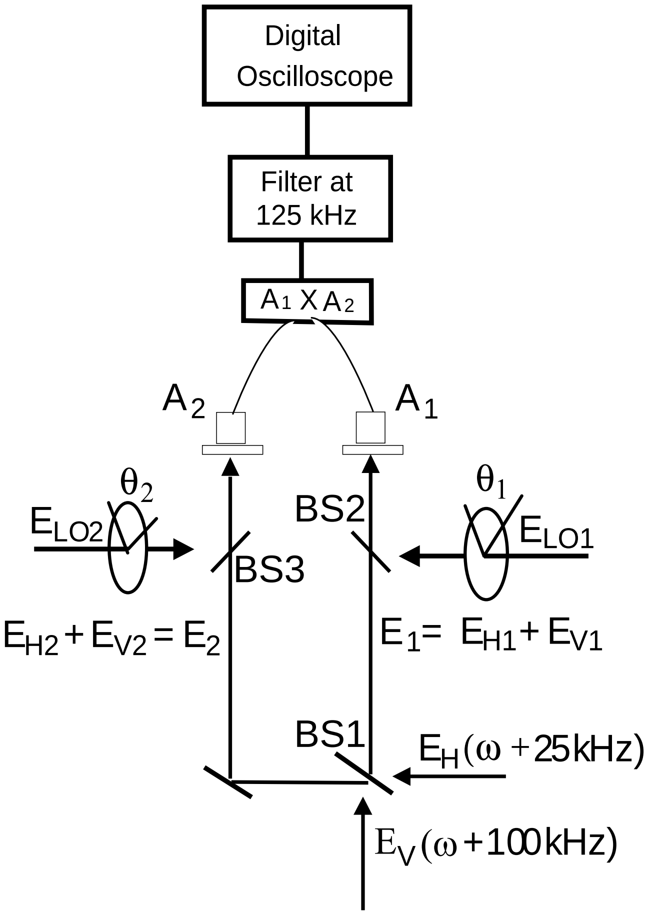

**Figure 4.10**: The experimental setup for measuring polarization correlations of two spatially separated classical fields.

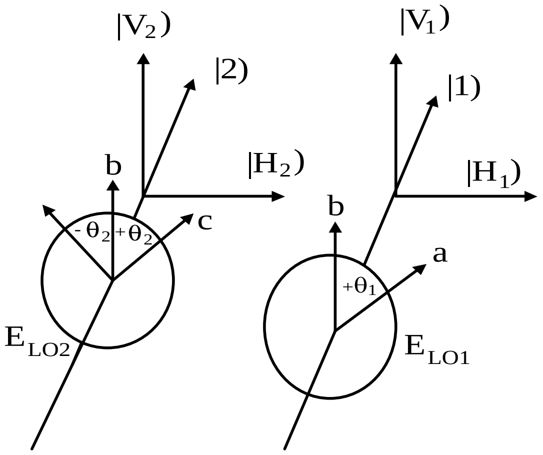

**Figure 4.11**: Polarization Configuration of the LO beams with respect to beams 1 and 2.

tively, can be represented as inner products in the parenthesis notation of Ref. [44],

$$\begin{aligned} A_1 &= (E_{LO1}|1) \\ &\equiv \int dxdy\, E^*_{LO1}(x,y,t)\, \hat{\mathbf{e}}^*_{LO1}\cdot\mathbf{E}_1(x,y,t) \end{aligned} \tag{4.3}$$

and similarly for LO2. Here, $E_{LO1}(x,y,t) = \mathcal{E}_{LO1}(x,y)\exp(i\omega t)$ is the LO1 field in the plane of a photodiode detector and $\mathbf{E}_1$ is the vector field amplitude from port 1 of BS1. By using Eq. (4.1) for $\mathbf{E}_1$ and $\mathbf{E}_2$ and the polarizations of the LO beam 2 in Eq. (4.2), the beat signal amplitudes $A_1$ and $A_2$ at detectors $D_1$ and $D_2$ are given as

$$\begin{aligned} A_1 &= (\mathcal{E}_{LO1}|\mathcal{E}_1)e^{-i\delta_H t}(\hat{\mathbf{e}}_{LO1}\cdot\hat{H}) + (\mathcal{E}_{LO1}|\mathcal{E}_1)e^{-i\delta_V t}(\hat{\mathbf{e}}_{LO1}\cdot\hat{V}) \\ A_2 &= (\mathcal{E}_{LO2}|\mathcal{E}_2)e^{-i\delta_H t}(\hat{\mathbf{e}}_{LO2}\cdot\hat{H}) + (\mathcal{E}_{LO2}|\mathcal{E}_2)e^{-i\delta_V t}(\hat{\mathbf{e}}_{LO2}\cdot\hat{V}) \end{aligned} \tag{4.4}$$

The beat signals are sent to an analog multiplier which yields a product signal proportional to the real part of the amplitude $A_1A_2 + A_1^*A_2$.

To select a particular classically entangled state, we take advantage of the fact that the product signal contains four different frequencies: The fields $\mathbf{E}_1$ and $\mathbf{E}_2$ contain frequencies $\omega + \delta_H$ and $\omega + \delta_V$. Hence, for arbitrary LO polarizations, the beat amplitudes $A_1$ and $A_2$ each contain two beat frequencies $\delta_H$ and $\delta_V$, yielding four nonzero frequency components in the product signal: $\delta_H \pm \delta_V$, $2\delta_H$ and $2\delta_V$. A band pass filter is used to select the product signal at frequency $\Delta_+ \equiv \delta_H + \delta_V = 125$ kHz. In this case, we measure only the signal corresponding to the real part of the amplitude $A_1 A_2$ which contains two contributions,

$$\gamma(\theta_1, \theta_2) \propto \sin\theta_1 \cos\theta_2 (\mathcal{E}_{LO1}|\mathcal{E}_1)(\mathcal{E}_{LO2}|\mathcal{E}_2) \pm \cos\theta_1 \sin\theta_2 (\mathcal{E}_{LO1}|\mathcal{E}_1)(\mathcal{E}_{LO2}|\mathcal{E}_2). \quad (4.5)$$

Here, $(\mathcal{E}_{LO1}|\mathcal{E}_1)$ denotes the spatial overlap integral of LO1 and the field from port 1 of BS1, and similarly for the other overlap integrals. The relative sign ± is controlled by placing a half-wave plate oriented at a zero degree angle in one output of BS1. The two terms in Eq. (4.5) arise because there are two ways to obtain a product signal at frequency 125 kHz. Note that the products of the spatial overlap integrals have the same amplitude and phase in both terms, i.e., $(\mathcal{E}_{LO1}|\mathcal{E}_1)(\mathcal{E}_{LO2}|\mathcal{E}_2) = (\mathcal{E}_{LO1}|\mathcal{E}_1)(\mathcal{E}_{LO2}|\mathcal{E}_2)$, which factors out in the signal amplitude. Hence, the overall phases of LO1 and LO2 cancel in the measurements and the signal can be normalized by finding the maximum value with $\theta_1 = 45^\circ = \pm\theta_2$. Dividing by the maximum value yields the normalized signal amplitude $\gamma_N(\theta_1, \theta_2) = \sin(\theta_1 \pm \theta_2)$.

The signal amplitude at $\Delta_+ = 125$ kHz can be rewritten in the form, $\gamma(\theta_1, \theta_2) \propto (\hat{e}_{LO1}, \hat{e}_{LO2}|\Psi_{cl}^{\pm})_{\Delta_+}$ where $|\Psi_{cl}^{\pm})_{\Delta_+}$ are the classical analogs of the entangled states

$$|\Psi_{cl}^{\pm})_{\Delta_+} \equiv \frac{1}{\sqrt{2}} \left[ |H_1)|V_2) \pm |V_1)|H_2) \right]. \quad (4.6)$$

Here, $|H_1)$ arises from the 25 kHz horizontally polarized field from port 1, etc. Eq. (4.6) shows that classical analogs of two different Bell states can be measured. The other two Bell states can be obtained by inserting a half-wave plate oriented at 45° in one output of BS1. This interchanges the horizontal and vertical polarizations in one port so that the product signal at frequency $\Delta_+$ contains the polarization states $|H_1)|H_2)$ and $|V_1)|V_2)$,

$$|\varphi_{cl}^{\pm})_{\Delta_+} \equiv \frac{1}{\sqrt{2}}\left[|H_1)|H_2) \pm |V_1)|V_2)\right]. \tag{4.7}$$

Here, the relative sign is again controlled by using an additional half-wave plate oriented along the output $V$ axis of one port.

By measuring the magnitude of $\gamma(\theta_1, \theta_2)$ using a digital oscilloscope (or lock-in detection at the frequency $\Delta_+$), we obtain $|\gamma_N(\theta_1, \theta_2)|^2$. Hence, after normalization to the maximum signal, we measure the classical joint intensity $P_{cl}(\hat{e}_{LO1}, \hat{e}_{LO2}) = |\gamma_N(\theta_1, \theta_2)|^2 = \sin^2(\theta_1 \pm \theta_2)$.

Note that if Eq. (4.6) were a true, normalized quantum state, then the joint probability for coincidence detection of two photons with polarizations $\hat{e}(\theta_1)$ and $\hat{e}(\theta_2)$ would be $\sin^2(\theta_1 \pm \theta_2)/2$. This differs from our classical result only by a multiplicative factor of 1/2, arising from our choice of normalization.

## 4.4 Experimental Results

### 4.4.1 Definition of Projection Angles

It is important to understand the definitions of the polarization angle of the LO fields with respect to the horizontal and vertical fields in beams 1 and 2. The positive and

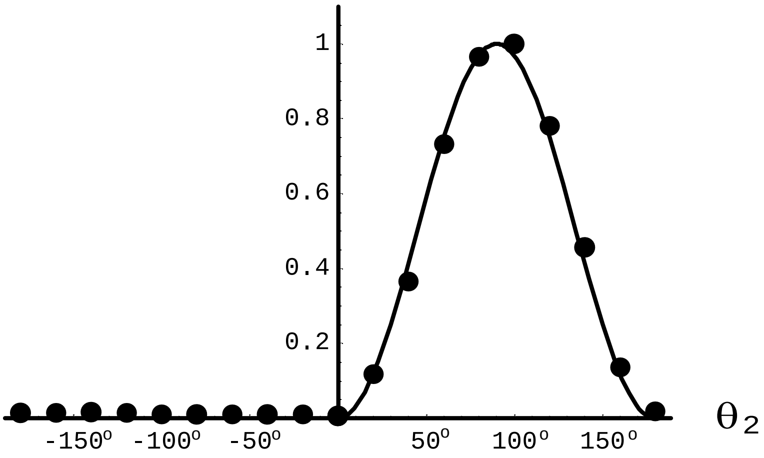

**Figure 4.12**: Measurement of the joint intensity $\sin^2(\theta_1+\theta_2)$ for the state $|\Psi_{cl}^{+}\rangle$ where the $\theta_1 = |\theta_2|$.

negative polarization angles of the LO1 and LO2 for the state $|\Psi_{cl}^{+}\rangle$ of Eq. (4.6) are shown in Figure 4.11. That is, looking along the propagation direction of the beams, the clockwise polarization angle is defined positive, $+\theta$, and the counter-clockwise is negative, $-\theta$. Our first measurement is to verify the $\sin^2(\theta_1+\theta_2)$ dependence of the projections of state $|\Psi_{cl}^{+}\rangle$. In this measurement, we rotate the polarization angle of the LO1 in the positive direction $+\theta_1$ from 0° to 90° and the polarization angle of the LO2 in the positive and negative directions in such a way that $\theta_2 = \pm\theta_1$. The result of this measurement is shown in Figure 4.12. The solid line is a theoretical prediction of $\sin^2(\theta_1+\theta_2)$ for the state $|\Psi_{cl}^{+}\rangle$ where $\theta_1 = |\theta_2|$.

Now, by inserting a half-wave plate at $0^o$ into beam 1 and using the same rotation procedure above for the LO1 and LO2, our measurements verify the $\sin^2(\theta_1-\theta_2)$ dependence for the state $|\Psi_{cl}^{-}\rangle$. It is shown in Figure 4.13 where the solid line is a theoretical prediction of $\sin^2(\theta_1-\theta_2)$ for the state $|\Psi_{cl}^{-}\rangle$ where $\theta_1 = |\theta_2|$.

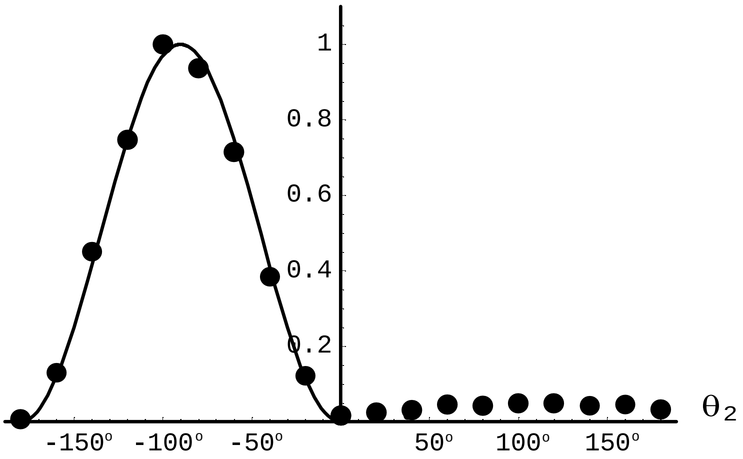

**Figure 4.13**: Measurement of the joint intensity $\sin^2(\theta_1 - \theta_2)$ for the state $|\Psi_{cl}^-\rangle$ where the $\theta_1 = |\theta_2|$.

### 4.4.2 Polarization Correlation Measurement of Four Bell States

In Figure 4.14, we measure the quantity $|\gamma_N(\theta_1 = 30°, \theta_2)|^2$ for the state $|\Psi_{cl}^-\rangle$ of Eq. (4.6) as a function of $\theta_2$ between $-90°$ and $90°$. The solid line is the theoretical prediction with $|\gamma_N(\theta_1, \theta_2)|^2 = \sin^2(\theta_1 - \theta_2)$. By inserting a half-wave plate in one port, we have measured $|\gamma_N|^2$ for the state $|\Psi_{cl}^+\rangle$, where $|\gamma_N(\theta_1, \theta_2)|^2 = \sin^2(\theta_1 + \theta_2)$ as shown in Figure 4.15.

We also measure the other two Bell states, $|\varphi_{cl}^{\pm}\rangle$, of Eq. (4.7). We insert a half-wave plate oriented at 45° in one output of BS1. A second half-wave plate oriented at 0° selects the relative phase ±. In this case, $|\gamma_N(\theta_1, \theta_2)|^2 = \cos^2(\theta_1 \mp \theta_2)$. Normalization is accomplished by measuring the maximum product signal with $\theta_1 = 45° = \pm\theta_2$. For the $|\varphi_{cl}^+\rangle$ state, measurements of the quantity $|\gamma_N(60°, \theta_2)|^2$ are shown in Figure 4.16. We have also measured $|\gamma_N(60°, \theta_2)|^2$ for the state $|\varphi_{cl}^-\rangle$ as shown in the Figure 4.17.

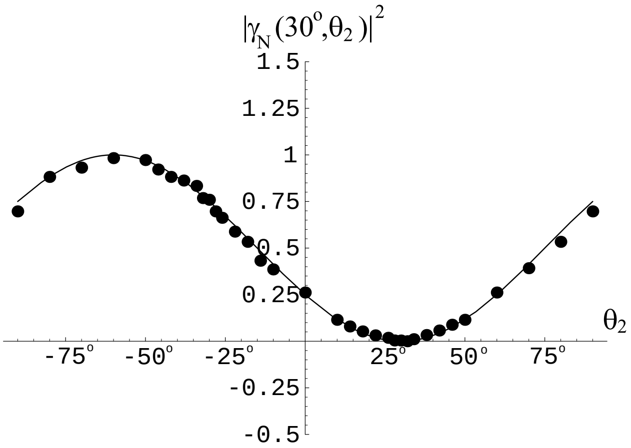

**Figure 4.14**: The correlation measurement for the state $|\Psi^-_{cl})$.

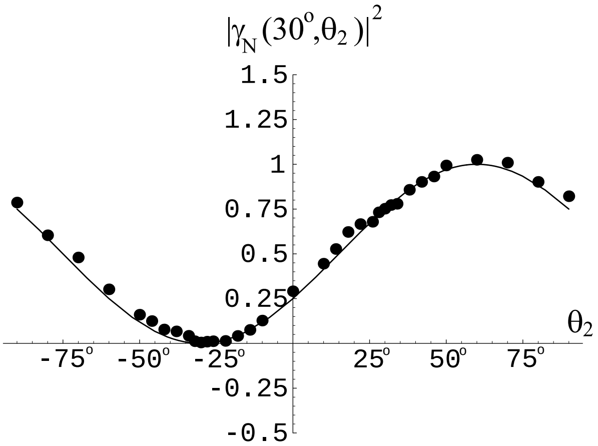

**Figure 4.15**: The correlation measurement for the state $|\Psi^+_{cl})$.

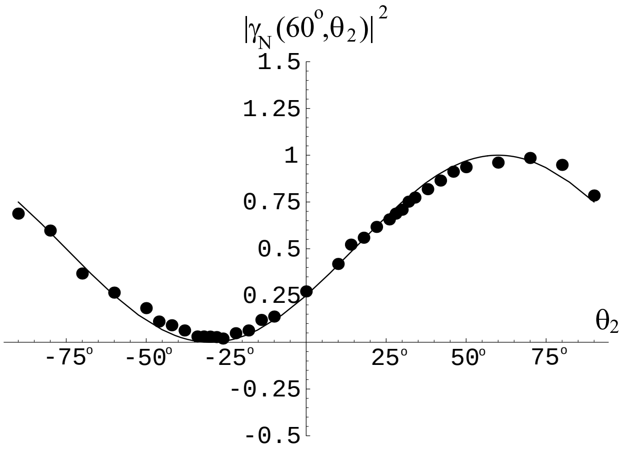

**Figure 4.16**: The correlation measurement for the state $|\varphi_{cl}^{+}\rangle$.

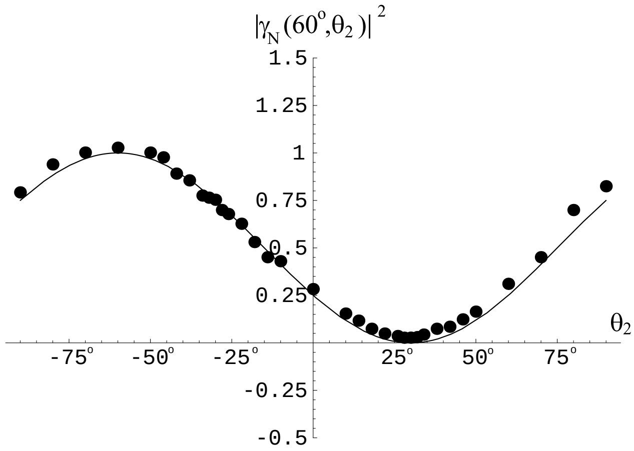

**Figure 4.17**: The correlation measurement for the state $|\varphi_{cl}^{-}\rangle$.

### 4.4.3 Classical Wave Violation of Bell's Inequality

For each of the four Bell states, the measured joint intensities take the same form as in a quantum joint-probability measurement. Hence, it is possible to violate formally a classical analog of the Bell's inequality used in recent quantum measurements of the joint detection probability for entangled photon pairs [24],

$$F_{cl}(\mathbf{a},\mathbf{b},\mathbf{c}) \equiv P_{cl}(\ \mathbf{a},\mathbf{b})\ +\ P_{cl}(\mathbf{b},\mathbf{c})\ -\ P_{cl}(\ \mathbf{a},\mathbf{c}) \geq 0, \tag{4.8}$$

where $P_{cl}(\mathbf{a},\mathbf{b}) = |\gamma_N(\theta_a,\theta_b)|^2$ is the joint intensity when the local oscillators have linear polarizations $\mathbf{a}$ and $\mathbf{b}$ respectively.

By proper choice of angles for the polarizations $\mathbf{a},\mathbf{b},\mathbf{c}$ in Eq. (4.8), the classical joint intensity exhibits a maximum violation of the Bell's inequality $F_{cl} \geq 0$. To demonstrate the violation for the state $|\Psi^+_{cl}\rangle$ of Eq. (4.6), we take $\mathbf{b} = \hat{V}$, i.e., $\theta_b = 0°$, $\mathbf{a} = \mathbf{c}$ and measure $F_{cl}(\mathbf{a},\mathbf{b},\mathbf{c})$ of Eq. (4.8) as a function of $\theta_a = \theta_c = \theta$ for $\theta$ between 0° and 90°. We obtain the data shown in Figure 4.18. The maximum violation occurs at $\theta = 30°$, as in a quantum joint probability measurement, and has the value $F_{cl} = -0.25$. The solid line shows the prediction $F_{cl}(\theta, 0°, \theta) = |\gamma_N(\theta, 0°)|^2 + |\gamma_N(0°,\theta)|^2 - |\gamma_N(\theta,\theta)|^2$ where $|\gamma_N(\theta_1,\theta_2)|^2 = \sin^2(\theta_1+\theta_2)$. Similarly, for the state $|\Psi^-_{cl}\rangle$ of Eq. (4.6), where we set $\mathbf{a} = -\mathbf{c}$, then we measure $F_{cl}(\mathbf{a},\mathbf{b},\mathbf{c})$ of Eq. (4.8) as a function of $\theta_a = \theta$ and $\theta_c = -\theta$ for $\theta$ between 0° and 90°. We obtain the data shown in Figure 4.19.

## 4.5 Discussion

We have demonstrated the classical wave simulation of projection measurement for coincidence detection of two photons by using analog multipliers and band pass

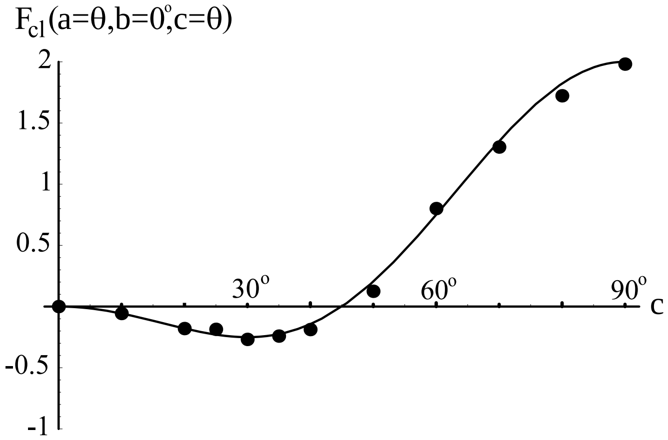

**Figure 4.18**: The classical analog of the violation of Bell inequality $F_{cl}(a = \theta, b = 0°, c = \theta) \geq 0$ for the $|\Psi^{+}_{cl}\rangle$ as a function of angle c. The maximum violation occurs for $c = 30°$ where $F_{cl} = -0.25$.

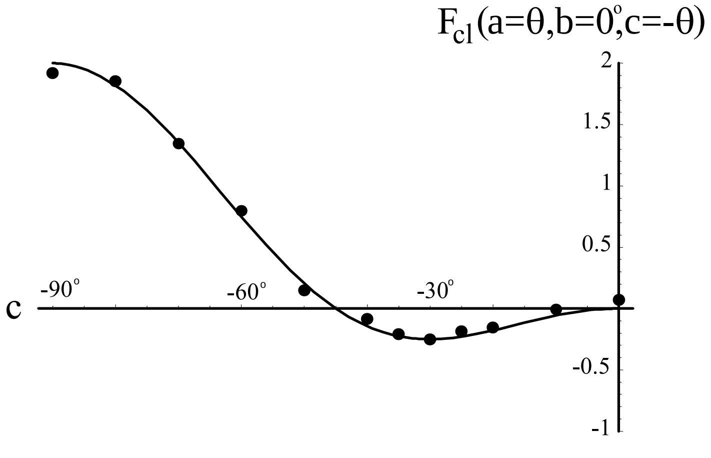

**Figure 4.19**: The classical analog of the violation of Bell inequality $F_{cl}(a = \theta, b = 0°, c = -\theta) \geq 0$ for the $|\Psi^{-}_{cl}\rangle$ as a function of angle c. The maximum violation occurs for $c = -30°$ where $F_{cl} = -0.25$.

filters. The correlated polarization measurements for our polarization entangled Bell states demonstrate a violation of Bell's inequality very similar to that obtained using polarization-entangled photons from a parametric down-converter, where coincidence detection performs a post-projection of the entangled state [62]. Further, the joint intensities depend only on $\theta_1 \pm \theta_2$, so that the results do not depend on a particular orientation of either LO. However, the system does not exhibit particle-like behavior or collapse and is deterministic, so that Bell's inequalities are not strictly applicable. Hence, if our experiments were done using polarizing beamsplitters in the two detection regions (and LO's with 45° polarization), all outputs would contain signals simultaneously. By contrast, in a true two-photon experiment, if a photon is detected in the horizontal port for beam 1, the polarization of the photon detected in beam 2 must be vertical. In our classical wave system, this corresponds to setting the LO in port 1 to project out the horizontal component, so that signal from detector 1 is at 25 kHz. If the product of this signal and that obtained at port 2 is obtained and band pass filtered at 125 kHz as before, then the maximum signal is obtained when the LO in port 2 is vertically polarized.

# Chapter 5

# Three-Field Correlations

## 5.1 Overview

For quantum information processing, it is necessary to entangle more than two qubits or particles. In this Chapter, we use the methods developed in the previous chapter to simulate three particle Greenberger-Horne-Zeilinger (GHZ) entanglement using classical wave fields. We are interested in demonstrating the GHZ entanglement because the three-particle nonlocal polarization correlation leads to a conflict with local realism for nonstatistical predictions of quantum mechanics. That is in contrast to the two entangled particles test of Bell's inequalities, where the conflict arises for statistical predictions of quantum mechanics.

We extend the previous measurement method and prepare four spatially separated classical beams, each consisting of two orthogonally polarized fields with different frequencies. We are able to simulate four-photon entanglement with the classical analog of four-particle entangled state $|\Psi^4_{GHZ})_{cl} = \frac{1}{\sqrt{2}}[|H_1H_2H_3H_4) + |V_1V_2V_3V_4)]$. By using three of the four spatially separated beams, we are able to simulate three-particle GHZ entanglement with a classical analog of the three-particle entangled state $|\Psi^3_{GHZ})_{cl} = \frac{1}{\sqrt{2}}[|H_1H_2H_3) + |V_1V_2V_3)]$. The correlation properties of our classical state are demonstrated by reproducing the 32 elements of the truth table obtained in the GHZ quantum entanglement experiments.

In the following sections of this chapter, it is important for us first to discuss the concept of GHZ entanglement in the violation of local realism theory. Then, we outline a brief description of our experimental simulation of reproducing the three-particle entangled state from the four-particle entangled state. We outline our detection diagram for the experiment, which consists of analog multipliers and band pass filters including notch filters and biquad band pass filters. Also, we describe the details of the experimental analysis and results for the simulation of GHZ entanglement. Our measurements are in agreement with the quantum prediction as reported in the quantum GHZ experiment [29].

We begin by introducing the concepts of GHZ entanglement and the violation of local realism theory in quantum mechanical experiments.

### 5.1.1 The Quantum Test of Nonlocality in GHZ Entanglement

In the quantum three particle entanglement experiment demonstrated by Zeilinger's group [29,63], two pairs of polarization entangled photons are transformed into three entangled photons and a fourth independent photon. The fourfold coincidence detection of these four photons provides a projection measurement onto the desired GHZ state $|\psi\rangle = \frac{1}{\sqrt{2}}\left(|H_1\rangle|H_2\rangle|V_3\rangle + |V_1\rangle|V_2\rangle|H_3\rangle\right)|H_4\rangle$. The fourth photon $|H_4\rangle$ is used as a trigger photon and the remaining three entangled photons are used to observe the GHZ entanglement. The fourth photon is always horizontally polarized and hence can be neglected in our discussion. By rotating the third photon polarization state to interchange the vertical and horizontal polarizations $V\rightleftharpoons H$, any measurement on the first three particles in the state $|\psi\rangle$ can be regarded as an measurement on the three-particle GHZ entangled state, $\frac{1}{\sqrt{2}}\left(|H_1\rangle|H_2\rangle|H_3\rangle + |V_1\rangle|V_2\rangle|V_3\rangle\right)$.

The measurements of polarization correlations between the three particles leads to a conflict with local realism for *nonstatistical* predictions of quantum mechanics [29]. As shown below, local realism predicts that certain correlations can be observed and others cannot. Quantum mechanics predicts the exact opposite, producing strong correlation where local realism predicts zero and vice-versa. That is in contrast to the two entangled particles test of Bell's inequality, where the conflict arises for statistical predictions of quantum mechanics.

The three-particle entangled state that used to describe GHZ entanglement in the violation of local realism theory is given by

$$|\Psi^3_{GHZ}\rangle \quad = \quad \frac{1}{\sqrt{2}}\left(|H_1\rangle|H_2\rangle|H_3\rangle + |V_1\rangle|V_2\rangle|V_3\rangle\right) \ . \tag{5.1}$$

Here the superscript 3 indicates three-photon. Eq. (5.1) is also called the GHZ state [29,63]. GHZ arguments about physical reality are based on the measurements of polarization correlations on three particles in this GHZ state. We demonstrate the GHZ argument for a three-particle test of local realism as follows: A photon $i$ is said to possess the element of reality $X_i$ with value +1 or -1 when its polarization state is $H'$ or $V'$, where $H'$ and $V'$ are at angles $45°$ and $-45°$ with respect to the original vertical direction $V$. Similarly, the photon is said to possess the element of reality $Y_i$ with value +1 or -1 when its circular polarization state is right-handed, R, or left-handed, L. The elements of reality for three photons in the GHZ state can be represented in terms of their polarization states, given by

$$\begin{aligned}
|H'\rangle &= \frac{1}{\sqrt{2}}(|H\rangle + |V\rangle) \\
|V'\rangle &= \frac{1}{\sqrt{2}}(|H\rangle - |V\rangle) \\
|R\rangle &= \frac{1}{\sqrt{2}}(|H\rangle + i|V\rangle) \\
|L\rangle &= \frac{1}{\sqrt{2}}(|H\rangle - i|V\rangle)
\end{aligned} \tag{5.2}$$

where $H(V)$ denotes the original horizontal (vertical) polarization state of the three photons.

One can define elements of reality for joint measurement of three particles as the product of the elements of reality for each particle. For example, a measurement $Y_1Y_2X_3$ on the GHZ state means that the first and second photons are each projected onto the polarization state $|R\rangle$ or $|L\rangle$, and the third photon is projected onto the polarization state $|H'\rangle$ or $|V'\rangle$. Since each of the photons has two orthogonal polarizations in the chosen basis, there is a complete set of $2^3 = 8$ orthogonal three-photon product states in this measurement. There are also eight possible combinations for measuring either circular $Y$ or linear $X$ polarization on three particles, and 8 possible three photon states for each combination. In the following, we consider four types of measurements for the GHZ state of Eq. (5.1), namely $Y_1Y_2X_3$, $Y_1X_2Y_3$ and $X_1Y_2Y_3$, and $X_1X_2X_3$.

In order to determine which elements of reality for three photon coincidences are also realizations predicted by quantum mechanics, we conduct measurements on polarization correlations of three photons in the GHZ state. Suppose now that certain measurements of $Y_1Y_2X_3$, $Y_1X_2Y_3$ and $X_1Y_2Y_3$ are predicted to be nonzero for the GHZ state. Then for an $X_1X_2X_3$ experiment, the expectations using a local realistic theory are exactly the opposite of the expectations using quantum physics, as we now show, following the arguments of Ref. [63].

To see why, let's demonstrate the argument with an example for the measurement $Y_1Y_2X_3$ in the GHZ state. We write Eq. (5.1) in a form which explicitly shows the possible outcomes of $Y_1Y_2X_3$ measurements.

For the three photons, the polarizations $|R_1\rangle$, $|L_1\rangle$, $|R_2\rangle$, $|L_2\rangle$, $|H_3'\rangle$ and $|V_3'\rangle$ are obtained from Eq. (5.2),

$$\begin{aligned}
|R_1\rangle &= \frac{1}{\sqrt{2}}(|H_1\rangle + i|V_1\rangle) \\
|L_1\rangle &= \frac{1}{\sqrt{2}}(|H_1\rangle - i|V_1\rangle) \\
|R_2\rangle &= \frac{1}{\sqrt{2}}(|H_2\rangle + i|V_2\rangle) \\
|L_2\rangle &= \frac{1}{\sqrt{2}}(|H_2\rangle - i|V_2\rangle) \\
|H_3'\rangle &= \frac{1}{\sqrt{2}}(|H_3\rangle + |V_3\rangle) \\
|V_3'\rangle &= \frac{1}{\sqrt{2}}(|H_3\rangle - |V_3\rangle) \ .
\end{aligned} \tag{5.3}$$

Then, from the Eq. (5.3), the states $|H_i\rangle$ and $|V_i\rangle$ where $i = 1, 2, 3$, are obtained as

$$\begin{aligned}
|H_1\rangle &= \frac{1}{\sqrt{2}}(|R_1\rangle + |L_1\rangle) \\
|V_1\rangle &= \frac{1}{i\sqrt{2}}(|R_1\rangle - |L_1\rangle) \\
|H_2\rangle &= \frac{1}{\sqrt{2}}(|R_2\rangle + |L_2\rangle) \\
|V_2\rangle &= \frac{1}{i\sqrt{2}}(|R_2\rangle - |L_2\rangle) \\
|H_3\rangle &= \frac{1}{\sqrt{2}}(|H_3'\rangle + |V_3'\rangle) \\
|V_3\rangle &= \frac{1}{\sqrt{2}}(|H_3'\rangle - |V_3'\rangle) \ .
\end{aligned} \tag{5.4}$$

Now, by using Eq. (5.4) for the three photons in the GHZ state $|\Psi^3_{GHZ}\rangle$ of Eq. (5.1), the $|\Psi^3_{GHZ}\rangle$ can be rewritten in the complete basis for the YYX measurements as

$$|\Psi_{GHZ}\rangle_{YYX} = \frac{1}{2}\left(|R_1L_2H'_3\rangle + |L_1R_2H'_3\rangle + |R_1R_2V'_3\rangle + |L_1L_2V'_3\rangle\right) \ . \tag{5.5}$$

One can see that each three photon element of reality in Eq. (5.5) for in the configuration $Y_1Y_2X_3$ has the product value of -1. Note that the $R_1L_2H'_3 = -1$ means that if the photon 1 is R-polarized and photon 2 is also L-polarized, then, the photon 3 must be $H'$-polarized. The existence of the component $|R_1\rangle|L_2\rangle|H'_3\rangle$ instead of its complementary component $|R_1\rangle|L_2\rangle|V'_3\rangle$ can be verified by their projections on the GHZ state $|\Psi^3_{GHZ}\rangle$, i.e., $\langle R_1|\langle L_2|\langle H'_3|\Psi^3_{GHZ}\rangle = \frac{1}{2}$ and $\langle R_1|\langle L_2|\langle V'_3|\Psi^3_{GHZ}\rangle = 0$. Thus, four of eight possible components of three-photon product states in the measurement $Y_1Y_2X_3$ are nonzero for the GHZ state. Similarly, by using the same procedure as discussed above for the YYX configuration, the GHZ state can be written in different complete bases to display the YXY, XYY and XXX configurations of reality,

$$|\Psi_{GHZ}\rangle_{YXY} = \frac{1}{2}\left(|L_1H'_2R_3\rangle + |R_1V'_2R_3\rangle + |R_1H'_2L_3\rangle + |L_1V'_2L_3\rangle\right) \tag{5.6}$$

$$|\Psi_{GHZ}\rangle_{XYY} = \frac{1}{2}\left(|H'_1L_2R_3\rangle + |V'_1R_2R_3\rangle + |H'_1R_2L_3\rangle + |V'_1L_2L_3\rangle\right) \tag{5.7}$$

$$|\Psi_{GHZ}\rangle_{XXX} = \frac{1}{2}\left(|H'_1H'_2H'_3\rangle + |V'_1V'_2H'_3\rangle + |H'_1V'_2V'_3\rangle + |V'_1H'_2V'_3\rangle\right) \ . \tag{5.8}$$

Each element of reality for the three photons in the configurations $X_1Y_2Y_3$ of Eq. (5.6) and $Y_1X_2Y_3$ of Eq. (5.7) has the product value of -1. According to the local realism theory, since $Y_iY_i = +1$, the product of three configurations

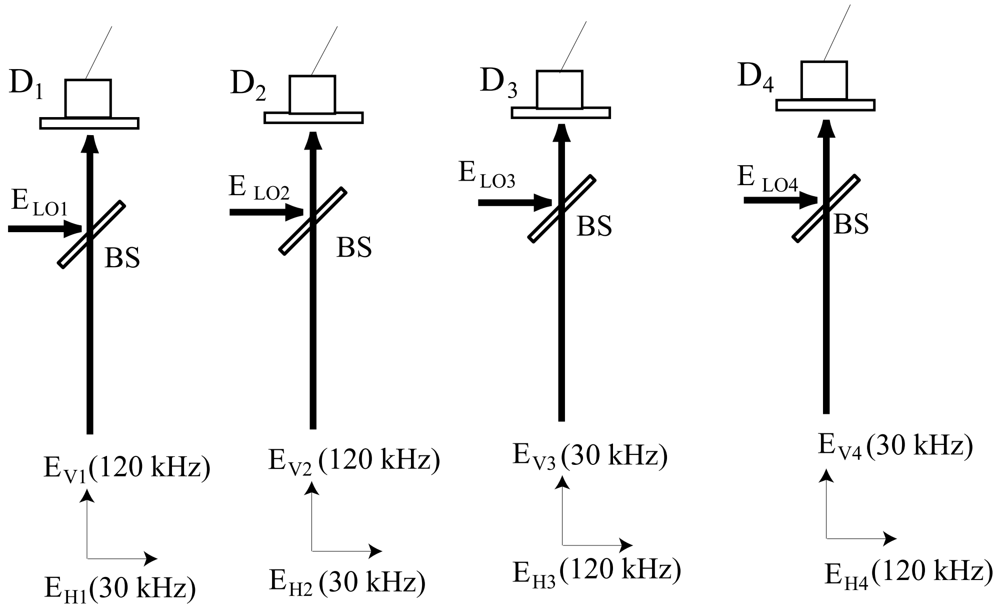

**Figure 5.1**: Four spatially-separated correlated classical beams are produced using three beamsplitters, where two independent classical beams are combined in the first beamsplitter. Each of the four outputs is mixed with a local oscillator beam in heterodyne detection.

$((X_1Y_2Y_3)(Y_1X_2Y_3)(Y_1Y_2X_3)) = X_1X_2X_3$ will lead to the prediction that $X_1X_2X_3$ =-1. However, this is in contradiction with the quantum results obtained in Eq. (5.8) for the GHZ state in the $X_1X_2X_3$ basis, where $X_1X_2X_3$ =+1.

In the following section, we give a brief description of the classical experiment which simulates the four particle entangled state $[|H_1H_2H_3H_4\rangle + |V_1V_2V_3V_4\rangle]\sqrt{2}$. Analogous to the quantum experiments, we use this state to measure a classical analog of the three-particle GHZ state of Eq. (5.1). To verify the polarization correlations in the classical analog state, we reproduce the 32 elements of the truth table predicted by quantum mechanics in the test of local realism theory.

### 5.1.2 Description of Three-Field Correlations

We give a brief description of the current experiment to simulate three-particle entangled state $|\Psi^3_{GHZ})_{cl}$ from the four-photon entangled state $|\Psi^4_{GHZ})_{cl}$ by using classical fields. We first prepare the four spatially separated classical beams by using three beamsplitters so that the phases and polarizations of these four classical beams are correlated. As shown in Figure 5.1, four spatially separated classical beams are prepared as follows: An optical beam of frequency $\omega_V = \omega + 2\pi \times 120$ kHz with vertical polarization and an optical beam of frequency $\omega_H = \omega + 2\pi \times 30$ kHz with horizontal polarization are combined through a 50/50 beamsplitter. The beamsplitter produces two spatially separated beams, beam 1 and beam 2. Beam 1 consists of the superposition state $|1) = [|H_1)exp(-i\omega_H t)+|V_1)exp(-i\omega_V t)]/\sqrt{2}$ and similarly for beam 2, $|2) = [|H_2)exp(-i\omega_H t) + |V_2)exp(-i\omega_V t)]/\sqrt{2}$. Beam 1 is then cloned by using a beamsplitter to obtain an identical copy, beam 3, where a half wave plate is used to rotate $|H)(|V))$ to $|V)(|H))$, yielding state $|3) = [|V_3)exp(-i\omega_H t) + |H_3)exp(-i\omega_V t)]/\sqrt{2}$. By using the same method, beam 2 is cloned by using another beamsplitter to obtain an identical copy, beam 4, which is also rotated by a half wave plate, so that $|4) = [|V_4)exp(-i\omega_H t) + |H_4)exp(-i\omega_V t)]/\sqrt{2}$.

These output beams are sent to four spatially separated measurement systems, each of which employs heterodyne detection with an independent local oscillator (LO) of frequency $\omega$ and at arbitrary polarization angle. The heterodyne signal at each detector contains two frequency components, at 30 kHz and 120 kHz. The beat signal from the detectors 1 and 2 are multiplied and then band pass filtered at two frequencies, 60 kHz to obtain a signal $\propto |H_1)|H_2)$ and at 240 kHz to obtain a signal $\propto |V_1)|V_2)$. The signals are added together and multiplied with the beat signal components from detector 3 by using a second analog multiplier. This product signal is band passed at 180 kHz to obtain a signal $\propto |H_1)|H_2)|H_3)$ and at 270 kHz to obtain a signal $\propto |V_1)|V_2)|V_3)$. Similarly, these signals are added and then multiplied with the beat signal from detector 4 by using a third analog multiplier. The final product signal is band passed at 300 kHz, and contains two indistinguishable, interfering contributions, $\propto |H_1)|H_2)|H_3)|H_4) + |V_1)|V_2)|V_3|V_4)$. The local oscillator at detector 4 is fixed at a $45^o$ polarization angle. The remaining three local oscillator beams are then subjected to arbitrary polarization projections by rotating the polarizations of the respective LO beams to reproduce the measurements of polarization correlations of three particle GHZ entanglement.

In the following section, we first discuss the detection apparatus used in this experiment.

## 5.2 Detection Apparatus

Using the above scheme, we are able to simulate four-photon entanglement by expanding the experimental arrangement that was used to simulate two-photon entanglement as discussed in Chapter 4. Since a beamsplitter can be used to clone an identical copy of the transverse mode of a classical beam, we add two extra beamsplitters to the previous experiment setup of Chapter 4 to produce two extra spatially separated beams. There are in total four spatially separated beams, each consisting of two orthogonally polarized fields i.e., $\hat{H}$ and $\hat{V}$ and two frequencies i.e., 30 and 120 kHz. As before, we use a heterodyne detection scheme for each beam. The photodetectors are obtained from Hamamatsu (model: S1223-01). Three analog multipliers are used to multiply the beat signals from the four detectors. Band pass frequency filtering is achieved by building a notch filter. Multiplication and band pass filtering are essential to obtain the desired product signal from the four detectors. The desired multiplication beat signal that simulates the four-photon entanglement is recorded and saved in a computer by using a LabView program.

### 5.2.1 Detection Diagram

The detection diagram is shown in Figure 5.2. The circuit diagram for the detection system is shown three parts in Figure 5.3, Figure 5.4 and Figure 5.5. The circuit is designed in such a way that the final band passed product signal is analogous to the fourfold coincidence detection of four particles. In this experiment, there are four spatially separated beams and each of them is sent to an optical heterodyne detection region. The beat signal $A_1$ from the detector $D_1$ has two frequency components i.e., 30 ($H_1$) kHz and 120 ($V_1$) kHz. The parenthesis is used to indicate that the 30 kHz signal is from the horizontally polarized beam and the 120 kHz signal is from the vertically polarized beam. Similarly, the beat signal $A_2$ from detector $D_2$ has frequencies 30 ($H_2$) kHz and 120 ($V_2$) kHz. The beat signals from the detectors $D_1$ and $D_2$ are multiplied in the analog multiplier AD835 as shown in the circuit diagram. Then, a band pass filter made of two cascaded notch filters centered at frequency 60 kHz is used to obtain the 60 kHz component of the product signal $H_1H_2$ of detectors $D_1$ and $D_2$. Similarly, an identical band pass filter centered at 240 kHz is used to obtain the product signal $V_1V_2$. These two product signals are added by using a summing amplifier. The amplifier is a model TL071A. The summation signal is then multiplied with the beat signal $A_3$ from the detector $D_3$. The beat signal $A_3$ has two frequency components i.e., 30 ($V_3$) kHz and 120 ($H_3$) kHz. One can see that the beat frequencies for the horizontal and vertical components have been interchanged. After the multiplication of the beat signals $A_3$ with the summation signal, two cascaded band pass notch filters centered at 180 and 270 kHz are used to obtain the product signal components $V_1V_2V_3$ and $H_1H_2H_3$ respectively. Then, these two signals are added using another summing amplifier. The summation signal is then multiplied with the beat signal $A_4$ by using a third analog multiplier. The beat signals $A_4$ obtained in detector $D_4$ have the same property as the beat signals $A_3$, that is the beat frequencies at 30 and 120 kHz are associated with the horizontal $V_4$ and vertical $H_4$ components respectively. We use another cascaded band pass notch filter centered at frequency 300 kHz to obtain the final band passed product signal which contains two indistinguishable and interfering contributions $\propto H_1H_2H_3H_4 + V_1V_2V_3V_4$. The product signal at 300 kHz is denoted as $\gamma_{300kHz}$ in the later sections. The detection diagram in this classical simulation experiment acts as a projection measurement on the desired GHZ state and filters out the other undesired components. Note that a more symmetrical scheme using only 60 kHz and 240 kHz filters can be used to obtain the same result. This scheme is described in Chapter 6 where it is used for entanglement swapping.

### 5.2.2 Notch Filter

The circuit diagram for the notch filter is shown in Figure 5.6. It has been used as outputs in Figure 5.4 and Figure 5.5. In this experiment, the notch filter is used together with the biquad active filters described in Chapter 4. The reason is that the former needs only one amplifier compared to the latter where three amplifiers are needed. Two or three notch filters are cascaded to narrow down the band pass frequency ranges. The variable resistors $R_1$ and $R_2$ are adjusted to vary the center frequency of the filter. When the circuit resonates at its center frequency, then the band passed signal is not phase shifted or distorted. As explained in the detection diagram of Figure 5.2, the band pass filter is essential to this experiment because

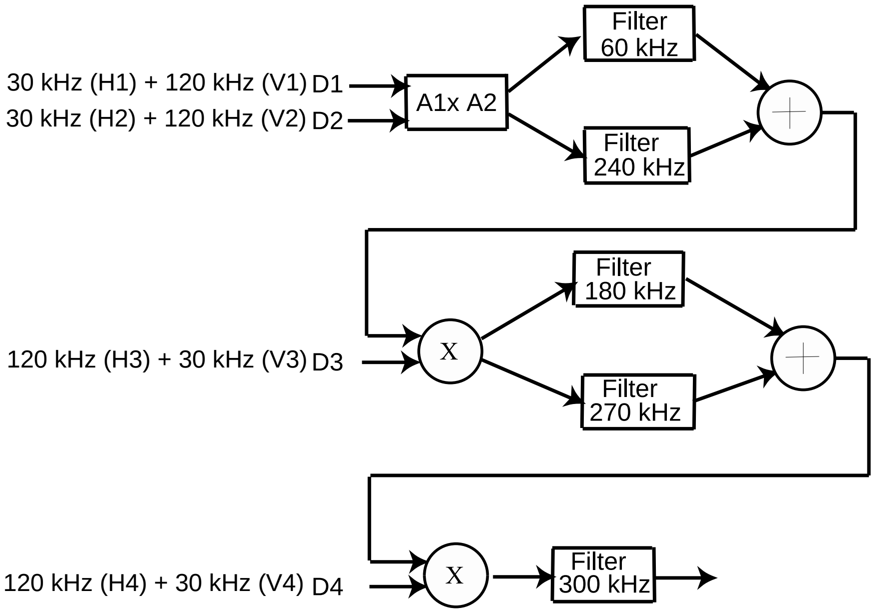

**Figure 5.2**: The detection diagram for simulation of four-particle GHZ entanglement.

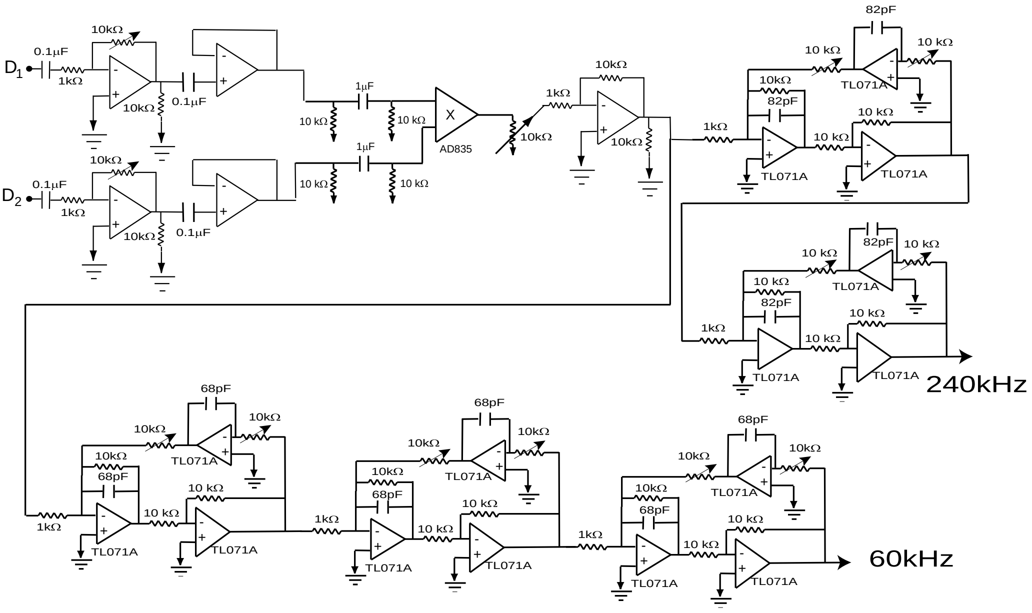

**Figure 5.3**: The circuit diagram for detecting beat signals from detectors 1 and 2.

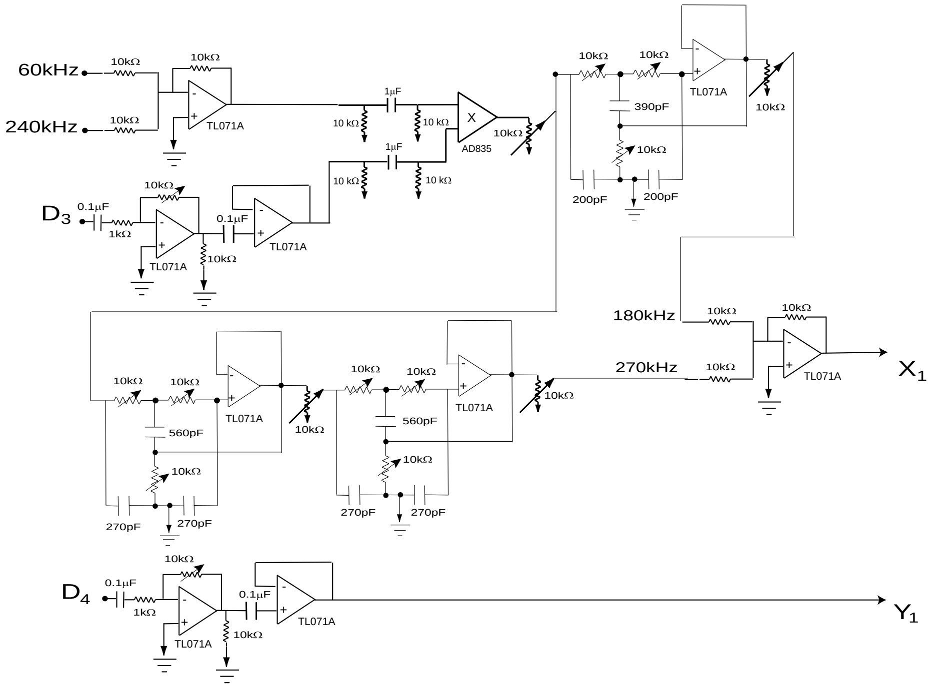

**Figure 5.4**: The circuit diagram for detecting beat signals from detectors 3 and 4.

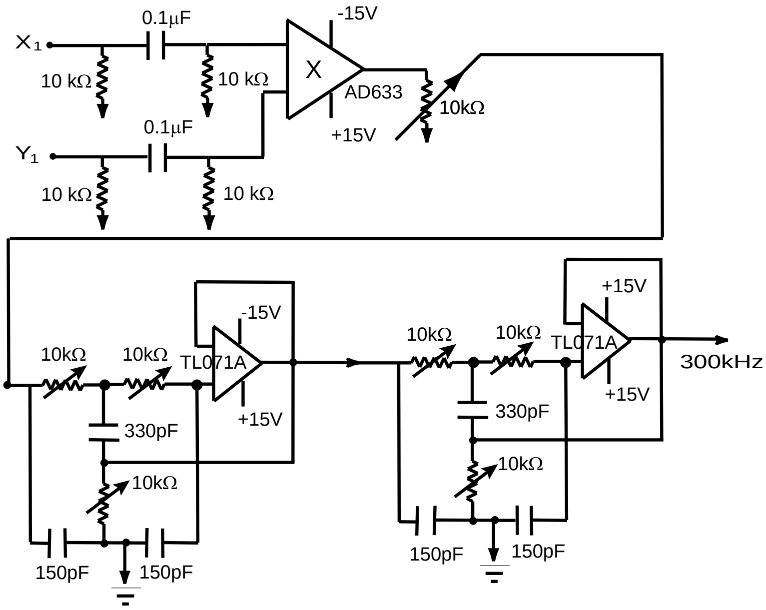

**Figure 5.5**: The circuit diagram for band pass filters centered at 300 kHz.

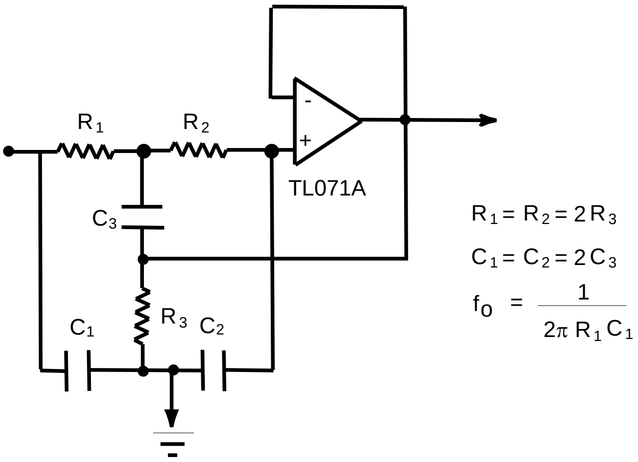

**Figure 5.6**: The notch filter at 300 kHz with $C_1 = 150\,pF$ and $R_1 = 3.5\,k\Omega$.

it selects the correct frequency component that contains the desired product states after the multiplication has taken place.

### 5.2.3 Analog Multiplier

The task of the analog multiplier in this experiment is to multiply the beat signals from the two spatially separated regions to simulate the coincidence detection of two particles. The type of analog multiplier used in this experiment is a model AD835. It is 4-quadrant multiplier. It is manufactured by Analog Devices. This multiplier has less noise than the analog multiplier (model:AD633) used in Chapter 4. The power supply for the multiplier is ±5 volts. The input signal for the multiplier is AC coupled before it is connected. This can be achieved by connecting a capacitor to each input port of the multiplier. The multiplier has low nonlinearity in the frequency operating region. The lower frequency used in this experiment is 30 kHz and the higher frequency is 120 kHz. The input signal amplitude cannot exceed ±1 volt. We avoid this problem by controlling the gain of a voltage amplifier for the beat signals from the photodetector. To simulate four-particle entanglement, three analog multipliers are used to multiply the beat signals from four detectors.

## 5.3 Experimental Setup and Analysis

In our experiments, in Figure 5.7, a HeNe laser beam is split and sent through two fixed-frequency acousto-optic modulators to produce a beam of frequency $\omega_H = \omega + \delta_H$ with horizontal polarization and a beam of frequency $\omega_V = \omega + \delta_V$ with vertical polarization, where $\delta_H = 2\pi \times 30$ kHz and $\delta_V = 2\pi \times 120$ kHz. These two beams are combined on beam splitter BS1. Note that the relative phase between the 30 and 120 kHz fields is the same for each port of BS1, except for a $\pi$ phase shift which arises from the beam splitter. Beam splitter BS2 in one of the outputs of the BS1 produces two identical copies of the transverse mode of one of the output fields of BS1 that are beam 1 (reflected) and beam 3 (transmitted). Similarly, beam splitter BS3 produces two identical copies, beam 2 (reflected) and beam 4 (transmitted). Half-wave plates oriented at $0^o$ in beams 1 and 2 induce a $\pi$ phase shift between the horizontal and vertical components. Then, the total fields $\mathbf{E}_1$ and $\mathbf{E}_2$ in beams 1 and 2 respectively are given by

$$\mathbf{E}_1 = \mathcal{E}_1 \exp(-i\omega_V t)\hat{V}_1 + \mathcal{E}_1 \exp(-i\omega_H t)\hat{H}_1 \ , \tag{5.9}$$

$$\mathbf{E}_2 = \mathcal{E}_2 \exp(-i\omega_V t)\hat{V}_2 + \mathcal{E}_2 \exp(-i\omega_H t)\hat{H}_2 \ . \tag{5.10}$$

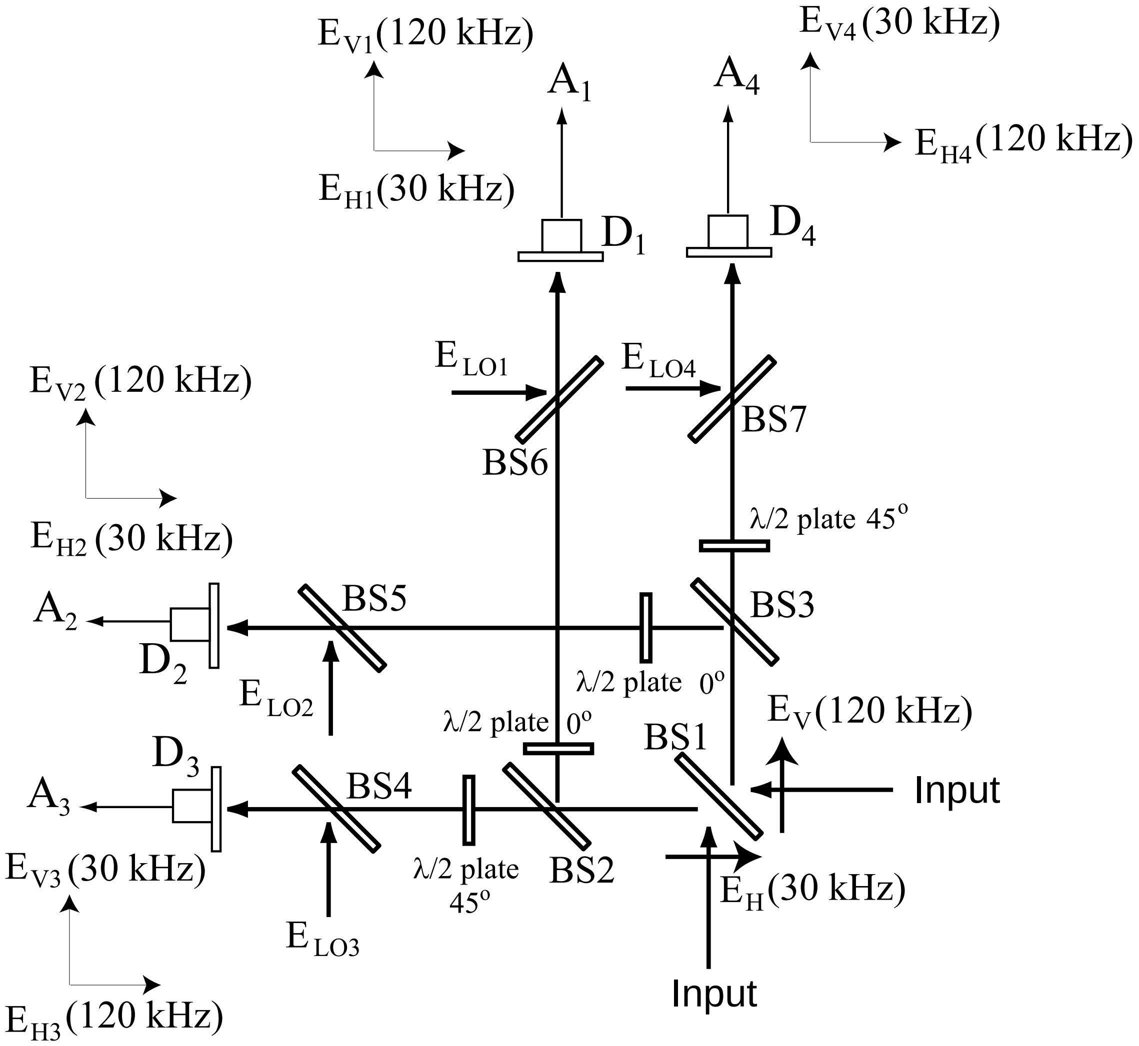

**Figure 5.7**: The experimental setup for reproducing the polarization correlations of four photon entanglement.

Half-wave plates oriented at $45^o$ in beams 3 and 4 interchange the horizontal and vertical components. Their optical fields $\mathbf{E}_3$ and $\mathbf{E}_4$ are given by

$$\mathbf{E}_3 = \mathcal{E}_3 \exp(-i\omega_H t)\hat{V}_3 + \mathcal{E}_3 \exp(-i\omega_V t)\hat{H}_3, \tag{5.11}$$

$$\mathbf{E}_4 = \mathcal{E}_4 \exp(-i\omega_H t)\hat{V}_4 + \mathcal{E}_4 \exp(-i\omega_V t)\hat{H}_4 \ . \tag{5.12}$$

Each of the four beams is sent to a heterodyne detector and mixed with a local oscillator beam of frequency $\omega$. The polarization state of each local oscillator beam is chosen to be in one of the four polarizations H$'$, V$'$, R and L by using a $\lambda/2$ plate and $\lambda/4$ plate independently.

Now, in order to demonstrate that our classical system can simulate a projection measurement on the GHZ state of Eq. (5.1), we choose the four local oscillator beams at a arbitrary polarization angles with unit vectors denoted by $\hat{\mathbf{e}}_{LOi}$, where $i = 1, 2, 3, 4$. The heterodyne beat signal is detected as shown in the detection diagram of Figure 5.2. In detector $D_1$, the heterodyne beat signal obtained from the interference between local oscillator LO1 and the field $\mathbf{E}_1$ can be written in the parenthesis notation of [44],

$$\begin{aligned} A_1 &= (\mathbf{E}_{LO1}|\mathbf{E}_1) \\ &\equiv \int dxdy\, E^*_{LO1}(x,y,t)\, \hat{\mathbf{e}}^*_{LO1} \cdot \mathbf{E}_1(x,y,t) \end{aligned} \tag{5.13}$$

and similarly for LO2, LO3 and LO4. Here, $E_{LO1}(x,y,t) = \mathcal{E}_{LO1}(x,y)\exp(-i\omega t)$ is the LO1 field amplitude in the plane of a photodiode detector and $\mathbf{E}_1$ is the vector field amplitude along beam 1. By using Eq. (5.9), the beat signal $A_1$ is then rewritten as

$$A_1 = (\hat{\mathbf{e}}_{LO1}|\hat{\mathbf{V}}_1)(\mathcal{E}_{LO1}|\mathcal{E}_1)\exp(-i\delta_V t) + (\hat{\mathbf{e}}_{LO1}|\hat{\mathbf{H}}_1)(\mathcal{E}_{LO1}|\mathcal{E}_1)\exp(-i\delta_H t)\ , \tag{5.14}$$

where $(\mathcal{E}_{LO1}|\mathcal{E}_1)$ denotes the spatial overlap integral of LO1 and the field of beam 1. The beat signal amplitudes in detectors $D_2$, $D_3$ and $D_4$ are then given by

$$\begin{aligned}
A_2 &= (\mathbf{E}_{LO2}|\mathbf{E}_2) \\
&\propto (\hat{\mathbf{e}}_{LO2}|\hat{\mathbf{V}}_2)(\mathcal{E}_{LO2}|\mathcal{E}_2)\exp(-i\delta_V t) + (\hat{\mathbf{e}}_{LO2}|\hat{\mathbf{H}}_2)(\mathcal{E}_{LO2}|\mathcal{E}_2)\exp(-i\delta_H t) \\
A_3 &= (\mathbf{E}_{LO3}|\mathbf{E}_3) \\
&\propto (\hat{\mathbf{e}}_{LO3}|\hat{\mathbf{V}}_3)(\mathcal{E}_{LO3}|\mathcal{E}_3)\exp(-i\delta_H t) + (\hat{\mathbf{e}}_{LO3}|\hat{\mathbf{H}}_2)(\mathcal{E}_{LO3}|\mathcal{E}_3)\exp(-i\delta_V t) \\
A_4 &= (\mathbf{E}_{LO4}|\mathbf{E}_4) \\
&\propto (\hat{\mathbf{e}}_{LO4}|\hat{\mathbf{V}}_4)(\mathcal{E}_{LO4}|\mathcal{E}_4)\exp(-i\delta_H t) + (\hat{\mathbf{e}}_{LO4}|\hat{\mathbf{H}}_4)(\mathcal{E}_{LO4}|\mathcal{E}_4)\exp(-i\delta_V t)\ .
\end{aligned} \tag{5.15}$$

As shown in the detection diagram from Figure 5.2, the beat signals from detectors $D_1$ and $D_2$ are sent to an analog multiplier which yields a product signal proportional to the real part of the amplitude $A_1A_2+A_1^*A_2$. The beat amplitudes $A_1$ and $A_2$ each contain two beat frequencies $\delta_H$ and $\delta_V$, yielding nonzero frequency components in the product signal: $\delta_H \pm \delta_V$, $2\delta_H$ =60 kHz and $2\delta_V$ =240 kHz. Band pass filters are used to select the product signals at frequency $2\delta_H$ and $2\delta_V$. The corresponding beat signal amplitudes are respectively,

$$\gamma_{60kHz}(A_1, A_2) \propto (\mathcal{E}_{LO1}|\mathcal{E}_1)(\mathcal{E}_{LO2}|\mathcal{E}_2)(\hat{\mathbf{e}}_{LO1}|\hat{\mathbf{H}}_1)(\hat{\mathbf{e}}_{LO2}|\hat{\mathbf{H}}_2) \tag{5.16}$$

and

$$\gamma_{240kHz}(A_1, A_2) \propto (\mathcal{E}_{LO1}|\mathcal{E}_1)(\mathcal{E}_{LO2}|\mathcal{E}_2)(\hat{\mathbf{e}}_{LO1}|\hat{\mathbf{V}}_1)(\hat{\mathbf{e}}_{LO2}|\hat{\mathbf{V}}_2)\ . \tag{5.17}$$

The product signals at 60 kHz and at 240 kHz are added by using a summing amplifier and then multiplied with the beat signal from detector $D_3$, $A_3 + A_3^*$. The resulting product signal is then band pass filtered at frequencies 180 kHz and 270 kHz, yielding two signals with the amplitudes

$$\gamma_{180kHz}(A_1, A_2, A_3) \propto (\mathcal{E}_{LO1}|\mathcal{E}_1)(\mathcal{E}_{LO2}|\mathcal{E}_2)(\mathcal{E}_{LO3}|\mathcal{E}_3)(\hat{\mathbf{e}}_{LO1}|\hat{\mathbf{H}}_1)(\hat{\mathbf{e}}_{LO2}|\hat{\mathbf{H}}_2)(\hat{\mathbf{e}}_{LO3}|\hat{\mathbf{H}}_3) \tag{5.18}$$

and

$$\gamma_{270kHz}(A_1, A_2, A_3) \propto (\mathcal{E}_{LO1}|\mathcal{E}_1)(\mathcal{E}_{LO2}|\mathcal{E}_2)(\mathcal{E}_{LO3}|\mathcal{E}_3)(\hat{\mathbf{e}}_{LO1}|\hat{\mathbf{V}}_1)(\hat{\mathbf{e}}_{LO2}|\hat{\mathbf{V}}_2)(\hat{\mathbf{e}}_{LO3}|\hat{\mathbf{V}}_3)\ . \tag{5.19}$$

Similarly, these product signals are added and then multiplied with the beat signal from detector 4, $A_4 + A_4^*$. Finally, using a band pass filter at 300 kHz, the resulting product signal amplitude is

$$\begin{aligned}\gamma_{300kHz}(A_1, A_2, A_3, A_4) \;&\propto\; (\mathcal{E}_{LO1}|\mathcal{E}_1)(\mathcal{E}_{LO2}|\mathcal{E}_2)(\mathcal{E}_{LO3}|\mathcal{E}_3)(\mathcal{E}_{LO4}|\mathcal{E}_4)\\ &\times\; \Big((\hat{\mathbf{e}}_{LO1}|\hat{\mathbf{V}}_1)(\hat{\mathbf{e}}_{LO2}|\hat{\mathbf{V}}_2)(\hat{\mathbf{e}}_{LO3}|\hat{\mathbf{V}}_3)(\hat{\mathbf{e}}_{LO4}|\hat{\mathbf{V}}_4)\\ &+\; (\hat{\mathbf{e}}_{LO1}|\hat{\mathbf{H}}_1)(\hat{\mathbf{e}}_{LO2}|\hat{\mathbf{H}}_2)(\hat{\mathbf{e}}_{LO3}|\hat{\mathbf{H}}_3)(\hat{\mathbf{e}}_{LO4}|\hat{\mathbf{H}}_4)\Big)\,.\end{aligned} \tag{5.20}$$

The amplitude $(\mathcal{E}_{LO1}|\mathcal{E}_1)(\mathcal{E}_{LO2}|\mathcal{E}_2)(\mathcal{E}_{LO3}|\mathcal{E}_3)(\mathcal{E}_{LO4}|\mathcal{E}_4)$ is a common factor in each path and it is controlled by a gain amplifier after each band pass filter. Hence, the product amplitude $\gamma_{300kHz}$ in Eq. (5.20) is analogous to the projection

$$(\hat{\mathbf{e}}_{LO1}|(\hat{\mathbf{e}}_{LO2}|(\hat{\mathbf{e}}_{LO3}||(\hat{\mathbf{e}}_{LO4}|\Psi^4_{GHZ})_{cl}\ , \tag{5.21}$$

where the $|\Psi^4_{GHZ})_{cl}$ is given by

$$|\Psi^4_{GHZ})_{cl} \ = \ \frac{1}{\sqrt{2}}\left(|H_1H_2H_3H_4) + |V_1V_2V_3V_4)\right)\ . \tag{5.22}$$

Here, for simplicity $\hat{H}$ and $\hat{V}$ are denoted as H and V respectively. The superscript 4 denotes a four field state. The field here is classical. The detection technique discussed above is analogous to fourfold coincidence detection in the quantum experiment to project out the desired four-particle GHZ state.

Now, in order to simulate the polarization correlations of GHZ entanglement by using the three-particle GHZ state, the polarization of LO4 is fixed at $45^o$,

$$\hat{e}_{LO4} \ = \ \frac{1}{\sqrt{2}}[|H_4) + |V_4)]\,, \tag{5.23}$$

so that the beat signal $A_4$ at detector $D_4$ is the analog of a trigger photon in the quantum GHZ experiment. Then, the beat signal amplitude at 300 kHz can be rewritten as

$$\begin{aligned}\gamma_{300kHz}(A_1, A_2, A_3, A_4) \ &\propto \ (\hat{\mathbf{e}}_{LO1}, \hat{\mathbf{e}}_{LO2}, \hat{\mathbf{e}}_{LO1}, \hat{\mathbf{e}}^{45^\circ}_{LO1}|\Psi^4_{GHZ})_{cl} \\ &= \ (\hat{\mathbf{e}}_{LO1}|V_1)(\hat{\mathbf{e}}_{LO2}|V_2)(\hat{\mathbf{e}}_{LO3}|V_3)(\hat{\mathbf{e}}^{45^\circ}_{LO4}|V_4) \\ &+ \ (\hat{\mathbf{e}}_{LO1}|H_1)(\hat{\mathbf{e}}_{LO2}|H_2)(\hat{\mathbf{e}}_{LO3}|H_3)(\hat{\mathbf{e}}^{45^\circ}_{LO4}|H_4) \\ &\propto \ (\hat{\mathbf{e}}_{LO1}, \hat{\mathbf{e}}_{LO2}, \hat{\mathbf{e}}_{LO1}|\Psi^3_{GHZ})_{cl}, \end{aligned} \tag{5.24}$$

where we can leave out the contribution from the LO4 in the simulation of the three particle GHZ entanglement i.e. $(\hat{\mathbf{e}}^{45^\circ}_{LO4}|V_4) = \frac{1}{\sqrt{2}}$ and $(\hat{\mathbf{e}}^{45^\circ}_{LO4}|H_4) = \frac{1}{\sqrt{2}}$. The state $|\Psi^3_{GHZ})_{cl} = \frac{1}{\sqrt{2}}[|H_1H_2H_3) + |V_1V_2V_3)]$. The superscript 3 of $|\Psi^3_{GHZ})_{cl}$ indicates the three-field state. Thus, in the following sections, the product amplitude at 300 kHz can be used to simulate three-particle GHZ entanglement where the polarizations of LO1, LO2 and LO3 are subjected to one of the four projections, $H'$, $V'$, $R$ and $L$.

## 5.4 Experimental Results

### Measurement of YYX Configuration

As a first demonstration of our classical system, we simulate the $Y_1Y_2X_3$ configuration for three-particle GHZ entanglement. The polarization states of the local oscillator beams LO1, LO2 and LO3 are given by

$$\begin{aligned}\hat{\mathbf{e}}^{R,L}_{LO1} &= \frac{1}{\sqrt{2}}(\hat{H}_1 \pm i\hat{V}_1)\\ \hat{\mathbf{e}}^{R,L}_{LO2} &= \frac{1}{\sqrt{2}}(\hat{H}_2 \pm i\hat{V}_2)\\ \hat{\mathbf{e}}^{H',V'}_{LO3} &= \frac{1}{\sqrt{2}}(\hat{H}_3 \pm \hat{V}_3). \qquad (5.25)\end{aligned}$$

For the classical analog of the measurement of the element of reality $R_1L_2H'_3$ in the $Y_1Y_2X_3$ configuration, the polarizations of the LO1, LO2 and LO3 beams are given accordingly as $\hat{\mathbf{e}}^{R}_{LO1}$, $\hat{\mathbf{e}}^{L}_{LO2}$, and $\hat{\mathbf{e}}^{H'}_{LO3}$. Now, from the above discussion, the magnitude of the beat signal $\gamma_{300kHz}$ is

$$\gamma_{300kHz}(A_1, A_2, A_3, A_4) \;\propto\; (\hat{\mathbf{e}}^{R}_{LO1}, \hat{\mathbf{e}}^{L}_{LO2}, \hat{\mathbf{e}}^{H'}_{LO1}|\Psi^3_{GHZ})_{cl}\ . \qquad (5.26)$$

This $\gamma_{300kHz}$ amplitude is analogous to the projection of $\langle R_1L_2H_3'|\Psi^3_{GHZ}\rangle$ of Eq. (5.5) which determines the existence of the element of reality $R_1L_2H_3'$ in the $Y_1Y_2X_3$ configuration. When the LO3 polarization state is changed to $V'$, this induces a minus sign in Eq. (5.26), hence the magnitude of the $\gamma_{300kHz}$ for the projection $(\hat{\mathbf{e}}^R_{LO1}, \hat{\mathbf{e}}^L_{LO2}, \hat{\mathbf{e}}^{V'}_{LO1}|\Psi^3_{GHZ})_{cl}$ is zero. This is analogous to the projection $\langle R_1L_2V_3'|\Psi^3_{GHZ}\rangle$ $= 0$ and so indicates that the elements $R_1L_2V_3'$ in YYX configuration is not predicted by GHZ entanglement. The projection measurement analog of 8 possible components of element of reality in the YYX configuration are given by

$$\begin{aligned}
(\hat{\mathbf{e}}^R_{LO1}, \hat{\mathbf{e}}^L_{LO2}, \hat{\mathbf{e}}^{H'}_{LO3}|\Psi^3_{GHZ})_{cl} &\propto \langle R_1L_2H_3'|\Psi^3_{GHZ}\rangle = \frac{1}{2} \\
(\hat{\mathbf{e}}^R_{LO1}, \hat{\mathbf{e}}^L_{LO2}, \hat{\mathbf{e}}^{V'}_{LO3}|\Psi^3_{GHZ})_{cl} &\propto \langle R_1L_2V_3'|\Psi^3_{GHZ}\rangle = 0 \\
(\hat{\mathbf{e}}^R_{LO1}, \hat{\mathbf{e}}^R_{LO2}, \hat{\mathbf{e}}^{V'}_{LO3}|\Psi^3_{GHZ})_{cl} &\propto (R_1R_2V_3'|\Psi^3_{GHZ}\rangle = \frac{1}{2} \\
(\hat{\mathbf{e}}^R_{LO1}, \hat{\mathbf{e}}^R_{LO2}, \hat{\mathbf{e}}^{H'}_{LO3}|\Psi^3_{GHZ})_{cl} &\propto (R_1R_2H_3'|\Psi^3_{GHZ}\rangle = 0 \\
(\hat{\mathbf{e}}^L_{LO1}, \hat{\mathbf{e}}^R_{LO2}, \hat{\mathbf{e}}^{H'}_{LO3}|\Psi^3_{GHZ})_{cl} &\propto \langle L_1R_2H_3'|\Psi^3_{GHZ}\rangle = \frac{1}{2} \\
(\hat{\mathbf{e}}^L_{LO1}, \hat{\mathbf{e}}^R_{LO2}, \hat{\mathbf{e}}^{V'}_{LO3}|\Psi^3_{GHZ})_{cl} &\propto \langle L_1R_2V_3'|\Psi^3_{GHZ}\rangle = 0 \\
(\hat{\mathbf{e}}^L_{LO1}, \hat{\mathbf{e}}^L_{LO2}, \hat{\mathbf{e}}^{V'}_{LO3}|\Psi^3_{GHZ})_{cl} &\propto \langle L_1L_2V_3'|\Psi^3_{GHZ}\rangle = \frac{1}{2} \\
(\hat{\mathbf{e}}^L_{LO1}, \hat{\mathbf{e}}^L_{LO2}, \hat{\mathbf{e}}^{H'}_{LO3}|\Psi^3_{GHZ})_{cl} &\propto \langle L_1L_2H_3'|\Psi^3_{GHZ}\rangle = 0. \qquad (5.27)
\end{aligned}$$

As shown in Figure 5.8, the $\gamma_{300kHz}$ produces nonzero and zero amplitudes according to Eq. (5.27). For each element in this configuration, the normalization of the classical joint intensity is obtained from dividing the absolute square of the signal amplitude $\gamma_{300kHz}$ of each element of reality by the sum of the absolute square of $\gamma_{300kHz}$ for all the elements.

The classical field measurements then yield the joint probability representation of the YYX configuration which is shown in Figure 5.8(i). Note, for comparison, that the predictions of quantum mechanics would yield a probability of $1/4 = 0.25$ for each large signal and zero for each small signal, showing that the classical simulation is in good agreement.

### Measurement of YXY Configuration

For the $Y_1X_2Y_3$ configuration, the polarization states of the local oscillator beams LO1, LO2 and LO3 are given by

$$\begin{aligned}
\hat{\mathbf{e}}_{LO1}^{R,L} &= \frac{1}{\sqrt{2}}(\hat{H}_1 \pm i\hat{V}_1) \\
\hat{\mathbf{e}}_{LO2}^{H',V'} &= \frac{1}{\sqrt{2}}(\hat{H}_2 \pm \hat{V}_2) \\
\hat{\mathbf{e}}_{LO3}^{R,L} &= \frac{1}{\sqrt{2}}(\hat{H}_3 \pm i\hat{V}_3). \qquad (5.28)
\end{aligned}$$

For the classical analog of the measurement of the elements of reality $R_1H_2'L_3$, $L_1H_2'R_3$, $R_1V_2'R_3$ and $L_1V_2'L_3$ in the $Y_1X_2Y_3$ configuration, the nonzero and zero classical analog projections are given by

$$\begin{aligned}
(\hat{\mathbf{e}}_{LO1}^{L}, \hat{\mathbf{e}}_{LO2}^{V'}, \hat{\mathbf{e}}_{LO3}^{L}|\Psi_{GHZ}^3)_{cl} &\propto \langle L_1V_2'L_3|\Psi_{GHZ}^3\rangle = \frac{1}{2} \\
(\hat{\mathbf{e}}_{LO1}^{L}, \hat{\mathbf{e}}_{LO2}^{H'}, \hat{\mathbf{e}}_{LO3}^{L}|\Psi_{GHZ}^3)_{cl} &\propto \langle L_1H_2'L_3|\Psi_{GHZ}^3\rangle = 0\ . \\
(\hat{\mathbf{e}}_{LO1}^{R}, \hat{\mathbf{e}}_{LO2}^{H'}, \hat{\mathbf{e}}_{LO3}^{L}|\Psi_{GHZ}^3)_{cl} &\propto \langle R_1H_2'L_3|\Psi_{GHZ}^3\rangle = \frac{1}{2} \\
(\hat{\mathbf{e}}_{LO1}^{R}, \hat{\mathbf{e}}_{LO2}^{V'}, \hat{\mathbf{e}}_{LO3}^{L}|\Psi_{GHZ}^3)_{cl} &\propto \langle R_1V_2'L_3|\Psi_{GHZ}^3\rangle = 0 \\
(\hat{\mathbf{e}}_{LO1}^{R}, \hat{\mathbf{e}}_{LO2}^{V'}, \hat{\mathbf{e}}_{LO3}^{R}|\Psi_{GHZ}^3)_{cl} &\propto \langle R_1V_2'R_3|\Psi_{GHZ}^3\rangle = \frac{1}{2} \\
(\hat{\mathbf{e}}_{LO1}^{R}, \hat{\mathbf{e}}_{LO2}^{H'}, \hat{\mathbf{e}}_{LO3}^{R}|\Psi_{GHZ}^3)_{cl} &\propto \langle R_1H_2'R_3|\Psi_{GHZ}^3\rangle = 0 \\
(\hat{\mathbf{e}}_{LO1}^{L}, \hat{\mathbf{e}}_{LO2}^{H'}, \hat{\mathbf{e}}_{LO3}^{R}|\Psi_{GHZ}^3)_{cl} &\propto \langle L_1H_2'R_3|\Psi_{GHZ}^3\rangle = \frac{1}{2} \\
(\hat{\mathbf{e}}_{LO1}^{L}, \hat{\mathbf{e}}_{LO2}^{V'}, \hat{\mathbf{e}}_{LO3}^{R}|\Psi_{GHZ}^3)_{cl} &\propto \langle L_1V_2'R_3|\Psi_{GHZ}^3\rangle = 0. \qquad (5.29)
\end{aligned}$$

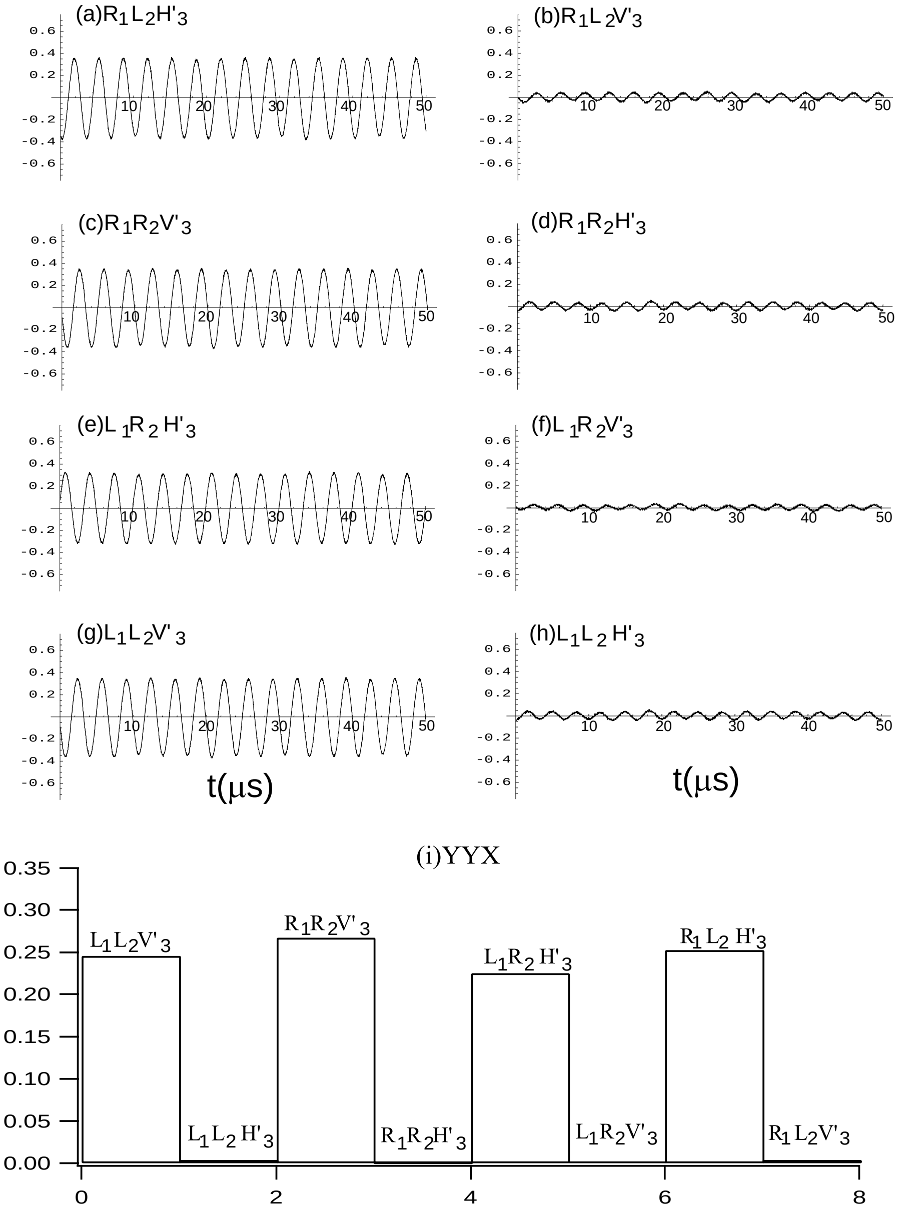

**Figure 5.8**: The YYX configuration.

The existence of each element of reality as predicted and not predicted by GHZ entanglement of Eq. (5.29) is shown in Figure 5.9. The joint probability representation of the YXY configuration is also shown in Figure 5.9(i).

### Measurement of XYY Configuration

Similarly, we simulate the $X_1Y_2Y_3$ configuration on the three-particle GHZ entanglement, the polarization states of the local oscillator beams LO1, LO2 and LO3 are then given by

$$\begin{aligned}\hat{\mathbf{e}}_{LO1}^{H',V'} &= \frac{1}{\sqrt{2}}(\hat{H}_1 \pm \hat{V}_1) \\ \hat{\mathbf{e}}_{LO2}^{R,L} &= \frac{1}{\sqrt{2}}(\hat{H}_2 \pm i\hat{V}_2) \\ \hat{\mathbf{e}}_{LO3}^{R,L} &= \frac{1}{\sqrt{2}}(\hat{H}_3 \pm i\hat{V}_3). \qquad (5.30)\end{aligned}$$

We measure $V_1'L_2L_3$, $H_1'L_2R_3$, $V_1'R_2R_3$ and $H_1'R_2L_3$ in the XYY configuration as predicted by GHZ entanglement of Eq. (5.7), the equivalent nonzero and zero clas-

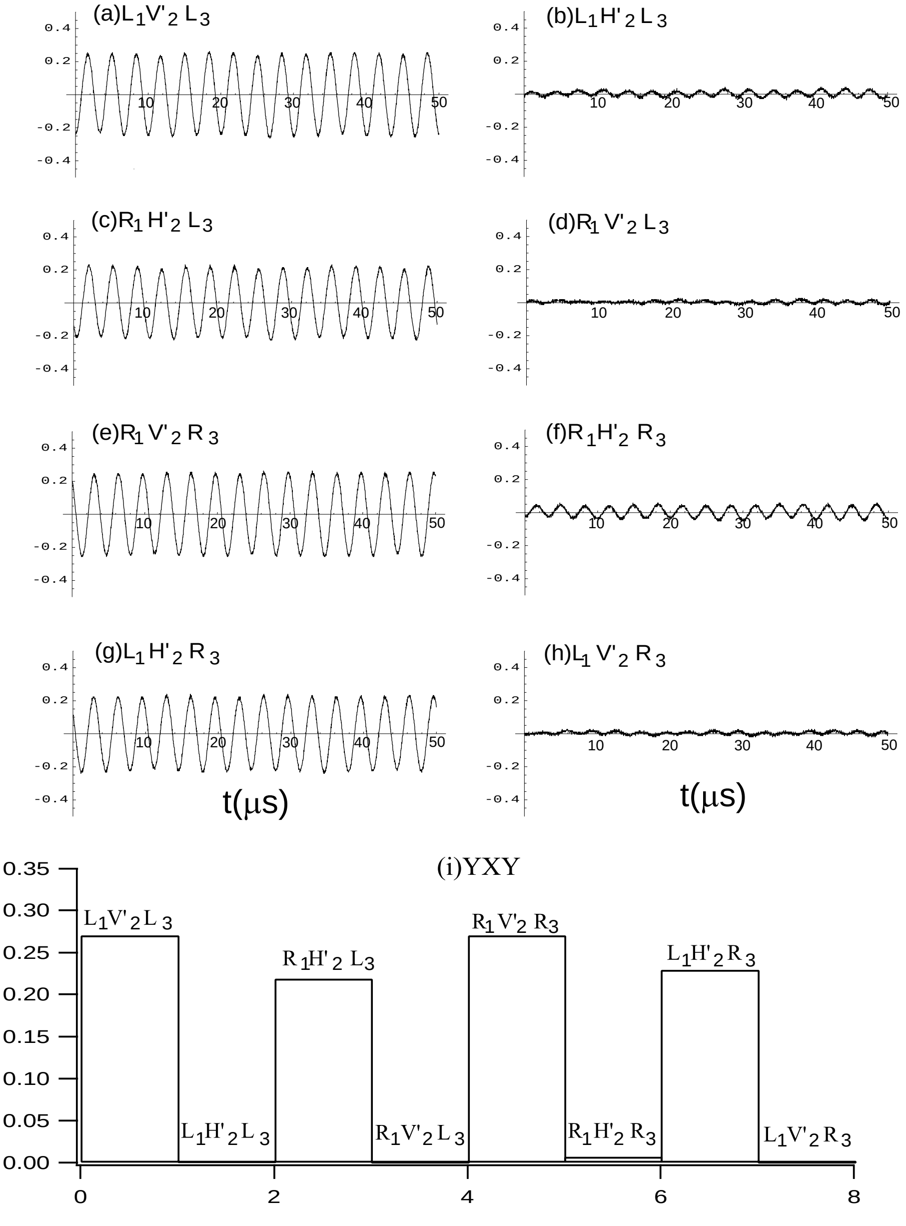

**Figure 5.9**: The YXY configuration.

sical analog projections are given by

$$\begin{aligned}
(\hat{\mathbf{e}}^{V'}_{LO1}, \hat{\mathbf{e}}^{R}_{LO2}, \hat{\mathbf{e}}^{R}_{LO3}|\Psi^3_{GHZ})_{cl} &\propto \langle V'_1 R_2 R_3|\Psi^3_{GHZ}\rangle = \frac{1}{2} \\
(\hat{\mathbf{e}}^{H'}_{LO1}, \hat{\mathbf{e}}^{R}_{LO2}, \hat{\mathbf{e}}^{R}_{LO3}|\Psi^3_{GHZ})_{cl} &\propto \langle H'_1 R_2 R_3|\Psi^3_{GHZ}\rangle = 0 \\
(\hat{\mathbf{e}}^{H'}_{LO1}, \hat{\mathbf{e}}^{R}_{LO2}, \hat{\mathbf{e}}^{L}_{LO3}|\Psi^3_{GHZ})_{cl} &\propto \langle H'_1 R_2 L_3|\Psi^3_{GHZ}\rangle = \frac{1}{2} \\
\hat{\mathbf{e}}^{V'}_{LO1}, \hat{\mathbf{e}}^{R}_{LO2}, \hat{\mathbf{e}}^{L}_{LO3}|\Psi^3_{GHZ})_{cl} &\propto \langle V'_1 R_2 L_3|\Psi^3_{GHZ}\rangle = 0\ . \\
(\hat{\mathbf{e}}^{V'}_{LO1}, \hat{\mathbf{e}}^{L}_{LO2}, \hat{\mathbf{e}}^{L}_{LO3}|\Psi^3_{GHZ})_{cl} &\propto \langle V'_1 L_2 L_3|\Psi^3_{GHZ}\rangle = \frac{1}{2} \\
(\hat{\mathbf{e}}^{H'}_{LO1}, \hat{\mathbf{e}}^{L}_{LO2}, \hat{\mathbf{e}}^{L}_{LO3}|\Psi^3_{GHZ})_{cl} &\propto \langle H'_1 L_2 L_3|\Psi^3_{GHZ}\rangle = 0 \\
(\hat{\mathbf{e}}^{H'}_{LO1}, \hat{\mathbf{e}}^{L}_{LO2}, \hat{\mathbf{e}}^{R}_{LO3}|\Psi^3_{GHZ})_{cl} &\propto \langle H'_1 L_2 R_3|\Psi^3_{GHZ}\rangle = \frac{1}{2} \\
(\hat{\mathbf{e}}^{V'}_{LO1}, \hat{\mathbf{e}}^{L}_{LO2}, \hat{\mathbf{e}}^{R}_{LO3}|\Psi^3_{GHZ})_{cl} &\propto \langle V'_1 L_2 R_3|\Psi^3_{GHZ}\rangle = 0. \qquad (5.31)
\end{aligned}$$

As shown in Figure 5.10, the $\gamma_{300kHz}$ produces zero and nonzero amplitudes according to Eq (5.31). The joint probability representation of the XYY configuration as predicted by the GHZ entanglement is shown in Figure 5.10(i).

### Measurement of XXX Configuration

Finally, we simulate the measurements $X_1X_2X_3$ configuration on the three-particle GHZ entanglement of Eq. (5.8). The polarization states of the local oscillator beams LO1, LO2 and LO3 are then given by

$$\begin{aligned}
\hat{\mathbf{e}}^{H',V'}_{LO1} &= \frac{1}{\sqrt{2}}(\hat{H}_1 \pm \hat{V}_1) \\
\hat{\mathbf{e}}^{H',V'}_{LO2} &= \frac{1}{\sqrt{2}}(\hat{H}_2 \pm \hat{V}_2) \\
\hat{\mathbf{e}}^{H',V'}_{LO3} &= \frac{1}{\sqrt{2}}(\hat{H}_3 \pm \hat{V}_3). \qquad (5.32)
\end{aligned}$$

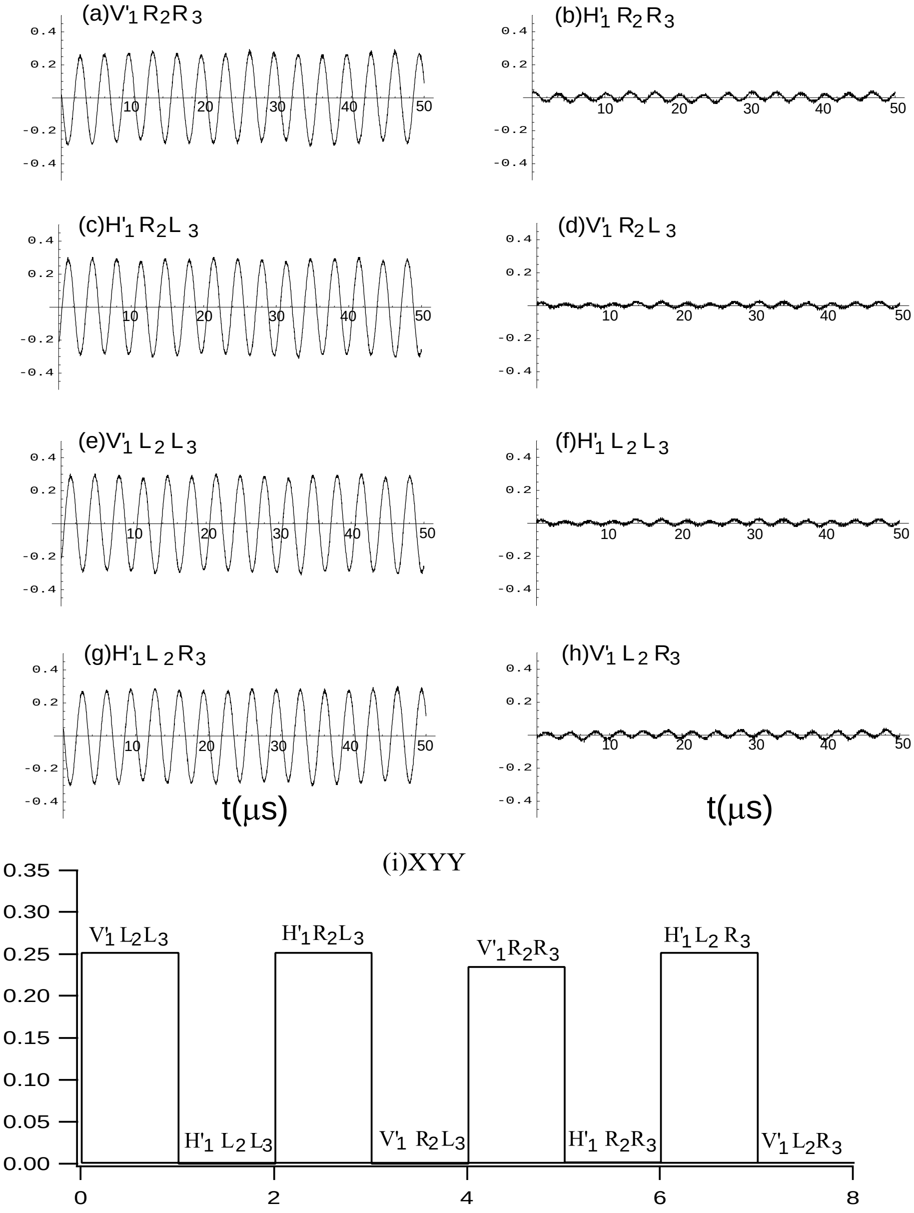

**Figure 5.10**: The XYY configuration

We demonstrate the classical analog of the measurement of the elements of reality $H_1'H_2'H_3'$, $V_1'V_2'H_3'$, $H_1'V_2'V_3'$ and $V_1'H_2'V_3'$ in the XXX configuration as predicted by GHZ entanglement of Eq. (5.8). For these polarizations, the nonzero and zero classical analog projections are given by

$$\begin{aligned}
(\hat{\mathbf{e}}_{LO1}^{V'}, \hat{\mathbf{e}}_{LO2}^{H'}, \hat{\mathbf{e}}_{LO3}^{V'}|\Psi_{GHZ}^3)_{cl} &\propto \langle V_1'H_2'V_3'|\Psi_{GHZ}^3\rangle = \frac{1}{2} \\
(\hat{\mathbf{e}}_{LO1}^{H'}, \hat{\mathbf{e}}_{LO2}^{H'}, \hat{\mathbf{e}}_{LO3}^{V'}|\Psi_{GHZ}^3)_{cl} &\propto \langle H_1'H_2'V_3'|\Psi_{GHZ}^3\rangle = 0\ . \\
(\hat{\mathbf{e}}_{LO1}^{H'}, \hat{\mathbf{e}}_{LO2}^{V'}, \hat{\mathbf{e}}_{LO3}^{V'}|\Psi_{GHZ}^3)_{cl} &\propto \langle H_1'V_2'V_3'|\Psi_{GHZ}^3\rangle = \frac{1}{2} \\
(\hat{\mathbf{e}}_{LO1}^{V'}, \hat{\mathbf{e}}_{LO2}^{V'}, \hat{\mathbf{e}}_{LO3}^{V'}|\Psi_{GHZ}^3)_{cl} &\propto \langle V_1'V_2'V_3'|\Psi_{GHZ}^3\rangle = 0 \\
(\hat{\mathbf{e}}_{LO1}^{V'}, \hat{\mathbf{e}}_{LO2}^{V'}, \hat{\mathbf{e}}_{LO3}^{H'}|\Psi_{GHZ}^3)_{cl} &\propto \langle V_1'V_2'H_3'|\Psi_{GHZ}^3\rangle = \frac{1}{2} \\
(\hat{\mathbf{e}}_{LO1}^{H'}, \hat{\mathbf{e}}_{LO2}^{V'}, \hat{\mathbf{e}}_{LO3}^{H'}|\Psi_{GHZ}^3)_{cl} &\propto \langle H_1'V_2'H_3'|\Psi_{GHZ}^3\rangle = 0 \\
(\hat{\mathbf{e}}_{LO1}^{H'}, \hat{\mathbf{e}}_{LO2}^{H'}, \hat{\mathbf{e}}_{LO3}^{H'}|\Psi_{GHZ}^3)_{cl} &\propto \langle H_1'H_2'H_3'|\Psi_{GHZ}^3\rangle = \frac{1}{2} \\
(\hat{\mathbf{e}}_{LO1}^{V'}, \hat{\mathbf{e}}_{LO2}^{H'}, \hat{\mathbf{e}}_{LO3}^{H'}|\Psi_{GHZ}^3)_{cl} &\propto \langle V_1'H_2'H_3'|\Psi_{GHZ}^3\rangle = 0. \qquad (5.33)
\end{aligned}$$

For the 8 possible measurements in the XXX configuration, the zero and nonzero signal amplitudes $\gamma_{300kHz}$ for each element of reality with $X_1X_2X_3 = \pm1$ is shown in Figure 5.11. For the elements of reality with $X_1X_2X_3 = -1$, i.e., $H_1'H_2'V_3'$, $V_1'V_2'V_3'$, $H_1'V_2'H_3'$, and $V_1'H_2'H_3'$, the signal amplitude $\gamma_{300kHz}$ is small. For the elements of reality with $X_1X_2X_3 = +1$, i.e., $V_1'H_2'V_3'$, $H_1'V_2'V_3'$, $V_1'V_2'H_3'$, and $H_1'H_2'H_3'$, the signal amplitude $\gamma_{300kHz}$ is large. The normalized joint intensity representation of the classical signals for the XXX configuration is also shown in Figure 5.11(i).

Figure 5.12 shows the probability representation of the measurement XXX configuration. The experimental observations for the $X_1X_2X_3$ configuration produced by our classical-wave system are in agreement with the quantum predictions of GHZ entanglement, giving strong signals only when $X_1X_2X_3 = +1$. This is in contrast to the predictions of local realism, where strong signals are predicted only if $X_1X_2X_3 = -1$. Of course, even though the classical system is able to reproduce the nonlocal correlation measurements exhibited by three quantum particles in the GHZ entanglement, the system lacks the particle-wave duality properties of a true quantum system. The complexity of our classical scheme is similar to that of the optical system employed in the quantum GHZ experiment, and can be simplified further by using the symmetrical detection scheme of Chapter 6.

## 5.5 Discussion

We have shown that the nonlocal correlations of a four-particle entangled state can be successfully reproduced by using a simple scheme employing heterodyne detection of classical fields, yielding large robust signals which are independent of the phases of the local oscillators. We use three analog multipliers and few band pass filters in order to simulate four-particle coincidence detection. The correlations for the classically entangled four field state are demonstrated by formally reproducing the 32 elements of the truth table obtained in a three-particle quantum GHZ experiment on the violation of local realism. Analogous to the quantum experiments, the simulation of four particle entanglement is easier than for three particles: To directly simulate a three particle entangled state, three frequencies are required. By contrast, only two frequencies and three beam splitters are required to generate an output that simulates four particle entanglement, because the polarizations can be interchanged in pairs. This is similar to the use of two pairs of parametric down converters in the corresponding quantum mechanical experiments. As in this classical experiments, it is easier to demonstrate three particle quantum GHZ entanglement starting from a four particle entangled state by using the fourth photon as a trigger.

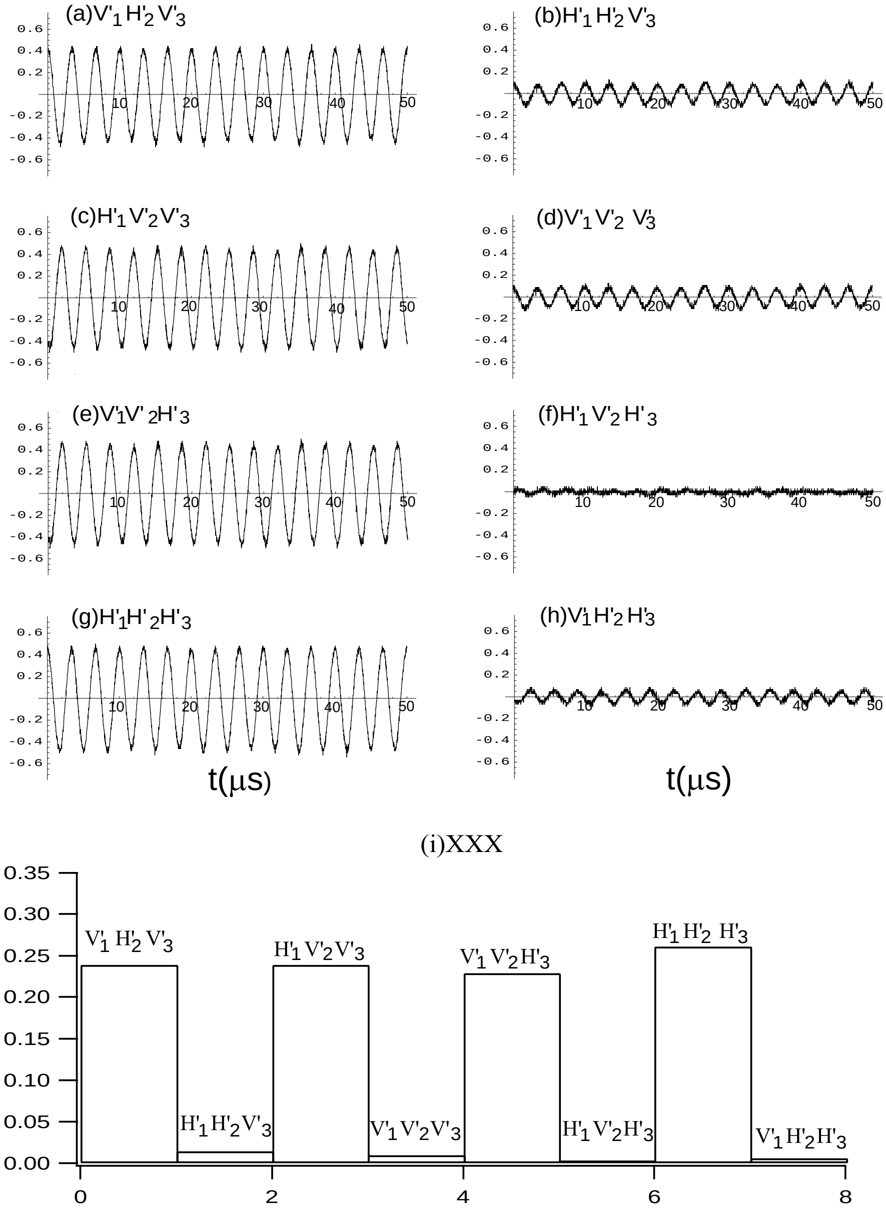

**Figure 5.11**: The XXX configuration

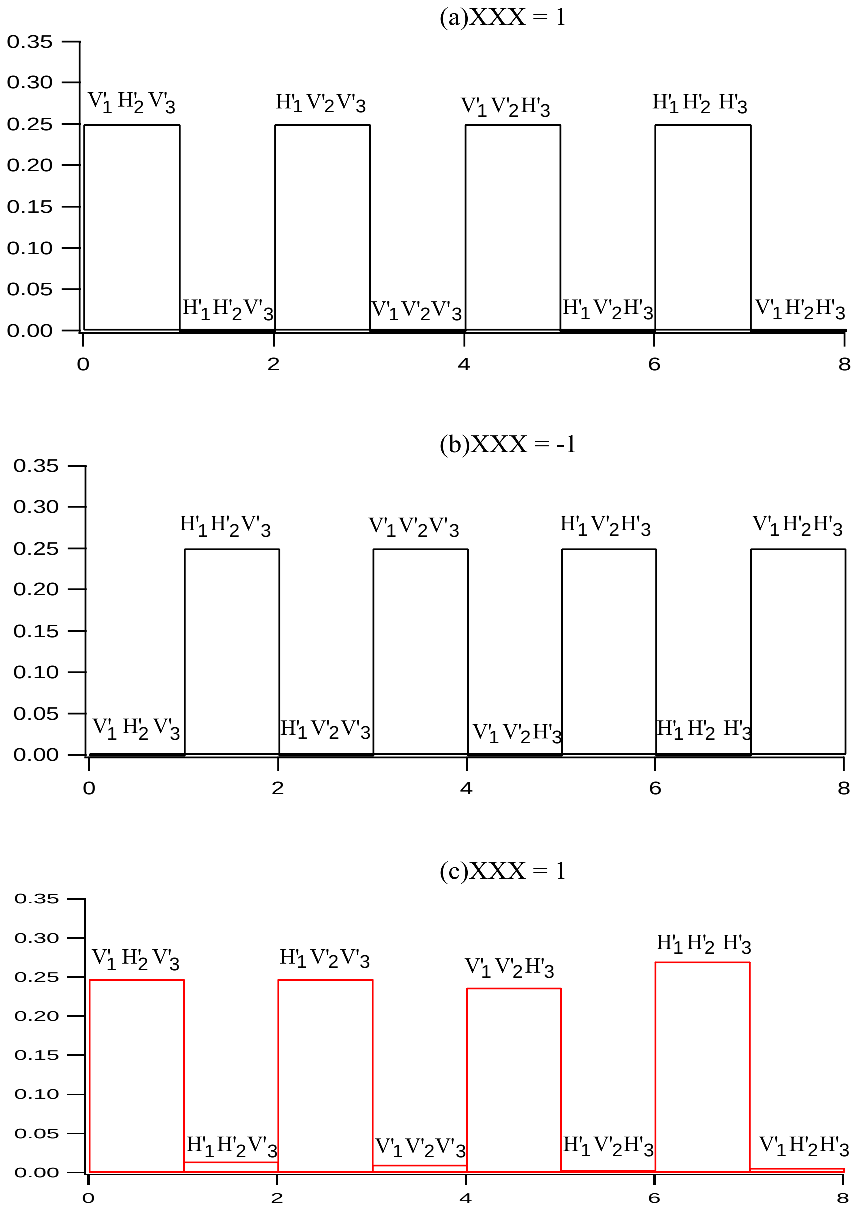

**Figure 5.12**: The probability representation of the XXX measurement. Elements of reality in the XXX configuration predicted by (a) quantum theory, XXX =+1 and (b) local realistic theory, XXX = -1. (c) the classical wave optics experiment reproduce measurements XXX =+1 in agreement with quantum theory.

# Chapter 6

# Entanglement Swapping With Classical Fields

## 6.1 Overview

In the previous chapter, we have demonstrated classical wave simulation of three particle GHZ entanglement by using a measurement method based on simulation of four photon entanglement.

In this chapter, we use the same experimental arrangement as in chapter 5 to discuss a type of entanglement swapping in a four photon basis. A symmetrical detection diagram is used for the demonstration of entanglement swapping, and could also have been employed in the simulation of GHZ entanglement.

In the following sections, we first give a brief discussion of quantum entanglement swapping for projection measurement in a four-photon basis. Then, we give a description of the experimental setup used to simulate entanglement swapping. We compare the properties of our classical analog of entanglement swapping with the predictions of quantum mechanics. We also discuss the problems in our experiment which are similar to the problems encountered in quantum entanglement swapping or teleportation, i.e., limitation in the basis of Bell states which can be swapped in a given experimental setup.

### 6.1.1 Description of Quantum Entanglement Swapping

In order to understand our simulation work in quantum entanglement swapping, we first need to describe the general concepts of the measuring process which is involved in quantum entanglement swapping. Entanglement swapping experiments require two independent measurement processes for two spatially separated observers A and B. A arranges to project out a given two-particle Bell state and sends trigger information to B. Then, B measures the correlations corresponding to the same state as A. The final state measured by these two observers in the entanglement swapping process is the *product* of the state $|\psi\rangle_A$ measured by observer A with the state $|\psi\rangle_B$ measured by observer B, that is $|\psi\rangle_A \times |\psi\rangle_B$. However, there is a different scheme for entanglement swapping which involves the measurement of a final state which is entangled, not a product state. The entanglement swapping scheme which involves projection measurement of an entangled state (discussed below) has higher fidelity compared to the scheme which involves the measurement of product state.

We are interested in simulating the entanglement swapping in a projection measurement of a four-photon GHZ entangled state as demonstrated by Zeilinger's group [64]. In the quantum mechanics experiments, two entangled photon pairs are *separately* generated from parametric down-conversion processes. The *separate* here means that these two pairs are obtained from two independent nonlinear interactions. The first pair consists of two entangled photons, denoted as photons 1 and 4. The second pair consists of the other two entangled photons denoted as photons 2 and 3. These two pairs form a product state, which is referred as *initial state* of the system. The initial state is given as

$$\begin{aligned}
|\Psi^i\rangle_{1234} &= \frac{1}{\sqrt{2}}[|H_1V_4\rangle - |V_1H_4\rangle] \\
&\times \frac{1}{\sqrt{2}}[|H_2V_3\rangle - |V_2H_3\rangle]\,. \qquad (6.1)
\end{aligned}$$

Suppose now that photon 1 from the first pair and photon 2 from the second pair are sent to observer A and similarly, photon 4 from the first pair and photon 3 from the second pair are sent to observer B. Then, the initial state can be rewritten as,

$$\begin{aligned}
|\Psi^i\rangle_{1234} &= \frac{1}{2}\big(|\varphi^+\rangle_{12}|\varphi^+\rangle_{34} + |\phi^+\rangle_{12}|\phi^+\rangle_{34} \\
&- |\varphi^-\rangle_{12}|\varphi^-\rangle_{34} + |\phi^-\rangle_{12}|\phi^-\rangle_{34}\big)\ , \qquad (6.2)
\end{aligned}$$

where

$$\begin{aligned}
|\varphi^\pm\rangle_{ij} &= \frac{1}{\sqrt{2}}\left(|H_iV_j\rangle \pm |V_iH_j\rangle\right) \\
|\phi^\pm\rangle_{ij} &= \frac{1}{\sqrt{2}}\left(|H_iH_j\rangle \pm |V_i)V_j\rangle\right)\ (i,j=1,2,3,4) \qquad (6.3)
\end{aligned}$$

are the four orthogonal Bell states.

Now, observer A makes a joint measurement on photons 1 and 2, and configures his measurements to project them onto one of the four Bell states, for example $|\phi^+\rangle_{12}{=}\frac{1}{\sqrt{2}}\left(|H_1H_2\rangle + |V_1V_2\rangle\right)$. The result of this measurement is then sent to observer B as a trigger signal. This trigger signal, together with signals from B's two detectors for photons 3 and 4 form a *fourfold coincidence detection.* Using the trigger signal from A, B finds that photons 3 and 4 are entangled in the same Bell state as A chooses for photons 1 and 2, that is, B measures $|\phi^+\rangle_{34} = \frac{1}{\sqrt{2}}\left(|H_3H_4\rangle + |V_3V_4\rangle\right)$. This is called entanglement swapping. In other words, after projection measurement of photons 1 and 2, photons 3 and 4 emerge entangled although they never interacted with one another in the past. This is the interesting feature of entanglement swapping. Eq. (6.2) implies that the projection measurement of photons 1 and 2 onto one of the four Bell states also projects photons 3 and 4 onto the same state.

In the entanglement swapping experiment demonstrated by Zeilinger's group [64], the four-fold coincidence detection projected out the four-photon entangled state $|\Psi^f\rangle = \frac{1}{\sqrt{2}}(|H_1H_2H_3H_4\rangle + |V_1V_2V_3V_4\rangle)$ not the product state $|\phi^+\rangle_{12}|\phi^+\rangle_{34}$. Note that the product pair $|\phi^+\rangle_{12}|\phi^+\rangle_{34}$ has four components in the four photon product basis while the final state $|\Psi^f\rangle$ is the four photon entangled state with only two components.

The above entanglement swapping scheme is totally different from the general concept of entanglement swapping [65], where the product pair $|\phi^+\rangle_{12}|\phi^+\rangle_{34}$ is measured. The advantage of the above version of entanglement swapping is that it achieves high fidelity in swapping, that is about 89% compared to 65% when the product pair is measured.

As shown in Ref [64], the projection measurement of the four-photon entangled state

$$|\Psi^f\rangle \;=\; \frac{1}{\sqrt{2}}(|H_1H_2H_3H_4\rangle + |V_1V_2V_3V_4\rangle) \tag{6.4}$$

can also be viewed as entanglement swapping: After observer A performs the joint Bell state measurement $|\phi^+\rangle_{12}$, the projection $\langle\phi^+_{12}|\Psi^f\rangle \propto \frac{1}{\sqrt{2}}(|H_3H_4\rangle + |V_3V_4\rangle)$, showing that observer B will measure the entangled state $|\phi^+\rangle_{34}$. In other words, the state of photon 2, $H(V)$, is swapped to photon 4, $H(V)$, and the state of photon 1, $H(V)$, is swapped to photon 3, $H(V)$. This can be easily seen from the four photon entangled state $|\Psi^f\rangle$.

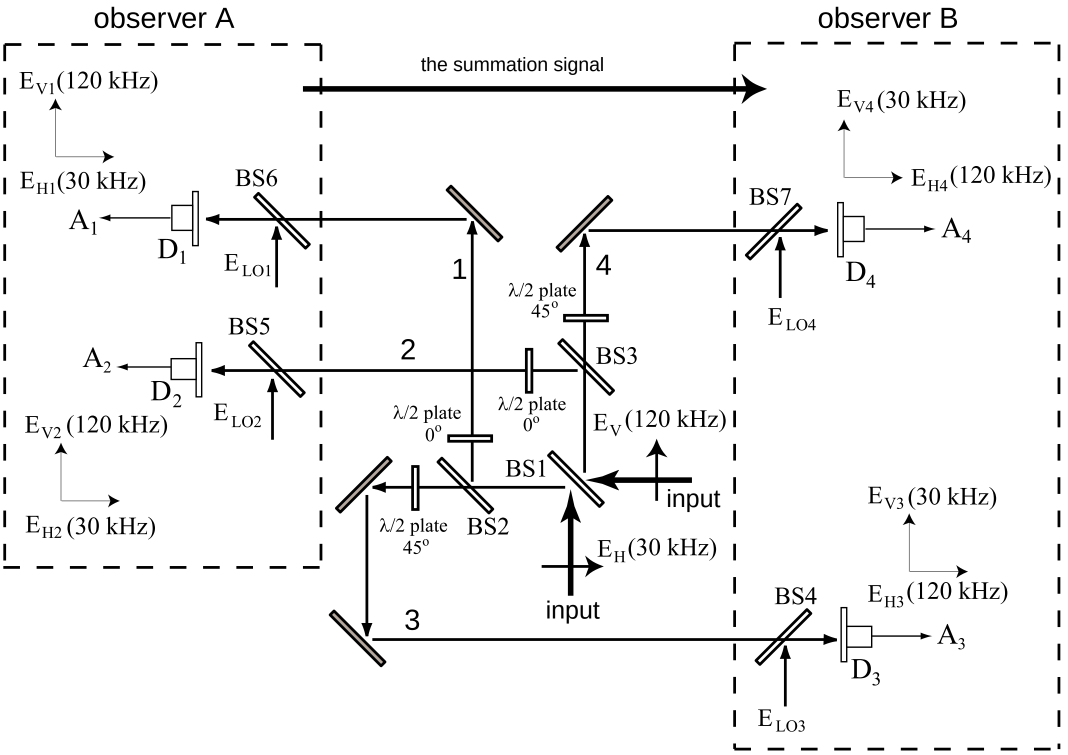

**Figure 6.1**: The experimental setup for simulation of entanglement swapping by using classical wave fields.

The entangled state $|\Psi^f\rangle$ demonstrates the working principle of entanglement swapping for the product pair $|\phi^+\rangle_{12}|\phi^+\rangle_{34}$.

In the following, an experimental simulation of the above version of entanglement swapping in a four field basis is given.

## 6.2 Entanglement Swapping With Classical Fields

### 6.2.1 Experimental Setup and Results

The experimental setup for demonstrating the process of entanglement swapping is shown in Figure 6.1. It is just a rearrangement of the experimental setup of Chapter

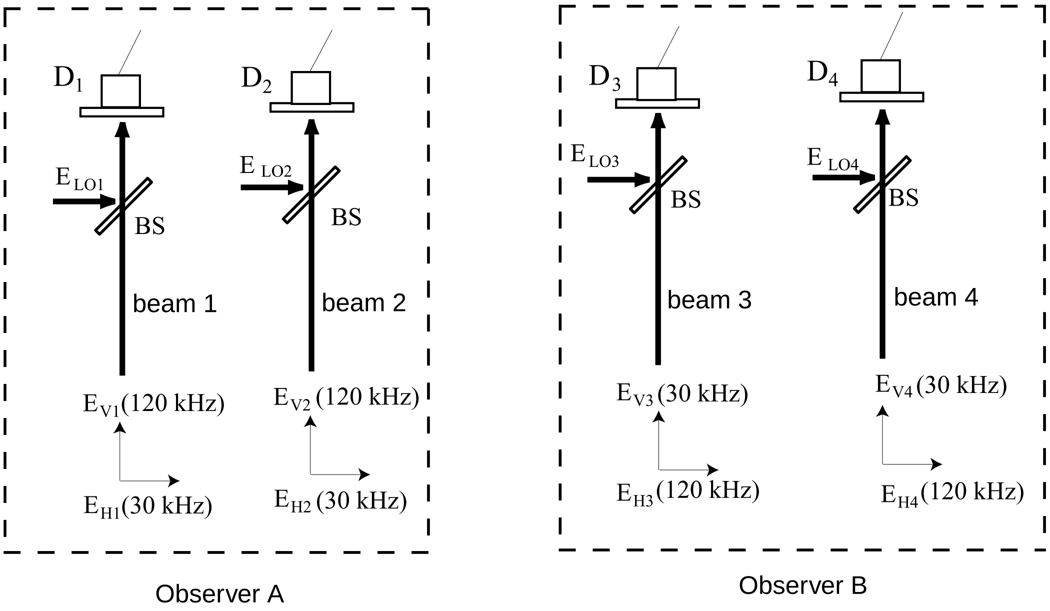

**Figure 6.2**: Beams 1 and 2 are detected by observer A and beams 3 and 4 are detected by observer B.

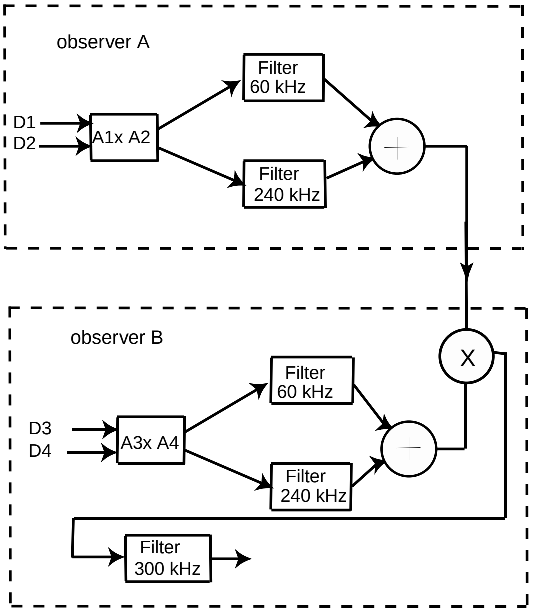

**Figure 6.3**: The detection diagram for simulation of entanglement swapping

5. Without frequency selection, beams 1, 2, 3 and 4 are all independent in the sense that the product of all four heterodyne signals factors.

We send beams 1 and 2 to observer A and beams 3 and 4 to observer B. As shown in Figure 6.2, observer A measures both beams 1 and 2, each consisting of superpositions of two orthogonally polarized fields with different frequencies. Similarly, observer B measures beams 3 and 4.

In this experiment, we modify the detection diagram used in Chapter 5 and use the symmetrical detection diagram as shown in Figure 6.3 to obtain a 300 kHz signal.

The detection diagram simulates entanglement swapping as follows: Suppose observer A orients the polarizations of local oscillator 1 ($E_{LO1}$) and local oscillator 2 ($E_{LO2}$) at arbitrary angles with unit vectors $\hat{\mathbf{e}}_{LO1}$ and $\hat{\mathbf{e}}_{LO2}$ respectively. The LO beams 1 and 2 mix with beams 1 and 2 and obtain beat signal amplitudes $A_1$ and $A_2$ as,

$$\begin{aligned} A_1 &= (\hat{\mathbf{e}}_{LO1}|\hat{\mathbf{V}}_1)\exp(-i\delta_V t) + (\hat{\mathbf{e}}_{LO1}|\hat{\mathbf{H}}_1)\exp(-i\delta_H t) \\ A_2 &= (\hat{\mathbf{e}}_{LO2}|\hat{\mathbf{V}}_2)\exp(-i\delta_V t) + (\hat{\mathbf{e}}_{LO2}|\hat{\mathbf{H}}_2)\exp(-i\delta_H t)\,. \end{aligned} \tag{6.5}$$

where $\delta_H = 2\pi \times 30\,kHz$ and $\delta_V = 2\pi \times 120\,kHz$. These signals are multiplied together and band pass filtered at 60 kHz and 240 kHz producing amplitudes given as

$$\begin{aligned} \gamma_{60kHz}(A_1, A_2) &\propto (\hat{\mathbf{e}}_{LO1}|\hat{\mathbf{H}}_1)(\hat{\mathbf{e}}_{LO2}|\hat{\mathbf{H}}_2) \\ \gamma_{240kHz}(A_1, A_2) &\propto (\hat{\mathbf{e}}_{LO1}|\hat{\mathbf{V}}_1)(\hat{\mathbf{e}}_{LO2}|\hat{\mathbf{V}}_2)\ . \end{aligned} \tag{6.6}$$

These two beat signal amplitudes denoted as $\gamma_{60kHz}$ ($\propto H_1H_2$) and $\gamma_{240kHz}$ ($\propto V_1V_2$)

are then added by using a summing amplifier as shown in the detection diagram. Note that the sum signal $S_{12}(t)$ is proportional to the projection

$$S_{12}(t) = (\hat{\mathbf{e}}_{LO1}, \hat{\mathbf{e}}_{LO2}|\phi_{cl}^{+}(t))_{12} \tag{6.7}$$

where

$$|\phi_{cl}^{+}(t))_{12} = \frac{1}{\sqrt{2}}[|H_1H_2)e^{i2\delta_H t} + |V_1V_2)e^{i2\delta_V t}] \tag{6.8}$$

is a time-dependent Bell state. Observer A sends the sum signal $S_{12}(t)$ to observer B.

Observer B, by using the same procedure as observer A and as shown in the detection diagram obtains the sum signal $S_{34}(t)$ which is proportional to the projection

$$S_{34}(t) = (\hat{\mathbf{e}}_{LO3}, \hat{\mathbf{e}}_{LO4}|\phi_{cl}^{+}(t))_{34} \tag{6.9}$$

where

$$|\phi_{cl}^{+}(t))_{34} = \frac{1}{\sqrt{2}}[|V_3V_4)e^{i2\delta_H t} + |H_3H_4)e^{i2\delta_V t}] \tag{6.10}$$

is a time-dependent Bell state. Note that the vertical and horizontal polarizations for observer B are interchanged with respect to those of observer A.

Observer B then uses the signal sent by observer A, $S_{12}(t)$, and multiplies this signal with the outcome of his projection measurement on beams 3 and 4, $S_{34}(t)$. This yields a signal amplitude at 300 kHz denoted as $\gamma_{300kHz}$, which is proportional to the projection

$$\gamma_{300kHz} \quad \propto \quad (\mathbf{\hat{e}}_{LO1}, \mathbf{\hat{e}}_{LO2}, \mathbf{\hat{e}}_{LO3}, \mathbf{\hat{e}}_{LO4}|\Psi^f_{cl}) \tag{6.11}$$

where

$$|\Psi^f_{cl}) \quad = \quad \frac{1}{\sqrt{2}}\left(|H_1)|H_2)|H_3)|H_4) + |V_1)|V_2)|V_3)|V_4)\right). \tag{6.12}$$

Note that $\gamma_{300kHz}$ has a time independent amplitude. The above equations are similar to Eq.(5.20) and Eq.(5.22) in Chapter 5. As discussed above, the detection diagram in Figure 6.3 functions similarly to the detection diagram used in chapter 5. However, the detection diagram in Figure 6.3 is more suitable for discussing classical simulation of entanglement swapping, and is more symmetrical than the scheme of Chapter 5.

It is clear that the classical entangled state $|\Psi^f_{cl})$ of Eq. (6.12) can demonstrate the simulation of entanglement swapping for the product pair $|\phi^+_{cl})_{12}|\phi^+_{cl})_{34}$. From the 300 kHz signal of Eq. (6.11) and the state of Eq. (6.12), the process of entanglement swapping can be viewed as follows: Suppose that observer A sets his polarization angles for LO1 and LO2 at +45° and +45° respectively. The projections $(\hat{e}^{45^\circ}_{LO1}|V_1)(\hat{e}^{45^\circ}_{LO2}|V_2)$ and $(\hat{e}^{45^\circ}_{LO1}|H_1)(\hat{e}^{45^\circ}_{LO2}|H_2)$ of Eq. (6.11) are obtained in Eq. (6.12). Analogous to the quantum projection $\langle\phi^+_{12}|\Psi^f\rangle$, after A's projection measurement $(\hat{e}^{45^\circ}_{LO1}|(\hat{e}^{45^\circ}_{LO2}|\Psi^f_{cl}) \propto \frac{1}{\sqrt{2}}[|H_3H_4) + |V_3V_4)]$, showing that observer B will measure the time independent entangled state $|\phi^+_{cl})_{34}$. This also implies that the remaining projections $(\hat{e}_{LO3}, \hat{e}_{LO4}|\phi^+_{cl})_{34}$ at 300 kHz of Eq. (6.11) by observer B will yield signals for beams 3 and 4 which are in a classical analog of the entangled state $|\phi^+_{cl})_{34}$. The maximum projection of this time-dependent Bell state $|\phi^+_{cl})_{34}$ is obtained by using the polarization angles of the LO3 and LO4 at 45° and 45° respectively.

Suppose now that the polarizations of LO3 and LO4 in observer B are at $-45°$ and 45° respectively, then the beat signal amplitude $\gamma_{60kHz}$ is proportional to -$V_3V_4$ and the $\gamma_{240kHz}$ is proportional to $H_3H_4$. The minus sign is due to the -45 polarization angle of the LO3. The summation of these two signals is proportional to the projection

$$(\hat{\mathbf{e}}_{LO3}^{-45^o}, \hat{\mathbf{e}}_{LO4}^{45°}|\phi_{cl}^{+}(t))_{34} \ . \tag{6.13}$$

Hence, by multiplying the summation signal of Eq. (6.13) with the summation signal from observer A, the beat signal $\gamma_{300kHz}$ is proportional to

$$\begin{aligned}\gamma_{300kHz} &\propto (\hat{\mathbf{e}}_{LO1}^{45°}, \hat{\mathbf{e}}_{LO2}^{45°}, \hat{\mathbf{e}}_{LO3}^{-45°}, \hat{\mathbf{e}}_{LO4}^{45°}|\Psi_{cl}^{f}) \\ &\propto \Big((\hat{\mathbf{e}}_{LO1}^{45°}|\hat{\mathbf{H}}_1)(\hat{\mathbf{e}}_{LO2}^{45°}|\hat{\mathbf{H}}_2)(\hat{\mathbf{e}}_{LO3}^{45°}|\hat{\mathbf{H}}_3)(\hat{\mathbf{e}}_{LO4}^{45°}|\hat{\mathbf{H}}_4) \\ &- (\hat{\mathbf{e}}_{LO1}^{45°}|\hat{\mathbf{V}}_1)(\hat{\mathbf{e}}_{LO2}^{45°}|\hat{\mathbf{V}}_2)(\hat{\mathbf{e}}_{LO3}^{45°}|\hat{\mathbf{V}}_3)(\hat{\mathbf{e}}_{LO4}^{45°}|\hat{\mathbf{V}}_4)\Big) \\ &= 0 \end{aligned} \tag{6.14}$$

where for the vertical component of beam 3 $(\hat{\mathbf{e}}_{LO3}^{-45°}|\hat{\mathbf{V}}_3)$ is replaced by -$(\hat{\mathbf{e}}_{LO3}^{45°}|\hat{\mathbf{V}}_3)$. The magnitude of horizontal components is equal to the magnitude of vertical components and so $\gamma_{300kHz}$ is zero. This is obvious since $(\hat{e}_{LO3}^{-45°}, \hat{e}_{LO4}^{-45°}|\phi_{cl}^{+})_{34} = 0$.

Figure 6.4(a) and (b) show the projection measurements of observer B corresponds to the classical analog of the Bell-state $|\phi_{cl}^{+})_{34}$. Since beams 3 and 4 are in a classical analog of the entangled state, $|\phi_{cl}^{+})_{34}$, then $\gamma_{300kHz}$ =0 due to a minus sign of the $-45^o$ polarization angle of the LO3 as shown in Eq. (6.14). By contrast, if beams 3 and 4 are in a classical analog of the entangled state, $|\phi_{cl}^{-})_{34}$, a nonzero signal amplitude at $\gamma_{300kHz}$ can only be measured when the polarizations of LO3 and LO4 are at $-45^o$ and $45^o$ respectively. If A sets his polarizations to $-45^\circ$, $45^\circ$, then B would measure $|\phi_{cl}^{-})_{34}$ and the strong and weak signals would be reversed.

As shown in the Figure 6.5, the signal amplitude at 300 kHz in Eq. (6.12) also implies that the state of beam 2, H(V), was swapped or teleported to beam 4, H(V) respectively, and similarly for the state of beam 1 to beam 3.

The classical simulation of entanglement swapping in this experimental arrangement can be attributed to the fact that the beam splitters BS2 and BS3 can produce identical copies of a classical light beam respectively. That is beam 1 copies to beam 3 through the BS2 and beam 2 copies to beam 4 through BS3.

Suppose now that we label a qubit by the frequency of an optical beam. Then the process of entanglement swapping can be viewed as swapping a qubit (for example an optical beam of frequency 120 kHz). The information of the polarization state in beam 2, V is swapped or teleported to another qubit (an optical beam of frequency 30 kHz) in beam 4, that is polarization state V.

## 6.3 Fundamental Technical Limitations of Full Entanglement Swapping

As discussed in [36] and also in Section 1.3.1, the use of a beamsplitter in coincidence detection schemes has restricted Bell state analysis to one Bell state $|\varphi_{cl}^{-})_{ij} = \frac{1}{\sqrt{2}}(|H_i)|V_j) - |V_i)|H_j))$ and hence reduces teleportation or swapping efficiency to 25%. The restriction of Bell state analysis is due to fundamental technical limitations of detection system which acts as a projective measurement on the desired state in the process of entanglement swapping or teleportation [28, 37, 64].

From the experimental setup in Figure 6.1 and detection diagram in Figure 6.3,

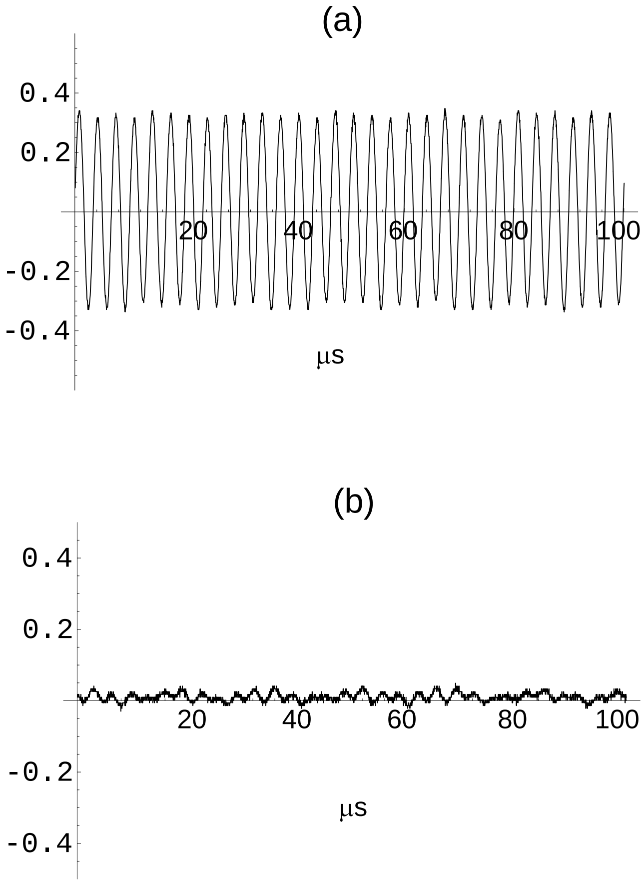

**Figure 6.4**: Entanglement swapping with classical fields. Observer A sets his local oscillator (LO) 1 and 2 polarizations at 45° and 45°, respectively, to select the Bell state $|\phi_{cl}^{+})_{12}$. Observer B's signal are then proportional to the projections of the corresponding Bell state $|\phi_{cl}^{+})_{34}$ (a) Observer B sets his LO3 and 4 polarizations at 45° and 45°, respectively, yielding a nonzero signal at 300 kHz. (b) Observer B sets his LO3 and 4 polarizations at $-45°$ and 45°, respectively, yielding a zero signal at 300 kHz.

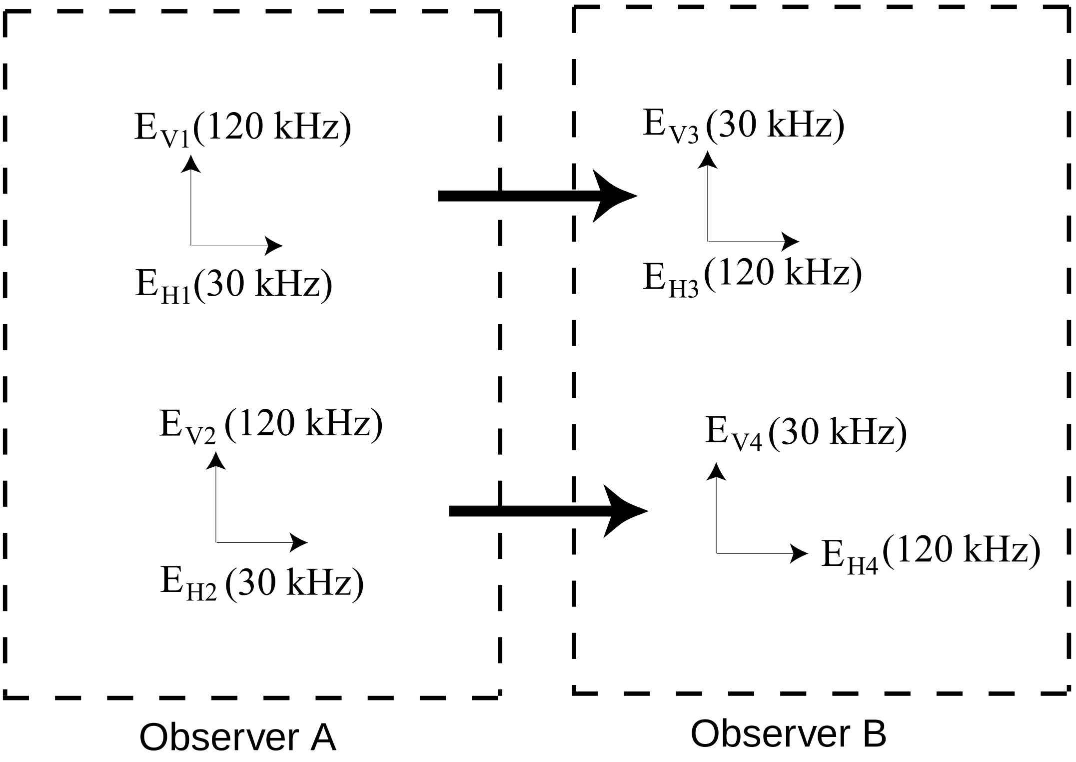

**Figure 6.5**: The polarization configurations of beams 1 and 2 for observer A and beams 3 and 4 for observer B. The polarization state in beam 1 is swapped to beam 3. Similarly for beam 2 to beam 4.

we are able to demonstrate classical analog of entanglement swapping for $|\phi_{cl}^{+})_{12}|\phi_{cl}^{+})_{34}$. We face the same technical problems as in the quantum optics experiment. So, the entanglement swapping or teleportation efficiency of our system is 25%. However, one can demonstrate entanglement swapping for the classical analog of the product pair $|\phi_{cl}^{-})_{12}|\phi_{cl}^{-})_{34}$ by applying a $\pi$ phase shift electronically after the band pass filtering at 240 kHz for observers A and B or by changing the polarizations of the LO1 and LO3 to -45° (anti-clockwise direction referred to the polarization configurations in the setup).

In the following section, we simulate the type of entanglement swapping for others product pairs such as $|\phi_{cl}^{-})_{12}|\phi_{cl}^{-})_{34}$, $|\varphi_{cl}^{+})_{12}|\varphi_{cl}^{+})_{34}$ and $|\varphi_{cl}^{-})_{12}|\varphi_{cl}^{-})_{34}$.

### 6.3.1 Entanglement Swapping for the Product Pair $|\phi_{cl}^{-})_{12}|\phi_{cl}^{-})_{34}$ with Classical Fields

For the product pairs $|\phi_{cl}^{-})_{12}|\phi_{cl}^{-})_{34}$, the polarizations of the LO1 and LO2 beams are at $-45^o$ and $45^o$ respectively and also the LO3 and LO4 beams are at $-45^o$ and $45^o$ respectively. Thus, the signal amplitude $\gamma_{300kHz}$ is proportional to the projection

$$\gamma_{300kHz} \quad \propto \quad (\hat{\mathbf{e}}_{LO1}^{-45^\circ}, \hat{\mathbf{e}}_{LO2}^{+45^\circ}, \hat{\mathbf{e}}_{LO3}^{-45^\circ}, \hat{\mathbf{e}}_{LO4}^{+45^\circ}|\Psi_{cl}^{f}) \tag{6.15}$$

Eq. (6.15) shows that after A's projection measurement on the Bell state $|\phi_{cl}^{-})_{12}$, the projection $(\hat{e}_{LO1}^{-45^\circ}|(\hat{e}_{LO2}^{+45^\circ}|\Psi_{cl}^{f}) \propto \frac{1}{\sqrt{2}}[|H_3H_4) - |V_3V_4)]$, showing that observer B will measure the entangled state $|\phi_{cl}^{-})_{34}$. This corresponds to projection measurements of $(\hat{\mathbf{e}}_{LO1}^{-45^o}, \hat{\mathbf{e}}_{LO2}^{+45^\circ}|\phi_{cl}^{-}(t))_{12}$ of observer A followed by the $(\hat{\mathbf{e}}_{LO3}^{-45^\circ}, \hat{\mathbf{e}}_{LO4}^{+45^\circ}|\phi_{cl}^{-}(t))_{23}$ of observer B , yielding a nonzero signal amplitude $\gamma_{300kHz}$ of Eq. (6.15) as shown in Figure 6.6(a). The zero amplitude of $\gamma_{300kHz}$ for the projection measurements of

$(\hat{\mathbf{e}}_{LO1}^{-45^\circ}, \hat{\mathbf{e}}_{LO2}^{+45^\circ}|\phi_{cl}^{+}(t))_{12}$ of observer A followed by the $(\hat{\mathbf{e}}_{LO3}^{+45^\circ}, \hat{\mathbf{e}}_{LO4}^{+45^\circ}|\phi_{cl}^{-}(t))_{34}$ of observer B are due to the minus sign introduced by the projection $(\hat{\mathbf{e}}_{LO3}^{+45^\circ}, \hat{\mathbf{e}}_{LO4}^{+45^\circ}|\phi_{cl}^{-}(t))_{34}$ as shown in Figure 6.6(b). This also indicates that beams 3 and 4 are in the state $|\phi_{cl}^{-})_{34}$ not the state $|\phi_{cl}^{+})_{34}$.

### 6.3.2 Entanglement Swapping for the Product Pair $|\varphi_{cl}^{+})_{12}|\varphi_{cl}^{+})_{34}$ with Classical Fields

By using a similar technique, entanglement swapping for the pair $|\varphi_{cl}^{+})_{12}|\varphi_{cl}^{+})_{34}$ can be implemented. Inserting a half-wave plate at $45^o$ in the lower arm of the outputs of the BS1 to interchange the H(V)$\rightleftharpoons$ V(H) of beams 1 and 3, the signal amplitude $\gamma_{300kHz}$ is given by

$$\gamma_{300kHz} \;\propto\; (\hat{\mathbf{e}}_{LO1}, \hat{\mathbf{e}}_{LO2}, \hat{\mathbf{e}}_{LO3}, \hat{\mathbf{e}}_{LO4}|\Psi_{cl}'^{f}) \tag{6.16}$$

where now the final state is

$$|\Psi_{cl}'^{f}) \;=\; \frac{1}{\sqrt{2}}\left(|H_1)|V_2)|H_3)|V_4) + |V_1)|H_2)|V_3)|H_4)\,.\right) \tag{6.17}$$

Suppose A sets the polarization angles of the LO1 and LO2 at 45°. Eq. (6.17) shows that A's projection measurement is equivalent to selecting the Bell state $|\varphi_{cl}^{+})_{12}$. The projection $(\hat{e}_{LO1}^{+45^\circ}|(\hat{e}_{LO2}^{+45^\circ}|\Psi_{cl}'^{f}) \propto \frac{1}{\sqrt{2}}[|H_3V_4)+|V_3H_4)]$, shows that observer B will measure the entangled state $|\varphi_{cl}^{+})_{34}$.

Figure 6.7(a) shows that the projection measurements of the $(\hat{\mathbf{e}}_{LO1}^{+45^\circ}, \hat{\mathbf{e}}_{LO2}^{+45^\circ}|\varphi_{cl}^{+}(t))_{12}$ of observer A followed by $(\hat{\mathbf{e}}_{LO3}^{+45^\circ}, \hat{\mathbf{e}}_{LO4}^{+45^\circ}|\varphi_{cl}^{+}(t))_{34}$ for observer B yields nonzero signal amplitude at 300 kHz as expected from Eq. (6.16). The nonzero signal for $(\hat{\mathbf{e}}_{LO3}^{+45^\circ}, \hat{\mathbf{e}}_{LO4}^{+45^\circ}|\varphi_{cl}^{+}(t))_{34}$ shows that beams 3 and 4 are in the state $|\varphi_{cl}^{+})_{34}$. Fig-

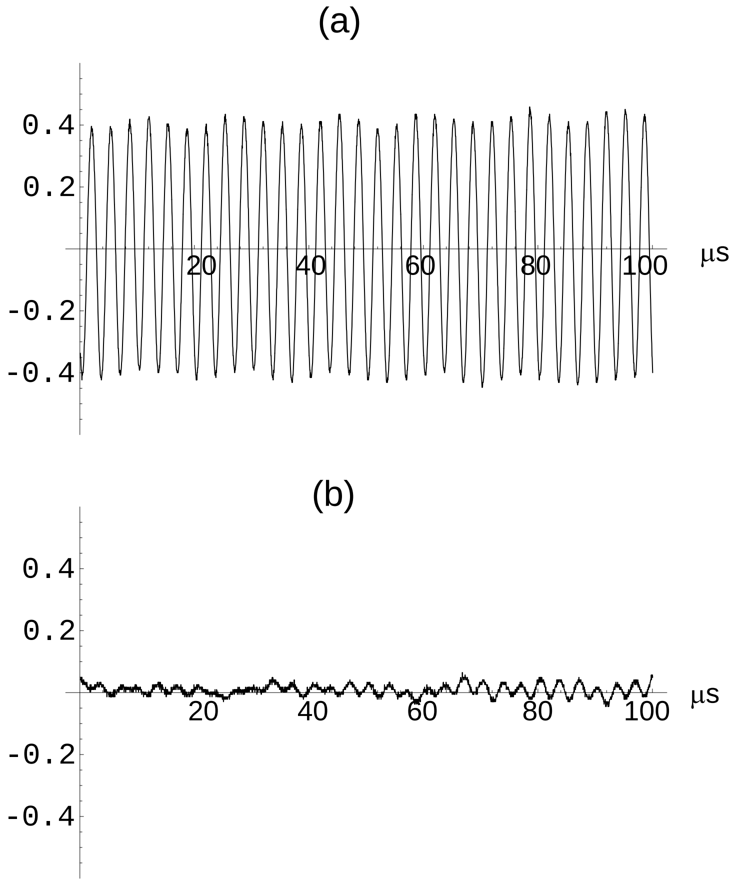

**Figure 6.6**: Entanglement swapping with classical fields. Observer A sets his local oscillator (LO) 1 and 2 polarizations at −45° and 45°, respectively, to select the Bell state $|\phi_{cl}^{-})_{12}$. Observer B's signal are then proportional to the projections of the corresponding Bell state $|\phi_{cl}^{-})_{34}$ (a) Observer B sets his LO3 and 4 polarizations at −45° and 45°, respectively, yielding a nonzero signal at 300 kHz. (b) Observer B sets his LO3 and 4 polarizations at 45° and 45°, respectively, yielding a zero signal at 300 kHz.

ure 6.7(b) shows that the projection measurements $(\hat{\mathbf{e}}_{LO1}^{+45^\circ}, \hat{\mathbf{e}}_{LO2}^{+45^\circ}|\varphi_{cl}^{+}(t))_{12}$ of observer A followed by the $(\hat{\mathbf{e}}_{LO3}^{-45^\circ}, \hat{\mathbf{e}}_{LO4}^{+45^\circ}|\varphi_{cl}^{+}(t))_{34}$ of observer B yields a zero signal amplitude at 300 kHz, because of the minus sign introduced by the polarization of the LO3 in Eq. (6.16). Note that this will not be the case if beams 3 and 4 are in the state $|\varphi_{cl}^{-})_{34}$ not $|\varphi_{cl}^{+})_{34}$.

### 6.3.3 Entanglement Swapping for the Product Pair $|\varphi_{cl}^{-})_{12}|\varphi_{cl}^{-})_{34}$ with Classical Fields

Finally, for the pairs $|\varphi_{cl}^{-})_{12}|\varphi_{cl}^{-})_{34}$, a half-wave plate at $45^o$ is again inserted in the lower arm of BS1 to interchange the H and V polarizations of beams 1 and 3. In this case, as before the signal amplitude $\gamma_{300kHz}$ is proportional to the projection

$$\gamma_{300kHz} \;\propto\; (\hat{\mathbf{e}}_{LO1}, \hat{\mathbf{e}}_{LO2}, \hat{\mathbf{e}}_{LO3}, \hat{\mathbf{e}}_{LO4}|\Psi_{cl}'^{f})\,. \tag{6.18}$$

Then, the polarizations of the LO1 and LO2 beams are rotated at $-45^o$ and $45^o$ respectively. Eq. (6.18) shows that after A's projection measurement on the Bell state $|\varphi_{cl}^{-})_{12}$, the projection $(\hat{e}_{LO1}^{-45^\circ}|(\hat{e}_{LO2}^{+45^\circ}|\Psi'^{f}) \propto \frac{1}{\sqrt{2}}[|H_3V_4) - |V_3H_4)]$, showing that observer B will measure the entangled state $|\varphi_{cl}^{-})_{34}$.

Figure 6.8(a) shows that the projection measurement $(\hat{\mathbf{e}}_{LO1}^{-45^o}, \hat{\mathbf{e}}_{LO2}^{+45^\circ}|$ of observer A followed by the $(\hat{\mathbf{e}}_{LO3}^{-45^\circ}, \hat{\mathbf{e}}_{LO4}^{+45^o}|$ of observer B, yielding nonzero signal amplitude at 300 kHz of Eq. (6.18). Figure 6.8(b) shows that beams 3 and 4 are not in the state $|\varphi_{cl}^{+})_{34}$. The projection measurements $(\hat{\mathbf{e}}_{LO1}^{-45^\circ}, \hat{\mathbf{e}}_{LO2}^{+45^\circ}|$ of observer A followed by the $(\hat{\mathbf{e}}_{LO3}^{+45^\circ}, \hat{\mathbf{e}}_{LO4}^{+45^\circ}|$ of observer B yields a zero signal amplitude at 300 kHz of Eq. (6.18) because of the minus sign introduced by the projection $(\hat{\mathbf{e}}_{LO3}^{+45^\circ}, \hat{\mathbf{e}}_{LO4}^{+45^\circ}|\varphi_{cl}^{-}(t))_{34}$.

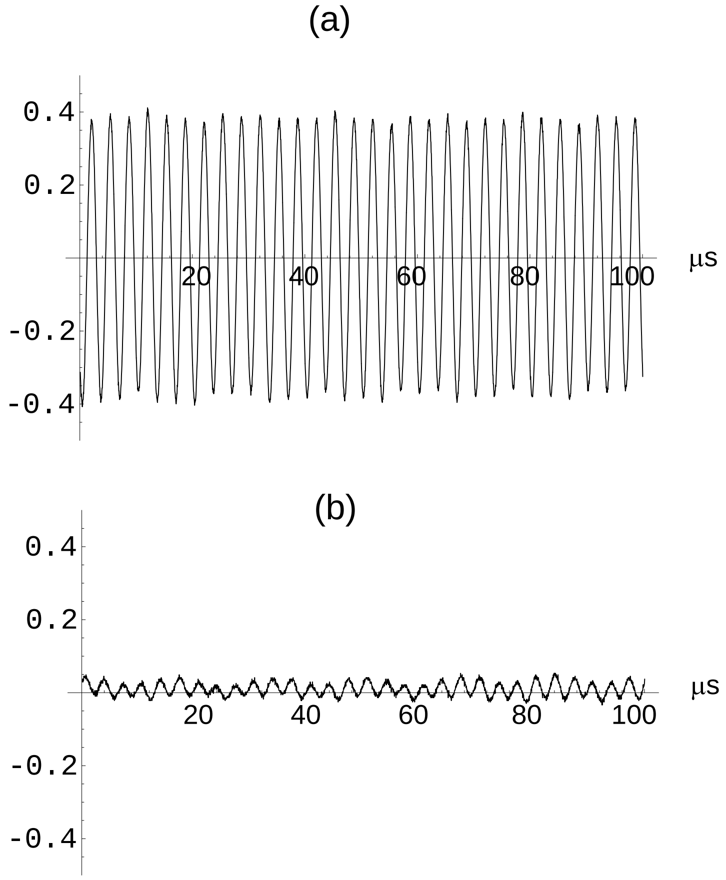

**Figure 6.7**: Entanglement swapping with classical fields. Observer A sets his local oscillator (LO) 1 and 2 polarizations at 45° and 45°, respectively, to select the Bell state $|\varphi_{cl}^{+})_{12}$. Observer B's signal are then proportional to the projections of the corresponding Bell state $|\varphi_{cl}^{+})_{34}$ (a) Observer B sets his LO3 and 4 polarizations at 45° and 45°, respectively, yielding a nonzero signal at 300 kHz. (b) Observer B sets his LO3 and 4 polarizations at $-45°$ and 45°, respectively, yielding a zero signal at 300 kHz.

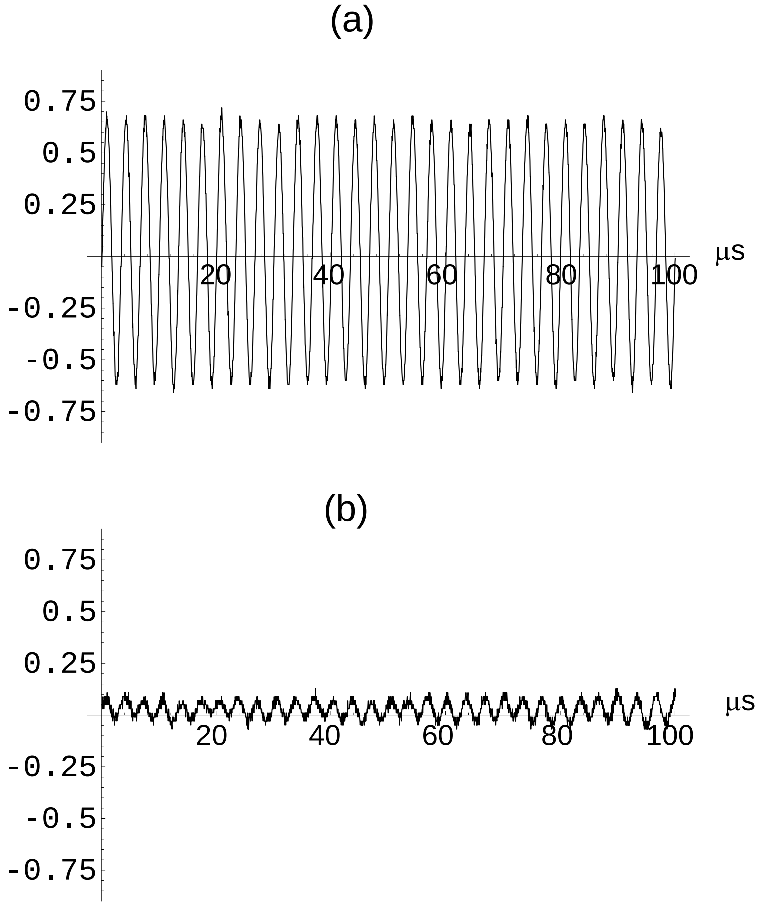

**Figure 6.8**: Entanglement swapping with classical fields. Observer A sets his local oscillator (LO) 1 and 2 polarizations at −45° and 45°, respectively, to select the Bell state $|\varphi_{cl}^{-})_{12}$. Observer B's signal are then proportional to the projections of the corresponding Bell state $|\varphi_{cl}^{-})_{34}$ (a) Observer B sets his LO3 and 4 polarizations at −45° and 45°, respectively, yielding a nonzero signal at 300 kHz. (b) Observer B sets his LO3 and 4 polarizations at 45° and 45°, respectively, yielding a zero signal at 300 kHz.

## 6.4 Discussion

In this chapter, we have demonstrated an analog of nonlocal teleportation of entanglement using a type of entanglement swapping based on classical wave optics. We are able to demonstrate entanglement swapping in a projection measurement of four-photon entanglement by using classical fields. Even though the classical wave system does not exhibit wave-particle duality properties, the technique demonstrates a type of entanglement swapping which is similar to generalized lock-in detection with two frequencies. In simulating entanglement swapping, we find a limitation in the basis of Bell states that can be swapped without changing the experimental configuration. This is similar to the limitation encountered in the quantum experiments [64]. However, by changing the configuration of the experiment and the polarizations of the LO beams, we are able to simulate entanglement swapping for all four product pairs which includes the projection measurements of four Bell states.

# Chapter 7

# Two-Field Correlations With Noise

## 7.1 Overview

In the previous Chapters 4 and 5, we simulated the quantum entanglement of up to four-particles by using *stable* classical fields. We have demonstrated that the techniques can formally reproduce the quantum correlations arising from multi-particle interferences including the violation of Bell's inequality and GHZ entanglement. However, for Bell's theorem to be applicable and for demonstrating violation of local hidden variable theory, the wave-particle duality is essential. Further, our multiplication signals are a stable oscillatory sinusoidal waves so that probability language is not applicable.

In this chapter, we develop a classical noise system to simulate in part particle-like behavior. We first mix a noise field and a classical stable field with parallel optical polarizations to produce an anti-correlated random interference signal. This anti-correlated signal in two spatially separated detectors is used to simulate the particle character of single photon experiments.

Following the single particle simulations, we extend this method to a two-particle system by using a noise field and a stable field with orthogonal polarizations. We measure an EPR nonlocal correlation function $\langle \mathcal{A}_1 \mathcal{B}_2 \rangle = -\cos 2(\theta_1 - \theta_2)$ of two observers $\mathcal{A}$ and $\mathcal{B}$ with their analyzers oriented along directions $\theta_1$ and $\theta_2$ respectively. Our setup is able to reproduce the measurement of the quantum mechanical correlation function as well as the random noise in each detector. Our classical system is able to simulate in part the wave-particle duality properties of a two-particle quantum system. We also demonstrate the ability of our optical noise system to reproduce the violation of Bell's Inequality(1965) [9].

First, we will discuss the derivation of the quantum mechanical correlation function of two spatially separated measuring devices in a two-photon system.

### 7.1.1 Derivation of the Correlation Function of Two Observers

In a quantum mechanical treatment of Bell's theorem for a two-photon system in an polarization-entangled state $|\psi^{\pm}\rangle = \frac{1}{\sqrt{2}}(|H_1V_2\rangle \pm |V_1H_2\rangle)$, the two entangled photons are sent to two spatially separated measuring devices A and B. Device A is an analyzer to test the linear polarization of the incoming photon. When analyzer A is oriented along the polarization angle $\theta_1$, the polarization state of the incoming photon is projected onto the state

$$|\theta_{1//}\rangle \quad = \quad \cos\theta_1|H_1\rangle + \sin\theta_1|V_1\rangle \tag{7.1}$$

where H, V are the horizontal and vertical axes. The corresponding orthogonal polarization state is given by

$$|\theta_{1\perp}\rangle \quad = \quad -\sin\theta_1|H_1\rangle + \cos\theta_1|V_1\rangle \tag{7.2}$$

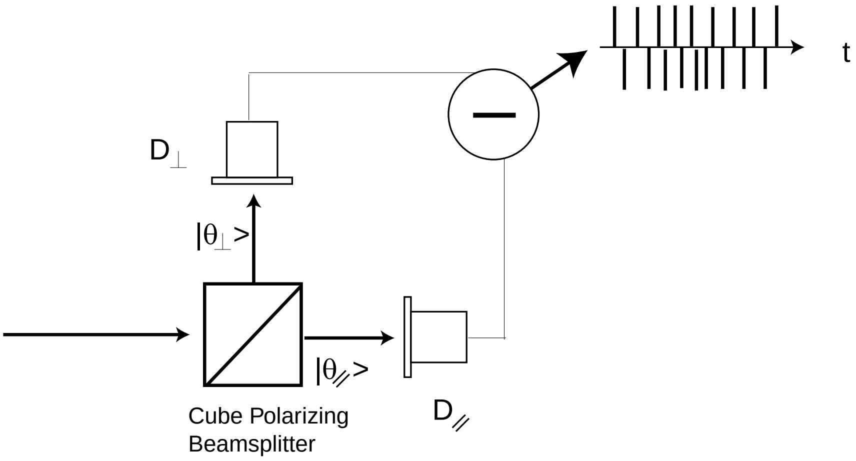

**Figure 7.1**: The detection scheme for measuring the quantum operator A or B . The detectors $D_{//}$ and $D_\perp$ are placed at each port of the cube polarizing beamsplitter and their signals are subtracted from each other

We take the operator associated with analyzer A to be represented as $A_1$ which is written in the form [66]

$$\begin{aligned} A_1 &= 2|\theta_{1//}\rangle\langle\theta_{1//}| - \big(|\theta_{1//}\rangle\langle\theta_{1//}| + |\theta_{1\perp}\rangle\langle\theta_{1\perp}|\big) \\ &= |\theta_{1//}\rangle\langle\theta_{1//}| - |\theta_{1\perp}\rangle\langle\theta_{1\perp}| \,. \end{aligned} \tag{7.3}$$

The operator $A_1$ then has eigenvalues ±1, i.e.,

$$\begin{aligned} A_1|\theta_{1//}\rangle &= 1\,|\theta_{1//}\rangle \\ A_1|\theta_{1\perp}\rangle &= -1\,|\theta_{1\perp}\rangle \,. \end{aligned} \tag{7.4}$$

depending on whether the photon is transmitted (//) or rejected ($\perp$) by the analyzer. Similarly, we define the operator $B_2$ for the analyzer B oriented along polarization angle $\theta_2$.

One should note that the operator $A_1$ with eigenvalues ±1 can be measured by using the detection scheme shown in Figure 7.1. Two detectors are placed at the two output ports of a cube polarizer beamsplitter. The output currents are subtracted from each other. The arrangement of this detection scheme corresponds to the measurement of operator $A_1$, that is the subtraction of the transmitted signal with projection $|\theta_{1//}\rangle\langle\theta_{1//}|$ and the reflected signal with projection $|\theta_{1\perp}\rangle\langle\theta_{1\perp}|$.

For a beam of photons incident on the polarizer, a photon goes through the polarizer and registers a 'click' or produces signal at detector $D_{//}$ and zero signal at detector $D_{\perp}$, then the subtractor yields positive signal as $D_{//} - D_{\perp} > 0$. If a second photon reflects from the polarizer and goes to the detector $D_{\perp}$, producing nonzero signal in detector $D_{\perp}$ and zero signal in detector $D_{//}$, then the subtractor yields negative signal as $D_{//} - D_{\perp} < 0$. For a certain amount of time, the subtractor records the random positive and negative spikes corresponding to the eigenvalues $\pm$ 1 of operator $A_1$ as shown in Figure 7.1. The incoming photon can be in the superposition $|\theta_{1//}\rangle$ and $|\theta_{1\perp}\rangle$ corresponding to the operator $A_1$ with eigenvalues +1 and -1 respectively. Hence, as the time elapses, device A records a series of discrete random values +1 and -1. Then, for a state with equal probability of // and $\perp$ photons, the mean value of $\langle A_1\rangle$ is zero and similarly $\langle B_2\rangle = 0$. The wave character of the operator $A_1$ is recognized as interference of the outcomes $\pm 1$ due to the linear superposition of the projected states $|\theta_{1//}\rangle$ and $|\theta_{1\perp}\rangle$. The particle character of the operator $A_1$ is the discreteness of random values +1 and -1. The correlation functions of the product of two operators $A_1$ and $B_2$ can be measured by using the same detection schemes for observers A and B and multiplying the output signals together.

The correlation functions for the state $|\psi^{\pm}\rangle = \frac{1}{\sqrt{2}}\left(|H_1V_2\rangle \pm |V_1H_2\rangle\right)$ are measured for A and B and are given by

$$C_q(\theta_1,\theta_2) = \langle\psi^{\pm}|A_1B_2|\psi^{\pm}\rangle = -\cos 2(\theta_1 \pm \theta_2)\,. \tag{7.5}$$

Eq. (7.5) is sometimes referred to as the expectation value of the product of operators $A_1$ and $B_2$. For the other two Bell states, $|\varphi^{\pm}\rangle = \frac{1}{\sqrt{2}}(|H_1H_2\rangle \pm |V_1V_2\rangle)$, the correlation functions are given by

$$C_q(\theta_1,\theta_2) = \langle\varphi^{\pm}|A_1B_2|\varphi^{\pm}\rangle = \cos 2(\theta_1 \mp \theta_2)\,. \tag{7.6}$$

Classical simulation models of wave particle duality have been attempted before by mixing a stable field and a noise field. The randomness of the eigenvalues of operators $A_1$ and $B_2$ were demonstrated by using radio frequency model [67] in an attempt to simulate nonlocal correlation of EPR experiment. However, this model only demonstrated the particle-like features of the operators $A_1$ and $B_2$, and obtained the expectation value in the form

$$\langle A_1B_2\rangle \;=\; 1 - 2\frac{\theta_1-\theta_2}{\pi}\,, \tag{7.7}$$

as predicted from a non-quantum model of EPR correlation [67]. The reason is this model digitized the random noise signals in $A_1$ and $B_2$ and hence erased the phase information which is in the wave interference character of the system. This is predicted by the complementary principle in quantum interference; once the particle character of a quantum system is revealed, the wave character of the system is lost.

In the following section, we give a discussion of the experimental simulation of the particle character of single photon experiment by using a noise field and a stable field. Then, we extend the method to two particle correlations.

### 7.1.2 Single-Field Experiments

In a single photon experiment, when a photon is incident on a 50-50 beamsplitter, it will be reflected or transmitted. If a detector is placed on each output port of the beamsplitter, the signal in the two detectors $D_1$ and $D_2$ are anti-correlated. This means that if one detector '*clicks*′ then the other one is silent and does not '*click*′.

In this section, we can simulate single photon experiments by measuring the anti-correlated noise amplitudes from two spatially separated detectors. As shown in Figure 7.2, a vertically polarized noise field and a vertically polarized stable field are used to simulate the particle-like behaviour of a single photon. We use a beamsplitter to combine the noise field $\mathbf{E}_N(t) = E_n(t)e^{-i(\omega+\Omega)t-i\phi(t)}$ and a stable field $\mathbf{E}_S(t) = E_s e^{-i(\omega+\Omega)t}$ where $\omega$ is optical frequency and $\Omega$ is modulation frequency at 110 MHz of acoustic-optic (AO) modulator and $\phi(t)$ is the random phase noise obtained from a tunable AO. The interference of these two fields in one detector, $D_1(t)$, yields the beat signal as,

$$\begin{aligned} \mathcal{A}_1(t) &= |E_s e^{-i(\omega+\Omega)t} + E_n(t)e^{-i(\omega+\Omega)t-i\phi(t)}|^2 \\ &\propto 2\Re[E_n^* E_s]\cos(\phi(t)) \end{aligned} \tag{7.8}$$

and similarly for the beat signal at the second detector, $D_2(t)$, is,

$$\mathcal{A}_2(t) \propto -2\Re[E_n^* E_s]\cos(\phi(t)) \tag{7.9}$$

where the minus sign is due to the $\pi$-phase shifted of the beamsplitter caused by a electromagnetic field reflected from the medium of higher refractive index to the

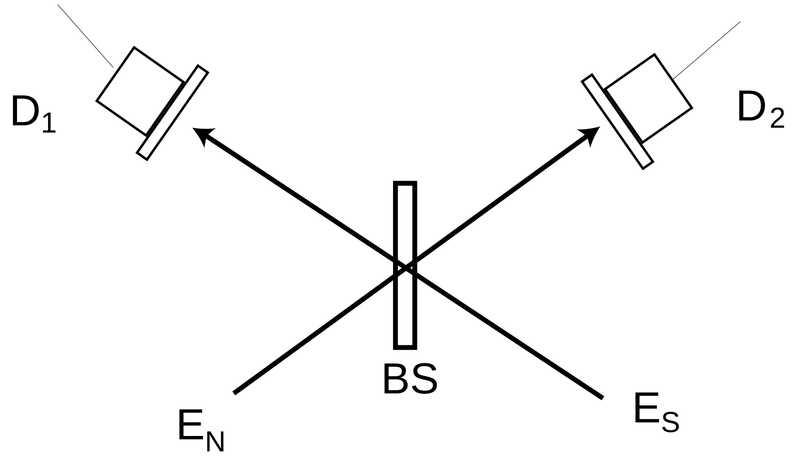

**Figure 7.2**: The setup for simulating single photon experiment by using a stable vertically polarized field and a noise vertically polarized field.

medium of lower refractive index.

The correlation $C(\tau)=\langle\mathcal{A}_1(t)\mathcal{A}_2(t+\tau)\rangle$ between these two detectors is anti-correlated as shown in Figure 7.3. The product of these two detectors is always negative value when $\tau=0$. This result is proportional to the intensity of the noise field $|E_n|^2$ and analogous to the $\delta-$correlation function for shot noise in quantum optics experiments. The negative sign shows that the ports of the beamsplitter are anti-correlated as expected.

### 7.1.3 Two-Field Correlations With Noise

In this section, we give a description of the experimental simulation of two-particle entanglement with noise as shown in Figure 7.4. We use a noise field and a stable field as in the previous section, but employ orthogonal polarizations. As shown below, the two beams are correlated as in two particles quantum mechanical experiments.

We use a beamsplitter to combine a noise field with horizontal polarization $H_N$

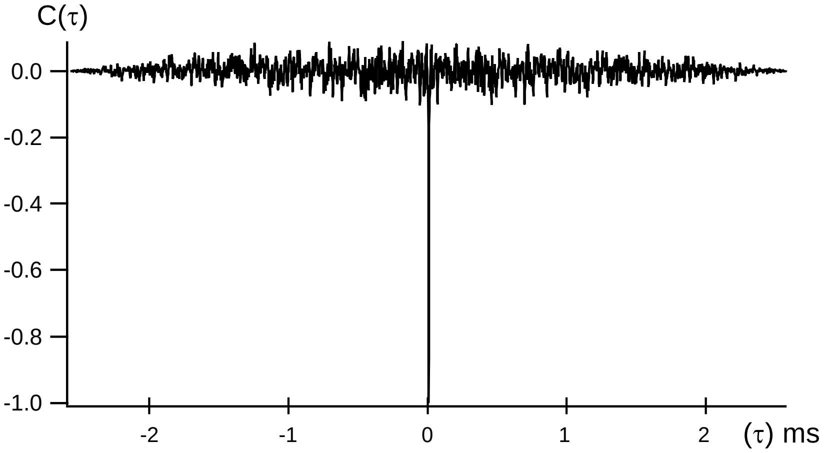

**Figure 7.3**: The correlation function $C(\tau) = \frac{\langle \mathcal{A}_1(t)\mathcal{A}_2(t+\tau)\rangle}{\langle \mathcal{A}_1(t)\mathcal{A}_2(t)\rangle}$ of the beat signals in detectors 1 and 2.

and a stable field with vertical polarization $V_S$. The output ports of the beamsplitter produce two spatially separated beams 1 and 2 with each consisting of superposition of horizontal and vertical components. A $\lambda/2$ wave plate at $0°$ is inserted in beam 2 to induce a $\pi$-phase shift between V and H components. The noise field and the stable field in beam 1 are transformed by the $\lambda/4$ plate 1 at $45°$ to left and right circular polarized fields respectively,

$$\begin{aligned} H_{N1} \quad &\rightarrow \quad \mathcal{E}_L = \frac{1}{\sqrt{2}}(\hat{H}_{N1} - i\hat{V}_{N1})e^{-i(\omega+\Omega)t - i\phi(t)} \\ V_{S1} \quad &\rightarrow \quad \mathcal{E}_R = \frac{1}{\sqrt{2}}(-i\hat{H}_{S1} + \hat{V}_{S1})e^{-i(\omega+\Omega)t} \,. \end{aligned} \tag{7.10}$$

Suppose now we use the same detection diagram for measuring the quantum operator A as shown in Figure 7.1 for our classical system. Then the field $\mathcal{E}_1 = (\mathcal{E}_R \pm \mathcal{E}_L)$ is projected onto $\hat{e}_1 = \cos\theta_1\,\hat{H} + \sin\theta_1\,\hat{V}$ of the analyzer 1 and yields the interference

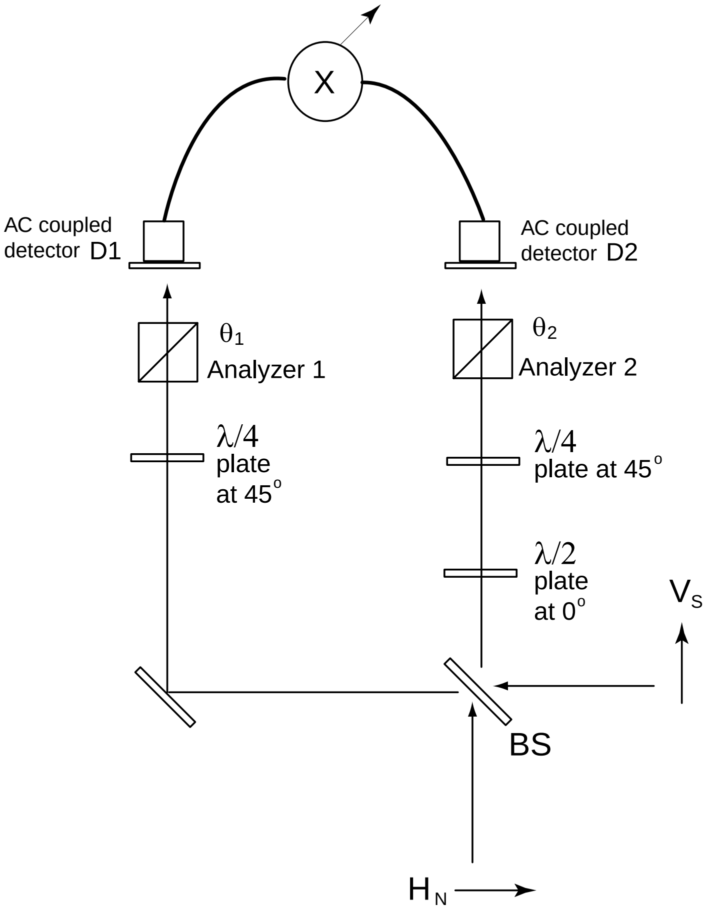

**Figure 7.4**: The experimental setup for noise simulation of two-particle entanglement. Measurement devices in each beam consist of a $\lambda/4$ plate and an analyzer placed before a detector. The two spatially separated beams consist of a superposition of a classical stable field with vertical polarization $V_S$ and a classical noise field with horizontal polarization $H_N$.

of these two fields in detector $D_{1//}$ as

$$\begin{aligned} D_{1//} &= |(\mathcal{E}_R + \mathcal{E}_L) \cdot \hat{e}_1|^2 \\ &\propto \frac{1}{2}|H_{N1}|^2 + \frac{1}{2}|V_{S1}|^2 + \Re[H^*_{N1} V_{S1}] \sin(2\theta_1 + \phi(t)) \end{aligned} \tag{7.11}$$

where the first two terms are intensities of the noise field and stable field so contributes the DC terms of Eq. (7.11) and the last term is the interference term with the random noise $\phi(t)$ so contributes the AC term of Eq. (7.11).

Similarly, for the detector $D_{1\perp}$ where $\theta_1$ changes to $\theta_1 + \frac{\pi}{2}$, the interference beat signal is

$$D_{1\perp} \propto \frac{1}{2}|H_{N1}|^2 + \frac{1}{2}|V_{S1}|^2 - \Re[H^*_{N1} V_{S1}] \sin(2\theta_1 + \phi(t))\,. \tag{7.12}$$

where the first two terms are DC terms and the last term is the AC term. Then, the subtractor yields the beat signal

$$D_{1//} - D_{1\perp} \propto 2\sin(2\theta_1 + \phi(t)) \tag{7.13}$$

where the intensities of the noise field $|H_{N1}|^2$ and the stable field $|V_{S1}|^2$ are subtracted. Similarly for the observer B measures $D_{2//} - D_{2\perp} \propto -2\sin(2\theta_2 + \phi(t))$.

One can see that the positive signal in detector $D_{1//}$ of Eq. (7.11) will yield negative signal with the same amplitude in detector $D_{1\perp}$ of Eq. (7.12) and vice versa, so the AC part of the subtracted signal $D_{1//} - D_{1\perp}$ is just twice the beat signal from one detector $\sin(2\theta_1 + \phi(t))$. The beat signal in the subtractor shows a striking similarity to the subtractor in the quantum version of the detection scheme for operator $A_1$ as discussed in Section 7.1.1. For arbitrary random phase $\phi(t)$, the signal $\sin(2\theta_1 + \phi(t))$ produces a positive amplitude corresponding to the eigenvalue +1 of operator $A_1$ of detecting a photon with projection $|\theta_{1//}\rangle\langle\theta_{1//}|$ and similarly a negative amplitude of the signal $\sin(2\theta_1 + \phi(t))$ corresponding to the eigenvalue -1 of operator $A_1$ of detecting a photon with projection $|\theta_{1\perp}\rangle\langle\theta_{1\perp}|$. Hence, the average value of the signal $\sin(2\theta_1 + \phi(t))$ is zero as expected for operator $A_1$ where $\langle A_1\rangle = 0$.

In our classical setup, one detector is used to simulate operator $A_1$. Detector 1 is ac coupled to obtain a beat signal proportional to $\sin(2\theta_1 + \phi(t))$. This beat signal in detector 1 is anti-correlated to the beam 2 interference in detector 2 which is $\propto -\sin(2\theta_2 + \phi(t))$ where the minus sign is due to the $\pi$-phase shift of the $\lambda/2$ wave plate at 0°. The random and anti-correlated noise amplitudes from detectors 1 and 2 are multiplied by using an analog multiplier. We measure the mean value of this multiplied anti-correlation signal and obtain the correlation function $C_{cl}(\theta_1, \theta_2) = -\cos 2(\theta_1 - \theta_2)$ analogous to the predictions of quantum mechanics.

In this classical model, we are able to reproduce the measurement of $\langle\mathcal{A}_1\mathcal{B}_2\rangle$ as predicted by quantum mechanics because our system does not erase the phase information of $2\theta_1 + \phi(t)$ but instead multiplies or correlates it with the another spatially separated beam containing the phase information of $2\theta_2 + \phi(t)$. The success of this measurement can be attributed to our detection system being able to keep both duality properties of random noise amplitudes that simulate the positive or negative values of the operators $A_1$ and $B_2$, and the phase information.

In order to simulate a Bell's theorem argument on two observers $A_1$ and $B_2$ in an anti-correlated polarization entangled state $|\psi^-\rangle$, the random noise amplitudes in detectors $\mathcal{A}$ and $\mathcal{B}$ can be interpreted as follows: When both analyzers are in parallel, the high (low) of the beat noise amplitude in detector $\mathcal{A}$ corresponds to eigenvalues $A_1 = +1$(-1) and hence simulates detection of a polarized photon with

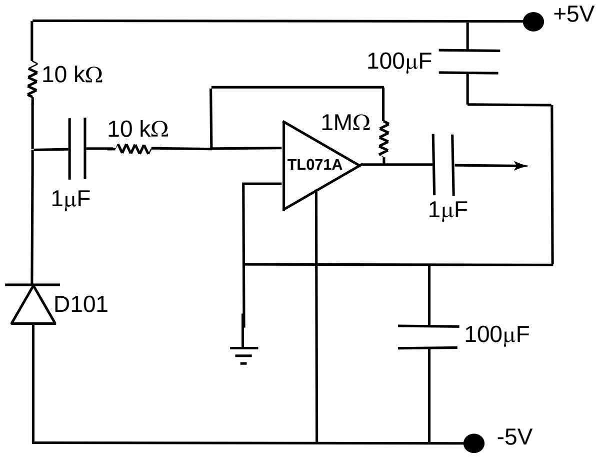

**Figure 7.5**: The circuit diagram for noise diode D101.

polarization $H_1(V_1)$. Simultaneously the low (high) in detector $\mathcal{B}$ corresponds to eigenvalues $B_2$ = -1(+1) and hence simulates detection of a polarized photon with polarization $V_2(H_2)$.

In the following sections, we show how the noise generator is built and tested in an optical system, and then describe our results.

## 7.2 Detection Apparatus

In this chapter, we use a noise generator and a DC voltage supply to modulate the frequency of an acoustic optic modulator(AO). The DC offset provides the frequency shift of a optical beam at 110 MHz. The noise amplitude ±0.5 V is added to the DC offset through a summing amplifier. The noise causes the AO to randomly modulate the phase of the optical field. Two photo-detectors are used to detect the interference noise signals in two regions. The detectors used are the same as in the previous experiments. The noise signals from the two detectors are multiplied by using an analog multiplier. The output of the analog multiplier is amplified and then

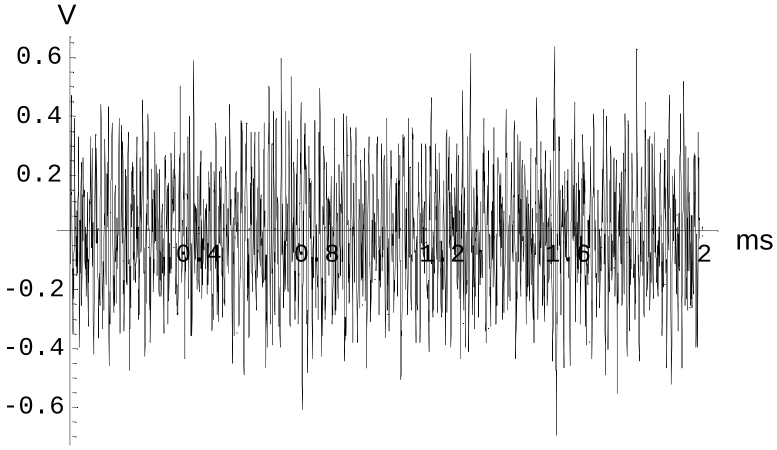

**Figure 7.6**: The random electronic noise from the noise circuit.

read by a oscilloscope. In this experiment, the analog multiplier is not connected through any band pass filters. The multiplied interference noise amplitude from both detectors is then recorded by using a LabView program interfaced with the oscilloscope.

### 7.2.1 Random Noise Generator

Figure 7.5 shows the circuit diagram of a noise generator based on the D101 noise diode. It is fed from ±5 volt supply lines. The total supply potential of 10 volts is sufficient to cause the D101 to break down and avalanche like a zener diode. A certain amount of noise is generated across the diode and then is coupled by a capacitor to a high gain amplifier. With the parameters given in the figure, the amplifier provides a voltage gain of about 100. The electronic noise generated by this circuit is measured as shown in Figure 7.6. The output is AC coupled with a capacitor. The peak to peak noise amplitude is about 1 volt. The horizontal time axis is 2 ms in full scale. It is taken from a Tektronix digital oscilloscope (model:TDS

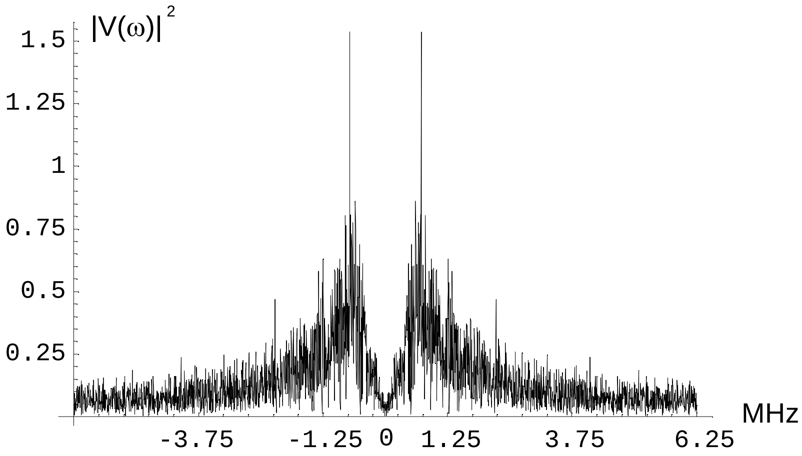

**Figure 7.7**: The electronic noise spectrum from the noise generator.

220 ) which is interfaced with the computer by using a LabView program. There are 2500 points along the time axis. The data is fourier transformed by using Mathematica to obtain the noise spectrum as shown in Figure 7.7. The noise spectrum shows that the circuit produces zero DC component and has its peak at about 750 kHz, and then drops to zero at about 3.0 MHz.

### 7.2.2 Optical Test of the Noise Generator

The noise generator is used to modulate the optical field via a tunable AO. The AO has a frequency to voltage scale factor about 4 MHz/V. Now, in order to measure the optical noise spectrum generated by this circuit, we interfere the noise field with a stable optical field which is frequency shifted by a fixed AO at 110 MHz. The optical power for the noise field is 25 $\mu$W and for the stable optical field is 87 $\mu$W. The interference of the noise field, $\mathbf{E}_N(t)$ and the stable field, $\mathbf{E}_S(t)$, can be written

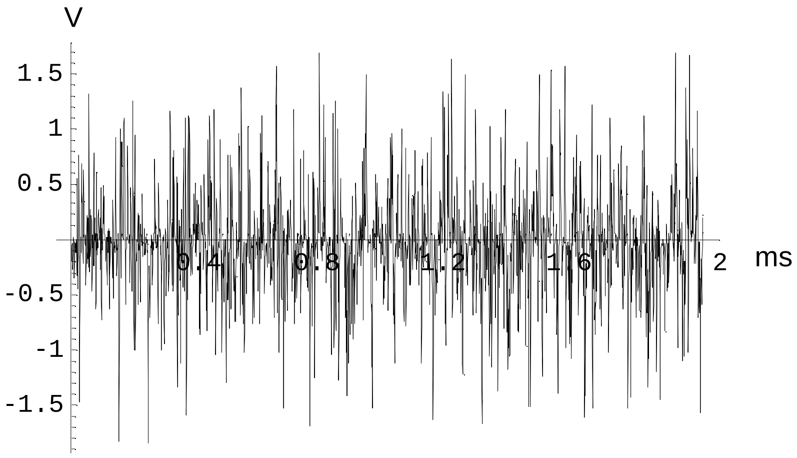

**Figure 7.8**: The random beat signal noise from the interference of a noise field and a stable field.

for parallel polarizations as,

$$\begin{aligned} |\mathbf{E}_N(t) + \mathbf{E}_S(t)|^2 &= |E_n e^{-i(\Omega t + \phi(t))} + E_s e^{-i\Omega t}|^2 \\ &= |E_n|^2 + |E_s|^2 + 2\Re[E_n^* E_s] \cos(\phi(t)) \end{aligned} \tag{7.14}$$

where $\Omega$ is the AO modulated frequency and $\phi(t)$ is the random phase of noise field. The optical frequency is neglected here for simplicity. The interference signal with a random noise amplitude is shown in Figure 7.8. The randomness of the beat amplitude looks similar to the electronic noise generated by this circuit. The optical noise spectrum is obtained by fourier transforming the noise signal. It is shown in Figure 7.9. The nonzero amplitude of the optical noise spectrum ranges from 0 →±2.25 MHz and is centered at 110 MHz. This is in agreement with the calculation done by multiplying the peak to peak electronic noise amplitude ±0.5 volts with the scale factor 4 MHz/V of the tunable AO. By comparing the frequency range with the cutoff frequency of the photodetector (Hamamatsu S1223-01) used

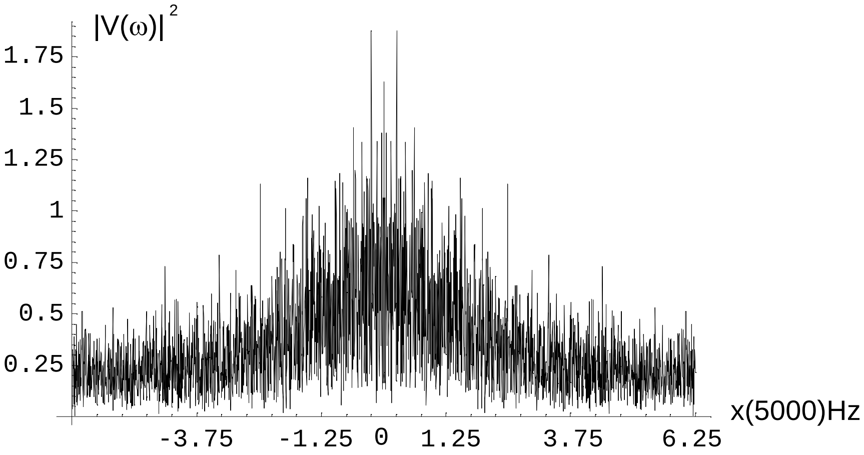

**Figure 7.9**: The spectrum of the optical beat noise where the 110 MHz is at the center zero.

in this experiment which is 20 MHz, our detectors are fast enough to detect the randomness of the optical noise and so to achieve the goal of this experiment, that is, to simulate the duality behavior of two polarization-entangled photons.

To determine whether the observed interference noise is not produced by the noise generator alone, first, we switch off the noise generator and send only the DC offset into the tunable AO. By blocking the noise beam or the stable beam, we can check the other optical and electronic noise sources in our experiment, such as the intensity noise from the laser, the electronic noise from the DC power supply or the amplifier in the photo-detector. Then, we switch on the noise generator and block out the stable optical field. This allows us to ensure that the tunable AO has negligible amplitude noise as shown in Figure 7.10. It is obvious that the amplitude shown in the noise beam alone is much smaller than the interference noise amplitude shown in Figure 7.8. The ratio of the intensity of the noise beam and the interference noise amplitude, $E_n^* E_n / 2E_s^* E_n = \frac{1}{2}\sqrt{P_n}/\sqrt{P_s}$, is about 1/200. Since the ratio of the optical power of the noise field and the stable field is 1/4

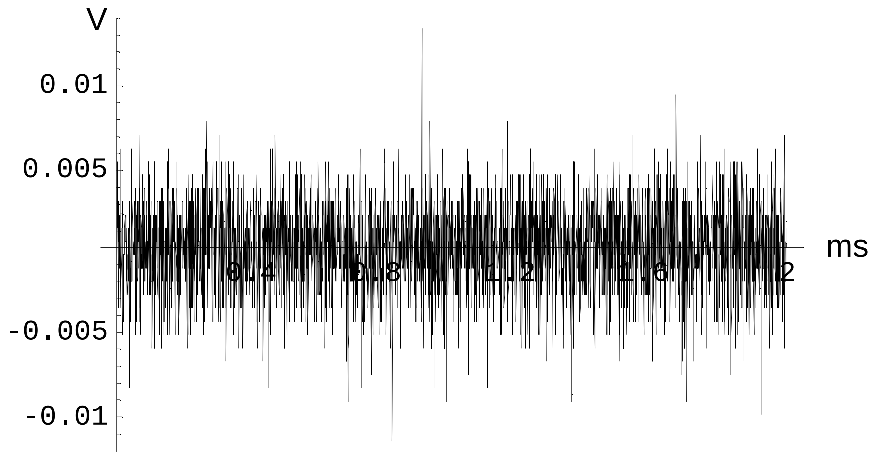

**Figure 7.10**: The residual random noise amplitude of the noise beam.

corresponding to the ratio $\sqrt{P_n}/\sqrt{P_s} \sim 1/2$, then it is obvious that the noise field is phase modulated and not amplitude modulated.

## 7.3 Particle Character in Two-Field Correlations

### 7.3.1 Experimental Analysis

Our experimental setup is shown in Figure 7.4. The source is a HeNe laser operated at 632 nm. The vertically polarized beam is a stable classical field $\mathbf{V}_S$ which is frequency shifted by 110 MHz. The horizontally polarized beam is a random phase-modulated field $\mathbf{H}_N$ produced by an acoustic optic modulator which is externally modulated by a random noise generator as described above. These two beams are then combined through a beamsplitter BS1. The beam 1 from the output port 1 of the beamsplitter BS1 contains a superposition of the horizontally polarized stable field and the vertically polarized noise field. Similarly for beam 2 from the output port 2 of the beamsplitter. A half wave plate at $0^o$ is inserted in beam 2 to induce a

$\pi$- phase shift between the horizontally and vertically polarized beams. The relative phases between $\mathbf{V}_{S1}$ and $\mathbf{H}_{N1}$ fields in beam 1 is 180° out of phase with that of $\mathbf{V}_{S2}$ and $\mathbf{H}_{N2}$ in beam 2. A quarter wave plate at $45^o$ is inserted at beams 1 and 2 to transform the linearly polarized states to circularly polarized states. By using a quarter wave plate transformation matrix [53], the field amplitudes $\mathbf{V}_{S1}$, $\mathbf{H}_{N1}$, $\mathbf{V}_{S2}$ and $\mathbf{H}_{N2}$ are transformed as,

$$\begin{aligned}
\mathbf{V}_{S1} &\rightarrow -i\hat{\mathbf{H}}_{S1}+\hat{\mathbf{V}}_{S1} \\
\mathbf{H}_{N1} &\rightarrow \hat{\mathbf{H}}_{N1}-i\hat{\mathbf{V}}_{N1} \\
\mathbf{V}_{S2} &\rightarrow -i\hat{\mathbf{H}}_{S2}+\hat{\mathbf{V}}_{S2} \\
\mathbf{H}_{N2} &\rightarrow -\hat{\mathbf{H}}_{N2}+i\hat{\mathbf{V}}_{N2}\,. \qquad (7.15)
\end{aligned}$$

For simplicity we use unit vector notation and drop the field amplitude notation. The factor $\frac{1}{\sqrt{2}}$ for each transformation is also neglected for simplicity.

The signals are analyzed in detail as follows: Analyzer $\mathcal{A}$ in beam 1 will experience a homogeneous superposition of a right circularly polarized stable field and a left circularly polarized noise field, and similarly for analyzer $\mathcal{B}$ in beam 2. An analyzer $\mathcal{A}(\mathcal{B})$ is placed before the detector 1(2) to project out the polarization state $\theta_1(\theta_2)$ as,

$$\begin{aligned}
\hat{e}_1 &= \cos\theta_1\,\hat{H}+\sin\theta_1\,\hat{V} \\
\hat{e}_2 &= \cos\theta_2\,\hat{H}+\sin\theta_2\,\hat{V}. \qquad (7.16)
\end{aligned}$$

The field amplitude in beam 1 after the $\lambda/4$ plate and the analyzer is, then,

$$\begin{aligned}\mathcal{E}_1(t) &= [(\hat{\mathbf{H}}_{N1} - i\hat{\mathbf{V}}_{N1})e^{-i(\omega+\Omega)t-i\phi(t)} + (-i\hat{\mathbf{H}}_{S1} + \hat{\mathbf{V}}_{S1})e^{-i(\omega+\Omega)t}] \cdot \hat{\mathbf{e}}_1 \\ &= (\cos\theta_1 - i\sin\theta_1)e^{-i(\omega+\Omega)t-i\phi(t)} + (-i\cos\theta_1 + \sin\theta_1)e^{-i(\omega+\Omega)t}\end{aligned} \tag{7.17}$$

and similarly for the field in beam 2,

$$\begin{aligned}\mathcal{E}_2(t) &= [(-\hat{\mathbf{H}}_{N2} + i\hat{\mathbf{V}}_{N2})e^{-i(\omega+\Omega)t-i\phi(t)} + (-i\hat{\mathbf{H}}_{S2} + \hat{\mathbf{V}}_{S2})e^{-i(\omega+\Omega)t}] \cdot \hat{\mathbf{e}}_2 \\ &= (-\cos\theta_2 + i\sin\theta_2)e^{-i(\omega+\Omega)t-i\phi(t)} + (-i\cos\theta_2 + \sin\theta_2)e^{-i(\omega+\Omega)t}\end{aligned} \tag{7.18}$$

where $\omega$ is the optical frequency and $\Omega$ is the 110 MHz modulation frequency. $\phi(t)$ is the random phase of the noise field. Thus, the random noise beat amplitudes obtained in detectors 1 and 2 can be written as,

$$\begin{aligned}\mathcal{A}_1(\phi(t)) &= |\mathbf{E}_1(t)|^2 \\ &= -ie^{i(2\theta_1+\phi(t))} + c.c \\ &\propto \sin(2\theta_1 + \phi(t)) \\ \mathcal{B}_2(\phi(t)) &= |\mathbf{E}_2(t)|^2 \\ &= ie^{i(2\theta_2+\phi(t))} + c.c \\ &\propto -\sin(2\theta_2 + \phi(t)),\end{aligned} \tag{7.19}$$

where we only use the real parts of the signals in detectors $\mathcal{A}_1$ and $\mathcal{B}_2$. The noise signal in detector 2 is anti-correlated to detector 1 because of the $\pi$ phase shift by the $\lambda/2$ plate in beam 2.

The random noise beat amplitude obtained in detector 1 can be written as,

$$\mathcal{A}_1(\phi(t)) \propto \cos(2\theta_1)\sin(\phi(t)) + \sin(2\theta_1)\cos(\phi(t)), \tag{7.20}$$

and similarly for $\mathcal{B}_2$. Eq. (7.20) is identical in structure with the quantum mechanical spin projection operator $A_1$ for a polarization angle $\theta_1$ as in Eq. (7.3),

$$A_1 = \cos 2\theta_1(|V_1\rangle\langle V_1| - |H_1\rangle\langle H_1|) + \sin 2\theta_1(|V_1\rangle\langle H_1| + |H_1\rangle\langle V_1|)\ . \tag{7.21}$$

Note that the polarization quantum projectors $(|V_1\rangle\langle V_1| - |H_1\rangle\langle H_1|)$ and $(|V_1\rangle\langle H_1| + |H_1\rangle\langle V_1|)$ in Eq. (7.21) yields discrete eigenvalues $\pm 1$ compared to continue variables of in-phase (cosine) and out-of-phase (sine) components of the noise field. For arbitrary random phase $\phi(t)$, the beat signal $A_1$ exhibits striking similarity of the output signal from the subtractor in the quantum version of the detection scheme for operator $A_1$ as shown in Figure 7.1. This is because the signal $\sin(2\theta_1 + \phi(t))$ in detector $D_1$ can have positive amplitude corresponding to the eigenvalue +1 of operator $A_1$ of detecting a photon with projection $|\theta_{1//}\rangle\langle\theta_{1//}|$ and also negative amplitude corresponding to the eigenvalue -1 of operator $A_1$ of detecting a photon with projection $|\theta_{1\perp}\rangle\langle\theta_{1\perp}|$. Hence, the average value of the signal $\sin(2\theta_1 + \phi(t))$ in $A_1$ is zero as expected for operator $A_1$ where $\langle A_1\rangle = 0$.

The random noise amplitudes in detectors 1 and 2 are then multiplied to obtain the anti-correlated random noise amplitude as,

$$\begin{aligned}\mathcal{A}_1 \times \mathcal{B}_2 &\propto -\sin(2\theta_1 + \phi(t))\sin(2\theta_2 + \phi(t)) \\ &\propto -\cos(2(\theta_1 - \theta_2)) - \cos(2(\theta_1 + \theta_2 + \phi(t)))\end{aligned} \tag{7.22}$$

Then, the mean value of this multiplied anti-correlation signal is obtained by averaging 10 shots with each shot in 2 ms scale, and hence, we obtain the correlation function $C_{cl}(\theta_1, \theta_2)$,

$$\overline{\mathcal{A}_1 \times \mathcal{B}_2} \;\; \propto \;\; C_{cl}(\theta_1, \theta_2) \propto -\cos(2(\theta_1 - \theta_2)) \tag{7.23}$$

where the noise term in Eq. (7.22) averages to zero.

Note that our classical system measures the classical analog of the correlation function $C_{cl}(\theta_1, \theta_2)$ directly by only using two photo-detectors. We can normalize the correlation function with measuring the mean values of the square beat signals $\overline{\mathcal{A}_1^2}$ and $\overline{\mathcal{B}_2^2}$ that is $\frac{\overline{\mathcal{A}_1 \times \mathcal{B}_2}}{\sqrt{\overline{\mathcal{A}_1^2}}\sqrt{\overline{\mathcal{B}_2^2}}}$. However, we normalize the correlation function $C_{cl}(\theta_1, \theta_2)$ by its maximum obtainable value that is for $\theta_1 = \theta_2$. Thus, with the analyzers set so that $\theta_1 = \theta_2$, the normalized correlation function $C_{cl}^N(\theta_1, \theta_2) = -1$. This shows that the two beams are anti-correlated corresponding to the projection of the classical analog of the entangled state $|\psi_{cl}^-\rangle = \frac{1}{\sqrt{2}}[|H_1|V_2\rangle - |V_1|H_2\rangle]$.

If now the $\lambda/4$ wave plate at beam 2 is rotated at -45°, then the beat signal $\mathcal{B}_2$ of Eq. (7.19) is given by

$$\mathcal{B}_2(\phi(t)) \propto -\sin(2\theta_2 - \phi(t))\,. \tag{7.24}$$

Hence, the correlation function of Eq. (7.23) is

$$C_{cl}(\theta_1, \theta_2) \propto -\cos 2(\theta_1 + \theta_2) \tag{7.25}$$

corresponding to the projections of the classical analog of the entangled state $|\psi_{cl}^+\rangle = \frac{1}{\sqrt{2}}[|H_1|V_2\rangle + |V_1|H_2\rangle]$

When the $\lambda/2$ plate in beam 2 is removed, the minus sign of the beat noise amplitude $\mathcal{B}_2$ of Eq. (7.19) is changed to positive sign, and then the correlation function of Eq. (7.23) is $\propto \cos 2(\theta_1 - \theta_2)$. Thus, the $C^N_{cl}(\theta_1, \theta_2) = +1$ for $\theta_1 = \theta_2$, and the projections of the classical analog of the entangled state is perfectly correlated, that is $|\varphi^+_{cl}) = \frac{1}{\sqrt{2}}[|H_1|H_2) + |V_1|V_2)]$.

Similarly without the $\lambda/2$ wave plate, by rotating the $\lambda/4$ wave plate in beam 2 to -45°, the beat noise amplitude $\mathcal{B}_2$ of Eq. (7.19) is $\propto \sin(2\theta_2 - \phi)$, and hence the correlation function of Eq. (7.23) is $\propto \cos 2(\theta_1 + \theta_2)$ corresponding to the projections of the classical analog of the entangled state $|\varphi^-_{cl}) = \frac{1}{\sqrt{2}}[|H_1|H_2) - |V_1|V_2)$.

## 7.4 Experimental Results

### 7.4.1 Characteristics of the Optical Noise System

As an illustration of our experimental observation for the correlation function $C_{cl}(\theta_1, \theta_2) = -\cos 2(\theta_1 - \theta_2)$, we take a single shot of the anti-correlated random noise amplitude at detectors 1 and 2 for $\theta_1 = \theta_2$ as shown in Figure 7.11(a) and (b) respectively. One may note that the mean value of beat signals $\langle \mathcal{A}_1 \rangle$ and $\langle \mathcal{B}_2 \rangle$ are zero as expected. The multiplied anti-correlated signal is shown in Figure 7.11(c) which has the maximum obtainable mean value in the experiment.

Figure 7.12 shows the case $\theta_1 = 0$ and $\theta_2 = 45$. The noise amplitudes in detectors 1 and 2 are shown in Figure 7.12(a) and (b) respectively. For this case, the multiplied anti-correlated signal is shown in Figure 7.12(c), where its mean value $C(\theta_1 = 0^o, \theta_2 = 45^o)$ is approximately zero.

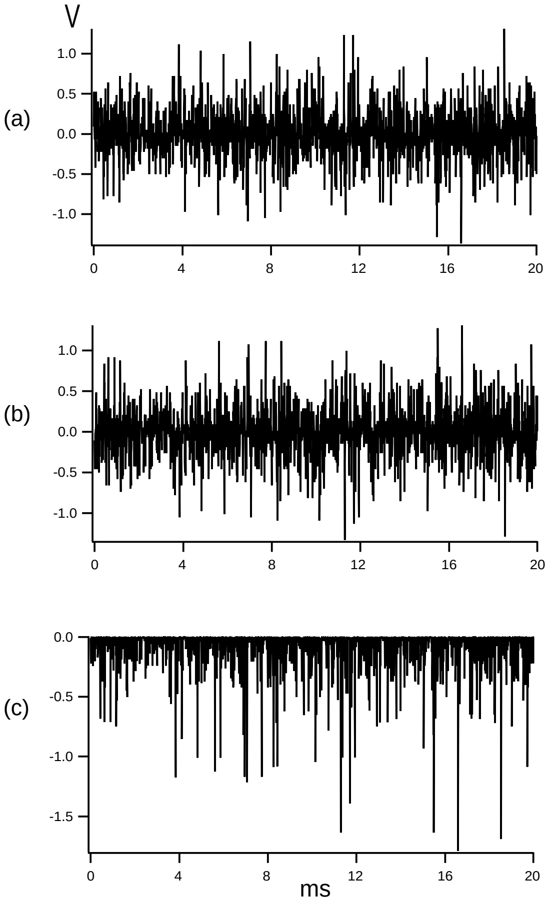

**Figure 7.11**: The experimental observation of the correlation function -$\cos 2(\theta_1 - \theta_2)$ for the case $\theta_1 = \theta_2$. The observed random noise beat signal in (a) detector 1 and (b) detector 2. (c) The multiplication of the noise amplitudes in detectors 1 and 2 for their analyzers in parallel.

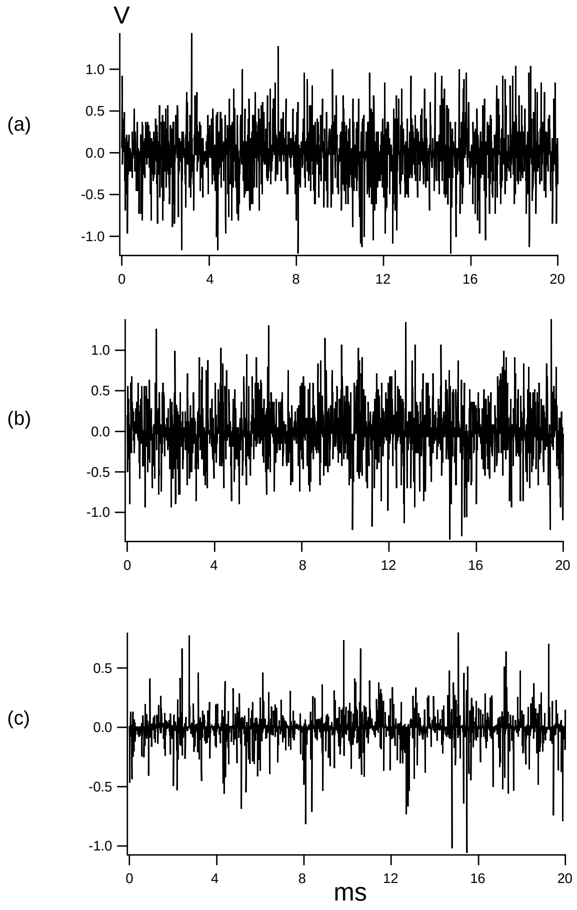

**Figure 7.12**: The experimental observation of the correlation function -$\cos 2(\theta_1 - \theta_2)$ for the case $\theta_1 - \theta_2 = 45°$. The random noise beat signal in (a) detector 1 and (b) detector 2. (c) The multiplication of the noise amplitudes in detectors 1 and 2 for their analyzers at a relative angle of $45^o$.

### 7.4.2 Classical Noise Violation of Bell's Inequality

We measure the classical correlation function $C_{cl}^{N}(\theta_1, \theta_2) = -\cos 2(\theta_1 - \theta_2)$ of the entangled state $|\psi_{cl}^{-}\rangle = \frac{1}{\sqrt{2}}[|H_1V_2\rangle - |V_1H_2\rangle]$ for the analyzers $\mathcal{A}$ and $\mathcal{B}$ along directions **a**, **b** and **c** respectively. The measurement allows us to reproduce the violation of Bell's Inequality (1965) for this case, which is given by,

$$|C_{cl}^{N}(a,b) - C_{cl}^{N}(a,c)| \leq 1 + C_{cl}^{N}(b,c) \tag{7.26}$$

or,

$$F(a,b,c) \;\; = \;\; |C_{cl}^{N}(a,b) - C_{cl}^{N}(a,c)| - 1 - C_{cl}^{N}(b,c)| \leq 0\,. \tag{7.27}$$

Maximum violation of Bell's inequality of Eq. (7.27) can be demonstrated when analyzer $\mathcal{A}$ chooses between two polarization measurements along the axes a=$0^o$ and b=$30^o$ and analyzer $\mathcal{B}$ chooses between b=$30^o$ and c=$60^o$. First, we fix $a = \theta_1 = 0$, then vary $c = \theta_2$ from $0^o$ to $90^o$ to obtain the correlation function $C_{cl}^{N}(a = 0^o, c = \theta_2)$ as shown in Figure 7.13(a). Second, we fix $\theta_1 = 30^o$ and vary $\theta_2$ from $0^o$ to $90^o$. The correlation function $C_{cl}^{N}(b = 30^o, c = \theta_2)$ is measured and shown in Figure 7.13(b).

By using the above measurement, we plot $F(a,b,c) = |C_{cl}^{N}(a = 0^o, b = 30^o) - C_{cl}^{N}(a = 0^o, c)| - 1 - C_{cl}^{N}(b = 30^o, c)$ as a function of $c = \theta_2$ as shown in Figure 7.13(c). The solid lines in the figures are theoretical predictions obtained by using $C_{cl}^{N}(\theta_1, \theta_2) = -\cos 2(\theta_1 - \theta_2)$. The experimental results show that the maximum violation value +0.5 occurs at the $c = \theta_2 = 60^o$, so that $F(a,b,c) \not\leq 0$.

For the entangled state $|\varphi_{cl}^{+}\rangle = \frac{1}{\sqrt{2}}[|H_1H_2\rangle + |V_1V_2\rangle]$ obtained by removing the $\lambda/2$-plate in beam 2, where $C_{cl}^{N}(\theta_1, \theta_2) = \cos 2(\theta_1 - \theta_2)$ for the perfectly correlated pairs. The right side of the Eq. (7.26) is changed to 1-$C_{cl}^{N}(a,b)$. This

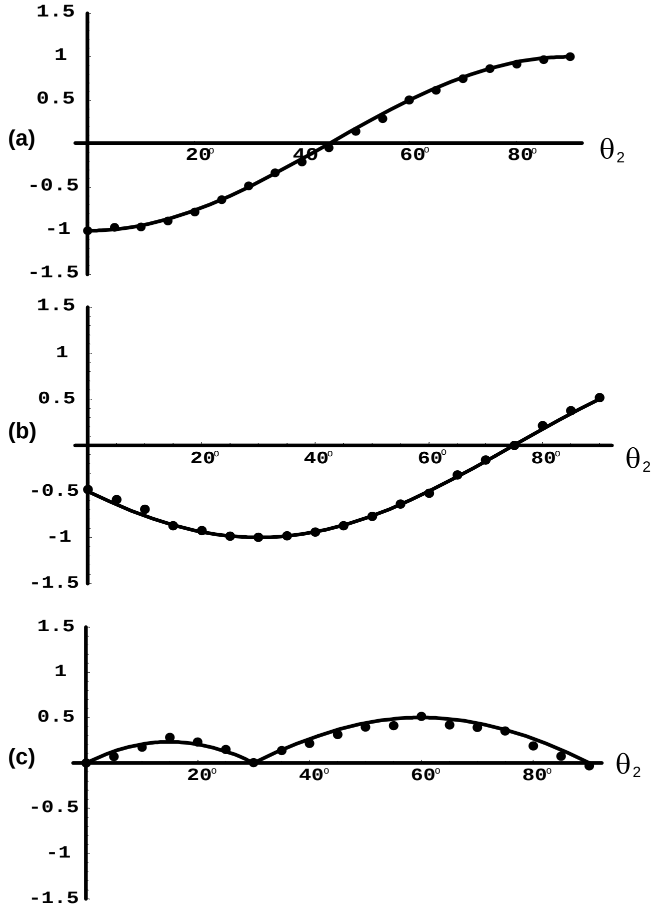

**Figure 7.13**: Violation of Bell's inequality, $F(a, b, c) = |C(a, b) - C(a, c)| - 1 - C(b, c) \leq 0$, where $C(a, b) = -cos(2(\theta_a - \theta_b))$ for the state $|\psi^-\rangle = \frac{1}{\sqrt{2}}(|H_1\rangle|V_2\rangle - |V_1\rangle|H_2\rangle)$. (a) The experimental observation of the correlation function $C^N_{cl}(a = 0^o, c = \theta_2)$. (b) The experimental observation of the correlation function $C^N_{cl}(b = 30^o, c = \theta_2)$. (c) The inequality is plotted as $F(a = 0, b = 30°, c = \theta_2) = |C(a = 0, b = 30°) - C(a = 0, c = \theta_2)| - 1 - C(b = 30°, c = \theta_2) \leq 0$. The maximum violation occurs at $\theta_2 = 60°$.

can be realized in the discussion of Section 2.3.1 for the perfect correlation function. The measurements on the correlation functions for $C_{cl}^N(a = 0^o, c = \theta_2)$ and $C_{cl}^N(b = 30^o, c = \theta_2)$ are shown in Figure 7.14(a) and (b) respectively. We measure $F(a, b, c) = |C_{cl}^N(a = 0^o, b = 30^o) - C_{cl}^N(a = 0^o, c)| - 1 + C_{cl}^N(b = 30^o, c)$ as a function of $c = \theta_2$ as in Figure 7.14(c) and observe the maximum violation occurs at $c = \theta_2$=60$^o$ with the value $F(a, b, c) = +0.5 \nleq 0$.

## 7.5 Discussion

In this experiment, we have developed a scheme to reproduce the correlated measurement of two quantum observables $A_1$ and $B_2$ for two entangled particles based on classical wave optics with noise. We are able to show that the detection schemes for quantum operators $A_1$ and $B_2$ are conceptually identical to the detection scheme for the classical noise experiment where the detectors are ac-coupled. In the classical detection scheme, the random and anti-correlated noise amplitudes in two spatially separated detectors created by the interferences of the noise field and the stable field can be used to simulate the wave-particle duality properties of operators $A_1$ and $B_2$, and hence reproduce the quantum correlations of two entangled photons. We use a signal multiplication technique to reproduce coincidence counting measurements and hence to obtain the nonlocal correlation function of two spatially separated beams.

In this experiment, the stable classical field is arranged to be orthogonal to the noise field, so that these two fields will not interfere before the measurement is made by observer $\mathcal{A}$ or $\mathcal{B}$. Our scheme suggests that two-particle quantum mechanical correlations can be considered to arise from correlated field noise. This scheme may be useful in simulating quantum networks where a random positive signal is desired

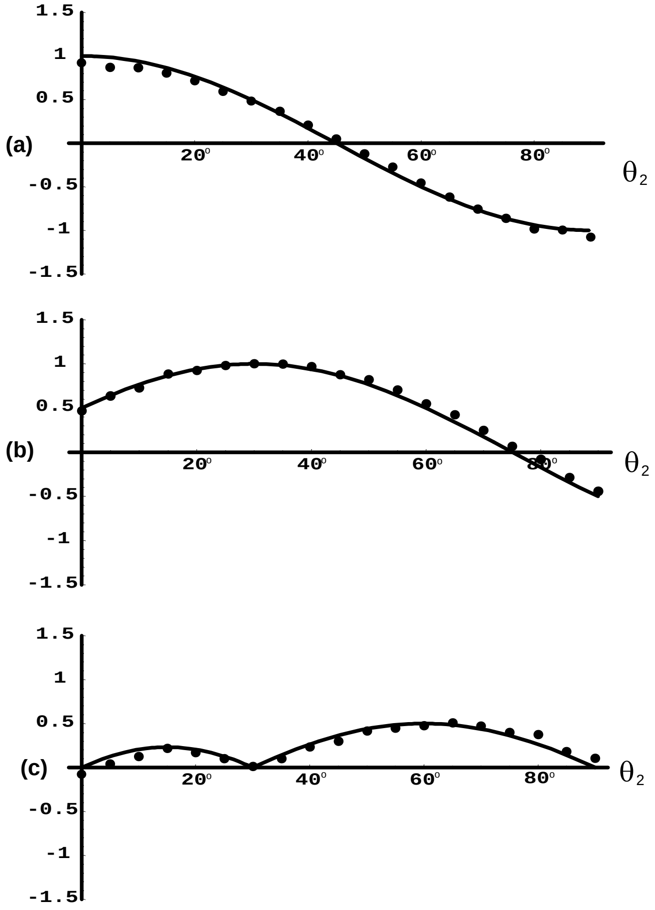

**Figure 7.14**: The violation of Bell's inequality, $F(a,b,c)$=$|C(a,b) - C(a,c)| - 1 + C(b,c) \leq 0$, where $C(a,b) = cos(2(\theta_a - \theta_b))$ for the state $|\varphi^+\rangle = \frac{1}{\sqrt{2}}(|H_1\rangle|H_2\rangle + |V_1\rangle|V_2\rangle)$. (a) The experimental observation of the correlation functions for $C_{cl}^N(a = 0^o, c = \theta_2)$ and (b) $C_{cl}^N(b = 30^o, c = \theta_2)$. (c) The inequality is plotted as $F(a = 0, b = 30°, c = \theta_2)$=$|C(a = 0, b = 30°) - C(a = 0, c = \theta_2)| - 1 + C(b = 30°, c = \theta_2) \leq 0$. The maximum violation occurs at $\theta_2$= 60°.

rather than stable signals.

# Chapter 8

# Conclusions

In this Chapter, we summarize this thesis and outline the future direction of this work. We have successfully simulated one particle wave mechanics and quantum entanglement for up to four particles by using classical fields. The reason we want to reproduce these features is to develop practical methods for producing correlations which are essential in quantum information processing. We have developed two-window heterodyne detection technique to measure Wigner phase-space distributions for classical fields. This measurement involves a single field optical analog of one particle wave mechanics. Then, we extend this single field measurement to many field-optical information processing to simulate projection measurement for up to four particles. This classical wave method makes use of analog multipliers as a nonlinear process to simulate coincidence detection techniques. In order to show that we can obtain the correct classical correlations, we reproduce violation of Bell's inequality and the truth table of GHZ test of local realism. Using noise fields, we are also able to simulate in part the wave and particle character of a quantum system. The simulation studies in this thesis illustrate some of the similarities and differences between classical wave and quantum systems. We also discuss the quantum properties that cannot be reproduced by our measurement method and the future direction of the measurement methods in quantum information processing. We summarize the achievements of our work in the following, chapter by chapter.

## 8.1 Summary

In Chapter 3, we measure the Wigner phase space distribution for a classical field by two-window heterodyne detection. A dual local oscillator beam comprising a focused beam and a collimated beam enables measure of the Wigner phase space distribution as a function of transverse position $x$ and momentum $p$. We originally proposed the two-window heterodyne imaging technique for application in biomedical imaging, to develop new optical phase space coherence tomography methods for a light field scattered from the tissue surface. However, in this thesis we use this technique to measure the Wigner distribution for a classical analog of Schrödinger cat state. The practical interest of this measurement is to demonstrate the similarities the transverse mode of a single classical field and one particle wave mechanics. We observe negative values of this Wigner function as discussed in Chapter 2. This contradicts the belief that negative values of the Wigner phase space distributions denote quantum mechanical behavior.

The LO beam in the two-window heterodyne detection technique is made of a phase-locked superposition of a large collimated gaussian beam and a small focused gaussian beam. In quantum optics terminology, a quantized harmonic field with an in-phase squeezed amplitude has an $x - p$ representation similar to a focussed gaussian beam. A quantized harmonic field with an out-of phase squeezed amplitude has a $x{-}p$ representation similar to a collimated gaussian beam. Thus, this LO beam is analogous to the EPR beams (the superposition of in-phase and out-of-phase squeezed fields) used in the teleportation experiment by Kimble' group [34]. We believe that the two-window technique is an excellent method to measure the Wigner phase-space distribution for classical fields. This measurement simply demonstrates single field optical processing which is similar to the one particle wave mechanics of a single photon experiment in quantum information processing.

In the second experiment of Chapter 3, we have shown that two local oscillator beams enable the measurement of the product field $E_H(x_1)E_V(x_2)$. This can be done by using an analog multiplier and lock-in detection. Even though we are not measuring the entangled state of two spatially separated classical fields, the technique suggest a method to simulate a projection measurement of entangled states as demonstrated in Chapter 4.

In Chapter 4, we have simulated the entanglement of two particles which is believed by some workers to be impossible by using classical fields. Most of quantum information processing (QIP) such as quantum teleportation and computations require at least two entangled particles. We have developed a classical method to simulate the measurement of two correlated classical fields instead of two correlated quantum particles. This may provide practical robust methods for simulating QIP.

We have shown that analog multiplication and frequency selection of heterodyne signals arising from two spatially separated classical fields leads to measurement in a product basis and permits simulation of two-particle entanglement. We are able to simulate the measurements of polarization correlations for classical analogs of four Bell states, namely, $|\Psi^{\pm}_{cl})_{\Delta_+} \equiv \frac{1}{\sqrt{2}}\left[|H1)|V2) \pm |V1)|H2)\right]$ and $|\varphi^{\pm}_{cl})_{\Delta_+} \equiv \frac{1}{\sqrt{2}}\left[|H1)|H2) \pm |V1)|V2)\right]$. The violation of Bell's inequality is observed for each of them as tabulated below.

| State | Correlation Function | Violation |
|---|---|---|
| $\|\Psi^{+}_{cl})$ | $\sin^2(\theta_1+\theta_2)$ | -0.2507 |
| $\|\Psi^{-}_{cl})$ | $\sin^2(\theta_1-\theta_2)$ | -0.2523 |
| $\|\varphi^{+}_{cl}\rangle)$ | $\cos^2(\theta_1-\theta_2)$ | -0.2531 |
| $\|\varphi^{-}_{cl}\rangle)$ | $\cos^2(\theta_1+\theta_2)$ | -0.2518 |

Bell's inequality predicts the last column must be $\geq 0$. The maximum violation value is -0.25 analogous to the predictions from quantum mechanics. The results imply that we can study quantum entanglement of two particles by simulating the wave character of a two-particle entangled state. The particle character of the system can be neglected. In addition, the classical simulation experiment can be used to simulate quantum information processing. The field at each frequency is considered to be a classical analog (c-bit) of a quantum bit (qu-bit) which can be in an arbitrary polarization state, i.e, a superposition of two orthogonal polarizations. It is also possible to reproduce the behavior of two-photon interferometers [68] for which the fringe frequency is twice that of a one-photon interferometer. The measurement techniques employed in Chapter 4 can be further developed to study the entanglement of more than two particles such as three-particle GHZ entanglement in Chapter 5.

In Chapter 5, we use classical fields to simulate three and four particle GHZ entanglement. The simulation demonstrated in this chapter is a first step to demonstrate a simple quantum network by using classical fields. In the quantum experiments, the measurements of polarization correlations between the three particles leads to a conflict with local realism for nonstatistical predictions of quantum mechanics. That is in contrast to the two entangled particles test of Bell's inequality where the conflict arises for statistical predictions of quantum mechanics.

We extend the measurement method of Chapter 4 to simulate three and four-photon Greenberger-Horne-Zeilinger (GHZ) entanglement. In the simulation of GHZ entanglement by using classical fields, we reproduce the 32 elements in the measurements of the quantum mechanics truth table. Field polarization correlations are measured. The measured polarizations for each field are right (R) or left (L) circular Y-type or ±45° linear X-type. The choices for three fields are taken to be YYX, YXY, XYY and XXX. Local realism assigns $+1(-1)$ for the field with R(L) circular Y-type and $\pm1$ for the field with ±45° linear X-type. The classical analog of the three-particle GHZ entangled state yield the choices YYX=-1, YXY=-1, XYY=-1 and XXX=+1 respectively. The final measurement XXX=+1 obtained in our classical system is analogous to the result predicted by GHZ entanglement and hence in contrast with local realism theory which predicts XXX=-1. The success of these tests in our classical system is due to the fact that the signal amplitude at a particular frequency is proportional to the projection $(\hat{e}_{LO1}, \hat{e}_{LO2}, \hat{e}_{LO3}|\Psi^3_{GHZ})_{cl}$, which has the same degrees of freedom and interference properties as the quantum GHZ state $|\Psi^3_{GHZ}\rangle$ prepared by Zeilinger's group [29, 63].

Of practical interest is that the experiments demonstrate nonlocal correlations of the four fields which simulate an optical communication system. The classical system employs four *independent*, spatially-separated local oscillator (LO) fields. In principle, the signal from each heterodyne detector can be recorded and at a later time, the signals can be correlated. This is possible since the relative phases of all of the pairs of superimposed fields are preserved in propagation to the detectors and the local oscillator phases appear only as a multi-factor in the signal amplitude.

The signals can then be analyzed numerically, using multiplication and appropriate frequency selection. For this system to work, it is necessary that the four observers synchronize their time origins with a precision small compared to the inverse of the frequency differences employed in the system. This can be accomplished with a light pulse from the source region to all observers. A similar problem arises in quantum experiments-observer must measure correlated photons produced in the same event.

In Chapter 6, we use the experimental setup in Chapter 5 to simulate entanglement swapping which is related to quantum teleportation. The ability to swap entangled states of many particles is essential to the development of quantum information processing methods. Generation of such states through entanglement swapping can be very challenging in real quantum systems, where loss and decoherence easily destroy the state and coincidence count rates tend to be low when the number of particles is large. We classically simulate a type of the entanglement swapping in a projection measurement of four-photon GHZ entanglement. Our classical system is not really swapping or teleporting an arbitrary quantum state, but is more like a generalized lock-in detection scheme. Our classical system exhibits similar problems to those encountered in teleportation of entanglement experiments, such as fundamental technical limitations on distinguishing between all four Bell states. The demonstration of a classical form of entanglement swapping in the four field basis is already a type of information processing, as it enables the correlation measurements of one observer to determine the correlation measurements for another observer.

From the simulation work in Chapters 4, 5 and 6, we believe that our measurement methods consisting analog multipliers and band pass filters can be utilized to produce generalized multi-particle entanglement in the development of quantum network.

One may note that our measurement method is not linear because we use analog multiplier to obtain the product signals from two spatially separated regions. Since the product signal is a stable oscillatory sinusoidal wave, probability language is not applicable especially in our simulation works in Chapters 4 and 5. In order to simulate probabilistic quantum systems, such as the mean of the product of two quantum observables $\langle A_1 B_2 \rangle$, we mix a classical stable wave field with a classical random noise field. As shown in Chapter 7, this produces beams with correlated noise.

In Chapter 7, first, we simulate the particle character of single photon experiment with a noise field. We are able to reproduce the $\delta$-correlated shot noise that is proportional to the intensity of the noise field. Second, we are able to simulate the detection of the quantum correlation function of two observers $A_1(\theta_1)$ and $B_2(\theta_2)$ with the function operator in the form $|\theta_{//}\rangle\langle\theta_{//}| - |\theta_\perp\rangle\langle\theta_\perp|$. Operator A with its eigenvalue $\pm 1$ can be detected and simulated by a cube polarizer beamsplitter with two detectors placed at each port and subtracted to each other. Similarly for the observable B. In the classical noise experiment, a stable classical field and a noise classical field with orthogonal polarization creates anti-correlated noise amplitudes between two separated detectors. The mean value obtained from the product of these random noise signals in the two spatially separated detectors $\mathcal{A}_1$ and $\mathcal{B}_2$ is analogous to the quantum correlation function of two observers.

We have also demonstrated that the violation of Bell's inequality by using noise field for the state $|\psi_{cl}^-\rangle = \frac{1}{\sqrt{2}}(|H_1\rangle|V_2\rangle - |V_1\rangle|H_2\rangle)$ and for the state $|\varphi_{cl}^+\rangle = \frac{1}{\sqrt{2}}(|H_1\rangle|H_2\rangle + |V_1\rangle|V_2\rangle)$. The product of the anti-correlated noise amplitudes or spikes appearing in two spatially separated detectors simulates the wave-particle duality properties of two entangled photons in the measurement of violation of Bell's inequality. The wave character of our classical system, such as state of polarization, leads interference between a stable field and a noise field in two spatially separated detectors that yields correlated noise fields. The particle character of the system is the random spikes of noise in the interference amplitude of each detector. However, these spikes do not correspond to the intensity of the photons as the spike has a random amplitude.

In conclusion, classical wave systems are able to simulate the wave-particle duality properties in the sense as discussed above, where the measurement quantity does not require particle behavior as in quantum systems. The ability of classical fields to reproduce the nonlocal correlations as predicted by quantum mechanics suggests an alternative approach to implement quantum information processing which does not require the collapse of the wave function. Our current communication systems are mostly based on fiber optics communication with classical light sources. Since the employment of quantum particles in current communication systems have many obstacles such as decoherence, then measurement methods based on the classical simulation of quantum entanglement may be an alternative tool to improve the efficiency of information processing. In view of the stability and high signal-to-noise ratio obtainable using classical optical waves, the study of classical-wave analogs of quantum measurements appears to be a worthwhile goal.

## 8.2 Similarities and Differences between Classical Wave and Quantum Systems

It is worth to discussing the properties of quantum systems that cannot be simulated by classical wave optics. In the simulation of two photon entanglement in Chapter 4, the beat amplitude at 125 kHz does not scale as the intensity of a particle and hence the joint probability obtained in the two-photon simulation experiment does not correspond to detecting of two entangled photons. In the quantum counterpart, one entangled photon will '*click*' or register on one photo-detector which produces a single electric pulse proportional to the intensity of the photon. Similarly, the second entangled photon will register on the second photo-detector and produces single electric pulse. A correlator is then used to obtain the product photo-count signals of two entangled photons, not the multiplication of two classical correlated fields. Similarly for the classical noise experiment in Chapter 7, we are able to simulate particle properties of two-particle entangled system by creating anti-correlated random noise amplitude in two spatially separated detectors, but the interference amplitude in either detector corresponds to two correlated classical fields not to two correlated photons. It will be challenging to develop a measurement method based on classical wave optics to simulate multi-particle entanglement by measuring the intensity rather than amplitudes of multi-classical beams. Note that single particle entanglement such as polarization-position entanglement can be simulated by using classical beam where the intensity of the classical beam is measured to simulate the detection of the particle [44].

Another fundamental feature of quantum mechanics which classical wave optics fails to simulate is quantum non-cloning principle. The quantum non-cloning principle prevents the information of two communicating parties to leak to a third party. The entangled photon which is used in the quantum cryptography process cannot be replaced by another photon generated from another independent source. In classical wave simulation of entanglement, classical fields are reflected and transmitted through a beamsplitter at the same time. The reflected and transmitted beams have identical spatial transverse mode and polarizations. The beamsplitter acts as a copying device for the transverse mode of a classical field, but not for a quantum field. Hence, classical wave optics is unable to improve the security of optical communication channels in the same way as a true quantum system.

## 8.3 Future Directions

In the future, we believe that the simulation method developed in this thesis can be extended for quantum information processing. The measurement methods developed in our simulation work employ local oscillator fields which are similar to heterodyne detection in phase sensitive experiments such as measurement of squeezed light. Hence, it will be intriguing to look at the quantum counterpart of the measurement methods developed in this thesis. We believe that the heterodyne measurement methods can be implemented by using quantum fields. If the quantum counterpart of the measurement method is successful, then it will provide us with a deeper insight into the fundamental concepts of violation of Bell's inequality and nonlocality tests of GHZ entanglement.

The classical method cannot simulate collapse of the wave function. However, much of the quantum information processing does not require collapse. The superposition principle obeyed by classical fields, is adequate to reproduce only the interferences of the multi-particle quantum states.

The next step will be toward the simulation of quantum algorithms such as Deutsch-Jozsa algorithms and Shor's quantum algorithm for factoring large numbers. The Deustch-Jozsa algorithm (D-J) [11,12] can be implemented as a controlled-Not gate. In this gate, two input bits are a control bit and target bit. When the control bit is in the state $|1\rangle$, the state in the target is flipped from $|1\rangle$ to $|0\rangle$ and vice versa. Similarly, if the control bit is in the state $|0\rangle$, then the state in the target is unchanged. If the target bit is in the superposition state of $|0\rangle + |1\rangle$, and the control bit is in the state $|0\rangle$, then the two output bits will have the product state $|0\rangle(|1\rangle + |0\rangle)$. If the control bit is in the state $|1\rangle$, then the two output bits will have the product state $|1\rangle(|1\rangle + |0\rangle)$. One can see that when the control bit is $|0\rangle$ or $|1\rangle$, the target bit is still in a superposition state of $|0\rangle + |1\rangle$. From the above argument, the D-J algorithm can be reproduced by the multiplication of the state of the control bit and the superposition state of the target bit. This can be readily accomplished using the simulation method developed in this thesis. However, if the target bit is in the superposition state of $|0\rangle - |1\rangle$, then our simulation method will fail to reproduce the phase of the product basis as predicted by D-J algorithm. In order to simulate D-J algorithm by using classical wave optics, one may use continuous variables such as in-phase and out-of-phase components of an optical interference beat signal instead of bits $|1\rangle$ and $|0\rangle$.

Shor's algorithm in factoring large numbers requires the understanding of quantum finite Fourier transforms and also large amount of resources. We have not yet determined whether the classical simulation methods discussed in this thesis can reproduce Shor's algorithm. However, we suggest that the functions of analog multipliers and band pass filters in our measurement methods will have to be described as operators or functions before they can be used to implement Shor's algorithm.

# Appendix A

# Heterodyne Beat $V_B$

For a given signal beam with optical power $P_S$ and a LO beam with optical power $P_{LO}$, the power of the heterodyne beat signal $P_B$ can be obtained for the balanced heterodyne detection scheme as,

$$\begin{aligned} \langle E_{LO} E_S^* \rangle + c.c &= \langle \sqrt{P_{LO}} e^{-i(\omega+\delta)t} \sqrt{P_S} e^{i\omega t} \rangle + c.c \\ &= 2\sqrt{P_{LO} P_S} \cos \delta t \\ &= P_B \cos \delta t \end{aligned} \tag{A.1}$$

where $\omega$ is the optical frequency and $\delta$ is a 10 MHz frequency shift. The power of the heterodyne beat signal $P_B$ is defined as 2 $\sqrt{P_{LO} P_S}$. The power $P_B$ of the heterodyne beat signal produces a photocurrent

$$i = \eta_D P_B \tag{A.2}$$

where $\eta_D$ is the responsivity of the photodiodes and is experimentally found to be 0.32 A/W at $\lambda = 633$ nm. The output of the transimpedence amplifier yields $F(\upsilon)Ri$, where $R$ =10 k$\Omega$ is the feedback resistance and $F(\upsilon) = 0.722$ is the frequency response of the amplifier at $\upsilon = 10$ MHz. Finally an efficiency $n_{het}$ must be included to account for wavefront alignment such as the mismatch of the diameters of the signal and LO beams. Thus, the output of the transimpedence amplifier is given by

$$V_B = \eta_D \times P_B \times R \times F(\upsilon) \times \eta_{het} \tag{A.3}$$

The heterodyne beat signal $V_B$ is measured with an oscilloscope.

In the spectrum analyzer, the voltage is divided by 2 due to its 50Ω input impedance in parallel with the 50Ω resistor at the output of the transimpedance amplifier and again by $\sqrt{2}$ because it measures the root mean square of the sinusoidal heterodyne beat. Hence, the maximum voltage of the beat signal in the spectrum analyzer is read as $V_{SA}=\frac{V_B}{2\sqrt{2}}$.

# Appendix B

# Heterodyne Imaging system

The heterodyne experiment for obtaining smoothed Wigner functions is shown in Figure B.1. The LO and the signal beam are frequency shifted by acousto-optic modulators that differ in frequency by 10 MHz. The signal beam is combined with the LO beam at a 50-50 beam splitter (BS1). The heterodyne beat signals are then detected by a balanced heterodyne detection scheme. The beat signal $V_B$ at 10 MHz is amplified and then measured with an analog spectrum analyzer. The analog output of the spectrum analyzer, which is proportional to $\sqrt{V_B^2}$, is squared using a low noise multiplier. The multiplier output is fed to a lock-in amplifier. The signal beam is chopped on and off at 500 Hz. In this way, electronic noise and LO shot noise are subtracted in real time, and the lock-in output is directly proportional to $|V_B|^2$. The mean square beat signal is directly proportional to the overlap of the Wigner phase space distributions for the local oscillator and signal fields at the input lenses L1 and L2.

Let's derive the measurement of smoothed Wigner function from the paraxial ray approximation. The beat amplitude $V_B$ is determined by the spatial overlap of the local oscillator ($LO$) and signal ($S$) fields in the plane of the detector at $Z = Z_D$ as,

$$V_B = \int dx' \mathcal{E}^*_{LO}(x', z_D) \mathcal{E}_S(x', z_D) \tag{B.1}$$

where $x'$ denotes the transverse position in the detector plane. When M1 is scanned

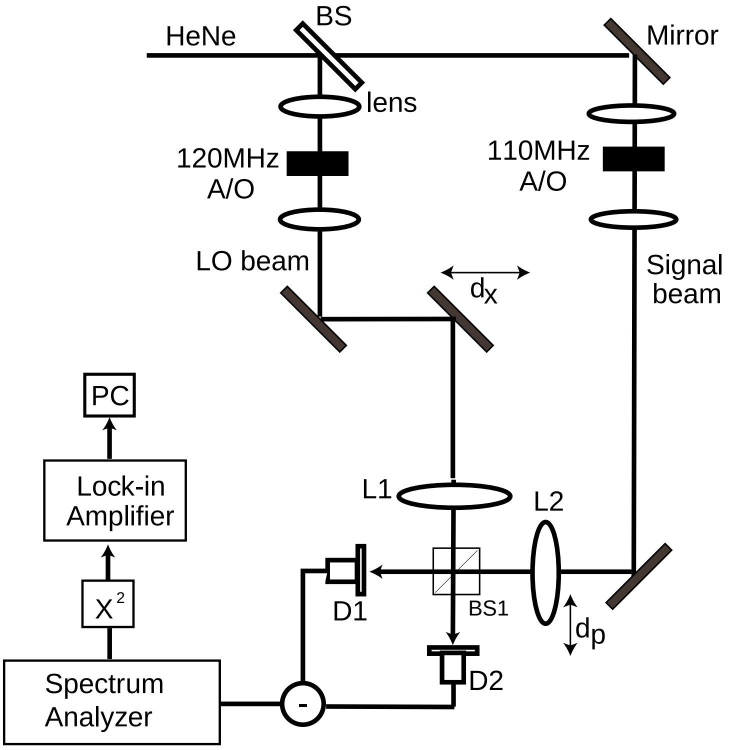

**Figure B.1**: The experimental setup for measuring the smoothed Wigner function.

by a distance $d_x$, the LO field has shifted accordingly to give

$$V_B(d_x) = \int dx' \mathcal{E}^*_{LO}(x' - d_x, z_D)\mathcal{E}_S(x', z_D) \tag{B.2}$$

The fields in the detector plane are related to the fields in the source planes ($z = 0$) of lenses L1 and L2, which have equal focal lengths f = 6 cm. The LO and signal fields at $z = 0$ after the lenses, L1 and L2, are

$$\begin{aligned} \mathcal{E}'_{LO}(x - d_x, z = 0) &= \exp[-i\frac{k}{2f}x^2]\mathcal{E}_{LO}(x - d_x, z = 0) \\ \mathcal{E}'_S(x, z = 0) &= \exp[-i\frac{k}{2f}x^2]\mathcal{E}_S(x, z = 0) \end{aligned} \tag{B.3}$$

When the lens L2 is scanned by a distance $d_p$, the signal field (B.3) is altered as

$$\mathcal{E}'_S(x, z = 0) = \exp[-i\frac{k}{2f}(x - d_p)^2]\mathcal{E}_S(x, z = 0)$$

The fields propagating a distance $d = f$ to the planes of the detectors can now be obtained by using Fresnel's diffraction integrals as,

$$\begin{aligned} \mathcal{E}_{LO}(x' - d_x, z_D) &= \sqrt{\frac{k}{i2\pi f}} \int dx \, \exp[i\frac{k}{2f}(x - x')^2] \\ &\times \exp[-i\frac{k}{2f}x^2] \, \mathcal{E}_{LO}(x - d_x, z = 0) \\ \mathcal{E}_S(x', z_D) &= \sqrt{\frac{k}{i2\pi f}} \int dx \, \exp[i\frac{k}{2f}(x - x')^2] \\ &\times \exp[-i\frac{k}{2f}(x - d_p)^2] \, \mathcal{E}_S(x, z = 0) \end{aligned} \tag{B.4}$$

The quadratic phases that depend on $x^2$ cancel in these expressions because the detector plane is in the focal plane of the lenses, L1 and L2. Leaving the above equations as,

$$\begin{aligned}\mathcal{E}_{LO}(x'-d_x,z_D) &= \sqrt{\frac{k}{i2\pi f}}\,exp[-i\frac{k}{2f}x'^2]\\ &\times \int dx\,exp[i\frac{k}{2f}xx']\mathcal{E}_{LO}(x-d_x,z=0)\\ \mathcal{E}_S(x',z_D) &= \sqrt{\frac{k}{i2\pi f}}\,exp[i\frac{k}{2f}(x'^2-d_p^2)]\\ &\times \int dx\,exp[i\frac{k}{2f}x(x'-d_p)]\mathcal{E}_S(x,z=0)\end{aligned} \tag{B.5}$$

By substituting the above equations into Eq. (B.2), the quadratic phases in $x'$ cancel, as,

$$\begin{aligned}V_B(d_x,d_p) &= \frac{k}{2\pi f}\,\exp[-i\frac{k}{2f}d_p^2]\int dx'\int dx_1\,\exp[-i\frac{k}{f}x_1x']\,\mathcal{E}^*_{LO}(x-d_x,z=0)\\ &\times \int dx_2\,\exp[i\frac{k}{f}x_2(x'-d_p)]\,\mathcal{E}_S(x_2,z=0)\end{aligned} \tag{B.6}$$

Integrating over $x'$ yields a delta function as

$$\int dx'\,\exp[-i\frac{k}{f}x'(x_1-x_2)] = 2\pi\delta(x_1-x_2) \tag{B.7}$$

Thus, Eq. (B.6) can be rewritten as

$$\begin{aligned} V_B(d_x, d_p) &= \frac{k}{f}\,\exp[i\frac{k}{2f}d_p^2]\int dx_2\,\exp[-i\frac{k}{f}x_2 d_p]\,\mathcal{E}_S(x_2, z=0) \\ &\times \int dx_1\,\mathcal{E}^*_{LO}(x_1 - d_x, z=0)\delta(x_1 - x_2) \end{aligned} \tag{B.8}$$

Integrating over $x_1$, the above equation becomes,

$$V_B(d_x, d_p) = \frac{k}{f}\,\exp[i\frac{k}{2f}d_p^2]\int dx_2\,\exp[-i\frac{k}{f}x_2 d_p] \times \mathcal{E}^*_{LO}(x_2 - d_x, z=0)\mathcal{E}_S(x_2, z=0)$$

By replacing $x_2$ by $x$ and dropping the term $z = 0$, the mean square beat amplitude is then given by

$$|V_B(d_x, d_p)|^2 \propto \left|\int dx\,\mathcal{E}^*_{LO}(x - d_x)\mathcal{E}_S(x)\,\exp(-ik\frac{d_p}{f}x)\right|^2 \tag{B.9}$$

We can explicitly write out the magnitude squared of the detected signal as

$$\begin{aligned} |V_B(d_x, d_p)|^2 &\propto \int dx\,\mathcal{E}^*_{LO}(x - d_x)\mathcal{E}_S(x)\,\exp(-ik\frac{d_p}{f}x) \\ &\times \int dx'\,\mathcal{E}_{LO}(x' - d_x)\mathcal{E}^*_S(x')\,\exp(ik\frac{d_p}{f}x). \end{aligned} \tag{B.10}$$

This can be rewritten using the variable transformations as

$$\begin{aligned} x &= x_o + \eta/2 \\ x' &= x_o - \eta/2. \end{aligned} \tag{B.11}$$

The Jacobian of this transformation is 1. Thus, the beat signal can be written in terms of these variables as

$$\begin{aligned}|V_B(d_x,d_p)|^2 \;\propto\;& \int dx_o \int d\eta\, \mathcal{E}^*_{LO}(x_o+\eta/2-d_x)\mathcal{E}_{LO}(x_o-\eta/2-d_x)\\ \times\;& \mathcal{E}^*_S(x_o-\eta/2)\mathcal{E}_S(x_o+\eta/2)\ \exp(-ik\frac{d_p}{f}\eta).\end{aligned} \tag{B.12}$$

Recall the definition of the Wigner distribution,

$$W(x,p)=\int\frac{d\epsilon}{2\pi}\ \exp(i\epsilon p)\langle\,\mathcal{E}^*(x+\epsilon/2)\mathcal{E}(x-\epsilon/2)\rangle \tag{B.13}$$

where its inverse transform is given by,

$$\mathcal{E}^*(x+\epsilon/2)\mathcal{E}(x-\epsilon/2)=\int dp\ \exp(-i\epsilon p)W(x,p). \tag{B.14}$$

Using this equation to replace the signal fields in Eq. (B.12) the beat signal becomes

$$\begin{aligned}V_B(d_x,d_p)|^2 \;\propto\;& \int dx_o \int d\eta\, \mathcal{E}^*_{LO}(x_o+\eta/2-d_x)\mathcal{E}_{LO}(x_o-\eta/2-d_x)\\ \times\;& \int dp\ \exp(-ik\frac{d_p}{f}\eta)\ \exp(-i\eta p)W_S(x,p).\end{aligned} \tag{B.15}$$

Again, since the LO Wigner distribution is

$$\begin{aligned}W_{LO}(x_\circ-d_x,p+k\frac{d_p}{f}) \;=\;& \int\frac{d\eta}{2\pi}\ \exp[-i\eta(p+k\frac{d_p}{f})]\\ \times\;& \mathcal{E}^*_{LO}(x_o+\eta/2-d_x)\mathcal{E}_{LO}(x_o-\eta/2-d_x).\end{aligned} \tag{B.16}$$

The LO fields in Eq. (B.15) can be replaced by the Wigner function in Eq. (B.16). Then finally, the mean square heterodyne beat signal $|V_B|^2$ can now be written as

$$|V_B(d_x, d_p)|^2 \propto \int dxdp\, W_{LO}(x - d_x, p + \frac{k}{d_p}) W_S(x, p) \tag{B.17}$$

where $W_S(x, p)$ is the Wigner distribution of the signal field in the plane of L2 (z =0) and $W_{LO}(x, p)$ is the LO Wigner distribution in the plane of L1 (z = 0).

# Appendix C

# Amplitudes of $S_R$ and $S_I$

The combined two LO beams are mixed with the signal beam in a beamsplitter in the balanced heterodyne detection scheme. The outputs of the beamsplitter $E_1(t)$ and $E_2(t)$ at the detectors D1 and D2 respectively are given by,

$$\begin{aligned}
E_1(t) &= E_S(x_1)e^{-i(\omega+\Omega_S)t} + E_{LO1}(x_1)e^{-i(\omega+\Omega_{LO1})t} + E_{LO2}(x_1)e^{-i(\omega+\Omega_{LO2})t} + cc \\
E_2(t) &= E_S(x_2)e^{-i(\omega+\Omega_S)t} - E_{LO1}(x_2)e^{-i(\omega+\Omega_{LO1})t} - E_{LO2}(x_2)e^{-i(\omega+\Omega_{LO2})t} + cc
\end{aligned} \tag{C.1}$$

where $\omega$ and $\Omega$ indicate optical and modulation frequencies. The minus signs in $E_2(t)$ are due to the $\pi$-phase shift of the beamsplitter. The $E_S(x)$, $E_{LO1}(x)$ and $E_{LO2}(x)$ are the amplitudes of the signal beam and two LO beams respectively. These fields are function of position coordinate in the detection plane of detectors $D_1$ and $D_2$. The heterodyne beat signal between the local oscillator beam and signal beam is given by spatial overlapping integration i.e., $\int dx_1 E_S^*(x_1)E_{LO1}(x_1)$, $\int dx_2 E_S^*(x_2)E_{LO2}(x_2)$ and etc. However, for simplicity we neglect these integrations in the following discussion. Then, the heterodyne beat signals $V_1(t)$ in detector D1 and $V_2(t)$ in detector D2 are given respectively by,

$$\begin{aligned}
V_1(t) &= E_1^*(t)E_1(t) + cc \\
&= E_S^*E_S + E_S^*E_{LO1}e^{-i(\Omega_{LO1}-\Omega_S)t} + E_S^*E_{LO2}e^{-i(\Omega_{LO2}-\Omega_S)t} \\
&+ E_{LO1}^*E_{LO1} + E_{LO1}^*E_Se^{-i(\Omega_S-\Omega_{LO1})t} + E_{LO1}^*E_{LO2}e^{-i(\Omega_{LO2}-\Omega_{LO1})t} \\
&+ E_{LO2}^*E_{LO2} + E_{LO2}^*E_Se^{-i(\Omega_S-\Omega_{LO2})t} + E_{LO2}^*E_{LO1}e^{-i(\Omega_{LO1}-\Omega_{LO2})t} + cc \\
V_2(t) &= E_2^*(t)E_2(t) + cc \\
&= E_S^*E_S - E_S^*E_{LO1}e^{-i(\Omega_{LO1}-\Omega_S)t} - E_S^*E_{LO2}e^{-i(\Omega_{LO2}-\Omega_S)t} \\
&+ E_{LO1}^*E_{LO1} - E_{LO1}^*E_Se^{-i(\Omega_S-\Omega_{LO1})t} + E_{LO1}^*E_{LO2}e^{-i(\Omega_{LO2}-\Omega_{LO1})t} \\
&+ E_{LO2}^*E_{LO2} - E_{LO2}^*E_Se^{-i(\Omega_S-\Omega_{LO2})t} + E_{LO2}^*E_{LO1}e^{-i(\Omega_{LO1}-\Omega_{LO2})t} + cc\,.
\end{aligned} \tag{C.2}$$

The output voltage $V_B(t)$=$V_1(t)$ − $V_2(t)$ from the balanced heterodyne detection before being fed into the spectrum analyzer is given by,

$$V_B(t) = 2E_S^*E_{LO1}e^{-i(\Omega_{LO1}-\Omega_S)t} + 2E_S^*E_{LO2}e^{-i(\Omega_{LO2}-\Omega_S)t} + cc \tag{C.3}$$

In spectrum analyzer, the power spectrum of the $V_B$ is measured as

$$|V_B(\Omega)|^2 = \int_{-\infty}^{\infty} \frac{d\tau}{2\pi}\, e^{i\Omega\tau}\, \langle V_B(t)V_B(t+\tau)\rangle \tag{C.4}$$

but it is displayed as $\sqrt{|V(\Omega)|^2}$. As mentioned in Chapter 3, it is squared by using a squarer to recover the beat signal $|V_B(\Omega)|^2$ which is denoted as $|V_\circ(t)|^2$ in Figure 3.2. From Eq. (C.4), the power spectrum can be calculated by keeping the slowly varying term $(\Omega_{LO1} - \Omega_{LO2})$ in time $t$ and other terms that depend on $\tau$, that is,

$$\begin{aligned}
\langle V_B(t)V_B(t+\tau)\rangle &= \frac{1}{T}\int_{-T/2}^{T/2} dt\, V_B(t)V_B(t+\tau) \\
&\propto E_S^* E_{LO1} E_S E_{LO1}^* e^{-i(\Omega_S-\Omega_{LO1})\tau} \\
&+ E_S^* E_{LO2} E_S E_{LO2}^* e^{-i(\Omega_S-\Omega_{LO2})\tau} \\
&+ E_S^* E_{LO1} E_S E_{LO2}^* e^{-i(\Omega_{LO1}-\Omega_{LO2})t} e^{-i(\Omega_S-\Omega_{LO2})\tau} \\
&+ E_S^* E_{LO2} E_S E_{LO1}^* e^{i(\Omega_{LO1}-\Omega_{LO2})t} e^{-i(\Omega_S-\Omega_{LO1})\tau} \\
&+ (\text{: the negative frequency contributions from the above terms:})
\end{aligned} \tag{C.5}$$

Here, $\Omega_S$=120 MHz, $\Omega_{LO1}$=110 MHz + 5 kHz and $\Omega_{LO2}$=110 MHz. Now, by substituting Eq. (C.5) into Eq. (C.4) to obtain the power spectrum for the beat $V_B$ and setting the analyzer at 10 MHz with the bandwidth of 100 kHz, the $|V_\circ(t)|^2$ at 5 kHz after the recovery by the squarer is

$$|V_\circ(t)|^2 \propto E_S^* E_{LO1} E_S E_{LO2}^* e^{-i(\Omega_{LO1}-\Omega_{LO2})t} + cc \tag{C.6}$$

Here $\Omega_{LO1} - \Omega_{LO2} = 5$ kHz. The in-phase and out-of-phase components of the $|V_\circ(t)|^2$ at 5 kHz correspond to $S_R$ and $S_I$ in Eq. (3.8). Note that $E_S^* E_{LO1}$ in integrated over the transverse plane as is $E_S E_{LO2}^*$. It is worth noting that the component $E_S^* E_{LO1}$ of Eq. (C.6) is corresponds to the measurement of the position distribution in $S(x_\circ, p_\circ)$ of Eq. (3.8) by the tightly focussed LO1 beam. Similarly, the component $E_S E_{LO2}^*$ of Eq. (C.6) indicates the measurement of the momentum distribution in $S(x_\circ, p_\circ)$ of Eq. (3.8) by the collimated LO2 beam.

# Bibliography

[1] D. Gottesman and H. K. Lo. From quantum cheating to quantum security. *Physics Today*, page 22, Nov 2000.

[2] S. J. D. Phonenix and P. D. Townsend. Quantum cryptography: how to beat the code breakers using quantum mechanics. *Contemporary Physics*, 36(3):165, 1995.

[3] A. Barenco. Quantum physics and computers. *Contemporary physics*, 37(5):375, 1996.

[4] A. Rauschenbeutel, G. Nogues, S. Osnaghi, P. Bertet, M. Brune, J. M. Raimond, and S. Haroche. Step-by-step engineered multiparticle entanglement. *science*, 288:2024, 2000.

[5] R. J. Hughes, D. M. Alde, P. Dyer, G. G. Luther, G. L. Morgan, and M. Schauer. Quantum cryptography. *Contemporary Physics*, 36(3):149, 1995.

[6] R. Feynman, R. B. Leighton, and M. L. Sands, editors. *The Feynman lectures on physics. Vol.III.* Addison-Wesley Publishing Co., 1989.

[7] A. Einstein, B. Podolsky, and N. Rosen. Can Quantum Mechanical Description of Physical Reality Be Considered Complete. *Phys. Rev.*, 47:777, May 1935.

[8] J. S. Bell, editor. *Speakable and Unspeakable in Quantum Mechanics.* Cambridge University Press, 1987.

[9] John F. Clauser and Abner Shimony. Bell's Theorem: Experimental Test and Implication. *Rep. Prog. Phys.*, 41:1881, 1978.

[10] Special Issue on Quantum Information. *Physics World*, page 33, March 1998.

[11] D. Deutsch. Quantum theory, the Church-Turing principle and the universal quantum computer. *Proc. R. Soc. Lond.*, A 400:97, 1985.

[12] D. Deutsch and R. Jozsa. Rapid solution of problems by quantum computation. *Proc. R. Soc. Lond.*, A 439:553, 1992.

[13] P. W. Shor. Polynomial-time algorithms for prime factorization and discrete logarithms on quantum computer. *SIAM J. Comput.*, 26:1484, 1997.

[14] L. Grover. Quantum computers can search arbitrarily large databases by a single query. *Phys. Rev. Lett.*, 79:4709, 1997.

[15] N. J. Cerf, C. Adami, and P. G. Kwiat. Optical simulation of quantum logic. *Phys. Rev. A*, 57(3):R1477, March 1998.

[16] N. Imoto, H. A. Haus, and Y. Yamamoto. Quantum nondemolition measurement of the photon number via the optical Kerr effect. *Phys. Rev. A*, 32(4):2287, October 1985.

[17] M. Kitagawa and Y. Yamamoto. Number-phase minimum-uncertainty state with reduced number uncertainty in a Kerr nonlinear interferometer. *Phys. Rev. A*, 34(5):3974, November 1986.

[18] E. Knill, R. Laflamme, and G. J. Milburn. A scheme for efficient quantum computation with linear optics. *Nature*, 409:46, January 2001.

[19] Hwang Lee, Pieter Kok, N. J. Cerf, and J. P. Dowling. Linear optics and projective measurements alone suffice to create large-photon-number path entanglement. *Phys. Rev. A*, 65:030101–1, 2002.

[20] J. H. Howell and J. A. Yeazell. Quantum computation through entangling single photons in multipath interferometers. *Phys. Rev. Lett.*, 85(1):198, July 2000.

[21] C. H. Bennett and G. Brassard. Linear optics and projective measurements alone suffice to create large-photon-number path entanglement. *Proceedings of the International Conference on Computer Systems and Signal Processing, Bangalore*, page 175, 1984.

[22] J. M. Merolla, Y. Mazurenko, J. P. Goedgebuer, and W. T. Rhodes. Single-photon interference in sidebands of phase modulated light for quantum cryptography. *Phys. Rev. Lett.*, 82(8):1656, February 1999.

[23] Artur K. Ekert. Quantum cryptography based on Bell's theorem. *Phys. Rev. Lett.*, 67(6):661, August 1991.

[24] T. Jennewein, C. Simon, G. Weihs, H. Weinfurter, and A. Zeilinger. Quantum cryptography with entangled photons. *Phys. Rev. Lett.*, 84(20):4729, May 2000.

[25] V. Buzek and M. Hillery. Quantum cryptography based on Bell's Theorem. *Phys. Rev. A*, 54(6):1844, August 1996.

[26] I. Chuang, L. M. K. Vandersypen, X. Zhou, D. W. Leung, and S. Lloyd. Experimental realization of a quantum algorithnm. *Nature*, 393:143, May 1998.

[27] C. H. Bennett, G. Brassard, C. Crepeau, R. Jozsa, A. Peres, and W. K. Wootters. Teleporting an unknown quantum state via dual classical and Einstein-Podolsky-Rosen channels. *Phys. Rev. Lett.*, 70(13):1895, March 1993.

[28] D. Bouwmeester, J. W. Pan, K. Mattle, M. Eibl, H. Weinfurter, and A. Zeilinger. Experimental quantum teleportation. *Nature*, 390:575, December 1997.

[29] D. Bouwmeester, J. W. Pan, M. Daniell, H. Weinfurter, and A. Zeilinger. Observation of three photon Greenberger-Horne-Zeilinger entanglement. *Phys. Rev. Lett.*, 82(7):1345, 1999.

[30] S. F. Pereira, Z. Y. Ou, and H. J. Kimble. Quantum communication with correlated nonclassical states. *Phys. Rev. A*, 62:042311–1, 2000.

[31] S. L. Braunstein P. V. Loock and H. J. Kimble. Broad band teleportation. *Phys. Rev. A*, 62:042311–1, 2000.

[32] A. S. Parkins and H. J. Kimble. Broad band teleportation. *J. Opt. Soc. Am. B*, 1:496, 1999.

[33] L. Vaidman. Teleportation of a state. *Phys. Rev. A*, 49:1473, 1994.

[34] A. Furusawa, J. L. Sorensen, S. L. Braunstein, C. A. Fuchs, K. J. Kimble, and E. S. Polzik. Unconditional quantum teleportation. *Science*, 282:706, October 1998.

[35] S. L. Braunstein and H. J. Kimble. Teleportation of continuous quantum variables. *Phys. Rev. Lett.*, 80(4):869, Jan 1998.

[36] S. L. Braunstein and A. Mann. Measurement of the bell operator and quantum teleportation. *Phys. Rev. A*, 51(3):R1727, March 1995.

[37] T. Jennewein, G. Weihs, J. W. Pan, and A. Zeilinger. Experimental nonlocality proof of quantum teleportation and entanglement swapping. *Phys. Rev. Lett.*, 88(1):017903–1, Jan 2002.

[38] D. Dragoman. Classical optical analogs of quantum Fock states. *Optik*, 111(9):393, 2000.

[39] K. F. Lee, F. Reil, S. Bali, A. Wax, and J. E. Thomas. Heterodyne measurement of Wigner distributions for classical optical fields. *Opt. Lett.*, 24(19):1370, Oct 1999.

[40] S. Wallentowitz, I. A. Walmsley, and J. H. Eberly. How big is a quantum computer? *e-print quant-ph/0009069*, 2000.

[41] Krysztof Wodkiewicz and G. H. Herling. Classical and nonclassical interference. *Phys. Rev. A*, 57:815, 1998.

[42] S. Massar, D. Bacon, N. J. Cerf, and R. Cleve. Classical simulation of quantum entanglement without local hidden variables. *Phys. Rev. A*, 63:052305–1, 2001.

[43] R. J. C. Spreeuw. Classical wave optics analogy of quantum information processing. *Phys. Rev. A*, 63:062302–1, 2001.

[44] R. J. C. Spreeuw. A classical analog of entanglement. *Found. Phys.*, 28(3):361, 1998.

[45] Seth Lloyd. Quantum search without entanglement. *Phys. Rev. A*, 61:010301–1, 1999.

[46] N. Bhattacharya, H. B. Van Linden, Van den Henvell, and R. J. C. Spreeuw. Implementation of quantum search algorithm using classical fourier optics. *Phys. Rev. Lett.*, 88(13):137901–1, April 2002.

[47] E. P. Wigner. On the quantum correction for thermodynamic equilibrium. *Phys. Rev.*, 40:749, Jun 1932.

[48] M. Hillery, R. F. O'Connell, M. O. Scully, and E. P. Wigner. Distribution functions in physics: fundamental. *Physics Reports*, 106(3):121, 1984.

[49] M. J. Bastiaans. The Wigner distribution function applied to optical signals and systems. *Opt. Commun.*, 25:26, 1978.

[50] A. Wax and J. E Thomas. Measurement of smoothed Wigner phase space distributions for a small-angle scattering in a turbid medium. *J. Opt. Soc. Am. A*, 15:1896, 1998.

[51] A. Wax, S. Bali, G. A. Alphonse, and J. E Thomas. Characterizing the coherence of broadband sources using optical phase space contours. *J. Biomed. Opt.*, 4(4):482, 1999.

[52] C. Iaconis and I. A. Walmsley. Direct measurement of the two-point field correlation function. *Opt. Lett.*, 21(21):1783, Nov 1996.

[53] Amnon Yariv, editor. *Optical Electronics.* Holt, Rinehart and Winston, New York, 1985.

[54] M. Freyberger and W. P. Schleich. True vision of a quantum state. *Nature*, 386:121, Mar 1997.

[55] Werner Vogel. Nonclassical states: An observable criterion. *Phys. Rev. Lett.*, 84(9):1849, Feb 2000.

[56] Wolfgang Schleich, editor. *Quantum optics in phase space.* WILEY-VCH Verlag, 2001.

[57] David J. Griffiths, editor. *Introduction to quantum mechanics.* Prentice-Hall, Inc., 1995.

[58] K. F. Lee and J. E. Thomas. Experimental simulation of two particle quantum entanglement using classical fields. *Phys. Rev. Lett.*, 88(9):097902–1, Mar 2002.

[59] John S. Townsend, editor. *A modern approach to quantum mechanics.* McGraw-Hill, Inc., 1992.

[60] A. Wax and J. E. Thomas. Optical heterodyne imaging and Wigner phase space distributions. *Opt. Lett.*, 21(18):1427, Sept 1996.

[61] Paul Horowitz and Winfield Hill, editors. *The Art of Electronics.* Cambridge University Press, 1997.

[62] Z. Y. Ou and L. Mandel. Violation of Bell's inequality and classical probability in a two-photon correlation experiment. *Phys. Rev. Lett.*, 61(1):50, July 1988.

[63] J. W. Pan, D. Bouwmeester, M. Daniell, H. Weinfurter, and A. Zeilinger. Experimental test of quantum nonlocality in three photon greenberger-horne-zeilinger entanglement. *Nature*, 403:515, February 2000.

[64] J. W. Pan, M. Daniell, S. Gasparoni, G. Weihs, and A. Zeilinger. Experimental demonstration of four-photon entanglement and high fidelity teleportation. *Phys. Rev. Lett.*, 86(20):4435, May 2001.

[65] J. W. Pan, D. Bouwmeester, H. Weinfurter, and A. Zeilinger. Experimental entanglement swapping: Entangling photons that never interacted. *Phys. Rev. Lett.*, 80(18):3891, May 1998.

[66] Asher Peres, editor. *Quantum Theory: Concepts and Methods.* Kluwer Academic Publishers, 1993.

[67] N. V. Evdokimov, D. N. Klyshko, V. P. Komolov, and V. A. Yarochkin. Bell's inequalities and EPR-Bohm correlations: working classical radiofrequency model. *Phys.-Uspk*, 39:83, May 1996.

[68] J. G. Rarity, P. R. Tapster, E. Jakeman, T. Larchuk, R. A. Campos, M. C. Teich, and B. E. A. Saleh. Two-photon interference in a Mach-Zehnder interferometer. *Phys. Rev. Lett.*, 65(11):1348, Sept 1990.